

Studies in Comp



Agus Budiyo
Bambang Riy
Endra Joelian

Intelligen

U

Agus Budiyo, Bambang Riyanto, and Endra Joelianto (Eds.)

Intelligent Unmanned Systems: Theory and Applications

Studies in Computational Intelligence, Volume 192

Editor-in-Chief

Prof. Janusz Kacprzyk
Systems Research Institute
Polish Academy of Sciences
ul. Newelska 6
01-447 Warsaw
Poland
E-mail: kacprzyk@ibspan.waw.pl

Further volumes of this series can be found on our homepage:
springer.com

Vol. 169. Nadia Nedjah, Luiza de Macedo Mourelle and Janusz Kacprzyk (Eds.)
Innovative Applications in Data Mining, 2009
ISBN 978-3-540-88044-8

Vol. 170. Lakhmi C. Jain and Ngoc Thanh Nguyen (Eds.)
Knowledge Processing and Decision Making in Agent-Based Systems, 2009
ISBN 978-3-540-88048-6

Vol. 171. Chi-Keong Goh, Yew-Soon Ong and Kay Chen Tan (Eds.)
Multi-Objective Memetic Algorithms, 2009
ISBN 978-3-540-88050-9

Vol. 172. I-Hsien Ting and Hui-Ju Wu (Eds.)
Web Mining Applications in E-Commerce and E-Services, 2009
ISBN 978-3-540-88080-6

Vol. 173. Tobias Grosche
Computational Intelligence in Integrated Airline Scheduling, 2009
ISBN 978-3-540-89886-3

Vol. 174. Ajith Abraham, Rafael Falcón and Rafael Bello (Eds.)
Rough Set Theory: A True Landmark in Data Analysis, 2009
ISBN 978-3-540-89886-3

Vol. 175. Godfrey C. Onwubolu and Donald Davendra (Eds.)
Differential Evolution: A Handbook for Global Permutation-Based Combinatorial Optimization, 2009
ISBN 978-3-540-92150-9

Vol. 176. Beniamino Murgante, Giuseppe Borruo and Alessandra Lapucci (Eds.)
Geocomputation and Urban Planning, 2009
ISBN 978-3-540-89929-7

Vol. 177. Dikai Liu, Lingfeng Wang and Kay Chen Tan (Eds.)
Design and Control of Intelligent Robotic Systems, 2009
ISBN 978-3-540-89932-7

Vol. 178. Swagatam Das, Ajith Abraham and Amit Konar
Metaheuristic Clustering, 2009
ISBN 978-3-540-92172-1

Vol. 179. Mircea Gh. Negoita and Sorin Hintea
Bio-Inspired Technologies for the Hardware of Adaptive Systems, 2009
ISBN 978-3-540-76994-1

Vol. 180. Wojciech Mitkowski and Janusz Kacprzyk (Eds.)
Modelling Dynamics in Processes and Systems, 2009
ISBN 978-3-540-92202-5

Vol. 181. Georgios Miaoulis and Dimitri Plemenos (Eds.)
Intelligent Scene Modelling Information Systems, 2009
ISBN 978-3-540-92901-7

Vol. 182. Andrzej Bargiela and Witold Pedrycz (Eds.)
Human-Centric Information Processing Through Granular Modelling, 2009
ISBN 978-3-540-92915-4

Vol. 183. Marco A.C. Pacheco and Marley M.B.R. Vellasco (Eds.)
Intelligent Systems in Oil Field Development under Uncertainty, 2009
ISBN 978-3-540-92999-4

Vol. 184. Ljupco Kocarev, Zbigniew Galias and Shiguo Lian (Eds.)
Intelligent Computing Based on Chaos, 2009
ISBN 978-3-540-95971-7

Vol. 185. Anthony Brabazon and Michael O'Neill (Eds.)
Natural Computing in Computational Finance, 2009
ISBN 978-3-540-95973-1

Vol. 186. Chi-Keong Goh and Kay Chen Tan
Evolutionary Multi-objective Optimization in Uncertain Environments, 2009
ISBN 978-3-540-95975-5

Vol. 187. Mitsuo Gen, David Green, Osamu Katai, Bob McKay, Akira Namatame, Ruhul A. Sarker and Byoung-Tak Zhang (Eds.)
Intelligent and Evolutionary Systems, 2009
ISBN 978-3-540-95977-9

Vol. 188. Agustín Gutiérrez and Santiago Marco (Eds.)
Biologically Inspired Signal Processing for Chemical Sensing, 2009
ISBN 978-3-642-00175-8

Vol. 189. Sally McClean, Peter Millard, Elia El-Darzi and Chris Nugent (Eds.)
Intelligent Patient Management, 2009
ISBN 978-3-642-00178-9

Vol. 190. K.R. Venugopal, K.G. Srinivasa and L.M. Patnaik
Soft Computing for Data Mining Applications, 2009
ISBN 978-3-642-00192-5

Vol. 191. Zong Woo Geem (Ed.)
Music-Inspired Harmony Search Algorithm, 2009
ISBN 978-3-642-00184-0

Vol. 192. Agus Budiyo, Bambang Riyanto and Endra Joelianto (Eds.)
Intelligent Unmanned Systems: Theory and Applications, 2009
ISBN 978-3-642-00263-2

Agus Budiyo
Bambang Riyanto
Endra Joelianto (Eds.)

Intelligent Unmanned Systems: Theory and Applications

Agus Budiyo, PhD
Dept. of Aerospace Information Engineering
(Smart Robot Center)
Konkuk University
1 Hwayang-dong Gwangjin-Gu
Seoul 143-701
Korea
Email: agus@konkuk.ac.kr

Endra Joelianto, PhD
Instrumentation and Control Research Group
Dept. of Engineering Physics
Institut Teknologi Bandung
Jl Ganesha 10
Bandung 40132
Indonesia
Email: ejoel@tf.itb.ac.id

Bambang Riyanto, PhD
School of Electrical and Information
Engineering
Institut Teknologi Bandung
Jl Ganesha 10
Bandung 40132
Indonesia
Email: briyanto@lskk.ee.itb.ac.id

ISBN 978-3-642-00263-2

e-ISBN 978-3-642-00264-9

DOI 10.1007/978-3-642-00264-9

Studies in Computational Intelligence

ISSN 1860949X

Library of Congress Control Number: 2009920516

© 2009 Springer-Verlag Berlin Heidelberg

This work is subject to copyright. All rights are reserved, whether the whole or part of the material is concerned, specifically the rights of translation, reprinting, reuse of illustrations, recitation, broadcasting, reproduction on microfilm or in any other way, and storage in data banks. Duplication of this publication or parts thereof is permitted only under the provisions of the German Copyright Law of September 9, 1965, in its current version, and permission for use must always be obtained from Springer. Violations are liable to prosecution under the German Copyright Law.

The use of general descriptive names, registered names, trademarks, etc. in this publication does not imply, even in the absence of a specific statement, that such names are exempt from the relevant protective laws and regulations and therefore free for general use.

Typeset & Cover Design: Scientific Publishing Services Pvt. Ltd., Chennai, India.

Printed in acid-free paper

9 8 7 6 5 4 3 2 1

springer.com

Preface

The book largely represents the extended version of select papers from the International Conference on Intelligent Unmanned System ICIUS 2007 which was jointly organized by the Center for Unmanned System Studies at Institut Teknologi Bandung, Artificial Muscle Research Center at Konkuk University and Institute of Bio-inspired Structure and Surface Engineering, Nanjing University of Aeronautics and Astronautics. The joint-event was the 3rd conference extending from International Conference on Emerging System Technology (ICEST) in 2005 and International Conference on Technology Fusion (ICTF) in 2006 both conducted in Seoul. ICIUS 2007 was focused on both theory and application primarily covering the topics on robotics, autonomous vehicles and intelligent unmanned technologies. The conference was arranged into three parallel symposia with the following scope of topics:

Unmanned Systems: Micro air vehicle, Underwater vehicle, Micro-satellite, Unmanned aerial vehicle, Multi-agent systems, Autonomous ground vehicle, Blimp, Swarm intelligence, learning and control

Robotics and Biomimetics: Artificial muscle actuators, Smart sensors, Design and applications of MEMS/NEMS system, Intelligent robot system, Evolutionary algorithm, Control of biological systems, AI and expert systems, Biological learning control systems, Neural networks, Genetic algorithm

Control and Intelligent System: Distributed intelligence, Distributed/decentralized intelligent control, Distributed or decentralized control methods, Distributed and embedded systems, Embedded intelligent control, Complex systems, Discrete event systems, Hybrid systems, Networked control systems, Delay systems, Fuzzy systems, Identification and estimation, Nonlinear systems, Precision motion control, Control applications, Control engineering education.

The book is organized into three parts which reflect the spectrum of the conference themes. The first part of the book consists of five chapters dealing with the study of unmanned systems. Space applications of unmanned systems are presented in the first two chapters. Chapter 1 deals with the application of image processing algorithm for the autonomous guidance of lunar probe. A new approach using computer vision is proposed for providing precise motion estimation for probe landing. The purpose of the image algorithm is to detect and track feature points which are factors of navigation. In this chapter, the algorithm is illustrated as two steps: firstly, fixation areas are detected as sub-images and matched. Secondly, feature points are extracted from

sub-images and tracked. Computer simulation demonstrates the result of algorithm takes less computation and fulfils requirements of navigation algorithm. Chapter 2 discusses classification of locomotion mechanism of intelligent unmanned explorer for deep space exploration. The chapter provides the comparison of the speed of hopping and wheeled robots and some simulation studies are performed to analyze the detailed mobility of wheeled robots.

The rest of the Part I center on the modeling, control and guidance for rotorcraft-based unmanned aerial vehicle. Chapter 3 addresses the need for global linear models of a small scale helicopter for control design. This chapter presents a step by step development of linear model for small scale helicopter based on first-principle approach. Beyond the previous work in literatures, the calculation of the stability derivatives is presented in detail. A computer program is used to solve the equilibrium conditions and then calculate the change in aerodynamics forces and moments due to the change in each degree of freedom and control input. Chapter 4 deals with the implementation of a novel control technique combining algebraic approach and LQ design. The viability of the method is demonstrated for hovering control of small-scale helicopter simultaneously subjected to plant parameter uncertainties and wind disturbances. Chapter 5 discusses the control strategy for four-rotor vertical take-off and landing (VTOL) aerial robot called X4-flyer. The kinematics control law is first derived using Astolfi's discontinuous control. A backstepping control method is then introduced providing the kinematic based inputs to construct the torque control of X4-flyer. The effectiveness of the approach is demonstrated through computer simulations.

The second part of the book deals with diverse issues in robotics and biomimetics. Chapter 6 introduces an insect-inspired flapper device mimicking general characteristics of flying insects. The flapper was actuated by a unimorph piezoelectric composite actuator and a compressed one, respectively, for force generation comparison. The chapter discusses flapping tests which were conducted both in the air and in a vacuum chamber to measure total vertical force and vertical inertia force. The optimal operation of the flapper is corroborated experimentally. Chapter 7 presents successful development on bio-mimetic wing design inspired from cicada. The aerodynamic force measurement, wing kinematics observation and wind tunnel test were conducted to evaluate the performance between normal wing and bio-mimetic wing. It was shown that the bio-mimetic wing is superior to the normal wing in terms of not only force generation but also the aspect of appropriate wing kinematics. Chapter 8 deals with application of multiple mobile robot types for management of environmental conditions. The authors propose a system which consists of a database center and various autonomous robots, each with different functions to allocate robots to manage environmental conditions. The overall concept and several important features of the proposed system are described. The study also proposes a position estimation method and explains the performance evaluation through experiments. In Chapter 9, the authors present a study of locomotion elicited by electrical stimulation in the mesencephalon of lizard *Gekko gekko*. Their results show that it is possible to carry-out artificial induction on *Gekko gekko* through electrical stimulation on the related nucleus in their brain. Chapter 10 discusses a concept of intelligent mechanical design for autonomous mobile robot. The design principle provides the guidance for investigating mechanics' self-controllability, reliability, realizability, and compatibility for autonomous mobile

robot. Chapter 11 is focused on a method for mobile robot path planning to a destination and obstacle avoidance based on neural network and genetic algorithm. The avoidance action of a wheeled type robot is determined from the obstacle configuration, the robot's self-state and destination information using a neural network where the design parameter is adjusted by using genetic algorithm. The effectiveness of present method is proved through a simulation.

Part III covers topics in control theory and intelligent system. Chapter 12 discusses the use of virtual reality simulation for robot design to meet certain criteria. The approach is emphasized through the simulation of Fire Fighting Robot in order to evaluate the performance of the robot design in meeting some of the contest rules such as navigating in a labyrinth arena without hitting walls, quickly extinguishing a flame in a room and return home. In Chapter 13, the authors study an important class of dynamics systems called under-actuated systems arising in robot manipulator. Monotonic decreasing energy and switching control are utilized to control such a system. Chapter 14 discusses feedback control system in which plant's sensors and actuators are connected to controller through a communication network. The technique extends point-to-point wired configuration found in conventional feedback control. Specifically, the authors address the synthesis of networked control systems that satisfy passivity requirements using linear matrix inequality approach. Chapter 15 deals with controlled switching dynamical systems using linear impulsive differential equations. The authors investigate a unified approach to analysis and to design the switching controller by formulating the phenomena as a hybrid system using linear impulsive differential equation representation. State jumps and mode changing of the controller responding to switched of plant dynamics are exploited and discussed. The switching controller is designed by using LMI method that will guarantee H_2 -type cost and implemented to a mini scale helicopter due to its complex dynamic and changing modes operation between hover and cruise. Chapter 16 discusses the use of neural networks for structural damage detection. The neural network was trained to recognize the behavior of static parameter of the undamaged structure as well as of the structure with various possible damage extent and location which were modeled as random states. The proposed techniques were applied to detect damage in a cantilever beam. The structure was analyzed using finite-element-method (FEM) and the damage identification was conducted by a back-propagation neural network using the change of the structural strain and displacement. Chapter 17 focuses on a methodology for simultaneous identification of fault parameters and mode switching events for hybrid systems. The authors propose a method based on the notion of Global Analytical Redundancy Relations (GARR) from the bond graph model of the hybrid system. A unified formula with mode change time sequence and initial mode coefficients (IMC) is derived to represent the mode switching. Fault parameters, mode switching time stamps and all IMC are encoded into one chromosome as a potential solution of the identification process. An electro-hydraulic system of vehicle is studied to illustrate the efficiency of the proposed algorithm.

The book covers multi-faceted aspects of intelligent unmanned systems. A wide array of relevant theory and applications are presented to address the current and future challenges in the area of unmanned systems. The editors would like to express their sincere appreciation for all the contributors for the cooperation in producing this

volume. Chapter 17 represents a contributed paper beyond the context of the conference. The contribution from the invited authors is gratefully acknowledged. Overall, all authors are to be congratulated for their efforts in preparing such excellent chapters. The editors wish that the readers from all relevant background will find this book not only stimulating but also useful and usable in whatever aspect of unmanned system design they are involved with and that it can inspire further advancement in other related research areas.

Agus Budiyo
Bambang Riyanto
Endra Joelianto

Contents

Image Processing in Optical Guidance for Autonomous Landing of Lunar Probe <i>Ding Meng, Cao Yun-feng, Wu Qing-xian, Zhang Zhen</i>	1
Locomotion Mechanism of Intelligent Unmanned Explorer for Deep Space Exploration <i>Takashi Kubota, Kei Takahashi, Shingo Shimoda, Tetsuo Yoshimitsu, Ichiro Nakatani</i>	11
Global Linear Modeling of Small Scale Helicopter <i>A. Budiyono, T. Sudiyanto, H. Lesmana</i>	27
Control of Small Scale Helicopter Using s-CDM and LQ Design <i>A. Budiyono, T. Sudiyanto</i>	63
Discontinuous Control and Backstepping Method for the Underactuated Control of VTOL Aerial Robots with Four Rotors <i>Keigo Watanabe, Kouki Tanaka, Kiyotaka Izumi, Kensaku Okamura, Rafiuddin Syam</i>	83
An Insect-Like Flapping-Wing Device Actuated by a Compressed Unimorph Piezoelectric Composite Actuator <i>Quoc Viet Nguyen, Hoon Cheol Park, Nam Seo Goo, Doyoung Byun</i>	101
Designing Cicada-Mimetic Flapping Wing with Composite Wing Structure and Application to Flapping MAV <i>Joon Hyuk Park, Kwang-Joon Yoon</i>	119
Robot-System for Management of Environmental Conditions Using Multiple Mobile Robot Types - Sample Application for Position Estimation - <i>N. Hashimoto, H. Adachi, S. Kato, K. Komoriya</i>	135

Locomotion Elicited by Electrical Stimulation in the Midbrain of the Lizard <i>Gekko gekko</i> <i>Wang Wenbo, Guo Ce, Sun Jiurong, Dai Zhendong</i>	145
How Does “Intelligent Mechanical Design Concept” Help Us to Enhance Robot’s Function? <i>Amir A.F. Nassiraei, Kazuo Ishii</i>	155
Multiple Moving Obstacles Avoidance for Wheeled Type Robots Using Neural Network <i>Tomohiro Yamaguchi, Yoshio Watanabe</i>	179
Virtual Reality Simulation of Fire Fighting Robot Dynamic and Motion <i>Joga D. Setiawan, Mochamad Subchan, Agus Budiyo</i>	191
Monotonic Decreasing Energy and Switching Control for Underactuated Manipulators <i>Kiyotaka Izumi, Keisuke Ichida, Keigo Watanabe, Yuichi Kamada</i>	205
Positive Real Synthesis of Networked Control System: An LMI Approach <i>Riyanto Bambang, Imam Arifin</i>	213
Controlled Switching Dynamical Systems Using Linear Impulsive Differential Equations <i>Endra Joeliyanto, Herman Y. Sutarto</i>	227
Structural Damage Detection Using Randomized Trained Neural Networks <i>Ismoyo Haryanto, Joga Dharma Setiawan, Agus Budiyo</i>	245
Fault and Mode Switching Identification for Hybrid Systems with Application to Electro-Hydraulic System in Vehicles <i>Ming Yu, Ming Luo, Shai Arogeti, Danwei Wang, Xinzheng Zhang</i>	257
Author Index	275

Image Processing in Optical Guidance for Autonomous Landing of Lunar Probe

Ding Meng^{1,*}, Cao Yun-feng^{1,2,**}, Wu Qing-xian¹, and Zhang Zhen¹

¹ School of Automatic Engineering of NanJing
University of Aeronautics and Astronautics
nuaa_dm@hotmail.com

² Academy of Frontier Science of NanJing
University of Aeronautics and Astronautics

Abstract. Because of the communication delay between earth and moon, the GNC technology of lunar probe is becoming more important than ever. Current navigation technology is not able to provide precise motion estimation for probe landing control system. Computer vision offers a new approach to solve this problem. In this paper, the authors introduce an image process algorithm of computer vision navigation for autonomous landing of lunar probe. The purpose of the algorithm is to detect and track feature points which are factors of navigation. Firstly, fixation areas are detected as sub-images and matched. Secondly, feature points are extracted from sub-images and tracked. Computer simulation demonstrates the result of algorithm takes less computation and fulfils requests of navigation algorithm.

Keywords: Fixation Area, Feature Point, Template Match, FPs Tracking.

1 Introduction

In paper[1], the status of China's deep space exploration plan is introduced including CE-1 lunar orbiter, the china's subsequent Lunar Exploration Program. It is an important purpose in the second stage of China lunar exploration to land accurately of probe on the moon's surface.

The guidance-navigation-control(GNC) technology of moon probe is becoming more important than ever. Because of the communication delay induced by the large distances between the earth and moon, human kinds are hardly able to guide probe to landing safely on the moon. Probe will have to use on-board sensors and algorithms. However, current navigation technology can't provide precision motion estimation for

* Ding Meng received B.E. and M.E degrees in School of Automatic Engineering of NanJing University of Aeronautics and Astronautics in 2003 and 2006. He is currently working toward Ph.D. in the same university. His interests are Computer Vision and Pattern Classification. Phone: 86-025-84890902.

** Cao Yun-feng received Ph.D in School of Automatic Engineering of NanJing University of Aeronautics and Astronautics in 2005. Now, he is the professor in Academy of Frontier Science of NanJing University of Aeronautics and Astronautics. His interests are Flight Control System and Intelligence Control.

probe landing control system [2]. Therefore, new motion estimation technology must be developed. Computer vision may offer an approach to solve this problem.

Up to now, computer vision has been successfully used for autonomous navigation of robot and Micro Air Vehicle [3], autonomous landing of Unmanned Helicopter [4], and intelligence traffic [5].

Some appliances are being researched in the field of space exploration. The Near Earth Asteroid Rendezvous (NEAR), rendezvoused with asteroid Eros 433 in February 2000, used optical navigation extensively for orbit determination and small body 3-D modeling [6]. The Deep Space 1 mission as a part of the New Millennium Program is flying an autonomous optical navigation technology demonstration. The DS-1 AutoOpNav system used onboard centroiding of reference asteroids for autonomous navigation during small body fly-bys [7]. However, for probe accurate landing, the new, more robust and more precise vision algorithm should be developed.

Image processing is the first step and a essential part of computer vision navigation. Generally, image processing of vision navigation study is mainly focused on feature detection and tracking. In 1997, Kawaguchi, from Japan, created a method, in which several fixed reference windows and a 2-D fast Fourier transform (FFT) algorithm were used in the correlation tracking [8]. In many case, flat areas must be chosen for landing security. Safe Landing Area Determination (SLAD), which offered by A. Johnson from Jet Propulsion Laboratory(JPL), achieved this task successfully [9]. However, there are no features or distinctive features on those landing sites. Although tracking by feature points is not the best way, feature points have to be filtered in order to avoid this problem. Point tracking is the usual way in vision navigation. In 1999, Andrew E. Johnson, from JPL, generated a method based on automatic feature point(FP) tracking between a pair of images followed by two frames [2]. As a part of MUSES-C, Japanese scientist Toshihiko Misu offered an algorithm based on fixation area, which fixates on the areas with local varying intensity, and employs shading pattern as a fixation area, and then tracked the center of the fixation area [10]. Real-time image processing is the essential request in computer vision navigation. Toshihiko's method requires less computation than Johnson's. Nevertheless, the Number of fixation area's center is difficult to satisfy the requirement of following navigation algorithm.

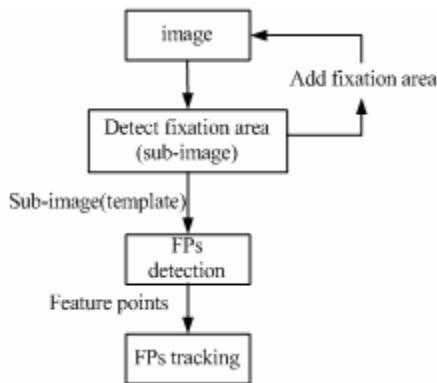


Fig.1. Procedure of algorithm

This paper introduces an image processing algorithm using feature point tracking in probe autonomous landing which built on the methods from Johnson and Toshihiko. The procedure is as follow (Fig. 1):

- Step1. Extract fixation areas as templates and sub-images.
- Step2. Match templates and detecting FPs from sub-images
- Step3. Match FPs

In section 2, fixation area detection algorithm is proposed. Feature point detection and tracking in the sub-images are explained in section 3 and section 4. Computer simulations of this algorithm are illustrated to demonstrate this image processing algorithm in section 5. In Section 6 we state conclusions.

2 Fixation Area Detection

In artificial environment, edges and vertexes are usually used as features in image tracking. But in natural environment, these shapes can't be found easily. Paper [11] proposed the use of ground control points based on Gabor function in image registration of natural terrain. In paper [10], shading pattern is employed as a fixation-area. To reduce computation, the averaging, Laplacian filtering and variance are used. In this paper, improved Toshihiko Misu's method is used firstly to pre-process primary image for obtaining sub-image. The purpose of this step is that block matching is more robust than point matching. We can match block firstly in entire image and then match points in sub-image.

The template for matching block is extracted as follows [10]:

- Step1. Enhance specific spatial wavelength of the original image by 2-D band-pass-filter.
- Step2. Calculate local variances of filtered image to evaluate "contrast".
- Step3. Extract high local-variance areas as templates.
- Step4. Least-square block matching. The matching is performed so as to minimize square error of the intensity between templates and region to be matched.

2.1 Band-Pass-Filter

The conception of filtering comes from the Fourier transform for signal processing in the frequency domain. Image processing is interested in filtering operations that are performed on the pixels of a digital image. The filter in the image processing is called spatial filtering. In generally, the image filter can be divided into smoothing spatial filter and sharpening spatial filter.

Firstly, original image should be processed by smoothing spatial filter to reduce noise. In fact, smoothing spatial filter is a type of low-pass-filter(LPF), includes linear filter, such as averaging filters, and nonlinear filter, such as median filters. To reduce the consumption of computational power and storage, we use averaging as LPF, which is different from averaging filter. The averaging filter can't change the size of original image and spend more time. The equation of averaging is:

$$E_s(u, v) = \frac{1}{S_x S_y} \sum_{i=0}^{S_x-1} \sum_{j=0}^{S_y-1} E(S_x u + i, S_y v + j) \quad (2.1)$$

Where $E_s(u, v)$ is the intensity of averaged and sub-sample image at (u, v) . The size of this image is $\frac{1}{S_x S_y}$ of size of original image. (S_x, S_y) is the sub-sampling interval.

Secondly, the 8-neighbor Laplacian is used as high-pass-filter. The mask of Laplacian as follows:

$$\begin{array}{|c|c|c|} \hline 1 & 1 & 1 \\ \hline 1 & -8 & 1 \\ \hline 1 & 1 & 1 \\ \hline \end{array}$$

2.2 Variance Map

To show locally varying intensity, the variance map is calculated. Statistical variance within a window and the size of which is equal to computed template is computed. The formulation is:

$$V(u, v) = \frac{S_x S_y}{W_x W_y} \sum_{i=0}^{w_x-1} \sum_{j=0}^{w_y-1} \{E_L(u+i, v+j)\}^2 - \left\{ \frac{S_x S_y}{W_x W_y} \sum_{i=0}^{w_x-1} \sum_{j=0}^{w_y-1} E_L(u+i, v+j) \right\}^2$$

Where $V(u, v)$ is the local variance of Laplacian-filtered image. $W_x \times W_y$ is the size of template. $E_L(u, v)$ is the intensity of Laplacian-filtered image at (u, v) . $w_x = \frac{W_x}{S_x}$,

$$w_y = \frac{W_y}{S_y}.$$

2.3 Template Extraction

Templates for tracking are extracted according to variance map. The high-local-variance points are selected as the template. We should pay attention: a. The points chosen as template in the variance map are not near the edge of the map, in order to easily track points in next frame image. b. Some other templates which aren't near extracted ones should be extracted also. This is because the cluster or single template would be weak to the observation noise which includes tracking error and error from the range measurement.

2.4 Template Matching

To track the fixation area, we employ least-square block matching. The matching is performed so as to minimize the square error of the intensity between template and region to be matched. The number of templates should be certain. If any template which has been out of the image can't be tracked, the new template is extracted instead.

3 FP Detection from Fixation Area

To the best of our knowledge, some real-time FPD algorithms have been described in many literatures. FPD based on Harris Corner Finding algorithm has been employed by ASSET-2 motion, segmentation and shape tracking system [12]. After detecting the fixation area, paper [10] assumed the center of the fixation area as an feature point. I don't think this is a good idea. In this paper, a FPD algorithm is selected to detect feature points from fixation area. We can use those points for match.

In this paper, we select and improve a FPD algorithm of Benedetti and Perona [14], which is based on the work of Tomasi and Kanada [13]. There are two reasons to select this algorithm.

- a) This algorithm decreased the complexity of Tomasi's method by eliminating the demand for any transcendental arithmetic operations and didn't require calculation of square root.
- b) This algorithm is easy to track across several frames.

It is difficult to detect an individual point because of the presence of noise and distortion. For this reason patches of pixels are actually considered. The method proposed in paper[14] for detect FP is expressed simply as follows:

Step 1. Computing the image gradient across the image at each pixel location

$$I_x(x, y, t) = \frac{I(x+1, y) - I(x-1, y)}{2} \quad (3.1)$$

$$I_y(x, y, t) = \frac{I(x, y+1) - I(x, y-1)}{2} \quad (3.2)$$

$I(x, y, t)$ denoted the continuous function defining the brightness values of a sequence of images captured by a camera. The partial derivatives of $I(x, y, t)$ with respect to x, y , are denoted respectively by $I_x(x, y, t)$ and $I_y(x, y, t)$.

Step 2. Defining matrix G

$$G = \begin{bmatrix} \sum_{W_1} (I_x(x, y, t))^2 & \sum_{W_1} I_x(x, y, t) I_y(x, y, t) \\ \sum_{W_1} I_x(x, y, t) I_y(x, y, t) & \sum_{W_1} (I_y(x, y, t))^2 \end{bmatrix} \quad (3.3)$$

$$= \begin{bmatrix} a & b \\ b & c \end{bmatrix}$$

W_1 denoted feature patch of pixels including pixel point (x, y) .

Step 3. Find $P_{\lambda}(i, j)$

$$P_{\lambda}(i, j) = (a - \lambda)(c - \lambda) - b^2 \quad (3.4)$$

Step 4. Retain pixel if $P_{\lambda}(i, j) > 0, a(i, j) > \lambda$, λ is a threshold value.

Step 5. Perform a final non-maximum suppression step on $\lambda_1(i, j)$, yielding the actual feature locations.

The fixation is the area with local varying intensity, so good features for tracking are expected to be abundant. At present, there are two strategies for feature point search: exhaustive search and random search strategy. The first one is traditional feature point detection algorithm which searches the image for every distinction exhaustively. Suppose that N feature points are needed for motion estimation which is the purpose of searching. The random search strategy selects a pixel at randomly from the image. If the randomly selected pixel has an interest value greater than a predetermined threshold, it is as a feature point. This procedure is repeated until N feature points are detected. Compared with the first algorithm, the second one raised the speed of detection. In this paper, we use exhaustive search to obtain enough FPs because the size of sub-image is small.

4 Feature Point Tracking

The next step is to locate the features detected in the first frame in the second frame. This procedure is called feature tracking. Feature tracking can be divided into two groups of algorithm: correlation based methods and optical flow based method. Correlation based methods require more computation and are appropriate when the motion of features in the image is large, Such as RANSAC. In this paper, we use Tomasi-Kanade's feature tracking which is optical flow based method [15].

When the camera moves, the patterns of image intensities change in a complex way. However, images taken at late time instants are usually strongly related to each other, because they refer to the same scene taken from only slightly different viewpoints.

$$I(x, y, t) = I(x + d_x, y + d_y, t + \tau) \quad (4.1)$$

Using Taylor-series expansion, obtaining:

$$I(x + d_x, y + d_y, t + \tau) \approx I(x, y, t) + I_x d_x + I_y d_y + I_t \tau \quad (4.2)$$

From (4.1) and (4.2):

$$I_x d_x + I_y d_y + I_t \tau = 0 \quad (4.3)$$

Equation (4.3) is called optical flow constraint equation.

If every pixel(N pixels) in the feature window has the same displacement, we can obtain:

$$\begin{bmatrix} I_x^1 & I_y^1 \\ \bullet & \bullet \\ \bullet & \bullet \\ \bullet & \bullet \\ I_x^N & I_y^N \end{bmatrix} \begin{bmatrix} d_x \\ d_y \end{bmatrix} = - \begin{bmatrix} I_t^1 \\ \bullet \\ \bullet \\ \bullet \\ I_t^N \end{bmatrix} \quad (4.4)$$

The displacement of window can be gained by least-square.

$$\begin{bmatrix} \sum_{k=1}^N (I_x^k)^2 & \sum_{k=1}^N I_x^k I_y^k \\ \sum_{k=1}^N I_x^k I_y^k & \sum_{k=1}^N (I_y^k)^2 \end{bmatrix} \begin{bmatrix} d_x \\ d_y \end{bmatrix} = - \begin{bmatrix} \sum_{k=1}^N I_x^k I_t^k \\ \sum_{k=1}^N I_y^k I_t^k \end{bmatrix} \quad (4.5)$$

$$\text{i.e., } Gd = e \quad (4.6)$$

$$\text{Displacement is: } d = G^{-1}e \quad (4.7)$$

5 Computer Simulations and Result

According to the algorithm which has been expounded in this paper, we give the result of computer simulations in this section. Fig. 2(a)(b)(c) are original images of continuous frame.

Fig. 2(a) is LPF image of Fig. 1(a), $S_x = S_y = 5$. Fig. 2(b) is the image by Laplacian filtering. Fig. 3(c) is variance map(4×4) of Fig. 1(a). Fig. 3(d) is the extracted areas on original image.

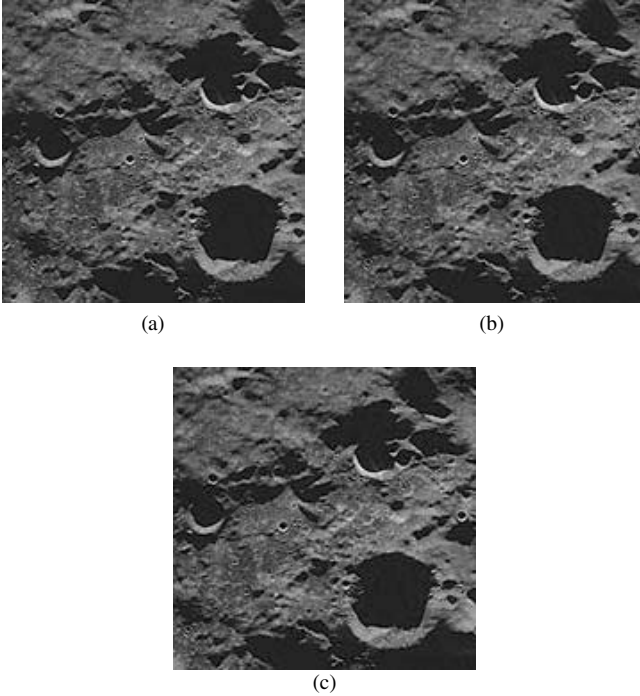


Fig. 2. Original images of continuous frame

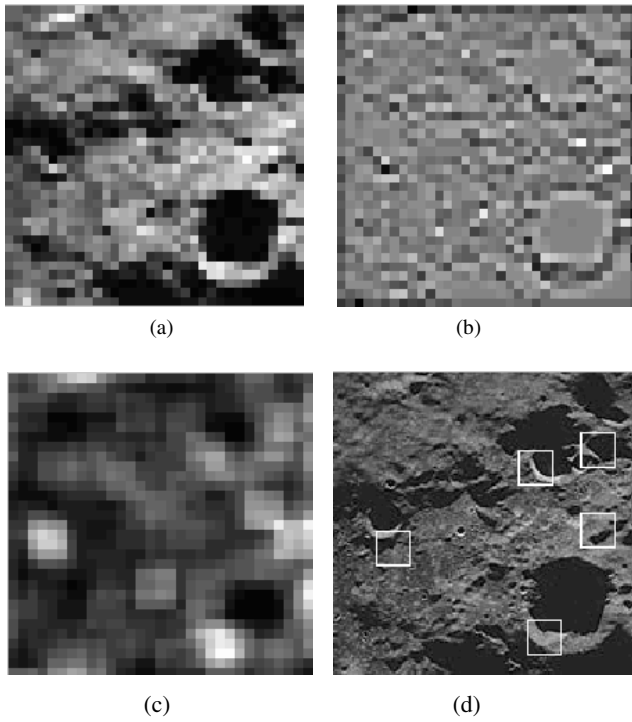


Fig. 3. Proceed image

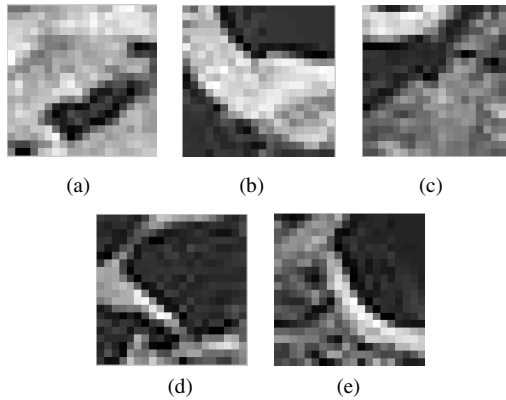


Fig. 4. Templates(sub-image)

Fig. 4(a)(b)(c)(d)(e) is five templates(20×20) from Fig. 2(a).

Fig. 5 illustrates the result of template match. White Square means the position of sub-images from 3 frames images in the first frame. Arrow means the direction of template moving.

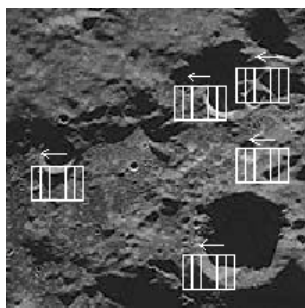


Fig. 5. Template match

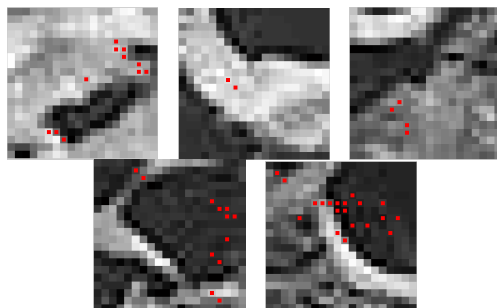


Fig. 6. FPs detection

Fig. 6 illustrates the results of FPs detection. $W1=3$, $\text{threshold}=1500$. Fig7 illustrates the result of FPs tracking in the sub-image. Fig8 is the result of FPs tracking in the whole image.

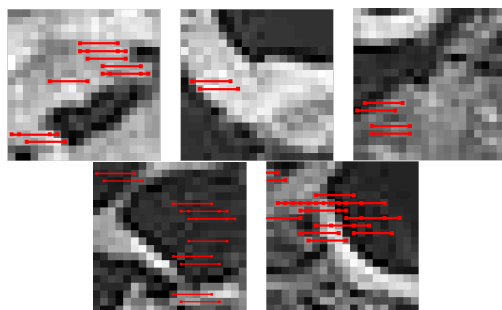


Fig. 7. FPs tracking of sub-image

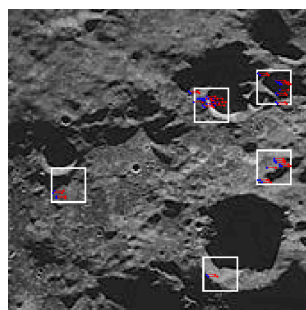


Fig. 8. FPs tracking of whole image

6 Conclusions

Computer simulation demonstrates that we can receive enough FPs real-timely and correctly. FPs can be extracted from the sub-images, as a result, FPs tracking algorithm cost less computation than other methods. At the same time, the field of FPs tracking becomes smaller, so the level of FPs matching becomes higher. This algorithm should be improved in the future. We should extend the distance between different feature points. The purpose is to make the result of motion estimation more correct.

References

- [1] Peijian, Y., Jing, P.: Deep Space Exploration and Prospect in China. Engineering Science 8(10) (October 2006)
- [2] Matthies, L.H., Johnson, A.E.: Precise Image-Based Motion Estimation for Autonomous Small Body Exploration. In: 5th International Symposium on Artificial Intelligence and Automation in Space, Noordwijk, pp. 627–634 (June 1999)

- [3] Ettinger, S.M., Nechyba, M.C., Ifju, P.D.: Vision-Guided Flight Stability and Control for Micro Air Vehicles. In: IEEE Int. Conf. on Intelligent Robots and Systems, pp. 2134–2140 (2002)
- [4] Saripalli, S., Montgomery, J.F., Sukhatme, G.S.: Vision-Based Autonomous Landing of an Unmanned Aerial Vehicle. In: Preceeding of IEEE International Conference on Robotics and Automation, pp. 2799–2804 (2002)
- [5] Cucchiara, R., Grana, C., Piccardi, M., et al.: Statistic and Knowledge-based moving object detection in traffic scenes. Proceedings of IEEE Intelligent Transportation Systems (2000)
- [6] Miller, J.K., et al.: Navigation analysis For Eros rendezvous and orbital phases. Journal Astronautical Sciences 43(4), 453–476 (1995)
- [7] Szeliski, R., Kang, S.B.: Recovering 3-D shape and motion from image streams using non-linear least squares. Journal Visual Communication and Image Representation 5(1), 10–28 (1994)
- [8] Kawaguchi, J., Hashimoto, T., Kubota, T., Sawai, S., Fujii, G.: Autonomous optical guidance and navigation strategy around a small body. AIAA Journal of Guidance, Control, and Dynamics 20(5), 1010–1017 (1997)
- [9] Johnson, A., Klump, A., Collier, J., AronWolf: LIDAR-Base Hazard Avoidance for Safe Landing on Mars. AAS/AIAA Space Flight Mechanics Meeting, Santa Barbara, CA (February 2001)
- [10] Misu, T., Hashimoto, T., Ninomiya, K.: Optical Guidance for Autonomous Landing of Spacecraft. IEEE Transactions on Aerospace and Electronic 35(2) (April 1999)
- [11] Zheng, Q., Chellappa, R.: A computational approach to image registration. IEEE Transactions on Image Processing 2(3), 311–326 (1993)
- [12] Smith, S., Brady, J.: 4sset-2: Real-time Motion Segmentation and Shape Tracking. IEEE Trans. on Pattern Analysis and Machine Intelligence 8(17), 814–820 (1995)
- [13] Shi, J., Tomasi, C.: Good Features to Track. In: IEEE Conf. Comput. Vision and Pattern Recognition, pp. 593–600 (1994)
- [14] Benedetti, A., Perona, P.: Real-time 2-D Feature Detection on a Reconfigurable Computer. In: IEEE Conf. Computer Vision and Pattern Recognition, pp. 586–593 (1998)
- [15] Tommasini, T., Fusiello, A.: Making Good Feature Tracker Better. In: IEEE Comput. Soc. Conf. Computer Vision and Pattern Recognition, Santa Barbara, USA, pp. 178–182 (1998)

Locomotion Mechanism of Intelligent Unmanned Explorer for Deep Space Exploration

Takashi Kubota, Kei Takahashi, Shingo Shimoda, Tetsuo Yoshimitsu,
and Ichiro Nakatani

Institute of Space and Astronautical Science
Japan Aerospace Exploration Agency
3-1-1, Yoshinodai, Sahamihara, Japan, 229-8510
kubota@isas.jaxa.jp

Abstract. In recent years, such small body exploration missions as asteroids or comets have received remarkable attention in the world. In small body explorations, especially, detailed in-situ surface exploration by tiny rover is one of effective and fruitful means and is expected to make strong contributions towards scientific studies. Performance of mobility on surface explorer is highly dependent on the gravitational environment. Some researchers have proposed novel locomotion mechanisms for extremely small terrestrial bodies like asteroids. Hopping is a possible method under micro-gravity. It is not proved, however, that the proposed method of locomotion is optimum for a given level of gravity. The purpose of this paper is to analyze which level of gravity is optimum for each mechanism, and which mechanism or parameter is optimum for each level of gravity. This paper discusses classification of locomotion mechanism. This paper compares the speed of hopping and wheeled robots and some simulation studies are performed to analyze the detailed mobility of wheeled robots.

1 Introduction

Small planetary bodies such as asteroids, comets and meteorites in deep space have received worldwide attentions in recent years. These studies have been motivated by a desire to shed light on the origin and evolution of the solar system. Hence, exploration missions for small bodies have been carried out continuously since the late 1990s. To date, the missions of NEAR [1], Deep Space 1 [2], Deep Impact [3], and Stardust [4] have been successfully performed, while MUSES-C [5] and Rosetta [6] are currently in operation. These missions have mainly provided remote sensing in the vicinity of the small body, at a distance which cannot be attained from the earth. In-situ observations of small bodies are scientifically very important because their sizes are too small to have experienced high internal pressures and temperatures, which means they should preserve the early chemistry of the solar system. For future missions, in-situ surface observation by robots will make strong contributions towards those studies.

Small bodies such as asteroids and comets have an extra low gravitational environment. Some researchers have proposed robots with hopping mechanism in order to perform scientific observation on a large number of sites on such small bodies [7-16] as shown in Figure 1. For example, a hopping rover called MINERVA [17-25], which was a part of the Hayabusa mission [5] of ISAS/JAXA, was taken to the asteroid Itokawa. MINERVA can hop on the surface in micro gravity environment by using

the hopping mechanism. A spherical robot is proposed, which contains iron ball inside and performs hopping using electromagnets around the ball [16]. A hop and soft-landing scheme is proposed, which is performed by converting kinetic energy to elastic energy with spring and linear actuator [26].

On the Earth, lives have developed in 1G gravitational environment. The locomotion methods for all the animals and artificial vehicles are highly adapted to the gravity of the planet [27]. However it is not proved that these robots with new concept aiming at low gravity environments are optimal.

The goal of this research is to identify which mechanisms or parameters are optimal when the level of gravity is given. In this paper, wheel-type locomotion is mainly discussed. This paper compares the speed of hopping and wheeled robots and some simulation studies are performed to analyze the detailed mobility of wheeled robots.

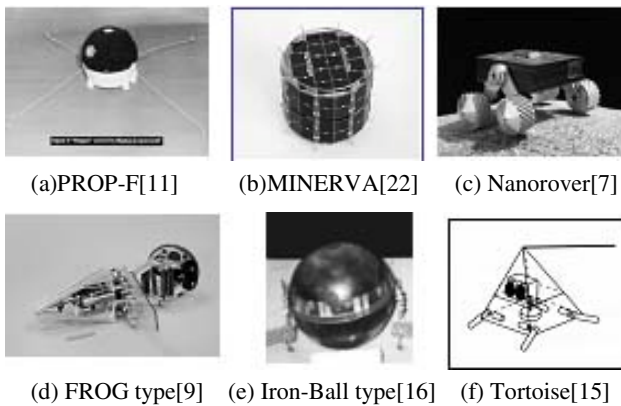


Fig. 1. Developed Hopping Robots

This paper presents locomotion mechanism based on gravitational environment. Section 2 discusses classification on mobility systems Section 3 describes the comparison between hop and wheel type locomotion. Section 4 presents the simulation study on wheel type locomotion. Two-wheel model is proposed and simulated. Section 6 discusses microgravity experiments. Conclusions are stated in Section 7.

2 Locomotion

Locomotion can be classified as follows, as shown in Figure 2.

- 1) Locomotion using friction
 - a) Friction only by gravity forces
 - b) Friction by gravity and dynamic forces
 - i) Continuous ground contact
 - ii) Intermittent ground contact
- 2) Locomotion utilizing the law of conservation of momentum
 - a) Internal conservation of momentum
 - b) Conservation of momentum between external environment

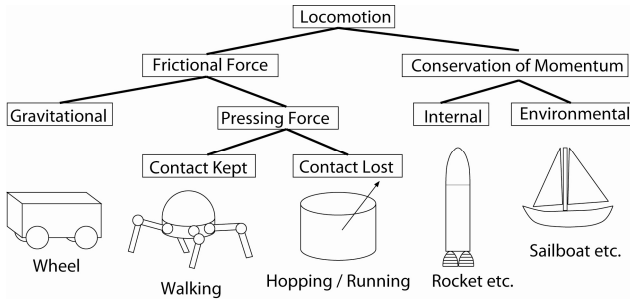


Fig. 2. Classification of Locomotion

Frictional driving does not need thrusters or an external environment like air fluid. Hence, locomotion using friction may be suitable for a planetary exploration robot. Therefore, locomotion using friction will be considered in this paper.

2.1 Locomotion Method Using Friction

Locomotion methods using friction can be classified into the following three categories.

- 1) Wheel-type locomotion
- 2) Leg-type locomotion
- 3) Hop-type locomotion

2.1.1 Wheel-Type Locomotion

Wheel-type locomotion is defined as the locomotion which only uses body weight to attain frictional force of propelling. The driving force of wheel-type locomotion f_w is given by

$$f_w \leq \mu m_w g \quad (1)$$

where

- μ : frictional coefficient
- m_w : total mass of wheel-type vehicle
- g : gravity acceleration.

Therefore, driving force is proportional to the gravity acceleration. In an ideal environment, robot with wheel-type locomotion can be accelerated unless it loses contact with the ground.

Most mobile robots that are used in lunar/planetary exploration missions are wheel-type [28].

2.1.2 Leg-Type Locomotion

Leg-type locomotion is defined as the locomotion which can push the ground and can attain greater frictional force than with only its own weight. Therefore, its center of

gravity can move up and down, but it keeps contact with the ground. The driving force of leg-type locomotion f_l is given by

$$f_l \leq \mu f_{il} \quad (2)$$

where

f_l : driving force of leg-type locomotion

f_{il} : pushing force applied to the ground.

This type of locomotion cannot apply large pushing force when the gravity is low because it is defined to keep contact with the ground.

2.1.3 Hop-Type Locomotion

Hop-type locomotion is defined as locomotion which can push the ground and loses contact with the ground. Driving force can be attained while the body is pushing the ground. The horizontal driving force of hop-type locomotion f_h is given by

$$f_h \leq \mu f_{ih} \quad (3)$$

where

f_h : driving force of leg-type locomotion

f_{ih} : pushing force applied to the ground.

Hop-type locomotion can assure certain magnitude of driving force even if gravity is extremely low ($g \approx 0$). However, the driving force can only be applied while in contact with the ground.

3 Comparison between Hop and Wheel Type

Optimality of locomotion is different depending on the purpose of the robot. Indices of optimality of locomotion are listed as follows.

- Locomotion speed
- Energy consumption
- Reliability / Robustness
- Precision of locomotion
- Load capacity
- Effects on environment

Among them, locomotion speed is one of the most important factor for planetary exploration robots. Therefore, optimality of speed is discussed in this paper. This paper does not deal with leg-type Locomotion, but will discuss in other paper. Hop-type and wheel-type locomotion robots will be compared by locomotion speed. A horizontal driving force expressed by Eq.(3), and a pushing force f_h as an impulsive force given by

$$f_h = I\delta(t) \quad (4)$$

is assumed. Therefore, horizontal speed (V_x) and vertical speed (V_y) of the hop robot immediately after take-off is given by

$$V_x = \frac{I}{m_h} \quad (5)$$

$$V_y = \frac{\mu I}{m_h} \quad (6)$$

where

m_h : total mass of hop-type robot

I : constant.

The duration of hop (T_1) depends on the initial vertical speed (V_y) and the gravity acceleration:

$$T_1 = \frac{2V_y}{g} = \frac{2I}{m_h g} \quad (7)$$

Thus, the hop distance (L_h) of one hop in an ideal environment is given by

$$L_h = V_x T_1 = \frac{2\mu I^2}{m_h^2 g} \quad (8)$$

In contrast, the driving force of wheeled robot is expressed by Eq.(1), which means that the acceleration of the wheeled robot is μg . The wheeled robot increases its horizontal speed to $\mu g T_1$ during the hop (T_1). The distance the wheeled robot traverses (L_w) during the hop is given by

$$L_w = \mu g (T_1)^2 / 2 = \frac{2\mu I^2}{m_h^2 g} \quad (9)$$

From Eq.(8) and Eq.(9), $L_h = L_w$.

Therefore, the hop distance travelled of the hop robot equals to the distance of wheeled robot during the hop duration as shown in Figure 3. Horizontal speed and horizontal distance of the hop robot and the wheeled robot are shown in Figure 4 and Figure 5 respectively. In these simulations, the parameters are as follows.

$$\begin{aligned} m_h, m_w &= 1.0 \text{ [kg]} \\ f_{ih} &= 0.2 \delta(t) \text{ [N]} \\ g &= 0.1 \text{ [G]} \\ \eta &= 0.5 \end{aligned}$$

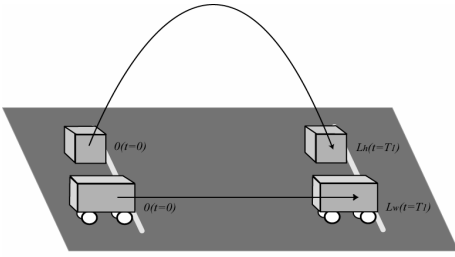


Fig. 3. Hop Robot and Wheeled Robot

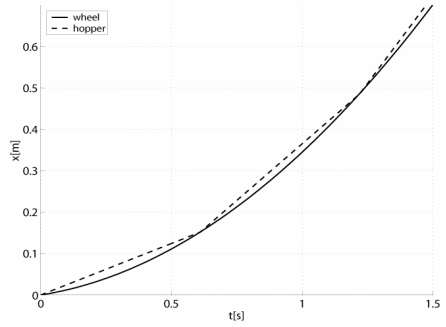


Fig. 4. Distance Comparison of Hop Robot and Wheeled Robot

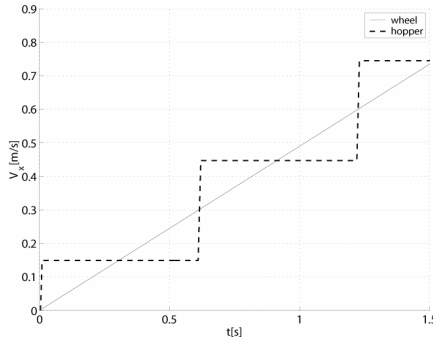


Fig. 5. Velocity Comparison of Hop Robot and Wheeled Robot

4 Simulation Study on Wheel-Type Locomotion

4.1 Objective

In an ideal environment, locomotion speed of hop robots equals that of wheeled robots. However, this is only when the ground is completely flat and the wheeled robot can attain a driving force given by $f_w = \mu m_w g$ at all times. If the terrain is not flat, it may cause some effect to the wheeled robot. A step could have the following consequences.

- 1) Horizontal speed decreases when the wheel passes over the step
- 2) Large momentum might cause the wheel to hop unintentionally. A wheeled robot cannot attain driving force from ground and can not accelerate once it loses contact with the ground.

Therefore, the locomotion speed may be lower when there are steps on the terrain than on completely flat ground. Some simulations are performed in this section to investigate the difference of the effect of steps on the ground.

4.2 Outline of Simulation

The simulations were performed on the two-dimensional plane. The model of the simulation is shown in Figure 6. A uni-wheeled robot passes through the step with a certain initial horizontal speed. The interaction between the ground / step and the wheel is modeled by spring-damper. The ground and wheel are assumed to be relatively stiff. The parameters used in simulation are defined as shown in Table 1.

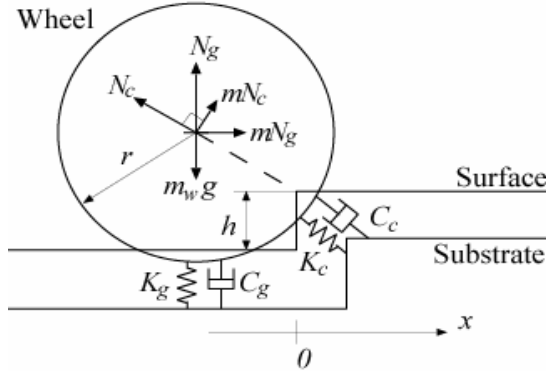


Fig. 6. Model of Wheel used in Simulation

Table 1. Simulation Parameters

η	: friction coefficient (= 0.5)
r	: wheel radius
h	: step height
K_c	: spring constant of the ground (=10000.0)
C_c	: damping coefficient at corner of step (=1000.0)
K_g	: spring constant of the ground (= K_c)
C_g	: damping coefficient of the ground (= C_c)
N_c	: normal force applied by the corner of the step
N_g	: normal force applied by the ground

The initial horizontal speed of the wheeled robot is set to 0.1[m/s]. The rotation speed is not limited, so the robot accelerates unless it loses its contact with the ground.

4.3 Evaluation of Simulation Results

Some examples of simulation results are shown in Figure 7, Figure 8, and Figure 9. Figure 7(a) shows the trajectory of the wheel, and Figure 7(b) shows the horizontal

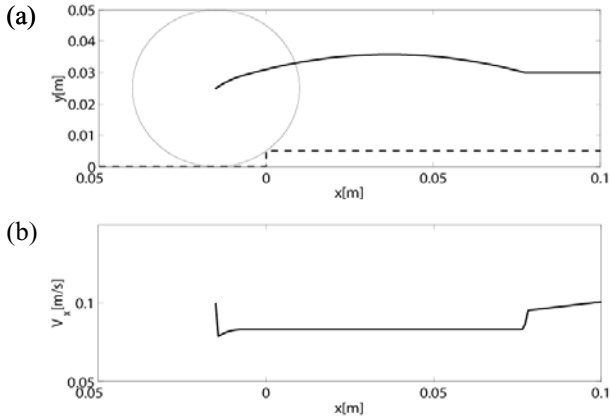


Fig. 7. Trajectory and Horizontal Velocity ($g = 0.005$ [G])

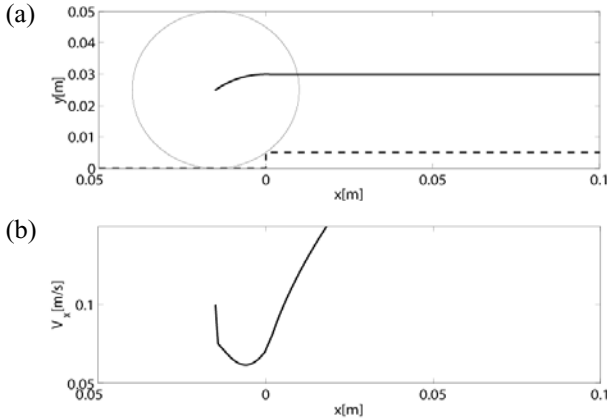


Fig. 8. Trajectory and Horizontal Velocity ($g = 0.02$ [G])

speed with respect to x -position of the wheel when the gravity acceleration is $g = 0.005$ [G]. Likewise, Figure 8 shows the results of $g = 0.02$ [G], Figure 9 shows the results of $g = 0.1$ [G]. Each simulation is performed with $r = 0.025$ [m] and $h = 0.005$ [m]. The wheeled robot does not hop in relatively high gravity as shown in Figure 9. However, the horizontal speed of wheeled robot decreases when the wheel passes over the step. Meanwhile, the wheel tends to hop largely if the gravity acceleration is lower as shown in Figure 7.

In order to evaluate the effect of a step which causes delay to wheeled locomotion, Delay Ratio (R_d) is defined as

$$R_d = \frac{T_{step} - T_{nostep}}{T_{nostep}} \tag{10}$$

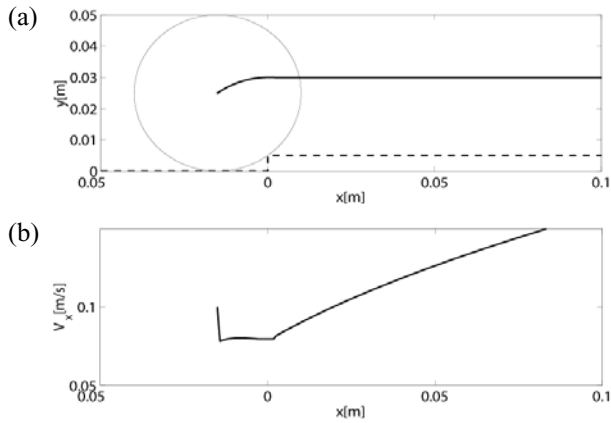


Fig. 9. Trajectory and Horizontal Velocity ($g = 0.005 [G]$)

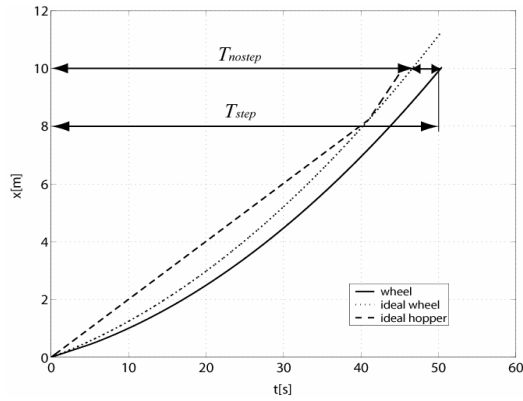


Fig. 10. Horizontal Distance under $0.001[G]$

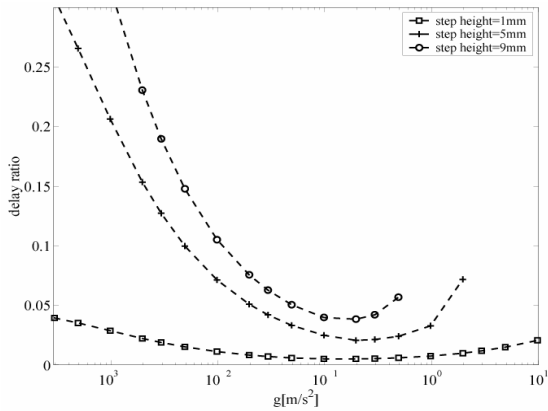


Fig. 11. Delay Ratio vs. Gravity Acceleration

where T_{step} is time for the wheeled robot to traverse a certain distance on the ground containing a step, and T_{nostep} is time to traverse the same distance on the ground without step. The meaning of R_d is shown graphically in Figure 10. R_d indicates the degree of delay caused by the step.

4.4 Delay Ratio and Step Height

R_d is plotted with respect to gravity acceleration in Figure 11. The ratio of step height h and wheel radius r is to be varied. The following results are obtained as shown in Figure 11.

- 1) R_d does not go negative. Therefore, a wheeled robot cannot traverse ground with a step faster than ground without step.
- 2) R_d decreases if the wheel radius is increased. Therefore, the larger the wheel radius is, the smaller its delay gets.
- 3) R_d has a minimum value for a given gravity acceleration.

If the gravity is low enough, as in $g = 0.005$ [G], the wheel loses contact with the ground (Figure 7). The horizontal speed of the wheel is constant throughout the hop. In the gravity of $g = 0.1$ [G], the wheel keeps contact with the ground (Figure 9). However, the horizontal speed decreases when the wheel passes over the step. Meanwhile, in the vicinity of the minimum point of R_d , the hop becomes far smaller (Figure 8). Therefore, the minimum point of R_d means the gravity in which the wheeled robot performs the smallest hop.

5 Simulation Study on Two-Wheel-Type Model

Uni-wheeled simulation model is quite simple, so the results of these simulations are not obvious to be applied to two-wheeled robots. Moreover, the behaviors of two-wheeled robots might be highly non-linear. Therefore, simulations of two-wheeled model are performed in this section.

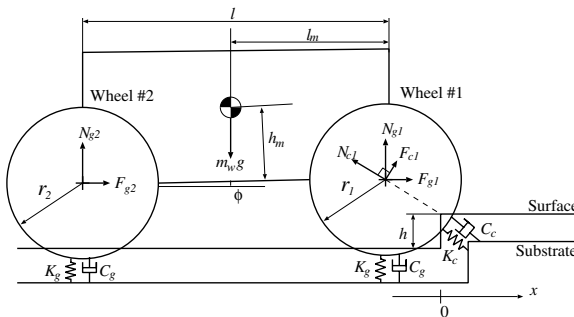


Fig. 12. Model of Two-Wheeled Robot

5.1 Outline of Simulation

The simulation model of two-wheeled robot is shown in Figure 12. The parameters are set as shown in Table 2 (the suffix 'n' indicates each wheel). The locomotion speed of the robot is limited in these simulations.

Table 2. Simulation Parameters

m_w	: Total mass of robot (= 0.9 [kg])
η	: friction coefficient (= 0.9)
r_n	: wheel radius (=0.216 [m])
h	: step height
l	: wheel base (=10000.0)
l_m	: distance between C.G. and front wheel (=0.111[m])
h_m	: height of C.G. from front wheel (=0.108[m])
N_{cn}	: normal force applied by the corner of the step
N_{gn}	: normal force applied by the ground
ω_n	: rotational velocity of each wheel (=2.86 [rad/s])

5.2 Simulation Results

The delay ratio is plotted against the gravity in Figure 13. The parameter of this plot is h/r . If the robot cannot pass over the step, then R_d cannot be defined, so not plotted. The conclusion from this figure is as follows.

- 1) The delay ratio has the minimum point. The higher the step is, the greater the delay ratio gets. These results can be also applied to the two-wheeled robot.
- 2) The gravity level in which the wheel-type robot is able to pass over the step is limited.

The robot cannot pass over the step if the gravity is large enough. This is because the energy required to pass over increases with the gravity level. On the other hand, the robot cannot pass over the step also if the gravity is small. It is considered that the pressing force against the step is not enough when the gravity is so small. In other words, there are upper/lower gravity limits for a wheel-type robot to pass over a given height of step. The higher the step is, the smaller the upper limit gets, and the larger the lower limit gets. The upper/lower limit of gravity is plotted against h/r in Figure 17. The fitted line to the upper limit g_u and the lower limit g_l of the gravity is

$$g_u = \exp(3.64 - 6.02h/r) \quad (11)$$

$$g_l = \exp(-6.85 - 2.14h/r) \quad (12)$$

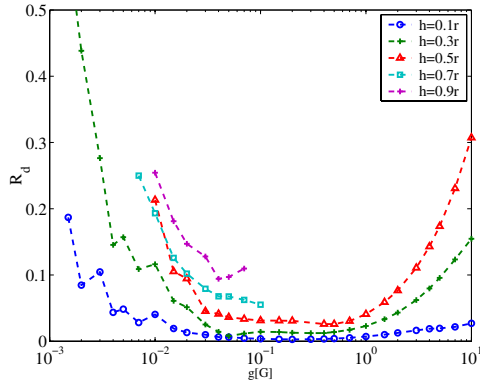


Fig. 13. Delay Ratio v.s. Gravity Acceleration (2-Wheeled Model)

respectively. The slant rate of the upper limit of gravity is triple as large as the lower limits. Nevertheless, it can be said that the higher the step is, the smaller the lower limit gets.

6 Microgravity Experiments

6.1 Outline of Experiments

Some microgravity experiment was performed to verify the results of simulation studies by aircraft free-fall. The wheeled robot [29] used in the experiments is shown in Figure 14. Each parameters of the robot is identical to the simulation. The robot runs over the step. The independent parameters of the experiment are height of the step, and the gravity. Two cases of step height (0.015[m] and 0.030[m]), and three cases of gravity (0.01[G], 0.1[G] and 0.5[G]) were performed. The step was made of wood, covered by thin rubber sheet in order to increase friction.

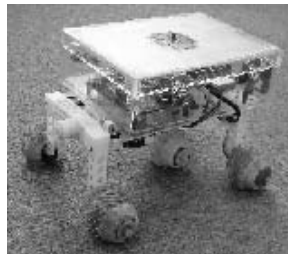


Fig. 14. Overview of Experimental Wheeled Robot

6.2 Coherence of Simulation Results and Experiments

An example of experimental result is shown in Figure 15. x, y position of C.G. of the robot and the angle of the robot are shown in Figure 15. The parameters are $g = 0.01$ [G],

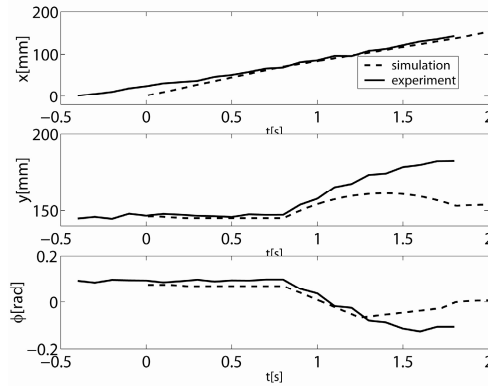


Fig. 15. Overview of Experimental Wheeled Robot

$h=0.015$ [m]. In these parameters, the hop of the robot was observed as shown in Figure 15. Although the experimental robot performs relatively larger hop than the simulation, the behavior is sufficiently similar.

6.3 Gravity and Delay Ratio

The delay ratio with respect to gained by the experiments and simulations are plotted vs. gravity in Figure 16. The step height is $h=0.015$ [m] ($h/r=0.5$). The experimental delay ratios are sufficiently close to the data of the simulations.

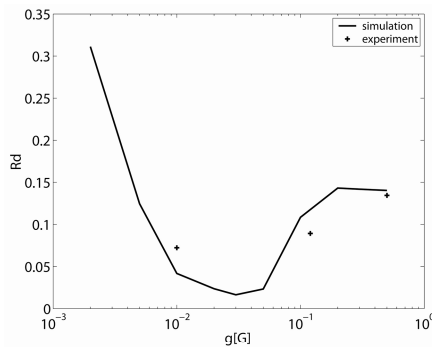


Fig. 16. Delay Ratio v.s. Gravity Acceleration

6.4 Gravity and Traversability of Wheel-Type Robot

The robot could not pass over the higher step ($h=0.03$ [m]) in the gravity level of $g=0.05$ [G]. On the other hand, the robot passed the lower step ($h=0.015$ [m]) in any of the tested gravity levels (0.01, 0.1, 0.5[G]). Figure 17 shows the upper/lower limits of gravity where the robot can pass over the step. The experimental result is

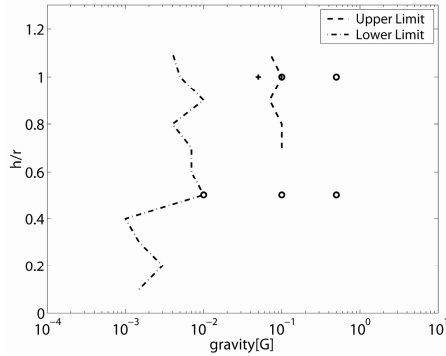


Fig. 17. Limit Gravity

shown as the symbol, 'o' for the conditions on which the robot passed over the step, and '+' for the condition on which the robot could not. The experimental result is different from the simulation result. For example, there are some cases which passed over the step even if the gravity is over the upper limit. It seems to be the effect of the fins on the wheels. The fins might be caught on the step, and the driving force exceeds the frictional force (Eq.(1)). Nevertheless, the gravity environment has much to do with the traversability of the wheel-type robot.

7 Conclusions

Locomotion speeds of hop robots and wheeled robots in an ideal environment have been compared in order to explore the optimal method of locomotion in each level of gravity. It can be concluded that each method of locomotion has the same capability of speed in an ideal environment.

Secondly, some simulations on wheel-type locomotion have been performed, and it is illustrated that in natural environments with a step, locomotion speed of wheeled robot is slower than on flat ground. Moreover, the delay caused by the existence of a step has a minimum point in terms of gravity acceleration. And the minimum point has much to do with designing of planetary exploration robots because it changes when the wheel radius varies. It is shown that wheel-type robots cannot pass over the step in case gravity is high or low enough. Lastly, the microgravity experiments were performed. The results of simulations roughly coincide with the experimental results.

Locomotion speed is just one index of optimality. Consideration about other indices such as energy consumption is needed in order to investigate locomotion in various gravity environments in a more integrated manner.

Acknowledgment

This work was partially supported by “Ground Research Announcement for Space Utilization” promoted by Japan Space Forum. The microgravity experiments were performed with the help by Diamond Air Service Co. Ltd.

References

- [1] Farquhar, R.: Near So Far. In: IAA Int. Conf. on Low-Cost Planetary Missions, No. IAA-L-0201 (2000)
- [2] Rayman, M.D., Varghese, P., Lehman, D.H., Livesay, L.L.: Results from the Deep Space 1 Technology Validation Mission. *Acta Astronautica Journal* 47, 475–487 (2000)
- [3] Chiu, M.C., Veverka, J., Reunolds, E.L.: The Contour Mission – Status of Implementation. In: IAA Int. Conf. on Low-Cost Planetary Missions, No. IAA-L-0205 (2000)
- [4] Atkins, K.L., Martin, B.D., Vellinga, J., Price, R.: STARDUST: Implementing a New Manage-to-Budget Paradigm. In: IAA Int. Conf. on Low-Cost Planetary Missions, No. IAA-L-0202 (2000)
- [5] Kawaguchi, J., Uesugi, K., Fujiwara, A.: The MUSES-C Mission for the Sample Return - Its Technology Development Status and Readiness. In: IAA Int. Conf. on Low-Cost Planetary Missions, No. IAA-L-0306 (2000)
- [6] Wittmann, K., Feuerbacher, B., Ulamec, S., Rosenbauer, H., Bibring, J.P., Moura, D., et al.: Rosetta Lander in situ Characterization of a Comet Nucleus. *Acta Astronautica Journal* 45, 389–395 (1999)
- [7] Wilcox, B., et al.: Nanorover Technology and the MUSES-C Mission. In: Proc. of 4th International Symposium on Artificial Intelligence, Robotics and Automation in Space, W-6-2 (1997)
- [8] Yoshimitsu, T., Nakatani, I., Kubota, T.: New Mobility System for Small Planetary Body Exploration. In: Proc. of the IEEE International Conference on Robotics and Automation, pp.1404–1409 (1999)
- [9] Fiorini, P., Hayati, S., Heverly, M., Gensler, J.: A Hopping Robot for Planetary Exploration. In: IEEE Aerospace Conference (1999)
- [10] Schell, S., Tretten, A., Burdick, J., Fuller, S.B., Fiorini, P.: Hopper on wheels: evolving the hopping robot concept. *IEEE Field and Service Robots* (2001)
- [11] http://www.planetary.org/mars/tpr_rover-rus.html
- [12] Yoshimitsu, T., Kubota, T., Nakatani, I., Adachi, T., Saito, H.: Hopping Rover MINERVA for Asteroid Exploration. In: Proc. 5th i-SAIRAS, pp. 83–88 (1999)
- [13] Hale, E., Schara, N., Burdick, J., Fiorini, P.: A Minimally Actuated Hopping Rover for Exploration of celestial Bodies. In: IEEE Int. Conf. on Robotics and Automation, pp. 420–427 (2000)
- [14] Hale, E., Schara, N., Burdick, J., Fiorini, P.: A Minimally Actuated Hopping Rover for Exploration of celestial Bodies. In: IEEE Int. Conf. on Robotics and Automation, pp. 420–427 (2000)
- [15] Yoshida, K.: The Jumping Tortoise: A Robot Design for Locomotion on Micro Gravity Surface. In: Proc. of 5th International Symposium on Artificial Intelligence, Robotics and Automation in Space, pp. 705–707 (1999)
- [16] Nakamura, Y., Shimoda, S., Shoji, S.: Mobility of a Microgravity Rover Using Internal Electro-Magnetic Levitation. In: Proc. of the 2000 IEEE/RSJ Int. Conf. on Intelligent Robots and Systems, pp. 1639–1645 (2000)
- [17] Yoshimitsu, T., Kubota, T., Nakatani, I.: Nano-Rover MINERVA for Deep Space Exploration. *Journal of Machine Intelligence and Robotics Control* 3(3), 113–119 (2001)
- [18] Yoshimitsu, T., Kubota, T., Nakatani, I., Adachi, T., Saito, H.: Analysis on Hopping Mechanism by Microgravity Experiments. *Drop Tower Days*, 63–65 (2000)
- [19] Yoshimitsu, T., Kubota, T., Nakatani, I., Adachi, T., Saito, H.: Microgravity Experiment of Hopping Rover. In: Proc. of the IEEE International Conference on Robotics and Automation, pp. 2692–2697 (1999)

- [20] Yoshimitsu, T., Kubota, T., Nakatani, I., Adachi, T., Saito, H.: Micro Hopping Robot for Asteroid Exploration. In: 4th IAA International Conference on Low-Cost Planetary Missions, IAA-L-1104 (2000)
- [21] Yoshimitsu, T., Kubota, T., Nakatani, I., Adachi, T., Saito, H.: Micro-hopping robot for asteroid exploration. *Acta Astronautica* 52, 441–446 (2003)
- [22] Yoshimitsu, T., Kubota, T., Aakabane, S., Nakatani, I., Adachi, T., Saito, H., Kunii, Y.: Autonomous Navigation and Observation on Asteroid Surface by Hopping Rover MINERVA. In: Proc. Sixth International Symposium on Artificial Intelligence, Robotics and Automation in Space, AS017 (2001)
- [23] Yoshimitsu, T., Kubota, T., Nakatani, I., Kawaguchi, J.: Robotic Lander MINERVA, Its Mobility and Surface Exploration. *Advances in the Astronautical Sciences* 108, 491–502 (2001)
- [24] Kubota, T., Shimoda, S., Yoshimitsu, T., Nakatani, I.: Small Body Exploration Robot with Hopping Mechanism. In: Proc. of the IASTED Int. Conf. on Robotics and Applications, No. 390-078, pp. 88–93 (2003)
- [25] Kubota, T., Yoshimitsu, T.: Intelligent Unmanned Explorer for Deep Space Exploration. In: Int. Conf. on Intelligent Unmanned Systems, A004, pp. 18–25 (2007)
- [26] Takahashi, K., Shimoda, S., Iizuka, K., Kubota, T., Nakatani, I.: A Study of Locomotion Mechanism Based on Gravitational Environment. In: IEEE/RSJ Int. Conf. on Intelligent Robots and Systems, SP2-K3 (2004)
- [27] Shimoda, S., Kubota, T., Nakatani, I.: New Mobility System Based on Elastic Energy under Microgravity. In: Proc. of IEEE Int. Conf. on R&A, No. 314 (2002)
- [28] Matijevic, J.: Mars pathfinder microrover -implementing a low cost planetary mission experiment. In: Proceedings of the Second IAA International Conference on Low-Cost Planetary Missions (1996)
- [29] Kuroda, Y., Teshima, T., Sato, Y., Kubota, T.: Mobility performance evaluation of planetary rover with similarity model experiment. In: IEEE International Conference on Robotics and Automation (2004)

Global Linear Modeling of Small Scale Helicopter

A. Budiyo¹, T. Sudiyanto², and H. Lesmana²

¹ Smart Robot Center, Department of Aerospace Information Engineering
Konkuk University, Seoul, Korea
budiyono@alum.mit.edu

² Center for Unmanned System Studies
Institut Teknologi Bandung, Indonesia
www.centurms-itb.org

Abstract. The establishment of global helicopter linear model is indispensable for the design of an onboard autonomous control system by using linear control laws. To date, however, it has never been afforded in the literatures. In the first principle approach, the mathematical model is developed using basic helicopter theory accounting for particular characteristic of the miniature helicopter. In this approach, no formal system identification procedures are required for the proposed model structure. The relevant published references however did not present rigorous linear models development required for the design of linear control laws. This chapter presents a step by step development of linear model for small scale helicopter based on first-principle approach. Beyond the previous work in literatures, the calculation of the stability derivatives is presented in detail. A computer program is used to solve the equilibrium conditions and then calculate the change in aerodynamics forces and moments due to the change in each degree of freedom and control input. The detail derivation allows the comprehensive analysis of relative dominance of vehicle states and input variables to force and moment components. The procedure can be implemented for various flight conditions. Hence it facilitates the development of global small scale helicopter dynamics model.

1 Introduction

The dynamics of rotary wing vehicles are substantially more complex than those of its fixed-wing counterparts. For full-scale helicopters the aerodynamics analysis was presented in literatures such as [1] and [2]. The treatment for stability and control were presented in [3] and [4]. The rigid body dynamics approach standard in the analysis of aircraft dynamics as in [5], [6] and [7] is insufficient to capture key dynamics of a rotorcraft vehicle. The rotorcraft dynamics are characteristically typified by the coupled rotor-fuselage dynamics. The small scale rotorcraft dynamics is further characterized by the existence of stabilizer bar and active-yaw damping system to ease the pilot workload.

The rotor head of small scale helicopter is significantly more rigid than that of its full-scale counterpart. This not only allows for larger rotor control moment but also alleviation of second order effects typically found in full-scale helicopter dynamics model. The majority developed model for UAVs are based on frequency-domain identification. It has been demonstrated that the relatively low order model developed using this approach is sufficient to describe the helicopter dynamics around trim

conditions. It must be noted however that the accuracy of this approach decreases with the presence of feedback which is needed for example to stabilize the helicopter in hover. The method is also unreliable to describe low-frequency modes, primarily due to pilot feedback [8]. Other linear model development was given by [9] by using time-domain identification. The system identification approach requires experimental input-output data collected from the flight tests of the vehicle. The flying test-bed must be outfitted with adequate instruments to measure both state and control variables.

The chapter presents an analytical development of linear model for small scale helicopter based on first principle approach. Beyond the previous work in [8], the calculation of stability and control derivatives to construct the linear model is presented in detail. The analytical model derivation allows the comprehensive analysis of relative dominance of vehicle states and input variables to force and moment components. And hence it facilitates the development of minimum complexity small scale helicopter dynamics model that differs from that of its full-scale counterpart. In the presented simplified model, the engine drive-train dynamics and inflow dynamics are not necessary to be taken into consideration. The additional rotor degrees of freedom for coning and lead-lag can be omitted for small scale helicopters. It is demonstrated analytically that the dynamics of small scale helicopter is dominated by the strong moments produced by the highly rigid rotor. The dominant rotor forces and moments largely overshadow the effects of complex interactions between the rotor wake and fuselage or tail. This tendency substantially reduces the need for complicated models of second-degree effects typically found in the literature on full-scale helicopters. The presented approach is not limited to specific trim conditions like hover or forward flights and therefore can be used to develop a global model of small scale rotorcraft vehicle to the purpose of practical control design.

2 Dynamics of Small-Scale Helicopter

The approach to helicopter modeling can be in general divided into two distinct methods. The first approach is known as first principle modeling based on direct physical understanding of forces and moments balance of the vehicle. The challenge of this approach is the complexity of the mathematical model involved along with the need for rigorous validation. The second method based on system identification basically arises from the difficulty of the former approach. The frequency domain identification starts with the estimation of frequency response from flight data recorder from an instrumented flight-test vehicle. The parameterized dynamic model can then be developed in the form of a linear state-space model using physical insight and frequency-response analysis. The identification can also be conducted in time-domain.

In practice, the above two methods can be used hand in hand in developing an accurate small scale rotorcraft vehicle model for the purpose of control design.

2.1 Small-Scale Helicopter Parameters

The X-Cell .60 SE small scale helicopter's parameters are used in developing mathematical model. The mini-helicopter as shown in Figure 1 is characterized by a



Fig. 1. Instrumented X-Cell 60 Helicopter

Table 1. Basic XCell Heli Parameters

Parameter		Description
m	8.2 kg	Helicopter mass
I_{xx}	0.18 kg m ²	Rolling moment of inertia
I_{yy}	0.34 kg m ²	Pitching moment of inertia
I_{zz}	0.28 kg m ²	Yawing moment of inertia
R_{MR}	0.775 m	Main rotor radius
c_{MR}	0.058 m	Main rotor chord
R_{TR}	0.13 m	Tail rotor radius
c_{TR}	0.029 m	Tail rotor chord
S_{VF}	0.012 m ²	Effective vertical fin area
S_{HF}	0.01 m ²	Horizontal fin area
h_{MR}	0.235 m	Main rotor hub height above c.g.
l_{TR}	0.91 m	Tail rotor hub location behind c.g.
h_{TR}	0.08 m	Tail rotor height above c.g.
Ω_{nom}	167 rad/sec	Nominal main rotor speed

hinge-less rotor with a diameter of 0.775 m and mass of 8 kg. The X-Cell blades both for main and tail rotors use symmetric airfoils. Table 1 shows basic X-cell 60 helicopter's specifications.

2.2 Euler-Newton Equation of Motion

Rigid body equations of motion are typically used for modeling the dynamics of fixed wing aircraft. This model is typified by the use of linear stability derivatives, which are a linearized form of the rigid-body dynamics, providing important analysis of the vehicle's dynamics, stability and control. This approach has a limited application for rotorcraft vehicles particularly for the design of high-bandwidth control design and rigorous handling-qualities analysis. However, it must be noted that the linear stability derivative models from rigid-body dynamics can be a good starting point for a development of more accurate rotorcraft model.

The motion of a vehicle in three-dimensional space can be represented by the position of the center of mass and the Euler angles for the vehicle rotation with respect to the inertial frame of reference. The Euler-Newton equations are derived from the law of conservation of linear and angular momentum. Assuming that vehicle mass m and inertial tensor \vec{I} , the equations are given by:

$$m \frac{d\vec{V}}{dt} = \vec{F}, \quad \vec{I} \frac{d\vec{\omega}}{dt} = \vec{M} \quad (1)$$

where $\vec{F} = [X \ Y \ Z]^T$ is the vector of external forces acting on the helicopter center of gravity and $\vec{M} = [L \ M \ N]^T$ is the vector of external moments. For helicopter, the external forces and moments consists of forces generated by the main rotor, tail rotor; aerodynamics forces from fuselage, horizontal fin and vertical fin and gravitational force. For computational convenience, the Euler-Newton equations describing the rigid-body dynamics of the helicopter is then represented with respect to body coordinate system by using the kinematic principles of moving coordinate frame of reference as the following:

$$m \dot{\vec{V}} + m (\vec{\omega} \times \vec{V}) = \vec{F}, \quad I \dot{\vec{\omega}} + (\vec{\omega} \times I \vec{\omega}) = \vec{M} \quad (2)$$

Here the vector $\vec{V} = [u \ v \ w]^T$ and $\vec{\omega} = [p \ q \ r]^T$ are the fuselage velocities and angular rates in the body coordinate system, respectively. For the helicopter moving in six degrees of freedom, the above equations produce six differential equations describing the vehicle's translational motion and angular motion about its three reference axes.

$$\sum X = m(\dot{u} - rv + qw) + mg \sin \theta \quad (3)$$

$$\sum Y = m(\dot{v} - pw + ru) - mg \sin \phi \cos \theta \quad (4)$$

$$\sum Z = m(\dot{w} - qu + pv) - mg \cos \phi \cos \theta \quad (5)$$

$$\sum L = I_{xx} \dot{p} - (I_{yy} - I_{zz}) qr \quad (6)$$

$$\sum M = I_{yy} \dot{q} - (I_{zz} - I_{xx}) pr \quad (7)$$

$$\sum N = I_{zz} \dot{r} - (I_{xx} - I_{yy}) pq \quad (8)$$

$$\dot{\phi} = p + (q \sin \phi + r \cos \phi) \tan \theta \quad (9)$$

$$\dot{\theta} = q \cos \phi - r \sin \phi \quad (10)$$

$$\dot{\psi} = (q \sin \phi + r \cos \phi) \sec \theta \quad (11)$$

2.2.1 Main Rotor and Tail Rotor

The forces generated by main and tail rotor are thrusts due to airflow momentum differential as it moves through rotor discs.

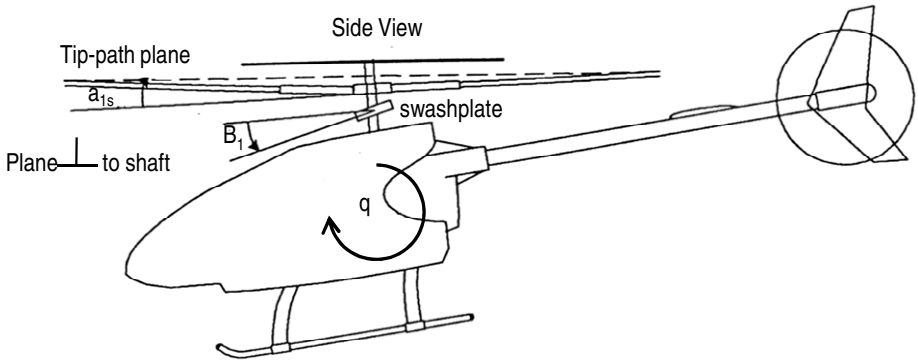


Fig. 2. Longitudinal Flapping Angle Illustration

2.2.1.1 *Main Rotor.* The main rotor thrust is calculated by the following expressions.

$$T_{MR} = \rho (\Omega R)_{MR}^2 (\pi R^2)_{MR} C_{TMR} \quad (12)$$

$$C_{TMR} = \frac{1}{2} a_{MR} \sigma_{MR} \left[\frac{1}{2} (\mu_{zMR} - \lambda_{0MR}) + \left(\frac{1}{3} + \frac{1}{2} \mu_{MR}^2 \right) \theta_{0MR} \right] \quad (13)$$

$$\lambda_{0MR} \equiv \frac{w_{iMR}}{(\Omega R)_{MR}} = \frac{C_{TMR}}{2\eta_w \sqrt{\mu_{MR}^2 + (\lambda_{0MR} - \mu_{zMR})^2}} \quad (14)$$

$$\mu_{MR} \equiv \frac{\sqrt{u_a^2 + v_a^2}}{(\Omega R)_{MR}}, \quad \mu_{zMR} \equiv \frac{w_a}{(\Omega R)_{MR}}$$

These expressions are solved by iteration.

The torque is given by the following expressions.

$$Q_{MR} = \rho (\Omega R)_{MR}^2 (\pi R^2)_{MR} R_{MR} C_{QMR} \quad (15)$$

$$C_{QMR} = \frac{1}{8} \sigma_{MR} \left(1 + \frac{7}{3} \mu_{MR}^2 \right) C_{D_0MR} + (\lambda_{0MR} - \mu_{zMR}) C_{TMR} \quad (16)$$

The main rotor flapping motions are given by the following expressions.

$$\tau_c \dot{a}_{1s} = -a_{1s} + \frac{\partial a_{1s}}{\partial \mu_{MR}} \frac{u_a}{(\Omega R)_{MR}} + \frac{\partial a_{1s}}{\partial \mu_{zMR}} \frac{w_a}{(\Omega R)_{MR}} - \tau_e q + A_{\delta_{Long}} \delta_{Long} \quad (17)$$

$$\tau_c \dot{b}_{1s} = -b_{1s} - \frac{\partial b_{1s}}{\partial \mu_{MR}} \frac{v_a}{(\Omega R)_{MR}} - \tau_e p + B_{\delta_{Lat}} \delta_{Lat} \quad (18)$$

Finally, the generated force and moment in body axis are calculated as:

$$X_{MR} = -T_{MR} \sin a_{1s} \quad (19)$$

$$Y_{MR} = T_{MR} \sin b_{1s} \quad (20)$$

$$Z_{MR} = T_{MR} \cos a_{1s} \cos b_{1s} \quad (21)$$

$$\begin{aligned} L_{MR} &= K_{\beta} b_{1s} + Y_{MR} h_{MR} \\ &= K_{\beta} b_{1s} + T_{MR} h_{MR} \sin b_{1s} \end{aligned} \quad (22)$$

$$\begin{aligned} M_{MR} &= K_{\beta} a_{1s} - X_{MR} h_{MR} \\ &= K_{\beta} a_{1s} + T_{MR} h_{MR} \sin a_{1s} \end{aligned} \quad (23)$$

$$N_{MR} = -Q_{MR} \quad (24)$$

The main rotor has a major influence over other parts of the helicopter as its induced airflow moves downstream. Such downwash airflow in turn affects the overall aerodynamics force and moment of the helicopter. Therefore, before proceeding any further, a main rotor downstream effect variable introduced:

$$K_{\lambda} = \begin{cases} 0, & \text{if } w_{iMR} \leq w_a \text{ or } u_a \leq g_i (w_{iMR} - w_a) \\ 1.5 \frac{\left(\frac{u_a}{w_{iMR} - w_a} \right) - g_i}{g_f - g_i}, & \text{if } g_i (w_{iMR} - w_a) < u_a < g_f (w_{iMR} - w_a) \\ 0, & \text{if } u_a \geq g_f (w_{iMR} - w_a) \end{cases} \quad (25)$$

where

$$g_i = \frac{l_{TR} - R_{MR} - R_{TR}}{h_{TR}}, \quad g_f = \frac{l_{TR} - R_{MR} + R_{TR}}{h_{TR}} \quad (26)$$

2.2.1.2 *Tail Rotor.* Tail rotor force is calculated as the same manner as that of main rotor, except that tail rotor is considered as a non-flapping rotor.

$$C_{TTR} = \frac{1}{2} a_{TR} \sigma_{TR} \left[\frac{1}{2} (\mu_{yTR} - \lambda_{0TR}) + \left(\frac{1}{3} + \frac{1}{2} \mu_{TR}^2 \right) \theta_{0TR} \right] \quad (27)$$

$$\lambda_{0TR} \equiv \frac{v_{iTR}}{(\Omega R)_{TR}} = \frac{C_{TTR}}{2\eta_v \sqrt{\mu_{TR}^2 + (\lambda_{0TR} - \mu_{yTR})^2}} \quad (28)$$

$$\mu_{TR} \equiv \frac{\sqrt{u_a^2 + w_a^2}}{(\Omega R)_{TR}}, \quad \mu_{yTR} \equiv \frac{v_a}{(\Omega R)_{TR}}$$

$$Q_{TR} = \rho (\Omega R)_{TR}^2 (\pi R^2)_{TR} R_{TR} C_{QTR} \quad (29)$$

$$C_{QTR} = \frac{1}{8} \sigma_{TR} \left(1 + \frac{7}{3} \mu_{TR}^2 \right) C_{D0TR} + (\lambda_{0TR} - \mu_{yTR}) C_{TTR} \quad (30)$$

The calculation also includes the main rotor wake K_λ , and vertical fin's blockage factor, f_i .

$$f_i = 1 - \frac{3}{4} \frac{S_{VF}}{\pi R_{TR}^2} \quad (31)$$

$$T_{TR} = f_i \rho (\Omega R)_{TR}^2 (\pi R^2)_{TR} C_{TTR} \quad (32)$$

The tail rotor force and moment in body axis then are expressed as the followings.

$$X_{TR} = 0 \quad (33)$$

$$Y_{TR} = -T_{TR} \quad (34)$$

$$Z_{TR} = 0 \quad (35)$$

$$L_{TR} = -T_{TR} h_{TR} \quad (36)$$

$$M_{\text{TR}} = -Q_{\text{TR}} \quad (37)$$

$$N_{\text{TR}} = T_{\text{TR}} l_{\text{TR}} \quad (38)$$

2.2.2 Fuselage, Horizontal Fin, and Vertical Fin

Fuselage, horizontal fin and vertical fin are subject to drag force generated by relative airspeed, which comes from the motion of helicopter's body relative to air and rotor's induced wind. Also, the main rotor downwash affects the fuselage and the horizontal fin to generate additional drag force, and the tail rotor downwash does it to the vertical fin.

2.2.2.1 Fuselage

$$X_{\text{Fus}} = -\frac{1}{2} \rho S_{x\text{Fus}} V_{\infty} u_a \quad (39)$$

$$Y_{\text{Fus}} = -\frac{1}{2} \rho S_{y\text{Fus}} V_{\infty} v_a \quad (40)$$

$$Z_{\text{Fus}} = -\frac{1}{2} \rho S_{z\text{Fus}} V_{\infty} (w_a - w_{i\text{MR}}) \quad (41)$$

$$V_{\infty} = \sqrt{u_a^2 + v_a^2 + (w_a - w_{i\text{MR}})^2} \quad (42)$$

$$\vec{M}_{\text{Fus}} = \vec{0} \quad (43)$$

2.2.2.2 Horizontal Fin

$$X_{\text{HF}} \approx 0 \quad (44)$$

$$Y_{\text{HF}} \approx 0 \quad (45)$$

$$Z_{\text{HF}} = -\frac{1}{2} \rho S_{\text{HF}} (C_{L\alpha\text{HF}} |u_a| + |w_{\text{HF}}|) w_{\text{HF}} \quad (46)$$

$$w_{\text{HF}} = w_a + l_{\text{HF}} q - K_{\lambda} w_{i\text{MR}} \quad (47)$$

$$L_{\text{HF}} = 0 \quad (48)$$

$$M_{\text{HF}} = Z_{\text{HF}} l_{\text{HF}} \quad (49)$$

$$N_{\text{HF}} = 0 \quad (50)$$

2.2.2.3 Vertical Fin

$$X_{VF} \approx 0 \quad (51)$$

$$Y_{VF} = -\frac{1}{2} \rho S_{VF} (C_{L\alpha VF} V_{\infty VF} + |v_{VF}|) v_{VF} \quad (52)$$

$$Z_{VF} \approx 0 \quad (53)$$

$$V_{\infty VF} = \sqrt{(u^2 + v^2)_{VF}} \quad (54)$$

$$u_{VF} = u_a \quad (55)$$

$$v_{VF} = v_a - \mathcal{E}_{VF/TR} v_{iTR} - l_{VF} r \quad (56)$$

$\mathcal{E}_{VF/TR}$ is the fraction of vertical fin area exposed to tail rotor downwash.

$$L_{VF} = Y_{VF} h_{VF} \quad (57)$$

$$M_{VF} = 0 \quad (58)$$

$$N_{VF} = -Y_{VF} l_{VF} \quad (59)$$

2.3 Trim Condition

For helicopter, there are in general two distinct trim conditions: hover and forward flight. The solution for trim condition at hover can be obtained easily from the balance of forces and moments. The calculation for trim condition at forward flight requires an iterative procedure. Other conditions include vertical flight, ascending flight, steady turns and helices, all of which can be calculated following the same procedure as that of forward flight.

2.3.1 Hover

The hover condition is characterized by zero velocities and angular rates.

$$\vec{V}_{\text{cq}} = [0 \quad 0 \quad 0]^T \quad \vec{\omega}_{\text{cq}} = [0 \quad 0 \quad 0]^T \quad (60)$$

This expression is used to solve Eqns. (3) – (8) for the trim value at hover. The result is summarized as the following calculated values of parameters.

$$\begin{aligned}
T_{MR} \Big|_{\text{hov}} &= 81.616 \text{ Newton} & C_{TMR} \Big|_{\text{hov}} &= 0.002256 \\
Q_{MR} \Big|_{\text{hov}} &= 6.247 \text{ N} \cdot \text{m} & C_{QMR} \Big|_{\text{hov}} &= 0.0002228 \\
w_{iMR} \Big|_{\text{hov}} &= 4.582 \text{ m/s} & \lambda_{0MR} \Big|_{\text{hov}} &= 0.0354 \\
\theta_{0MR} \Big|_{\text{hov}} &= 0.1047 \text{ rad} \\
&= 6.001^\circ
\end{aligned} \tag{61}$$

$$\begin{aligned}
T_{TR} \Big|_{\text{hov}} &= 6.8656 \text{ Newton} & C_{TTR} \Big|_{\text{hov}} &= 0.01329 \\
Q_{TR} \Big|_{\text{hov}} &= 0.1268 \text{ N} \cdot \text{m} & C_{QTR} \Big|_{\text{hov}} &= 0.001568 \\
w_{iTR} \Big|_{\text{hov}} &= 8.693 \text{ m/s} & \lambda_{0TR} \Big|_{\text{hov}} &= 0.0859 \\
\theta_{0TR} \Big|_{\text{hov}} &= 0.2412 \text{ rad} \\
&= 13.82^\circ
\end{aligned} \tag{62}$$

$$\begin{aligned}
a_{1s} \Big|_{\text{hov}} &= 0.0014258 \text{ rad} & \delta_{\text{Long}} \Big|_{\text{hov}} &= 0.0003395 \text{ rad} \\
&= 0.0817^\circ & &= 0.01945^\circ
\end{aligned} \tag{63}$$

$$\begin{aligned}
b_{1s} \Big|_{\text{hov}} &= 0.0074866 \text{ rad} & \delta_{\text{Lat}} \Big|_{\text{hov}} &= 0.001783 \text{ rad} \\
&= 0.4290^\circ & &= 0.1021^\circ
\end{aligned}$$

$$\begin{aligned}
\phi \Big|_{\text{hov}} &= 0.077643 \text{ rad} & \theta \Big|_{\text{hov}} &= -0.0014471 \text{ rad} \\
&= 4.4486^\circ & &= -0.0829
\end{aligned} \tag{64}$$

2.3.2 Forward Flight

The trim conditions for forward flight are derived for the following flight condition.

$$\vec{V}_{\text{eq}} = [16.5557 \quad 0.7456 \quad 0]^T \quad \vec{\omega}_{\text{eq}} = [0 \quad 0 \quad 0]^T \tag{65}$$

The flight condition represents a nearly straight level flight. The result of calculation is presented as follows:

$$\begin{aligned}
T_{MR}|_{cr} &= 82.145 \text{ Newton} & C_{TMR}|_{cr} &= 0.002270 \\
Q_{MR}|_{cr} &= 4.660 \text{ N} \cdot \text{m} & C_{QMR}|_{cr} &= 0.000166 \\
w_{iMR}|_{cr} &= 1.275 \text{ m/s} & \lambda_{0MR}|_{cr} &= 0.0099 \\
\theta_{0MR}|_{cr} &= 0.0622 \text{ rad} \\
&= 3.564^\circ
\end{aligned} \tag{66}$$

$$\begin{aligned}
T_{TR}|_{cr} &= 5.1032 \text{ Newton} & C_{TTR}|_{cr} &= 0.00988 \\
Q_{TR}|_{cr} &= 0.0571 \text{ N} \cdot \text{m} & C_{QTR}|_{cr} &= 0.000706 \\
w_{iTR}|_{cr} &= 3.336 \text{ m/s} & \lambda_{0TR}|_{cr} &= 0.0330 \\
\theta_{0TR}|_{cr} &= 0.1171 \text{ rad} \\
&= 6.71^\circ
\end{aligned} \tag{67}$$

$$\begin{aligned}
a_{1s}|_{cr} &= 0.00547335 \text{ rad} & \delta_{Long}|_{cr} &= 0.00039302 \text{ rad} \\
&= 0.3136^\circ & &= 0.0225^\circ
\end{aligned} \tag{68}$$

$$\begin{aligned}
b_{1s}|_{cr} &= 0.00558899 \text{ rad} & \delta_{Lat}|_{cr} &= 0.001613 \text{ rad} \\
&= 0.3202^\circ & &= 0.0924^\circ
\end{aligned}$$

$$\begin{aligned}
\phi|_{cr} &= 0.0790896 \text{ rad} & \theta|_{cr} &= -0.203044 \text{ rad} \\
&= 4.5315^\circ & &= -11.6336^\circ
\end{aligned} \tag{69}$$

2.4 Linearized Equation of Motion

The vehicle equations of motion in general can be represented by a nonlinear vector differential equation as follows.

$$\dot{\vec{x}} = \vec{f}(\vec{x}, \vec{u}) \tag{70}$$

where \bar{x} is the vehicle state vector and \bar{u} is the control input vector. This nonlinear differential equation of motion is linearized around an equilibrium state \bar{x}_0 :

$$\delta \dot{\bar{x}} = \left(\frac{\partial \vec{f}}{\partial \bar{x}} \right)_{\bar{x}_{eq}, \bar{u}_{eq}} \delta \bar{x} + \left(\frac{\partial \vec{f}}{\partial \bar{u}} \right)_{\bar{x}_{eq}, \bar{u}_{eq}} \delta \bar{u} \quad (71)$$

Eqn. (71) uses the linear perturbations of the state and input vectors of the vehicle. This principle of small perturbations is then applied to each of the expression for forces and moments of the helicopter: Eqns. (3) – (11).

$$d\dot{u} = \frac{1}{m} \sum dX + r dv - q dw - w dq + v dr - g \sin \theta d\theta \quad (72)$$

$$d\dot{v} = \frac{1}{m} \sum dY - r du + p dw + w dp - u dr + g \cos \phi \cos \theta d\phi - g \sin \phi \sin \theta d\theta \quad (73)$$

$$d\dot{w} = -\frac{1}{m} \sum dZ - q du + p dv + v dp - u dq + g \cos \theta \sin \phi d\phi + g \cos \phi \sin \theta d\theta \quad (74)$$

$$d\dot{p} = \frac{1}{I_{xx}} \sum dL + \frac{(I_{yy} - I_{zz})}{I_{xx}} r dq + \frac{(I_{yy} - I_{zz})}{I_{xx}} q dr \quad (75)$$

$$d\dot{q} = \frac{1}{I_{yy}} \sum dM + \frac{(I_{zz} - I_{xx})}{I_{yy}} r dp + \frac{(I_{zz} - I_{xx})}{I_{yy}} p dr \quad (76)$$

$$d\dot{r} = \frac{1}{I_{zz}} \sum dN + \frac{(I_{xx} - I_{yy})}{I_{zz}} q dp + \frac{(I_{xx} - I_{yy})}{I_{zz}} p dq \quad (77)$$

$$d\dot{\phi} = dp + \sin \phi \tan \theta dq + \cos \phi \tan \theta dr \dots \dots + (q \cos \phi - r \sin \phi) \tan \theta d\phi + (q \sin \phi + r \cos \phi) \sec \theta d\theta \quad (78)$$

$$d\dot{\theta} = \cos \phi dq - \sin \phi dr - (q \sin \phi + r \cos \phi) d\phi \quad (79)$$

$$d\dot{\psi} = \sin \phi \sec \theta dq + \cos \phi \sec \theta dr \dots \dots + (q \cos \phi - r \sin \phi) \sec \theta d\phi + (q \sin \phi + r \cos \phi) \tan \theta \sec \theta d\theta \quad (80)$$

where

$$\begin{aligned} \sum d(\bullet) = & \frac{\partial d(\bullet)}{\partial du} du + \frac{\partial d(\bullet)}{\partial dv} dv + \frac{\partial d(\bullet)}{\partial dw} dw + \frac{\partial d(\bullet)}{\partial dp} dp + \frac{\partial d(\bullet)}{\partial dq} dq + \frac{\partial d(\bullet)}{\partial dr} dr \dots \\ & \dots + \frac{\partial d(\bullet)}{\partial d\phi} d\phi + \frac{\partial d(\bullet)}{\partial d\theta} d\theta + \frac{\partial d(\bullet)}{\partial d\psi} d\psi \dots \\ & \dots + \frac{\partial d(\bullet)}{\partial d\delta_{\text{Coll}}} d\delta_{\text{Coll}} + \frac{\partial d(\bullet)}{\partial d\delta_{\text{Ped}}} d\delta_{\text{Ped}} + \frac{\partial d(\bullet)}{\partial d\delta_{\text{Lat}}} d\delta_{\text{Lat}} + \frac{\partial d(\bullet)}{\partial d\delta_{\text{Long}}} d\delta_{\text{Long}} \end{aligned} \quad (81)$$

$$(\bullet) = X, Y, Z, L, M, N$$

Eqns.(72) – (80) can be expressed in compact form.

$$\dot{\bar{x}} = \mathbf{A}\bar{x} + \mathbf{B}\bar{u} \quad (82)$$

where

$$\mathbf{A} = \begin{bmatrix} X_u & X_v & X_w & X_p & X_q & X_r & X_\phi & X_\theta & X_\psi \\ Y_u & Y_v & Y_w & Y_p & Y_q & Y_r & Y_\phi & Y_\theta & Y_\psi \\ Z_u & Z_v & Z_w & Z_p & Z_q & Z_r & Z_\phi & Z_\theta & Z_\psi \\ L_u & L_v & L_w & L_p & L_q & L_r & L_\phi & L_\theta & L_\psi \\ M_u & M_v & M_w & M_p & M_q & M_r & M_\phi & M_\theta & M_\psi \\ N_u & N_v & N_w & N_p & N_q & N_r & N_\phi & N_\theta & N_\psi \\ 0 & 0 & 0 & \Phi_p & \Phi_q & \Phi_r & \Phi_\phi & \Phi_\theta & 0 \\ 0 & 0 & 0 & 0 & \Theta_q & \Theta_r & \Theta_\phi & 0 & 0 \\ 0 & 0 & 0 & 0 & \Psi_q & \Psi_r & \Psi_\phi & \Psi_\theta & 0 \end{bmatrix} \quad (83)$$

$$\mathbf{B} = \begin{bmatrix} X_{\delta_{\text{Coll}}} & X_{\delta_{\text{Ped}}} & X_{\delta_{\text{Lat}}} & X_{\delta_{\text{Long}}} \\ Y_{\delta_{\text{Coll}}} & Y_{\delta_{\text{Ped}}} & Y_{\delta_{\text{Lat}}} & Y_{\delta_{\text{Long}}} \\ Z_{\delta_{\text{Coll}}} & Z_{\delta_{\text{Ped}}} & Z_{\delta_{\text{Lat}}} & Z_{\delta_{\text{Long}}} \\ L_{\delta_{\text{Coll}}} & L_{\delta_{\text{Ped}}} & L_{\delta_{\text{Lat}}} & L_{\delta_{\text{Long}}} \\ M_{\delta_{\text{Coll}}} & M_{\delta_{\text{Ped}}} & M_{\delta_{\text{Lat}}} & M_{\delta_{\text{Long}}} \\ N_{\delta_{\text{Coll}}} & N_{\delta_{\text{Ped}}} & N_{\delta_{\text{Lat}}} & N_{\delta_{\text{Long}}} \\ \Phi_{\delta_{\text{Coll}}} & \Phi_{\delta_{\text{Ped}}} & \Phi_{\delta_{\text{Lat}}} & \Phi_{\delta_{\text{Long}}} \\ \Theta_{\delta_{\text{Coll}}} & \Theta_{\delta_{\text{Ped}}} & \Theta_{\delta_{\text{Lat}}} & \Theta_{\delta_{\text{Long}}} \\ \Psi_{\delta_{\text{Coll}}} & \Psi_{\delta_{\text{Ped}}} & \Psi_{\delta_{\text{Lat}}} & \Psi_{\delta_{\text{Long}}} \end{bmatrix} \quad (84)$$

$$\bar{x} = [du \quad dv \quad dw \quad dp \quad dq \quad dr \quad d\phi \quad d\theta \quad d\psi]^T \quad (85)$$

$$\bar{u} = [d\delta_{\text{Coll}} \quad d\delta_{\text{Ped}} \quad d\delta_{\text{Lat}} \quad d\delta_{\text{Long}}]^T \quad (86)$$

The elements of **A** and **B** are obtained by partially derived the total force and moment perturbation toward each degree of freedom plus re-expressing the kinematic relation in term of each degree of freedom.

$$\left. \begin{aligned} X_u &= \frac{1}{m} \frac{\partial dX}{\partial du}, X_v = \left(\frac{1}{m} \frac{\partial dX}{\partial dv} + r \right), \dots \\ \dots, Y_v &= \frac{1}{m} \frac{\partial dY}{\partial dv}, Y_w = \left(\frac{1}{m} \frac{\partial dY}{\partial dw} + p \right), \dots \\ \dots, Z_w &= -\frac{1}{m} \frac{\partial dZ}{\partial dw}, Z_p = \left(-\frac{1}{m} \frac{\partial dZ}{\partial dp} + v \right), \dots \\ \dots, L_p &= \frac{1}{I_{xx}} \frac{\partial dL}{\partial dp}, L_q = \frac{1}{I_{xx}} \left(\frac{\partial dL}{\partial dq} + (I_{yy} - I_{zz})r \right), \dots \\ \dots, M_q &= \frac{1}{I_{yy}} \frac{\partial dM}{\partial dq}, M_r = \frac{1}{I_{yy}} \left(\frac{\partial dM}{\partial dr} + (I_{zz} - I_{xx})p \right), \dots \\ \dots, N_r &= \frac{1}{I_{zz}} \frac{\partial dN}{\partial dr}, N_\phi = \frac{1}{I_{zz}} \frac{\partial dN}{\partial d\phi}, \dots \\ \Phi_p &= 1, \Phi_q = \sin \phi \tan \theta, \Phi_r = \cos \phi \tan \theta, \dots \\ \dots, \Phi_\phi &= (q \cos \phi - r \sin \phi) \tan \theta, \Phi_\theta = (q \sin \phi + r \cos \phi) \sec \theta. \\ \Theta_q &= \cos \phi, \Theta_r = -\sin \phi, \Theta_\phi = -(q \sin \phi + r \cos \phi). \\ \Psi_q &= \sin \phi \sec \theta, \Psi_r = \cos \phi \sec \theta, \dots \\ \dots, \Psi_\phi &= (q \cos \phi - r \sin \phi) \sec \theta, \Psi_\theta = (q \sin \phi + r \cos \phi) \tan \theta \sec \theta. \end{aligned} \right\} \quad (87)$$

2.5 The Stability Derivatives

The force and moment derivatives of each helicopter component can be obtained by analytical calculation, except for those of main rotor's and tail rotor's, which require iterative calculation (see sect. 2.2.1). A computer program is used to solve the equilibrium condition and to calculate the change in aerodynamic forces and moments due to the change in each degree of freedom and control input. The following subsections summarized the values of the derivatives.

2.5.1 Main Rotor Derivatives

To assign the values to the derivatives, all parameters are plotted as function of the states and inputs. The value of the derivative can be calculated as the gradient of the curve evaluated at the trim condition.

2.5.1.1 Flapping Derivatives

Table 2. Main Rotor Flapping Derivatives

Derivatives	Unit	Hover	Cruise	Ratio
Longitudinal flapping derivatives				
$\begin{bmatrix} \frac{\partial a_{1s}}{\partial u} & \frac{\partial a_{1s}}{\partial v} & \frac{\partial a_{1s}}{\partial w} \end{bmatrix}^T$	rad·s/m	$\begin{bmatrix} 0.000322 \\ 0 \\ 0 \end{bmatrix}$	$\begin{bmatrix} 0.000232 \\ 0 \\ 0.000318 \end{bmatrix}$	$\begin{bmatrix} 0.72 \\ - \\ - \end{bmatrix}$
$\begin{bmatrix} \frac{\partial a_{1s}}{\partial p} & \frac{\partial a_{1s}}{\partial q} & \frac{\partial a_{1s}}{\partial r} \end{bmatrix}^T$	s	$\begin{bmatrix} 0 \\ -0.1 \\ 0 \end{bmatrix}$	$\begin{bmatrix} 0 \\ -0.1 \\ 0 \end{bmatrix}$	$\begin{bmatrix} 0 \\ 1 \\ 0 \end{bmatrix}$
$\begin{bmatrix} \frac{\partial a_{1s}}{\partial \delta_{\text{Coll}}} & \frac{\partial a_{1s}}{\partial \delta_{\text{Ped}}} \end{bmatrix}^T$	1	$\begin{bmatrix} 0 \\ 0 \end{bmatrix}$	$\begin{bmatrix} 0.068218 \\ 0 \end{bmatrix}$	$\begin{bmatrix} - \\ - \end{bmatrix}$
$\begin{bmatrix} \frac{\partial a_{1s}}{\partial \delta_{\text{Lat}}} & \frac{\partial a_{1s}}{\partial \delta_{\text{Long}}} \end{bmatrix}^T$	1	$\begin{bmatrix} 0 \\ -4.2 \end{bmatrix}$	$\begin{bmatrix} 0 \\ 4.1988 \end{bmatrix}$	$\begin{bmatrix} - \\ -0.99 \end{bmatrix}$
Lateral flapping derivatives				
$\begin{bmatrix} \frac{\partial b_{1s}}{\partial u} & \frac{\partial b_{1s}}{\partial v} & \frac{\partial b_{1s}}{\partial w} \end{bmatrix}^T$	rad·s/m	$\begin{bmatrix} 0 \\ 0.000322 \\ 0 \end{bmatrix}$	$\begin{bmatrix} 0 \\ 0.000259 \\ 0 \end{bmatrix}$	$\begin{bmatrix} - \\ 0.80 \\ - \end{bmatrix}$
$\begin{bmatrix} \frac{\partial b_{1s}}{\partial p} & \frac{\partial b_{1s}}{\partial q} & \frac{\partial b_{1s}}{\partial r} \end{bmatrix}^T$	s	$\begin{bmatrix} -0.1 \\ 0 \\ 0 \end{bmatrix}$	$\begin{bmatrix} -0.1 \\ 0 \\ 0 \end{bmatrix}$	$\begin{bmatrix} 1 \\ - \\ - \end{bmatrix}$
$\begin{bmatrix} \frac{\partial b_{1s}}{\partial \delta_{\text{Coll}}} & \frac{\partial b_{1s}}{\partial \delta_{\text{Ped}}} \end{bmatrix}^T$	1	$\begin{bmatrix} 0 \\ 0 \end{bmatrix}$	$\begin{bmatrix} 0.003073 \\ 0 \end{bmatrix}$	$\begin{bmatrix} - \\ - \end{bmatrix}$
$\begin{bmatrix} \frac{\partial b_{1s}}{\partial \delta_{\text{Lat}}} & \frac{\partial b_{1s}}{\partial \delta_{\text{Long}}} \end{bmatrix}^T$	1	$\begin{bmatrix} 4.2 \\ 0 \end{bmatrix}$	$\begin{bmatrix} 4.1988 \\ 0 \end{bmatrix}$	$\begin{bmatrix} 0.99 \\ - \end{bmatrix}$

2.5.1.2 Thrust Derivative

Table 3. Main Rotor Thrust Derivatives

Derivatives	Unit	Hover	Cruise	Ratio
$\begin{bmatrix} \frac{\partial T_{\text{MR}}}{\partial u} & \frac{\partial T_{\text{MR}}}{\partial v} & \frac{\partial T_{\text{MR}}}{\partial w} \end{bmatrix}^T$	N·s/m	$\begin{bmatrix} 0 \\ 0 \\ 0.000335 \end{bmatrix}$	$\begin{bmatrix} 1.315574 \\ 0.057189 \\ 14.2086 \end{bmatrix}$	$\begin{bmatrix} - \\ - \\ 42413.73 \end{bmatrix}$
$\begin{bmatrix} \frac{\partial T_{\text{MR}}}{\partial \delta_{\text{Coll}}} & \frac{\partial T_{\text{MR}}}{\partial \delta_{\text{Ped}}} \end{bmatrix}^T$	N/rad	$\begin{bmatrix} 1043.6 \\ 0 \end{bmatrix}$	$\begin{bmatrix} 1262.5898 \\ 0 \end{bmatrix}$	$\begin{bmatrix} 1.20 \\ - \end{bmatrix}$
$\begin{bmatrix} \frac{\partial T_{\text{MR}}}{\partial \delta_{\text{Lat}}} & \frac{\partial T_{\text{MR}}}{\partial \delta_{\text{Long}}} \end{bmatrix}^T$	N/rad	$\begin{bmatrix} 0 \\ 0 \end{bmatrix}$	$\begin{bmatrix} 0 \\ 0 \end{bmatrix}$	$\begin{bmatrix} - \\ - \end{bmatrix}$

2.5.1.3 Torque Derivative

Table 4. Main Rotor Torque Derivatives

Derivatives	Unit	Hover	Cruise	Ratio
$\left[\frac{\partial Q_{MR}}{\partial u} \quad \frac{\partial Q_{MR}}{\partial v} \quad \frac{\partial Q_{MR}}{\partial w} \right]^T$	N·s/m	$\begin{bmatrix} 0 \\ 0 \\ 0 \end{bmatrix}$	$\begin{bmatrix} -0.001048 \\ -0.000043 \\ -0.292165 \end{bmatrix}$	$\begin{bmatrix} - \\ - \\ - \end{bmatrix}$
$\left[\frac{\partial Q_{MR}}{\partial \delta_{Coll}} \quad \frac{\partial Q_{MR}}{\partial \delta_{Ped}} \right]^T$	N/rad	$\begin{bmatrix} 42.935 \\ 0 \end{bmatrix}$	$\begin{bmatrix} 17.094606 \\ 0 \end{bmatrix}$	$\begin{bmatrix} 0.39 \\ - \end{bmatrix}$

2.5.1.4 Induced Velocity Derivative

Table 5. Main Rotor Induced Velocity Derivatives

Derivatives	Unit	Hover	Cruise	Ratio
$\left[\frac{\partial w_{iMR}}{\partial u} \quad \frac{\partial w_{iMR}}{\partial v} \quad \frac{\partial w_{iMR}}{\partial w} \right]^T$	1	$\begin{bmatrix} 0 \\ 0 \\ -0.000018 \end{bmatrix}$	$\begin{bmatrix} -0.055941 \\ -0.002430 \\ 0.223859 \end{bmatrix}$	$\begin{bmatrix} - \\ - \\ -12436.61 \end{bmatrix}$
$\left[\frac{\partial w_{iMR}}{\partial \delta_{Coll}} \quad \frac{\partial w_{iMR}}{\partial \delta_{Ped}} \right]^T$	m/rad·s	$\begin{bmatrix} 29.301 \\ 0 \end{bmatrix}$	$\begin{bmatrix} 19.468431 \\ 0 \end{bmatrix}$	$\begin{bmatrix} 0.66 \\ - \end{bmatrix}$
$\left[\frac{\partial w_{iMR}}{\partial \delta_{Lat}} \quad \frac{\partial w_{iMR}}{\partial \delta_{Long}} \right]^T$	m/rad·s	$\begin{bmatrix} 0 \\ 0 \end{bmatrix}$	$\begin{bmatrix} 0 \\ 0 \end{bmatrix}$	$\begin{bmatrix} - \\ - \end{bmatrix}$

2.5.1.5 Force and Moment Derivatives. Provided with data obtained in 2.5.1.1 to 2.5.2.3, the main rotor force and moment derivatives can then be calculated by the following expression.

$$\begin{aligned} \frac{\partial X_{MR}}{\partial u} &= - \left(a_{1seq} \frac{\partial T_{MR}}{\partial u} + T_{MR eq} \cos a_{1seq} \frac{\partial a_{1s}}{\partial u} \right) \\ &\vdots \end{aligned} \tag{88}$$

$$\frac{\partial X_{MR}}{\partial \delta_{Long}} = - \left(a_{1seq} \frac{\partial T_{MR}}{\partial \delta_{Long}} + T_{MR eq} \cos a_{1seq} \frac{\partial a_{1s}}{\partial \delta_{Long}} \right)$$

$$\frac{\partial X_{MR}}{\partial a_{1s}} = -T_{MR eq} \cos a_{1seq} \quad \frac{\partial X_{MR}}{\partial b_{1s}} = -T_{MR eq} \cos a_{1seq} \frac{\partial a_{1s}}{\partial b_{1s}} \tag{89}$$

$$\begin{aligned} \frac{\partial Y_{MR}}{\partial u} &= b_{1seq} \frac{\partial T_{MR}}{\partial u} + T_{MR eq} \cos b_{1seq} \frac{\partial b_{1s}}{\partial u} \\ &\vdots \end{aligned} \tag{90}$$

$$\frac{\partial Y_{MR}}{\partial \delta_{Long}} = b_{1seq} \frac{\partial T_{MR}}{\partial \delta_{Long}} + T_{MR eq} \cos b_{1seq} \frac{\partial b_{1s}}{\partial \delta_{Long}}$$

$$\frac{\partial Y_{MR}}{\partial a_{1s}} = T_{MR\text{eq}} \cos b_{1\text{seq}} \frac{\partial b_{1s}}{\partial a_{1s}} \quad \frac{\partial Y_{MR}}{\partial b_{1s}} = T_{MR\text{eq}} \cos b_{1\text{seq}} \quad (91)$$

$$Z_{MR} = T_{MR} \cos a_{1s} \cos b_{1s}$$

$$\frac{\partial Z_{MR}}{\partial(\bullet)} = \cos a_{1\text{seq}} \cos b_{1\text{seq}} \frac{\partial T_{MR}}{\partial(\bullet)} - T_{MR\text{eq}} \sin a_{1\text{seq}} \cos b_{1\text{seq}} \frac{\partial a_{1s}}{\partial(\bullet)} - T_{MR\text{eq}} \cos a_{1\text{seq}} \sin b_{1\text{seq}} \frac{\partial b_{1s}}{\partial(\bullet)}$$

$$\begin{aligned} \frac{\partial Z_{MR}}{\partial u} &= \cos a_{1\text{seq}} \cos b_{1\text{seq}} \frac{\partial T_{MR}}{\partial u} - T_{MR\text{eq}} \sin a_{1\text{seq}} \cos b_{1\text{seq}} \frac{\partial a_{1s}}{\partial u} - T_{MR\text{eq}} \cos a_{1\text{seq}} \sin b_{1\text{seq}} \frac{\partial b_{1s}}{\partial u} \\ &\vdots \\ \frac{\partial Z_{MR}}{\partial \delta_{\text{Long}}} &= \cos a_{1\text{seq}} \cos b_{1\text{seq}} \frac{\partial T_{MR}}{\partial \delta_{\text{Long}}} - T_{MR\text{eq}} \sin a_{1\text{seq}} \cos b_{1\text{seq}} \frac{\partial a_{1s}}{\partial \delta_{\text{Long}}} - T_{MR\text{eq}} \cos a_{1\text{seq}} \sin b_{1\text{seq}} \frac{\partial b_{1s}}{\partial \delta_{\text{Long}}} \end{aligned} \quad (92)$$

$$\frac{\partial Z_{MR}}{\partial a_{1s}} = -T_{MR\text{eq}} \left(\sin a_{1\text{seq}} \cos b_{1\text{seq}} + \cos a_{1\text{seq}} \sin b_{1\text{seq}} \frac{\partial b_{1s}}{\partial a_{1s}} \right) \quad (93)$$

$$\frac{\partial Z_{MR}}{\partial b_{1s}} = -T_{MR\text{eq}} \left(\sin a_{1\text{seq}} \cos b_{1\text{seq}} \frac{\partial a_{1s}}{\partial b_{1s}} + \cos a_{1\text{seq}} \sin b_{1\text{seq}} \right)$$

$$\frac{\partial \bar{F}_{MR}}{\partial \phi} = \bar{0} \quad \frac{\partial \bar{F}_{MR}}{\partial \theta} = \bar{0} \quad \frac{\partial \bar{F}_{MR}}{\partial \psi} = \bar{0} \quad (94)$$

$$\frac{\partial L_{MR}}{\partial u} = h_{MR} \sin b_{1\text{seq}} \frac{\partial T_{MR}}{\partial u} + (K_{\beta} + T_{MR\text{eq}} h_{MR} \cos b_{1\text{seq}}) \frac{\partial b_{1s}}{\partial u} \quad (95)$$

$$\frac{\partial L_{MR}}{\partial \delta_{\text{Long}}} = h_{MR} \sin b_{1\text{seq}} \frac{\partial T_{MR}}{\partial \delta_{\text{Long}}} + (K_{\beta} + T_{MR\text{eq}} h_{MR} \cos b_{1\text{seq}}) \frac{\partial b_{1s}}{\partial \delta_{\text{Long}}}$$

$$\frac{\partial L_{MR}}{\partial a_{1s}} = (K_{\beta} + T_{MR\text{eq}} h_{MR} \cos b_{1\text{seq}}) \frac{\partial b_{1s}}{\partial a_{1s}} \quad (96)$$

$$\frac{\partial L_{MR}}{\partial b_{1s}} = K_{\beta} + T_{MR\text{eq}} h_{MR} \cos b_{1\text{seq}}$$

$$\frac{\partial M_{MR}}{\partial u} = h_{MR} \sin a_{1\text{seq}} \frac{\partial T_{MR}}{\partial u} + (K_{\beta} + T_{MR\text{eq}} h_{MR} \cos a_{1\text{seq}}) \frac{\partial a_{1s}}{\partial u} \quad (97)$$

$$\frac{\partial M_{MR}}{\partial \delta_{\text{Long}}} = h_{MR} \sin a_{1\text{seq}} \frac{\partial T_{MR}}{\partial \delta_{\text{Long}}} + (K_{\beta} + T_{MR\text{eq}} h_{MR} \cos a_{1\text{seq}}) \frac{\partial a_{1s}}{\partial \delta_{\text{Long}}}$$

$$\frac{\partial M_{MR}}{\partial a_{1s}} = K_{\beta} + T_{MR\text{eq}} h_{MR} \cos a_{1\text{seq}} \quad (98)$$

$$\frac{\partial M_{MR}}{\partial b_{1s}} = (K_{\beta} + T_{MR\text{eq}} h_{MR} \cos a_{1\text{seq}}) \frac{\partial a_{1s}}{\partial b_{1s}}$$

$$\frac{\partial N_{MR}}{\partial u} = -\frac{\partial Q_{MR}}{\partial u}$$

$$\vdots$$

$$\frac{\partial N_{MR}}{\partial \delta_{\text{Long}}} = -\frac{\partial Q_{MR}}{\partial \delta_{\text{Long}}} \quad (99)$$

$$\frac{\partial N_{MR}}{\partial a_{1s}} = 0 \quad \frac{\partial N_{MR}}{\partial b_{1s}} = 0 \quad (100)$$

$$\frac{\partial \bar{M}_{MR}}{\partial \phi} = \bar{0} \quad \frac{\partial \bar{M}_{MR}}{\partial \theta} = \bar{0} \quad \frac{\partial \bar{M}_{MR}}{\partial \psi} = \bar{0} \quad (101)$$

2.5.2 Tail Rotor Derivatives

2.5.2.1 Thrust Derivative

Table 6. Tail Rotor Thrust Derivatives

Derivatives	Unit	Hover	Cruise	Ratio
$\left[\frac{\partial T_{TR}}{\partial u} \quad \frac{\partial T_{TR}}{\partial v} \quad \frac{\partial T_{TR}}{\partial w} \right]^T$	N·s/m	$\begin{bmatrix} 0 \\ 0 \\ 0 \end{bmatrix}$	$\begin{bmatrix} 0.13098 \\ 0.558553 \\ -0.013237 \end{bmatrix}$	$\begin{bmatrix} - \\ - \\ - \end{bmatrix}$
$\left[\frac{\partial T_{TR}}{\partial p} \quad \frac{\partial T_{TR}}{\partial q} \quad \frac{\partial T_{TR}}{\partial r} \right]^T$	N·s/rad	$\begin{bmatrix} 0 \\ 0 \\ 0 \end{bmatrix}$	$\begin{bmatrix} 0.044684 \\ -0.018719 \\ -0.508284 \end{bmatrix}$	$\begin{bmatrix} - \\ - \\ - \end{bmatrix}$
$\left[\frac{\partial T_{TR}}{\partial \delta_{\text{Coll}}} \quad \frac{\partial T_{TR}}{\partial \delta_{\text{Ped}}} \right]^T$	N/rad	$\begin{bmatrix} 0 \\ 38.849 \end{bmatrix}$	$\begin{bmatrix} 0 \\ 40.389359 \end{bmatrix}$	$\begin{bmatrix} - \\ 1.03 \end{bmatrix}$
$\left[\frac{\partial T_{TR}}{\partial \delta_{\text{Lat}}} \quad \frac{\partial T_{TR}}{\partial \delta_{\text{Long}}} \right]^T$	N/rad	$\begin{bmatrix} 0 \\ 0 \end{bmatrix}$	$\begin{bmatrix} 0 \\ 0 \end{bmatrix}$	$\begin{bmatrix} - \\ - \end{bmatrix}$

2.5.2.2 Torque Derivative

Table 7. Tail Rotor Torque Derivatives

Derivatives	Unit	Hover	Cruise	Ratio
$\left[\frac{\partial Q_{TR}}{\partial u} \quad \frac{\partial Q_{TR}}{\partial v} \quad \frac{\partial Q_{TR}}{\partial w} \right]^T$	N·s/m	$\begin{bmatrix} 0 \\ 0 \\ 0 \end{bmatrix}$	$\begin{bmatrix} -0.000053 \\ -0.0026 \\ 0.000005 \end{bmatrix}$	$\begin{bmatrix} - \\ - \\ - \end{bmatrix}$
$\left[\frac{\partial Q_{TR}}{\partial p} \quad \frac{\partial Q_{TR}}{\partial q} \quad \frac{\partial Q_{TR}}{\partial r} \right]^T$	N·s/rad	$\begin{bmatrix} 0 \\ 0 \\ 0 \end{bmatrix}$	$\begin{bmatrix} -0.000021 \\ 0.000005 \\ 0.002391 \end{bmatrix}$	$\begin{bmatrix} - \\ - \\ - \end{bmatrix}$
$\left[\frac{\partial Q_{TR}}{\partial \delta_{Coll}} \quad \frac{\partial Q_{TR}}{\partial \delta_{Ped}} \right]^T$	N/rad	$\begin{bmatrix} 0 \\ 0.78383 \end{bmatrix}$	$\begin{bmatrix} 0 \\ 0.362617 \end{bmatrix}$	$\begin{bmatrix} - \\ 0.46 \end{bmatrix}$

2.5.2.3 Induced Velocity Derivative

Table 8. Tail Rotor Induced Velocity Derivatives

Derivatives	Unit	Hover	Cruise	Ratio
$\left[\frac{\partial v_{iTR}}{\partial u} \quad \frac{\partial v_{iTR}}{\partial v} \quad \frac{\partial v_{iTR}}{\partial w} \right]^T$	1	$\begin{bmatrix} 0 \\ 0 \\ 0 \end{bmatrix}$	$\begin{bmatrix} -0.106211 \\ 0.383865 \\ 0.010723 \end{bmatrix}$	$\begin{bmatrix} - \\ - \\ - \end{bmatrix}$
$\left[\frac{\partial v_{iTR}}{\partial p} \quad \frac{\partial v_{iTR}}{\partial q} \quad \frac{\partial v_{iTR}}{\partial r} \right]^T$	m/rad	$\begin{bmatrix} 0 \\ 0 \\ 0 \end{bmatrix}$	$\begin{bmatrix} 0.030709 \\ 0.009618 \\ -0.349317 \end{bmatrix}$	$\begin{bmatrix} - \\ - \\ - \end{bmatrix}$
$\left[\frac{\partial v_{iTR}}{\partial \delta_{Coll}} \quad \frac{\partial v_{iTR}}{\partial \delta_{Ped}} \right]^T$	m/rad·s	$\begin{bmatrix} 0 \\ 24.592 \end{bmatrix}$	$\begin{bmatrix} 0 \\ 25.628783 \end{bmatrix}$	$\begin{bmatrix} - \\ 1.04 \end{bmatrix}$

2.5.2.4 *Force and Moment Derivatives.* Provided with data obtained in 2.5.2.1 to 2.5.2.3, the tail rotor force and moment derivatives can then be calculated by the following expression.

$$\begin{aligned} \frac{\partial X_{TR}}{\partial u} &= 0 & \frac{\partial Y_{TR}}{\partial u} &= -\frac{\partial T_{TR}}{\partial u} & \frac{\partial Z_{TR}}{\partial u} &= 0 \\ &\vdots & &\vdots & &\vdots \end{aligned} \quad (102)$$

$$\begin{aligned} \frac{\partial X_{TR}}{\partial \delta_{Long}} &= 0 & \frac{\partial Y_{TR}}{\partial \delta_{Long}} &= -\frac{\partial T_{TR}}{\partial \delta_{Long}} & \frac{\partial Z_{TR}}{\partial \delta_{Long}} &= 0 \\ & & \frac{\partial \bar{F}_{TR}}{\partial a_{1s}} &= \bar{0} & \frac{\partial \bar{F}_{TR}}{\partial b_{1s}} &= \bar{0} \end{aligned} \quad (103)$$

$$\frac{\partial \bar{F}_{TR}}{\partial \phi} = \bar{0} \quad \frac{\partial \bar{F}_{TR}}{\partial \theta} = \bar{0} \quad \frac{\partial \bar{F}_{TR}}{\partial \psi} = \bar{0} \quad (104)$$

$$\begin{aligned} \frac{\partial L_{\text{TR}}}{\partial u} &= -\frac{\partial T_{\text{TR}}}{\partial u} h_{\text{TR}} & \frac{\partial M_{\text{TR}}}{\partial u} &= -\frac{\partial Q_{\text{TR}}}{\partial u} & \frac{\partial N_{\text{TR}}}{\partial u} &= \frac{\partial T_{\text{TR}}}{\partial u} l_{\text{TR}} \\ &\vdots & &\vdots & &\vdots \end{aligned} \quad (105)$$

$$\begin{aligned} \frac{\partial L_{\text{TR}}}{\partial \delta_{\text{Long}}} &= -\frac{\partial T_{\text{TR}}}{\partial \delta_{\text{Long}}} h_{\text{TR}} & \frac{\partial M_{\text{TR}}}{\partial \delta_{\text{Long}}} &= -\frac{\partial Q_{\text{TR}}}{\partial \delta_{\text{Long}}} & \frac{\partial N_{\text{TR}}}{\partial \delta_{\text{Long}}} &= \frac{\partial T_{\text{TR}}}{\partial \delta_{\text{Long}}} l_{\text{TR}} \\ & & \frac{\partial \bar{M}_{\text{TR}}}{\partial a_{1s}} &= \bar{0} & \frac{\partial \bar{M}_{\text{TR}}}{\partial b_{1s}} &= \bar{0} \end{aligned} \quad (106)$$

$$\frac{\partial \bar{M}_{\text{TR}}}{\partial \phi} = \bar{0} \quad \frac{\partial \bar{M}_{\text{TR}}}{\partial \theta} = \bar{0} \quad \frac{\partial \bar{M}_{\text{TR}}}{\partial \psi} = \bar{0} \quad (107)$$

2.5.3 Fuselage Derivatives

The fuselage effect on the X -force is given in the following expression. During hover the fuselage gives no contribution to the force in the X -axis.

$$\begin{aligned} \frac{\partial X_{\text{Fus}}}{\partial u} &= -\frac{1}{2} \rho S_{x\text{Fus}} \left[\left(u_{\text{eq}} - (w_{\text{eq}} - w_{i\text{MR eq}}) \frac{\partial w_{i\text{MR}}}{\partial u} \right) \frac{u_{\text{eq}}}{V_{\infty\text{Fus}}} + V_{\infty\text{Fus}} \right] \\ \frac{\partial X_{\text{Fus}}}{\partial u} \Big|_{\text{cr}} &= -\frac{1}{2} \rho S_{x\text{Fus}} \left[\left(u_{\text{eq}} + w_{i\text{MR eq}} \frac{\partial w_{i\text{MR}}}{\partial u} \right) \frac{u_{\text{eq}}}{V_{\infty\text{Fus}}} + V_{\infty\text{Fus}} \right] \end{aligned} \quad (108)$$

$$\begin{aligned} \frac{\partial X_{\text{Fus}}}{\partial v} &= -\frac{1}{2} \rho S_{x\text{Fus}} \left(v_{\text{eq}} - (w_{\text{eq}} - w_{i\text{MR eq}}) \frac{\partial w_{i\text{MR}}}{\partial v} \right) \frac{u_{\text{eq}}}{V_{\infty\text{Fus}}} \\ \frac{\partial X_{\text{Fus}}}{\partial v} \Big|_{\text{cr}} &= -\frac{1}{2} \rho S_{x\text{Fus}} \left(v_{\text{eq}} + w_{i\text{MR eq}} \frac{\partial w_{i\text{MR}}}{\partial v} \right) \frac{u_{\text{eq}}}{V_{\infty\text{Fus}}} \end{aligned} \quad (109)$$

$$\begin{aligned} \frac{\partial X_{\text{Fus}}}{\partial w} &= -\frac{1}{2} \rho S_{x\text{Fus}} (w_{\text{eq}} - w_{i\text{MR eq}}) \left(1 - \frac{\partial w_{i\text{MR}}}{\partial w} \right) \frac{u_{\text{eq}}}{V_{\infty\text{Fus}}} \\ \frac{\partial X_{\text{Fus}}}{\partial w} \Big|_{\text{cr}} &= \frac{1}{2} \rho S_{x\text{Fus}} w_{i\text{MR eq}} \left(1 - \frac{\partial w_{i\text{MR}}}{\partial w} \right) \frac{u_{\text{eq}}}{V_{\infty\text{Fus}}} \end{aligned} \quad (110)$$

$$\begin{aligned} \frac{\partial X_{\text{Fus}}}{\partial p} &= \frac{1}{2} \rho S_{x\text{Fus}} (w_{\text{eq}} - w_{i\text{MR eq}}) \frac{\partial w_{i\text{MR}}}{\partial p} \frac{u_{\text{eq}}}{V_{\infty\text{Fus}}} \\ \frac{\partial X_{\text{Fus}}}{\partial p} \Big|_{\text{cr}} &= 0 \end{aligned} \quad (111)$$

$$\frac{\partial X_{\text{Fus}}}{\partial q} = \frac{1}{2} \rho S_{x\text{Fus}} (w_{\text{eq}} - w_{i\text{MR eq}}) \frac{\partial w_{i\text{MR}}}{\partial q} \frac{u_{\text{eq}}}{V_{\infty\text{Fus}}}$$

$$\left. \frac{\partial X_{\text{Fus}}}{\partial q} \right|_{\text{cr}} = 0 \quad (112)$$

$$\frac{\partial X_{\text{Fus}}}{\partial r} = \frac{1}{2} \rho S_{x\text{Fus}} (w_{\text{eq}} - w_{i\text{MR eq}}) \frac{\partial w_{i\text{MR}}}{\partial r} \frac{u_{\text{eq}}}{V_{\infty\text{Fus}}}$$

$$\left. \frac{\partial X_{\text{Fus}}}{\partial r} \right|_{\text{cr}} = 0 \quad (113)$$

$$\frac{\partial X_{\text{Fus}}}{\partial \delta_{\text{Coll}}} = \frac{1}{2} \rho S_{x\text{Fus}} (w_{\text{eq}} - w_{i\text{MR eq}}) \frac{\partial w_{i\text{MR}}}{\partial \delta_{\text{Coll}}} \frac{u_{\text{eq}}}{V_{\infty\text{Fus}}}$$

$$\left. \frac{\partial X_{\text{Fus}}}{\partial \delta_{\text{Coll}}} \right|_{\text{cr}} = -\frac{1}{2} \rho S_{x\text{Fus}} w_{i\text{MR eq}} \frac{\partial w_{i\text{MR}}}{\partial \delta_{\text{Coll}}} \frac{u_{\text{eq}}}{V_{\infty\text{Fus}}} \quad (114)$$

$$\left. \frac{\partial X_{\text{Fus}}}{\partial \delta_{\text{Ped}}} \right|_{\text{cr}} = 0 \quad \left. \frac{\partial X_{\text{Fus}}}{\partial \delta_{\text{Lat}}} \right|_{\text{cr}} = 0 \quad \left. \frac{\partial X_{\text{Fus}}}{\partial \delta_{\text{Long}}} \right|_{\text{cr}} = 0 \quad (115)$$

$$\frac{\partial Y_{\text{Fus}}}{\partial u} = -\frac{1}{2} \rho S_{y\text{Fus}} \left(u_{\text{eq}} - (w_{\text{eq}} - w_{i\text{MR eq}}) \frac{\partial w_{i\text{MR}}}{\partial u} \right) \frac{v_{\text{eq}}}{V_{\infty\text{Fus}}}$$

$$\left. \frac{\partial Y_{\text{Fus}}}{\partial u} \right|_{\text{cr}} = -\frac{1}{2} \rho S_{y\text{Fus}} \left(u_{\text{eq}} + w_{i\text{MR eq}} \frac{\partial w_{i\text{MR}}}{\partial u} \right) \frac{v_{\text{eq}}}{V_{\infty\text{Fus}}} \quad (116)$$

$$\frac{\partial Y_{\text{Fus}}}{\partial v} = -\frac{1}{2} \rho S_{y\text{Fus}} \left[\left(v_{\text{eq}} - (w_{\text{eq}} - w_{i\text{MR eq}}) \frac{\partial w_{i\text{MR}}}{\partial v} \right) \frac{v_{\text{eq}}}{V_{\infty\text{Fus}}} + V_{\infty\text{Fus}} \right]$$

$$\left. \frac{\partial Y_{\text{Fus}}}{\partial v} \right|_{\text{cr}} = -\frac{1}{2} \rho S_{y\text{Fus}} \left[\left(v_{\text{eq}} + w_{i\text{MR eq}} \frac{\partial w_{i\text{MR}}}{\partial v} \right) \frac{v_{\text{eq}}}{V_{\infty\text{Fus}}} + V_{\infty\text{Fus}} \right] \quad (117)$$

$$\frac{\partial Y_{\text{Fus}}}{\partial w} = -\frac{1}{2} \rho S_{y\text{Fus}} (w_{\text{eq}} - w_{i\text{MR eq}}) \left(1 - \frac{\partial w_{i\text{MR}}}{\partial w} \right) \frac{v_{\text{eq}}}{V_{\infty\text{Fus}}}$$

$$\left. \frac{\partial Y_{\text{Fus}}}{\partial w} \right|_{\text{cr}} = \frac{1}{2} \rho S_{y\text{Fus}} w_{i\text{MR eq}} \left(1 - \frac{\partial w_{i\text{MR}}}{\partial w} \right) \frac{v_{\text{eq}}}{V_{\infty\text{Fus}}} \quad (118)$$

$$\frac{\partial Y_{\text{Fus}}}{\partial p} = \frac{1}{2} \rho S_{y\text{Fus}} (w_{\text{eq}} - w_{i\text{MR}\text{eq}}) \frac{\partial w_{i\text{MR}}}{\partial p} \frac{v_{\text{eq}}}{V_{\infty\text{Fus}}} \quad (119)$$

$$\left. \frac{\partial Y_{\text{Fus}}}{\partial p} \right|_{\text{cr}} = 0$$

$$\frac{\partial Y_{\text{Fus}}}{\partial q} = \frac{1}{2} \rho S_{y\text{Fus}} (w_{\text{eq}} - w_{i\text{MR}\text{eq}}) \frac{\partial w_{i\text{MR}}}{\partial q} \frac{v_{\text{eq}}}{V_{\infty\text{Fus}}} \quad (120)$$

$$\left. \frac{\partial Y_{\text{Fus}}}{\partial q} \right|_{\text{cr}} = 0$$

$$\frac{\partial Y_{\text{Fus}}}{\partial r} = \frac{1}{2} \rho S_{y\text{Fus}} (w_{\text{eq}} - w_{i\text{MR}\text{eq}}) \frac{\partial w_{i\text{MR}}}{\partial r} \frac{v_{\text{eq}}}{V_{\infty\text{Fus}}} \quad (121)$$

$$\left. \frac{\partial Y_{\text{Fus}}}{\partial r} \right|_{\text{cr}} = 0$$

$$\frac{\partial Y_{\text{Fus}}}{\partial \delta_{\text{Coll}}} = \frac{1}{2} \rho S_{y\text{Fus}} (w_{\text{eq}} - w_{i\text{MR}\text{eq}}) \frac{\partial w_{i\text{MR}}}{\partial \delta_{\text{Coll}}} \frac{v_{\text{eq}}}{V_{\infty\text{Fus}}} \quad (122)$$

$$\left. \frac{\partial Y_{\text{Fus}}}{\partial \delta_{\text{Coll}}} \right|_{\text{cr}} = -\frac{1}{2} \rho S_{y\text{Fus}} w_{i\text{MR}\text{eq}} \frac{\partial w_{i\text{MR}}}{\partial \delta_{\text{Coll}}} \frac{v_{\text{eq}}}{V_{\infty\text{Fus}}}$$

$$\left. \frac{\partial Y_{\text{Fus}}}{\partial \delta_{\text{Ped}}} \right|_{\text{cr}} = 0 \quad \left. \frac{\partial Y_{\text{Fus}}}{\partial \delta_{\text{Lat}}} \right|_{\text{cr}} = 0 \quad \left. \frac{\partial Y_{\text{Fus}}}{\partial \delta_{\text{Long}}} \right|_{\text{cr}} = 0 \quad (123)$$

$$\frac{\partial Z_{\text{Fus}}}{\partial u} = -\frac{1}{2V_{\infty}} \rho S_{z\text{Fus}} \left[u_{\text{aeq}} (w_a - w_{i\text{MR}})_{\text{eq}} - \left((w_a - w_{i\text{MR}})_{\text{eq}}^2 - V_{\infty\text{eq}}^2 \right) \frac{\partial w_{i\text{MR}}}{\partial u} \right]$$

$$= -\frac{1}{2V_{\infty\text{eq}}} \rho S_{z\text{Fus}} \left[u_{\text{aeq}} (w_a - w_{i\text{MR}})_{\text{eq}} + (u_a^2 + v_a^2)_{\text{eq}} \frac{\partial w_{i\text{MR}}}{\partial u} \right] \quad (124)$$

$$\left. \frac{\partial Z_{\text{Fus}}}{\partial u} \right|_{\text{cr}} = -\frac{1}{2V_{\infty\text{eq}}} \rho S_{z\text{Fus}} \left[(u_a^2 + v_a^2)_{\text{eq}} \frac{\partial w_{i\text{MR}}}{\partial u} - u_{\text{aeq}} w_{i\text{MR}\text{eq}} \right]$$

$$\begin{aligned}\frac{\partial Z_{\text{Fus}}}{\partial v} &= -\frac{1}{2V_{\infty \text{eq}}} \rho S_{z\text{Fus}} \left[v_{\text{aeq}} (w_a - w_{i\text{MR}})_{\text{eq}} - \left((w_a - w_{i\text{MR}})_{\text{eq}}^2 - V_{\infty \text{eq}}^2 \right) \frac{\partial w_{i\text{MR}}}{\partial v} \right] \\ &= -\frac{1}{2V_{\infty \text{eq}}} \rho S_{z\text{Fus}} \left[v_{\text{aeq}} (w_a - w_{i\text{MR}})_{\text{eq}} + (u_a^2 + v_a^2)_{\text{eq}} \frac{\partial w_{i\text{MR}}}{\partial v} \right]\end{aligned}\quad (125)$$

$$\begin{aligned}\frac{\partial Z_{\text{Fus}}}{\partial v} \Big|_{\text{cr}} &= -\frac{1}{2V_{\infty \text{eq}}} \rho S_{z\text{Fus}} \left[(u_a^2 + v_a^2)_{\text{eq}} \frac{\partial w_{i\text{MR}}}{\partial v} - v_{\text{aeq}} w_{i\text{MR} \text{eq}} \right] \\ \frac{\partial Z_{\text{Fus}}}{\partial w} &= -\frac{1}{2V_{\infty \text{eq}}} \rho S_{z\text{Fus}} \left[(w_a - w_{i\text{MR}})_{\text{eq}}^2 + V_{\infty}^2 \right] \left(1 - \frac{\partial w_{i\text{MR}}}{\partial w} \right)\end{aligned}\quad (126)$$

$$\frac{\partial Z_{\text{Fus}}}{\partial w} \Big|_{\text{cr}} = -\frac{1}{2V_{\infty \text{eq}}} \rho S_{z\text{Fus}} (w_{i\text{MR} \text{eq}}^2 + V_{\infty}^2) \left(1 - \frac{\partial w_{i\text{MR}}}{\partial w} \right)$$

$$\begin{aligned}\frac{\partial Z_{\text{Fus}}}{\partial p} &= \frac{1}{2V_{\infty \text{eq}}} \rho S_{z\text{Fus}} \left[(w_a - w_{i\text{MR}})_{\text{eq}}^2 + V_{\infty \text{eq}}^2 \right] \frac{\partial w_{i\text{MR}}}{\partial p} \\ &= 0\end{aligned}\quad (127)$$

$$\begin{aligned}\frac{\partial Z_{\text{Fus}}}{\partial q} &= \frac{1}{2V_{\infty \text{eq}}} \rho S_{z\text{Fus}} \left[(w_a - w_{i\text{MR}})_{\text{eq}}^2 + V_{\infty \text{eq}}^2 \right] \frac{\partial w_{i\text{MR}}}{\partial q} \\ &= 0\end{aligned}\quad (128)$$

$$\begin{aligned}\frac{\partial Z_{\text{Fus}}}{\partial r} &= \frac{1}{2V_{\infty \text{eq}}} \rho S_{z\text{Fus}} \left[(w_a - w_{i\text{MR}})_{\text{eq}}^2 + V_{\infty \text{eq}}^2 \right] \frac{\partial w_{i\text{MR}}}{\partial r} \\ &= 0\end{aligned}\quad (129)$$

$$\begin{aligned}\frac{\partial Z_{\text{Fus}}}{\partial \delta_{\text{Coll}}} &= \frac{1}{2V_{\infty \text{eq}}} \rho S_{z\text{Fus}} \left[(w_a - w_{i\text{MR}})_{\text{eq}}^2 + V_{\infty \text{eq}}^2 \right] \frac{\partial w_{i\text{MR}}}{\partial \delta_{\text{Coll}}}\end{aligned}\quad (130)$$

$$\frac{\partial Z_{\text{Fus}}}{\partial \delta_{\text{Coll}}} \Big|_{\text{cr}} = \frac{1}{2V_{\infty \text{eq}}} \rho S_{z\text{Fus}} (w_{i\text{MR} \text{eq}}^2 + V_{\infty \text{eq}}^2) \frac{\partial w_{i\text{MR}}}{\partial \delta_{\text{Coll}}}$$

$$\begin{aligned}\frac{\partial Z_{\text{Fus}}}{\partial \delta_{\text{Ped}}} &= 0 & \frac{\partial Z_{\text{Fus}}}{\partial \delta_{\text{Lat}}} &= 0 & \frac{\partial Z_{\text{Fus}}}{\partial \delta_{\text{Long}}} &= 0\end{aligned}\quad (131)$$

$$\begin{aligned}\frac{\partial \vec{F}_{\text{Fus}}}{\partial a_{1s}} &= \vec{0} & \frac{\partial \vec{F}_{\text{Fus}}}{\partial b_{1s}} &= \vec{0}\end{aligned}\quad (132)$$

$$\begin{aligned}\frac{\partial \vec{F}_{\text{Fus}}}{\partial \phi} &= \vec{0} & \frac{\partial \vec{F}_{\text{Fus}}}{\partial \theta} &= \vec{0} & \frac{\partial \vec{F}_{\text{Fus}}}{\partial \psi} &= \vec{0}\end{aligned}\quad (133)$$

$$\begin{aligned}
\frac{\partial L_{\text{Fus}}}{\partial \bar{x}} &= \bar{0}_{n_{\text{state}}} & \frac{\partial L_{\text{Fus}}}{\partial \bar{u}} &= \bar{0}_{n_{\text{input}}} \\
\frac{\partial M_{\text{Fus}}}{\partial \bar{x}} &= \bar{0}_{n_{\text{state}}} & \frac{\partial M_{\text{Fus}}}{\partial \bar{u}} &= \bar{0}_{n_{\text{input}}} \\
\frac{\partial N_{\text{Fus}}}{\partial \bar{x}} &= \bar{0}_{n_{\text{state}}} & \frac{\partial N_{\text{Fus}}}{\partial \bar{u}} &= \bar{0}_{n_{\text{input}}}
\end{aligned} \tag{134}$$

2.5.4 Horizontal Fin Derivatives

$$\frac{\partial X_{\text{HF}}}{\partial \bar{x}} = \bar{0}_{n_{\text{state}}} \qquad \frac{\partial X_{\text{HF}}}{\partial \bar{u}} = \bar{0}_{n_{\text{input}}} \tag{135}$$

$$\frac{\partial Y_{\text{HF}}}{\partial \bar{x}} = \bar{0}_{n_{\text{state}}} \qquad \frac{\partial Y_{\text{HF}}}{\partial \bar{u}} = \bar{0}_{n_{\text{input}}} \tag{136}$$

$$\frac{\partial Z_{\text{HF}}}{\partial u} = \left\{ \begin{array}{l}
-\frac{1}{2} \rho S_{\text{HF}} \left[\left(C_{L\alpha\text{HF}} |u_{\text{aeq}}| + |w_{\text{HFeq}}| \right) \frac{\partial w_{\text{HF}}}{\partial u} \dots \right. \\
\qquad \qquad \qquad \left. + \left(C_{L\alpha\text{HF}} + \frac{\partial w_{\text{HF}}}{\partial u} \right) w_{\text{HFeq}} \right]; \quad u_{\text{a}} \geq 0, w_{\text{HF}} \geq 0 \\
-\frac{1}{2} \rho S_{\text{HF}} \left[\left(C_{L\alpha\text{HF}} |u_{\text{aeq}}| + |w_{\text{HFeq}}| \right) \frac{\partial w_{\text{HF}}}{\partial u} \dots \right. \\
\qquad \qquad \qquad \left. + \left(C_{L\alpha\text{HF}} - \frac{\partial w_{\text{HF}}}{\partial u} \right) w_{\text{HFeq}} \right]; \quad u_{\text{a}} \geq 0, w_{\text{HF}} < 0 \\
-\frac{1}{2} \rho S_{\text{HF}} \left[\left(C_{L\alpha\text{HF}} |u_{\text{aeq}}| + |w_{\text{HFeq}}| \right) \frac{\partial w_{\text{HF}}}{\partial u} \dots \right. \\
\qquad \qquad \qquad \left. - \left(C_{L\alpha\text{HF}} - \frac{\partial w_{\text{HF}}}{\partial u} \right) w_{\text{HFeq}} \right]; \quad u_{\text{a}} < 0, w_{\text{HF}} \geq 0 \\
-\frac{1}{2} \rho S_{\text{HF}} \left[\left(C_{L\alpha\text{HF}} |u_{\text{aeq}}| + |w_{\text{HFeq}}| \right) \frac{\partial w_{\text{HF}}}{\partial u} \dots \right. \\
\qquad \qquad \qquad \left. - \left(C_{L\alpha\text{HF}} + \frac{\partial w_{\text{HF}}}{\partial u} \right) w_{\text{HFeq}} \right]; \quad u_{\text{a}} < 0, w_{\text{HF}} < 0
\end{array} \right. \tag{137}$$

$$\frac{\partial w_{\text{HF}}}{\partial u} = - \left(w_{\text{iMReq}} \frac{\partial K_{\lambda}}{\partial u} + K_{\lambda\text{eq}} \frac{\partial w_{\text{iMR}}}{\partial u} \right)$$

$$\frac{\partial K_{\lambda}}{\partial u} = \frac{1.5}{(g_f - g_i)(w_{\text{iMR}} - w_{\text{a}})_{\text{eq}}} \left[1 - \frac{u_{\text{aeq}}}{(w_{\text{iMR}} - w_{\text{a}})_{\text{eq}}} \frac{\partial w_{\text{iMR}}}{\partial u} \right]$$

$$\begin{aligned} \frac{\partial Z_{\text{HF}}}{\partial v} &= -\frac{1}{2} \rho S_{\text{HF}} \left[\left(C_{L\alpha\text{HF}} |u_{\text{aeq}}| + |w_{\text{HFeq}}| \right) \pm w_{\text{HFeq}} \right] \frac{\partial w_{\text{HF}}}{\partial v}; \quad w_{\text{HF}} = \begin{cases} \geq 0 \\ < 0 \end{cases} \\ \frac{\partial w_{\text{HF}}}{\partial v} &= - \left(w_{\text{iMReq}} \frac{\partial K_{\lambda}}{\partial v} + K_{\lambda\text{eq}} \frac{\partial w_{\text{iMR}}}{\partial v} \right) \\ \frac{\partial K_{\lambda}}{\partial v} &= - \frac{1.5}{(g_f - g_i)} \frac{u_{\text{aeq}}}{(w_{\text{iMR}} - w_a)_{\text{eq}}^2} \frac{\partial w_{\text{iMR}}}{\partial v} \end{aligned} \quad (138)$$

$$\begin{aligned} \frac{\partial Z_{\text{HF}}}{\partial w} &= -\frac{1}{2} \rho S_{\text{HF}} \left[\left(C_{L\alpha\text{HF}} |u_{\text{aeq}}| + |w_{\text{HFeq}}| \right) \pm w_{\text{HFeq}} \right] \frac{\partial w_{\text{HF}}}{\partial w}; \quad w_{\text{HF}} = \begin{cases} \geq 0 \\ < 0 \end{cases} \\ \frac{\partial w_{\text{HF}}}{\partial w} &= 1 - \left(w_{\text{iMReq}} \frac{\partial K_{\lambda}}{\partial w} + K_{\lambda\text{eq}} \frac{\partial w_{\text{iMR}}}{\partial w} \right) \\ \frac{\partial K_{\lambda}}{\partial w} &= - \frac{1.5}{(g_f - g_i)} \frac{u_{\text{aeq}}}{(w_{\text{iMR}} - w_a)_{\text{eq}}^2} \left(\frac{\partial w_{\text{iMR}}}{\partial w} - 1 \right) \end{aligned} \quad (139)$$

$$\begin{aligned} \frac{\partial Z_{\text{HF}}}{\partial p} &= -\frac{1}{2} \rho S_{\text{HF}} \left[\left(C_{L\alpha\text{HF}} |u_{\text{aeq}}| + |w_{\text{HFeq}}| \right) \pm w_{\text{HFeq}} \right] \frac{\partial w_{\text{HF}}}{\partial p}; \quad w_{\text{HF}} = \begin{cases} \geq 0 \\ < 0 \end{cases} \\ \frac{\partial w_{\text{HF}}}{\partial p} &= - \left(w_{\text{iMReq}} \frac{\partial K_{\lambda}}{\partial p} + K_{\lambda\text{eq}} \frac{\partial w_{\text{iMR}}}{\partial p} \right) \\ \frac{\partial K_{\lambda}}{\partial p} &= - \frac{1.5}{(g_f - g_i)} \frac{u_{\text{aeq}}}{(w_{\text{iMR}} - w_a)_{\text{eq}}^2} \frac{\partial w_{\text{iMR}}}{\partial p} \end{aligned} \quad (140)$$

$$\begin{aligned} \frac{\partial Z_{\text{HF}}}{\partial q} &= -\frac{1}{2} \rho S_{\text{HF}} \left[\left(C_{L\alpha\text{HF}} |u_{\text{aeq}}| + |w_{\text{HFeq}}| \right) \pm w_{\text{HFeq}} \right] \frac{\partial w_{\text{HF}}}{\partial q}; \quad w_{\text{HF}} = \begin{cases} \geq 0 \\ < 0 \end{cases} \\ \frac{\partial w_{\text{HF}}}{\partial q} &= l_{\text{HF}} - \left(w_{\text{iMReq}} \frac{\partial K_{\lambda}}{\partial q} + K_{\lambda\text{eq}} \frac{\partial w_{\text{iMR}}}{\partial q} \right) \\ \frac{\partial K_{\lambda}}{\partial q} &= - \frac{1.5}{(g_f - g_i)} \frac{u_{\text{aeq}}}{(w_{\text{iMR}} - w_a)_{\text{eq}}^2} \frac{\partial w_{\text{iMR}}}{\partial q} \end{aligned} \quad (141)$$

$$\begin{aligned} \frac{\partial Z_{\text{HF}}}{\partial r} &= -\frac{1}{2} \rho S_{\text{HF}} \left[\left(C_{L\alpha\text{HF}} |u_{\text{aeq}}| + |w_{\text{HFeq}}| \right) \pm w_{\text{HFeq}} \right] \frac{\partial w_{\text{HF}}}{\partial r}; \quad w_{\text{HF}} = \begin{cases} \geq 0 \\ < 0 \end{cases} \\ \frac{\partial w_{\text{HF}}}{\partial r} &= - \left(w_{\text{iMReq}} \frac{\partial K_{\lambda}}{\partial r} + K_{\lambda\text{eq}} \frac{\partial w_{\text{iMR}}}{\partial r} \right) \\ \frac{\partial K_{\lambda}}{\partial r} &= - \frac{1.5}{(g_f - g_i)} \frac{u_{\text{aeq}}}{(w_{\text{iMR}} - w_a)_{\text{eq}}^2} \frac{\partial w_{\text{iMR}}}{\partial r} \end{aligned} \quad (142)$$

$$\frac{\partial Z_{\text{HF}}}{\partial \delta_{\text{Coll}}} = -\frac{1}{2} \rho S_{\text{HF}} \left[\left(C_{L\alpha\text{HF}} |u_{\text{aeq}}| + |w_{\text{HFeq}}| \right) \pm w_{\text{HFeq}} \right] \frac{\partial w_{\text{HF}}}{\partial \delta_{\text{Coll}}}; \quad w_{\text{HF}} = \begin{cases} \geq 0 \\ < 0 \end{cases}$$

$$\frac{\partial w_{\text{HF}}}{\partial \delta_{\text{Coll}}} = - \left(w_{\text{iMReq}} \frac{\partial K_{\lambda}}{\partial \delta_{\text{Coll}}} + K_{\lambda\text{eq}} \frac{\partial w_{\text{iMR}}}{\partial \delta_{\text{Coll}}} \right) \quad (143)$$

$$\frac{\partial K_{\lambda}}{\partial \delta_{\text{Coll}}} = -\frac{1.5}{(g_f - g_i)} \frac{u_{\text{aeq}}}{(w_{\text{iMR}} - w_{\text{a}})_{\text{eq}}^2} \frac{\partial w_{\text{iMR}}}{\partial \delta_{\text{Coll}}}$$

$$\frac{\partial Z_{\text{HF}}}{\partial \delta_{\text{Ped}}} = 0 \quad \frac{\partial Z_{\text{HF}}}{\partial \delta_{\text{Long}}} = 0 \quad \frac{\partial Z_{\text{HF}}}{\partial \delta_{\text{Lat}}} = 0 \quad (144)$$

$$\frac{\partial \bar{F}_{\text{HF}}}{\partial a_{1s}} = \bar{0} \quad \frac{\partial \bar{F}_{\text{HF}}}{\partial b_{1s}} = \bar{0} \quad (145)$$

$$\frac{\partial \bar{F}_{\text{HF}}}{\partial \phi} = \bar{0} \quad \frac{\partial \bar{F}_{\text{HF}}}{\partial \theta} = \bar{0} \quad \frac{\partial \bar{F}_{\text{HF}}}{\partial \psi} = \bar{0} \quad (146)$$

$$\frac{\partial L_{\text{HF}}}{\partial \bar{x}} = \bar{0}_{n_{\text{state}}} \quad \frac{\partial L_{\text{HF}}}{\partial \bar{u}} = \bar{0}_{n_{\text{input}}} \quad (147)$$

$$\frac{\partial M_{\text{HF}}}{\partial \bar{x}} = l_{\text{HF}} \frac{\partial Z_{\text{HF}}}{\partial \bar{x}} \quad \frac{\partial M_{\text{HF}}}{\partial \bar{u}} = l_{\text{HF}} \frac{\partial Z_{\text{HF}}}{\partial \bar{u}} \quad (148)$$

$$\frac{\partial N_{\text{HF}}}{\partial \bar{x}} = \bar{0}_{n_{\text{state}}} \quad \frac{\partial N_{\text{HF}}}{\partial \bar{u}} = \bar{0}_{n_{\text{input}}} \quad (149)$$

$$\frac{\partial \bar{M}_{\text{HF}}}{\partial a_{1s}} = \bar{0} \quad \frac{\partial \bar{M}_{\text{HF}}}{\partial b_{1s}} = \bar{0} \quad (150)$$

$$\frac{\partial \bar{M}_{\text{HF}}}{\partial \phi} = \bar{0} \quad \frac{\partial \bar{M}_{\text{HF}}}{\partial \theta} = \bar{0} \quad \frac{\partial \bar{M}_{\text{HF}}}{\partial \psi} = \bar{0} \quad (151)$$

2.5.5 Vertical Fin Derivatives

$$\frac{\partial X_{\text{VF}}}{\partial \bar{x}} = \bar{0}_{n_{\text{state}}} \quad \frac{\partial X_{\text{VF}}}{\partial \bar{u}} = \bar{0}_{n_{\text{input}}} \quad (152)$$

$$\frac{\partial Y_{\text{VF}}}{\partial u} = -\frac{1}{2} \rho S_{\text{VF}} \left[\left(\frac{C_{L\alpha\text{VF}}}{V_{\infty\text{VFeq}}} \left[u_{\text{aeq}} - v_{\text{VFeq}} \varepsilon_{\text{VF/TR}} \frac{\partial v_{\text{iTR}}}{\partial u} \right] \mp \varepsilon_{\text{VF/TR}} \frac{\partial v_{\text{iTR}}}{\partial u} \right) v_{\text{VFeq}} \dots \right. \\ \left. - \left(C_{L\alpha\text{VF}} V_{\infty\text{VFeq}} + |v_{\text{VFeq}}| \right) \varepsilon_{\text{VF/TR}} \frac{\partial v_{\text{iTR}}}{\partial u} \right], \quad v_{\text{VF}} = \begin{cases} \geq 0 \\ < 0 \end{cases} \quad (153)$$

$$\begin{aligned} \frac{\partial Y_{VF}}{\partial v} = & -\frac{1}{2} \rho S_{VF} \left[\left(C_{L\alpha VF} \frac{v_{VFeq}}{V_{\infty VFeq}} \pm 1 \right) v_{VFeq} \cdots \right. \\ & \left. + \left(C_{L\alpha VF} V_{\infty VFeq} + |v_{VFeq}| \right) \right] \left(1 - \varepsilon_{VF/TR} \frac{\partial v_{iTR}}{\partial v} \right), \quad v_{VF} \begin{cases} \geq 0 \\ < 0 \end{cases} \end{aligned} \quad (154)$$

$$\begin{aligned} \frac{\partial Y_{VF}}{\partial w} = & \frac{1}{2} \rho S_{VF} \left[\left(C_{L\alpha VF} \frac{v_{VFeq}}{V_{\infty VFeq}} \pm 1 \right) v_{VFeq} \cdots \right. \\ & \left. + \left(C_{L\alpha VF} V_{\infty VFeq} + |v_{VFeq}| \right) \right] \varepsilon_{VF/TR} \frac{\partial v_{iTR}}{\partial w}, \quad v_{VF} \begin{cases} \geq 0 \\ < 0 \end{cases} \end{aligned} \quad (155)$$

$$\begin{aligned} \frac{\partial Y_{VF}}{\partial p} = & \frac{1}{2} \rho S_{VF} \left[\left(C_{L\alpha VF} \frac{v_{VFeq}}{V_{\infty VFeq}} \pm 1 \right) v_{VFeq} \cdots \right. \\ & \left. + \left(C_{L\alpha VF} V_{\infty VFeq} + |v_{VFeq}| \right) \right] \varepsilon_{VF/TR} \frac{\partial v_{iTR}}{\partial p}, \quad v_{VF} \begin{cases} \geq 0 \\ < 0 \end{cases} \\ = & 0 \end{aligned} \quad (156)$$

$$\begin{aligned} \frac{\partial Y_{VF}}{\partial q} = & \frac{1}{2} \rho S_{VF} \left[\left(C_{L\alpha VF} \frac{v_{VFeq}}{V_{\infty VFeq}} \pm 1 \right) v_{VFeq} \cdots \right. \\ & \left. + \left(C_{L\alpha VF} V_{\infty VFeq} + |v_{VFeq}| \right) \right] \varepsilon_{VF/TR} \frac{\partial v_{iTR}}{\partial q}, \quad v_{VF} \begin{cases} \geq 0 \\ < 0 \end{cases} \\ = & 0 \end{aligned} \quad (157)$$

$$\begin{aligned} \frac{\partial Y_{VF}}{\partial r} = & \frac{1}{2} \rho S_{VF} \left[\left(C_{L\alpha VF} \frac{v_{VFeq}}{V_{\infty VFeq}} \pm 1 \right) v_{VFeq} \cdots \right. \\ & \left. + \left(C_{L\alpha VF} V_{\infty VFeq} + |v_{VFeq}| \right) \right] \left(\varepsilon_{VF/TR} \frac{\partial v_{iTR}}{\partial r} + l_{VF} \right), \quad v_{VF} \begin{cases} \geq 0 \\ < 0 \end{cases} \\ = & 0 \end{aligned} \quad (158)$$

$$\begin{aligned} \frac{\partial Y_{VF}}{\partial \delta_{Ped}} = & \frac{1}{2} \rho S_{VF} \left[\left(C_{L\alpha VF} \frac{v_{VFeq}}{V_{\infty VFeq}} \pm 1 \right) v_{VFeq} \cdots \right. \\ & \left. + \left(C_{L\alpha VF} V_{\infty VFeq} + |v_{VFeq}| \right) \right] \varepsilon_{VF/TR} \frac{\partial v_{iTR}}{\partial \delta_{Ped}}, \quad v_{VF} \begin{cases} \geq 0 \\ < 0 \end{cases} \end{aligned} \quad (159)$$

$$\frac{\partial Y_{VF}}{\partial \delta_{Coll}} = 0 \quad \frac{\partial Y_{VF}}{\partial \delta_{Long}} = 0 \quad \frac{\partial Y_{VF}}{\partial \delta_{Lat}} = 0 \quad (160)$$

$$\frac{\partial Z_{VF}}{\partial \bar{x}} = \bar{0}_{n_{state}} \quad \frac{\partial Z_{VF}}{\partial \bar{u}} = \bar{0}_{n_{input}} \quad (161)$$

$$\frac{\partial \bar{F}_{VF}}{\partial a_{1s}} = \bar{0} \quad \frac{\partial \bar{F}_{VF}}{\partial b_{1s}} = \bar{0} \quad (162)$$

$$\frac{\partial \bar{F}_{VF}}{\partial \phi} = \bar{0} \quad \frac{\partial \bar{F}_{VF}}{\partial \theta} = \bar{0} \quad \frac{\partial \bar{F}_{VF}}{\partial \psi} = \bar{0} \quad (163)$$

$$\frac{\partial L_{VF}}{\partial \bar{x}} = h_{VF} \frac{\partial Y_{VF}}{\partial \bar{x}} \quad \frac{\partial L_{VF}}{\partial \bar{u}} = h_{VF} \frac{\partial Y_{VF}}{\partial \bar{u}} \quad (164)$$

$$\frac{\partial M_{VF}}{\partial \bar{x}} = 0 \quad \frac{\partial M_{VF}}{\partial \bar{u}} = 0 \quad (165)$$

$$\frac{\partial N_{VF}}{\partial \bar{x}} = -l_{VF} \frac{\partial Y_{VF}}{\partial \bar{x}} \quad \frac{\partial N_{VF}}{\partial \bar{u}} = -l_{VF} \frac{\partial Y_{VF}}{\partial \bar{u}} \quad (166)$$

$$\frac{\partial \bar{M}_{VF}}{\partial a_{1s}} = \bar{0} \quad \frac{\partial \bar{M}_{VF}}{\partial b_{1s}} = \bar{0} \quad (167)$$

$$\frac{\partial \bar{M}_{VF}}{\partial \phi} = \bar{0} \quad \frac{\partial \bar{M}_{VF}}{\partial \theta} = \bar{0} \quad \frac{\partial \bar{M}_{VF}}{\partial \psi} = \bar{0} \quad (168)$$

3 Stability Analysis

To simplify the stability analysis, we assume that the cross-coupling dynamics is insignificant. The assumption can be justified by doing norm analysis or eigen value analysis of the partitioned system matrix. Therefore, rearranging (83) and (84) for consecutive longitudinal and lateral-directional states respectively (including main rotor flapping dynamic as augmented states), we have these expressions for \mathbf{A} and \mathbf{B} .

$$\mathbf{A} = \begin{bmatrix} \mathbf{A}_{LongVer} & \mathbf{A}_{LatDir2LongVer} \\ \mathbf{A}_{LongVer2LatDir} & \mathbf{A}_{LatDir} \end{bmatrix} \quad (169)$$

$$\mathbf{B} = \begin{bmatrix} \mathbf{B}_{LongVer} & \mathbf{B}_{LatDir2LongVer} \\ \mathbf{B}_{LongVer2LatDir} & \mathbf{B}_{LatDir} \end{bmatrix}$$

where

$$\mathbf{A}_{\text{long-ver}} = \begin{bmatrix} X_u & X_w & X_q & X_\theta & X_{a_{1s}} \\ Z_u & Z_w & Z_q & Z_\theta & Z_{a_{1s}} \\ M_u & M_w & M_q & M_\theta & M_{a_{1s}} \\ \Theta_u & \Theta_w & \Theta_q & \Theta_\theta & \Theta_{a_{1s}} \\ \frac{1}{\tau_c} A_u & \frac{1}{\tau_c} A_w & \frac{1}{\tau_c} A_q & \frac{1}{\tau_c} A_\theta & \frac{1}{\tau_c} A_{a_{1s}} \end{bmatrix} \quad \mathbf{B}_{\text{long-ver}} = \begin{bmatrix} X_{\delta_{\text{Coll}}} & X_{\delta_{\text{Long}}} \\ Z_{\delta_{\text{Coll}}} & Z_{\delta_{\text{Long}}} \\ M_{\delta_{\text{Coll}}} & M_{\delta_{\text{Long}}} \\ \Theta_{\delta_{\text{Coll}}} & \Theta_{\delta_{\text{Long}}} \\ \frac{1}{\tau_c} A_{\delta_{\text{Coll}}} & \frac{1}{\tau_c} A_{\delta_{\text{Long}}} \end{bmatrix} \quad (170)$$

$$\mathbf{A}_{\text{lat-dir}} = \begin{bmatrix} Y_v & Y_p & Y_r & Y_\phi & Y_{b_{1s}} \\ L_v & L_p & L_r & L_\phi & L_{b_{1s}} \\ N_v & N_p & N_r & N_\phi & N_{b_{1s}} \\ \Phi_v & \Phi_p & \Phi_r & \Phi_\phi & \Phi_{b_{1s}} \\ \frac{1}{\tau_c} B_v & \frac{1}{\tau_c} B_p & \frac{1}{\tau_c} B_r & \frac{1}{\tau_c} B_\phi & \frac{1}{\tau_c} B_{b_{1s}} \end{bmatrix} \quad \mathbf{B}_{\text{lat-dir}} = \begin{bmatrix} Y_{\delta_{\text{Ped}}} & Y_{\delta_{\text{Lat}}} \\ L_{\delta_{\text{Ped}}} & L_{\delta_{\text{Lat}}} \\ N_{\delta_{\text{Ped}}} & N_{\delta_{\text{Lat}}} \\ \Phi_{\delta_{\text{Ped}}} & \Phi_{\delta_{\text{Lat}}} \\ \frac{1}{\tau_c} B_{\delta_{\text{Ped}}} & \frac{1}{\tau_c} B_{\delta_{\text{Lat}}} \end{bmatrix} \quad (171)$$

$$\bar{\mathbf{x}}_{\text{long-ver}} = [u \quad w \quad q \quad \theta \quad a_{1s}]^T \quad (172)$$

$$\bar{\mathbf{x}}_{\text{lat-dir}} = [v \quad p \quad r \quad \phi \quad b_{1s}]^T$$

$$\bar{\mathbf{u}}_{\text{long-ver}} = [\delta_{\text{Coll}} \quad \delta_{\text{Long}}]^T \quad (173)$$

$$\bar{\mathbf{u}}_{\text{lat-dir}} = [\delta_{\text{Ped}} \quad \delta_{\text{Lat}}]^T$$

3.1 Hover Dynamics

The hover regime is characterized by weak coupling between longitudinal and lateral directional mode. The longitudinal hover dynamics of the X-cell helicopter is represented by the following system and input matrices.

$$\mathbf{A}_{\text{LongVer}} = \begin{bmatrix} -0.0352 & 0 & 0.9953 & -9.8066 & -9.9532 \\ 0 & -0.096 & 0 & 0.0161 & 0.0161 \\ 0.0693 & 0 & -21.5235 & 0 & 102.4125 \\ 0 & 0 & 0.997 & 0 & 0 \\ 0.0032 & 0 & -1 & 0 & -10 \end{bmatrix} \quad (174)$$

$$\mathbf{B}_{\text{LongVer}} = \begin{bmatrix} -0.2063 & -41.8033 \\ 124.4615 & 0 \\ 1.1691 & 903.9850 \\ 0 & 0 \\ 0 & 42 \end{bmatrix}$$

The lateral directional hover dynamics of the X-cell helicopter is represented by the following system and input matrices.

$$\begin{aligned}
 \mathbf{A}_{\text{LatDir}} &= \begin{bmatrix} -0.0698 & -0.9953 & 0 & 9.7771 & -9.9529 \\ 0.1212 & -40.6551 & 0 & 0 & 193.4487 \\ 0.0708 & 0 & 0.0001 & 0 & 0 \\ 0 & 1 & -0.0016 & 0 & 0 \\ 0.0032 & -1 & 0 & 0 & -10 \end{bmatrix} \\
 \mathbf{B}_{\text{LatDir}} &= \begin{bmatrix} -4.7246 & 41.8026 \\ -17.2186 & 1707.5153 \\ 125.9109 & 0 \\ 0 & 0 \\ 0 & 42 \end{bmatrix}
 \end{aligned} \tag{175}$$

The corresponding eigen values along with their frequency and damping for the system matrix are summarized in the following table.

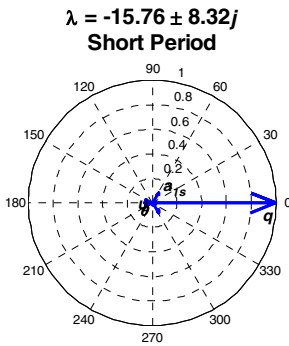
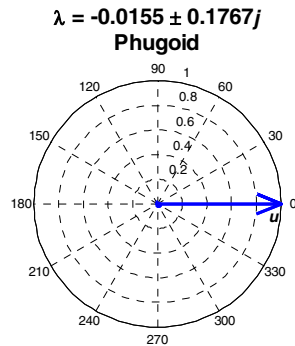
Table 9. Hover, Longitudinal

Mode	Eigen Value	Eigen Vector	Damping Ratio	Frequency (rad/s)
Short Period	$-15.7638 \pm 8.3194j$	$\begin{bmatrix} -0.0597 \pm 0.0032j \\ 0 \\ 0.9918 \\ -0.0491 \mp 0.0259j \\ 0.0558 \pm 0.0806j \end{bmatrix}$	0.884	17.8
Phugoid	$-0.0155 \pm 0.1767j$	$\begin{bmatrix} -0.9998 \\ -0.0014 \mp 0.0005j \\ 0.0032 \\ -0.0017 \mp 0.0180j \\ 0 \end{bmatrix}$	0.0873	0.177
Heaving	-0.0960	$\begin{bmatrix} 0 \\ -1 \\ 0 \\ 0 \\ 0 \end{bmatrix}$	1	0.096

The longitudinal-vertical eigen values show that the longitudinal-vertical dynamics, which consists of two oscillatory modes and one non-oscillatory mode, is stable. The lateral-directional dynamics is fully non-oscillatory motion consisting five modes. Two of them are unstable. The plots of the eigen vectors are presented in Figure 3 to Figure 10.

Table 10. Hover, Lateral-Directional

Mode	Eigen Value	Eigen Vector	Damping Ratio	Frequency (rad/s)
Hi-damping Subsidence	-31.7598	$\begin{bmatrix} 0.0554 \\ 0.9969 \\ -0.0001 \\ -0.0314 \\ 0.0458 \end{bmatrix}$	1	31.76
Hi-damping Subsidence	-18.8916	$\begin{bmatrix} 0.1374 \\ 0.9830 \\ -0.0005 \\ -0.0520 \\ 0.1105 \end{bmatrix}$	1	18.89
Lo-damping Subsidence	-0.2272	$\begin{bmatrix} 0.9546 \\ 0.0029 \\ -0.2974 \\ -0.0151 \\ 0.0000 \end{bmatrix}$	1	0.227
Divergence	0.1068	$\begin{bmatrix} -0.8333 \\ -0.0025 \\ -0.5527 \\ -0.0153 \\ 0.0000 \end{bmatrix}$	-1	0.107
Divergence	0.0468	$\begin{bmatrix} 0.5514 \\ 0.0017 \\ 0.8342 \\ 0.0068 \\ 0.0000 \end{bmatrix}$	-1	0.04

**Fig. 3.** Short period mode eigen vector**Fig. 4.** Phugoid mode eigen vector

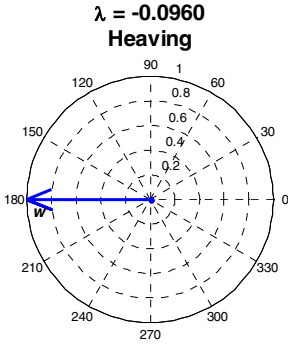


Fig. 5. Heaving mode eigen vector

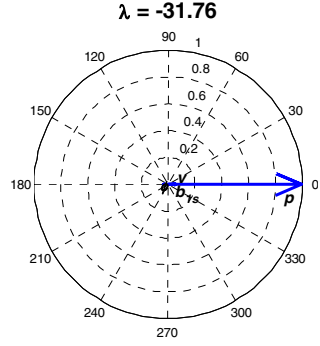


Fig. 6. 1st subsidence mode eigen vector in lateral-directional dimension

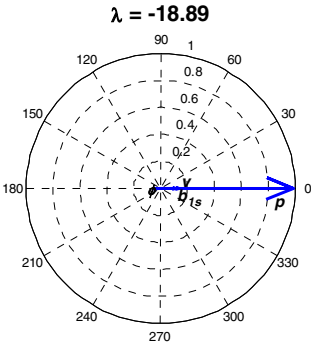


Fig. 7. 2nd subsidence mode eigen vector in lateral-directional dimension

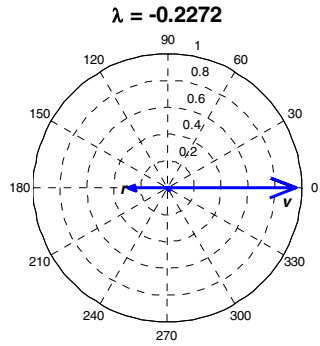


Fig. 8. 3rd subsidence mode eigen vector in lateral-directional dimension

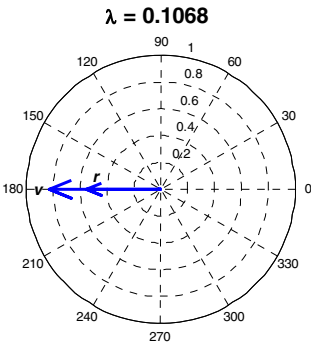


Fig. 9. 4th subsidence mode eigen vector in lateral-directional dimension

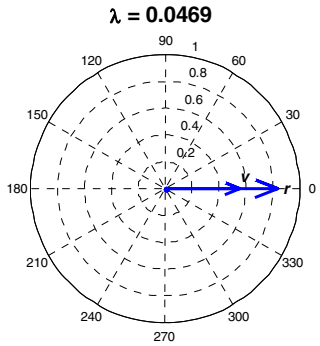


Fig. 10. 5th subsidence mode eigen vector in lateral-directional dimension

3.2 Forward Flight Dynamics

The longitudinal forward flight dynamics of the X-cell helicopter is represented by the following system and input matrices.

$$\mathbf{A}_{\text{LongVer}} = \begin{bmatrix} -0.2339 & -0.0072 & 0.7432 & -9.6060 & -10.0177 \\ -0.1422 & -1.8927 & 16.5294 & 1.9675 & 0 \\ 0.3534 & -0.2983 & -22.0095 & 0 & 215.6001 \\ 0 & 0 & 0.9969 & 0 & 0 \\ 0.0019 & 0 & -1 & 0 & -8.35 \end{bmatrix} \quad (176)$$

$$\mathbf{B}_{\text{LongVer}} = \begin{bmatrix} -1.6635 & -42.0612 \\ -149.4974 & 0 \\ 37.9729 & 905.2517 \\ 0 & 0 \\ 0 & 35.07 \end{bmatrix}$$

The lateral-directional forward flight dynamics of the X-cell helicopter is represented by the following state and input matrices.

$$\mathbf{A}_{\text{LatDir}} = \begin{bmatrix} -0.3468 & -0.7485 & -16.5191 & 9.576 & 10.0177 \\ -0.2366 & -40.7435 & 0.1335 & 0 & 407.2447 \\ 2.5045 & 0.1406 & -0.976 & 0 & 0 \\ 0 & 1 & -0.2048 & 0 & 0 \\ 0.0019 & -1 & 0 & 0 & -8.35 \end{bmatrix} \quad (177)$$

$$\mathbf{B}_{\text{LatDir}} = \begin{bmatrix} -4.782 & 42.0612 \\ -17.4277 & 1709.9 \\ 127.4399 & 0 \\ 0 & 0 \\ 0 & 35.07 \end{bmatrix}$$

The corresponding eigen values along with their frequency and damping for the system matrix are summarized in the following table.

The longitudinal-vertical eigen values show that the system is stable. The first pair of eigen values represent a fairly damped and high frequency pitch oscillation. The other pair of eigen values represent a lightly damped, long period oscillation which is comparable to phugoid mode in fixed-wing aircraft. These pairs of eigen values are comparable to those in fixed-wing aircraft. The fifth eigen value represents a damped heaving mode. The dominant states at each mode can be examined from the eigen vector plot in Figure 11 to Figure 13.

Table 11. Forward Flight, Longitudinal

Mode	Eigen Value	Eigen Vector	Damping Ratio	Frequency (rad/s)
Short Period	$-15.1402 \pm 13.1348j$	$\begin{bmatrix} -0.0296 \mp 0.0118j \\ -0.4704 \mp 0.4629j \\ 0.7480 \\ -0.0281 \mp 0.0244j \\ 0.0232 \pm 0.0449j \end{bmatrix}$	0.755	20
Phugoid	$-0.1139 \pm 0.2633j$	$\begin{bmatrix} 0.9991 \\ -0.0170 \mp 0.0256j \\ 0.0085 \pm 0.0002j \\ -0.0110 \mp 0.0273j \\ -0.0008 \end{bmatrix}$	0.397	0.287
Heaving	-1.9780	$\begin{bmatrix} 0.0258 \\ 0.9996 \\ -0.0052 \\ 0.0026 \\ 0.0008 \end{bmatrix}$	1	1.9780

Table 12. Forward Flight, Lateral Directional

Mode	Eigen Value	Eigen Vector	Damping Ratio	Frequency (rad/s)
Roll Oscillatory	$-24.549 \pm 12.0325j$	$\begin{bmatrix} 0.0217 \pm 0.0025j \\ 0.9978 \\ -0.0064 \mp 0.0036j \\ -0.0328 \mp 0.0161j \\ 0.0397 \pm 0.0295j \end{bmatrix}$	0.898	27.3
Dutch-Roll	$-0.6004 \pm 6.4205j$	$\begin{bmatrix} 0.9318 \\ -0.0018 \mp 0.0018j \\ 0.0211 \mp 0.3622j \\ 0.0113 \mp 0.0001j \\ -0.0004 \end{bmatrix}$	0.0931	6.45
Spiral	-0.1176	$\begin{bmatrix} -0.1688 \\ -0.0005 \\ -0.4925 \\ -0.8538 \\ 0 \end{bmatrix}$	1	0.1176

The lateral-directional eigen values show that the system is stable. The first pair of complex-conjugate eigen values represents a highly damped roll oscillation. The next pair of complex-conjugate eigen values represent motion consisting a combination of side velocity and yaw motion corresponding to dutch-roll mode in fixed-wing aircraft. The real value eigen value represents a stable spiral mode.

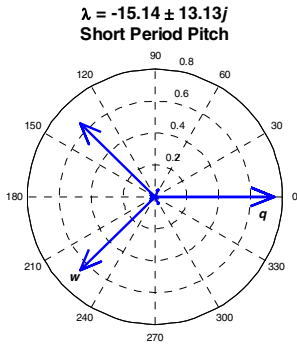


Fig. 11. Short period pitch mode eigen vector

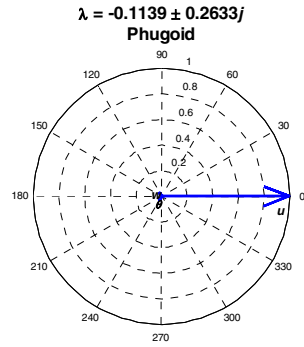


Fig. 12. Phugoid mode eigen vector

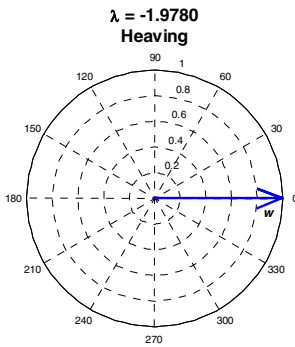


Fig. 13. Heaving mode eigen vector

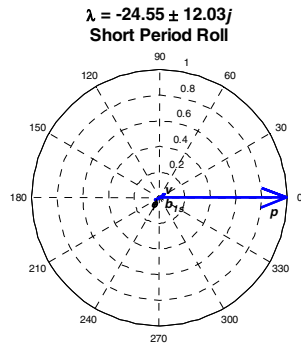


Fig. 14. Short period roll mode eigen vector

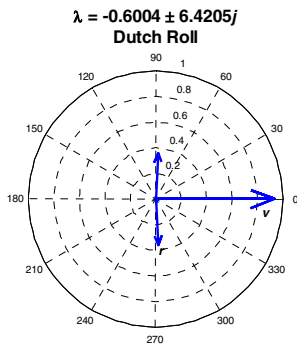


Fig. 15. Dutch-roll eigen vector

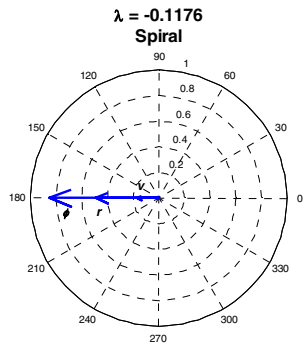


Fig. 16. Spiral eigen vector

4 Concluding Remarks

The linear model developed in this chapter is obtained by analytically deriving the stability and control derivatives of the small scale helicopter. The calculation of the stability and control derivatives is started from calculating trim conditions for the selected flight condition. A computer program is used to solve the equilibrium conditions and then calculate the change in aerodynamics forces and moments due to the change in each degree of freedom and control input. The procedure can be implemented for various flight conditions. Hence it facilitates the development of global small scale helicopter dynamics model which is adequately simple to be practical for control design and analysis.

References

- [1] Bramwell, A.R.S.: Helicopter Dynamics. Edward Arnold Ltd (1976)
- [2] Gessow, Myers: Aerodynamics of the helicopter. Ungar Publishing Company (1952)
- [3] Prouty, R.W.: Helicopter performance, stability and control. PWS Publishers, Boston (1986)
- [4] Seckel: Stability and Control of airplanes and helicopters. Academic Press, New York (1964)
- [5] McRuer, D.T., Ashkenas, I., Graham, D.: Aircraft dynamics and automatic control. Princeton University Press, Princeton (1973)
- [6] Etkin, B.: Dynamics of Atmospheric Flight. Dover Publications (2005)
- [7] Stevens, B., Lewis, F.: Aircraft control and simulation. John Wiley and Sons Inc., Chichester (1992)
- [8] Gavrilets, V.: Autonomous Aerobatic Maneuvering of Miniature Helicopter, PhD thesis, Massachusetts Institute of Technology (2003)
- [9] Shim, D.H., Kim, H.J., Sastry, S.: Control System Design for Rotorcraft-based Unmanned Aerial Vehicles using Time-domain System Identification. In: IEEE International Conference on Control Applications, Anchorage (2000)

Control of Small Scale Helicopter Using s-CDM and LQ Design

A. Budiyo¹ and T. Sudiyanto²

¹ Department of Aerospace Information Engineering
Konkuk University, Korea
budiyono@alum.mit.edu

² Center for Unmanned System Studies
Institut Teknologi Bandung, Indonesia

Abstract. The control of small-scale helicopter is a MIMO problem. To use the classical control approach to formally solve a MIMO problem, one needs to come up with multi-dimensional Root Locus diagram to tune the control parameters. The problem with the required dimension of the RL diagram for MIMO design has forced the design procedure of classical approach to be conducted in cascaded multi-loop SISO system starting from the innermost loop outward. To implement this control approach for a helicopter, a pitch and roll attitude control system is often subordinated to a, respectively, longitudinal and lateral velocity control system in a nested architecture. The requirement for this technique to work is that the inner attitude control loop must have a higher bandwidth than the outer velocity control loop which is not the case for high performance mini helicopter. To address the above problems, an algebraic design approach is proposed in this work. The designed control using s-CDM approach is demonstrated for hovering control of small-scale helicopter simultaneously subjected to plant parameter uncertainties and wind disturbances.

1 Introduction

The control for a small scale helicopter has been designed using various methods. During the period of 1990s, the classical control systems such as single-input-single-output SISO proportional-derivative (PD) feedback control systems have been used extensively. Their controller parameters were usually tuned empirically. This trial-and-error approach to design an "acceptable" control system however is not agreeable with complex multi-input multi-output MIMO systems with sophisticated performance criteria. For more advanced multivariable controller synthesis approaches, an accurate model of the dynamics is required. To control a model helicopter as a complex MIMO system, an approach that can synthesize a control algorithm to make the helicopter meet performance criteria while satisfying some physical constraints is required. More recent development in this area include the use of optimal control (Linear Quadratic Regulator) implemented on a small aerobatic helicopter designed at MIT [1]. Similar approach based on μ -synthesis has been also independently developed for a rotor unmanned aerial vehicle at UC Berkeley [2]. An adaptive high-bandwidth helicopter controller algorithm was synthesized at Georgia Tech. [3].

To address a MIMO problem, LQR and H_∞ are the most popular control design procedures. However, these methods are not up to expectation for practical application in aerospace community, because of the following reasons [4]:

1. Parameter tuning procedures are not provided.
2. Weight selection rules are not established.
3. The controller order is unnecessarily high.
4. Robustness is guaranteed only for predefined ones.
5. Some times, traditionally accepted good controllers are excluded.
6. Extension of gain scheduling or inclusion of proper saturation of state variable is difficult.
7. LQR and LQG designs sometimes fail to produce a robust controller for the plant with flexibility.

Due to the above limitations, the classical control design by experienced engineers is still common in the aerospace community. However, the inheritance of such experiences is often difficult, thus an improvement of the method is highly desired. In particular, the drawbacks of this approach to be used as control design tool for a small scale helicopter can be elaborated as follows.

1. The control of small-scale helicopter is a MIMO problem. To use the classical control approach to formally solve a MIMO problem, one needs to come up with multi-dimensional Root Locus diagram to tune the control parameters. Such diagram however is not presently available.
2. The problem with the required dimension of the RL diagram for MIMO design has forced the design procedure of classical approach to be conducted in cascaded multi-loop SISO system starting from the innermost loop outward. As shown in the design example in this work, this type of approach is unnecessarily cumbersome.
3. The cascaded multi-loop SISO approach has limitations in its implementation. To implement this control approach for a helicopter, a pitch and roll attitude control system is often subordinated to a, respectively, longitudinal and lateral velocity control system in a nested architecture. The requirement for this technique to work is that the inner attitude control loop must have a higher bandwidth than the outer velocity control loop. For a class of high-performance helicopters, such as the X-Cell 60, or helicopters where this bandwidth separation is not sufficient, a simultaneous design is necessary[5].
4. The classical control approach is associated with the use of transfer function which can become inaccurate when pole-zero cancellation occurs due to uncontrollable and unobservable modes.

To address the above problems, a third approach generally called as algebraic design approach is proposed in this paper.

2 Dynamics of Small Scale Helicopter

The dynamics model of a small scale RUAV has been elaborated in [6] for X-Cell 60 RC helicopter. The model is developed using first principle approach. The mathematical model was developed using basic helicopter theory accounting for particular characteristic of the miniature helicopter. Following [1], most of the parameters were measured directly, several were estimated using collected data from simple flight test experiment involving step and impulse response in various actuator inputs. No formal system identification procedures are required for the proposed model structure.

2.1 First Principle Approach

Beyond the previous work in [1], the calculation of stability and control derivatives to construct the linear model is presented in detail. The analytical model derivation allows the comprehensive analysis of relative dominance of vehicle states and input variables to force and moment components. And hence it facilitates the development of minimum complexity small scale helicopter dynamics model that differs from that of its full-scale counterpart. In the presented simplified model, the engine drive-train dynamics and inflow dynamics are not necessary to be taken into consideration. The additional rotor degrees of freedom for coning and lead-lag can be omitted for small scale helicopters. It is demonstrated analytically that the dynamics of small scale helicopter is dominated by the strong moments produced by the highly rigid rotor. The dominant rotor forces and moments largely overshadow the effects of complex interactions between the rotor wake and fuselage or tail. This tendency substantially reduces the need for complicated models of second-degree effects typically found in the literature on full-scale helicopters.

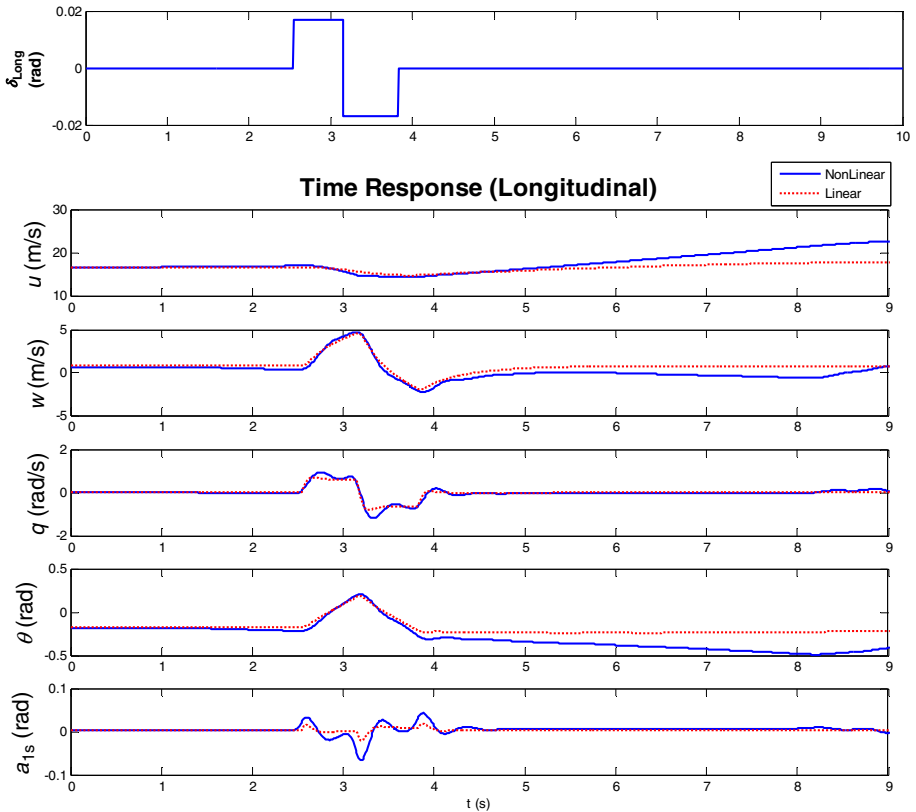


Fig. 1. Response Comparison between Linear and Nonlinear Model

2.2 Linear Model of Small Scale Helicopter

The presented approach is not limited to specific trim conditions like hover or forward flights and therefore can be used to develop a global model of small scale rotorcraft vehicle to the purpose of practical control design.

The developed model is presented in the form of state-space with ten states and four inputs. Subsequently, it was shown by eigen value analysis and the Frobenius' norm analysis that the coupling between longitudinal and lateral directional is small. Thus the control design uses the decoupled model in longitudinal and lateral directional mode [6].

3 Coefficient Diagram Method for Control Design

In this study, a novel approach pioneered by Manabe [7] using algebraic representation applied to polynomial loop in the parameter space, is proposed as control design candidate. With this technique, a unique coefficient diagram is used as the means to convey the necessary practical design information and as the criteria of good design. The eventual application of CDM in this work is in the LQ design framework to be elaborated in the next section.

3.1 Design Principle

3.1.1 Mathematical Model

The mathematical model of the CDM design is described in general as a block diagram shown in Figure 2. In this figure, r is the reference input signal, u is the control signal, d is the disturbance and n is the noise generated by the measuring device at the output; $N(s)$ and $D(s)$ are the numerator and denominator polynomial of the plant

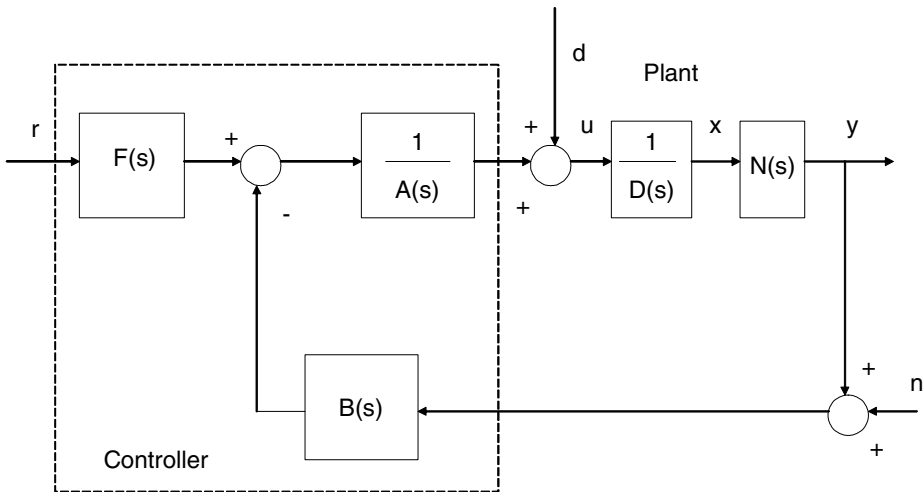


Fig. 2. CDM block diagram

transfer function, respectively. $A_{(s)}$, $F_{(s)}$ and $B_{(s)}$ are the polynomials associated with the CDM controller which are the denominator polynomial matrix of the controller, the reference and the feedback numerator polynomial matrix of the controller respectively. For MIMO case, the variables and components are in the form of vectors and matrices with the appropriate dimension.

The plant equation is given by:

$$\begin{aligned} y &= N_{(s)}x \\ y &= \frac{N_{(s)}}{D_{(s)}}(u + d) \end{aligned} \quad (1)$$

which after some algebraic manipulation, can be completely written as:

$$y = \frac{N_{(s)}F_{(s)}}{P_{(s)}}r + \frac{A_{(s)}N_{(s)}}{P_{(s)}}d - \frac{N_{(s)}B_{(s)}}{P_{(s)}}n \quad (2)$$

where $P(s)$ is the closed-loop system polynomial matrix expressed by:

$$P_{(s)} = A_{(s)}D_{(s)} + B_{(s)}N_{(s)} = \sum_{i=0}^n a_i s^i \quad (3)$$

The characteristic polynomial $\Delta_{(s)}$ is given by:

$$\Delta_{(s)} = P_{(s)} \quad (4)$$

To write the input-output relation of the system, the expression for the state and the controllers are needed. The controller equation can be written as:

$$A_{(s)}u = F_{(s)}r - B_{(s)}(n + y) \quad (5)$$

Whereas the state equation can be obtained by eliminating u and y from the controller and output equations as follows:

$$P_{(s)}x = F_{(s)}r + A_{(s)}d - B_{(s)}n \quad (6)$$

Combining the output, state and controller equations, Eqs. (1), (5) and (6), the matrix input-output equation can finally be expressed as:

$$\begin{bmatrix} x \\ y \\ z \end{bmatrix} = \frac{1}{\Delta_{(s)}} \begin{bmatrix} I \\ N_{(s)} \\ D_{(s)} \end{bmatrix} \text{adj} A_{(s)} \left[F_{(s)}r + A_{(s)}d - B_{(s)}n \right] - \begin{bmatrix} 0 \\ 0 \\ d \end{bmatrix} \quad (7)$$

3.1.2 CDM Controller Design

The design parameters in CDM are the stability indices γ_i 's, the stability limit indices γ_i^* 's and the equivalent time constant, τ . The stability index and the stability limit index determine the system stability and the transient behavior of the time domain response. In addition, they determine the robustness of the system to parameter variations. The equivalent time constant, which is closely related to the bandwidth, determines the rapidity of the time response. Those parameters are defined as follows:

$$\begin{aligned}\gamma_i &= \frac{a_i^2}{a_{i-1} \cdot a_{i+1}}, \quad i = 1, 2, 3, \dots, n-1 \\ \tau &= \frac{a_1}{a_0} \\ \gamma_i^* &= \frac{1}{\gamma_{i+1}} + \frac{1}{\gamma_{i-1}}, \quad \gamma_0 = \gamma_n \triangleq \infty\end{aligned}\tag{8}$$

where a_i 's are coefficients of the characteristic polynomial $\Delta_{(s)}$. The equivalent time constant of the i -th order τ_i is defined in the same way as τ .

$$\tau = \frac{a_{i+1}}{a_i}\tag{9}$$

By using the above equations, the relation between τ_i 's can be written as:

$$\frac{\tau_i}{\tau_{i-1}} = \frac{a_{i+1}}{a_i} \frac{a_{i-1}}{a_i} = \frac{1}{\gamma_i}\tag{10}$$

Also, by simple manipulation, a_i can be written as:

$$\begin{aligned}a_i &= \tau_{i-1} \cdot \tau_{i-2} \cdots \tau_1 \cdot \tau_0 \cdot a_0 \\ a_i &= \frac{a_0 \cdot \tau^i}{\gamma_{i-1} \cdot \gamma_{i-2}^2 \cdots \gamma_2^{j-2} \cdot \gamma_1^{j-1}}, \quad i \geq 2\end{aligned}\tag{11}$$

The characteristic polynomial can then be expressed as:

$$\Delta_{(s)} = a_0 \left[\left\{ \sum_{i=2}^n \left(\prod_{j=1}^{i-1} \frac{1}{\gamma_{i-j}} \right) (\tau s)^i \right\} + \tau s + 1 \right]\tag{12}$$

The sufficient condition for stability is given as:

$$\begin{aligned}a_i &> 1.12 \left[\frac{a_{i-1}}{a_{i+1}} a_{i+2} + \frac{a_{i+1}}{a_{i-1}} a_{i-2} \right] \\ \gamma_i &> 1.12 \gamma_i^*, \quad \forall i = 2, 3, \dots, n-2\end{aligned}\tag{13}$$

And the sufficient condition for instability is:

$$\begin{aligned} a_{i+1} \cdot a_i &\leq a_{i+2} \cdot a_{i-1} \\ \gamma_{i+1} \cdot \gamma_i &> 1, \quad \text{for some } i = 2, 3, \dots, n-2 \end{aligned} \quad (14)$$

3.2 Application to Helicopter Control

To control a model helicopter as a complex MIMO system, an approach that can synthesize a control algorithm to make the helicopter meet performance criteria while satisfying some physical constraints is required. Overall it is always desired to have a controller that can accommodate the unmodeled dynamics or parameter changes and perform well in such situations. Coefficient Diagram Method (CDM) is chosen as the candidate to synthesize such a controller due to its simplicity and convenience in demonstrating integrated performance measures including equivalent time constant, stability indices and robustness. To use CDM approach, the dynamics model should be first developed. In our case, the dynamics model of the small scale helicopter has been derived analytically.

4 Hover and Cruise Control Design

To demonstrate the viability of the algebraic approach, the hover stabilization and cruise control are taken as case studies. The well-known hover control problem represents a unique challenging problem in the real world. Many helicopter applications (both manned and unmanned) require the stable hovering capability for different missions: video air surveillance, air photography, precision targeting etc. The preliminary study conducted by the author for R-50 Yamaha helicopter hover control was given in [8]. The control during cruise is also important for different types of missions and serves as the basis for autonomous capability such as way-point following navigation and auto-piloting. As the baseline control design, multi-loop SISO system based on classical approach is first proposed. The CDM method is then proposed as an improvement of such an approach. For the sake of brevity, the speed control is taken as an example.

4.1 Classical Approach to Speed Control

The classical approach to speed control of small scale helicopter is the extension of the SAS and Hold system in a cascaded control architecture. For the purpose of illustration, the result is presented for the design of forward speed u control. Figure 3 describes the root locus diagram of speed control to be used for control parameter optimization. The gain selected for the design using the root locus diagram is $ku = -0.0221$. The time response diagram for the speed control subject to step is given in Figure 4.

The time response diagram shows that the design for the forward speed control using classical approach does not meet the expectation. The multi-loop cascaded design is also in general cumbersome and ineffective to handle the MIMO problem.

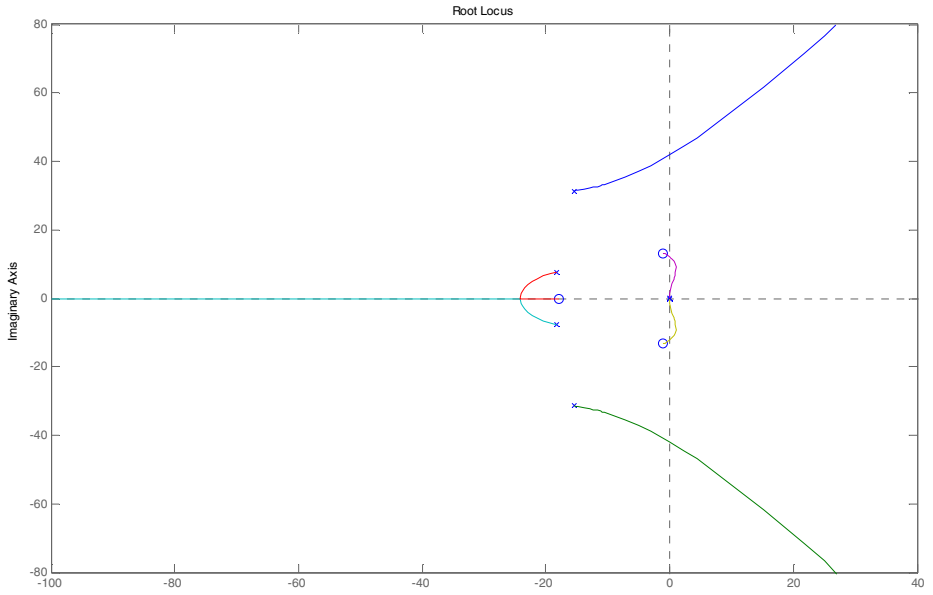


Fig. 3. Root locus speed control system

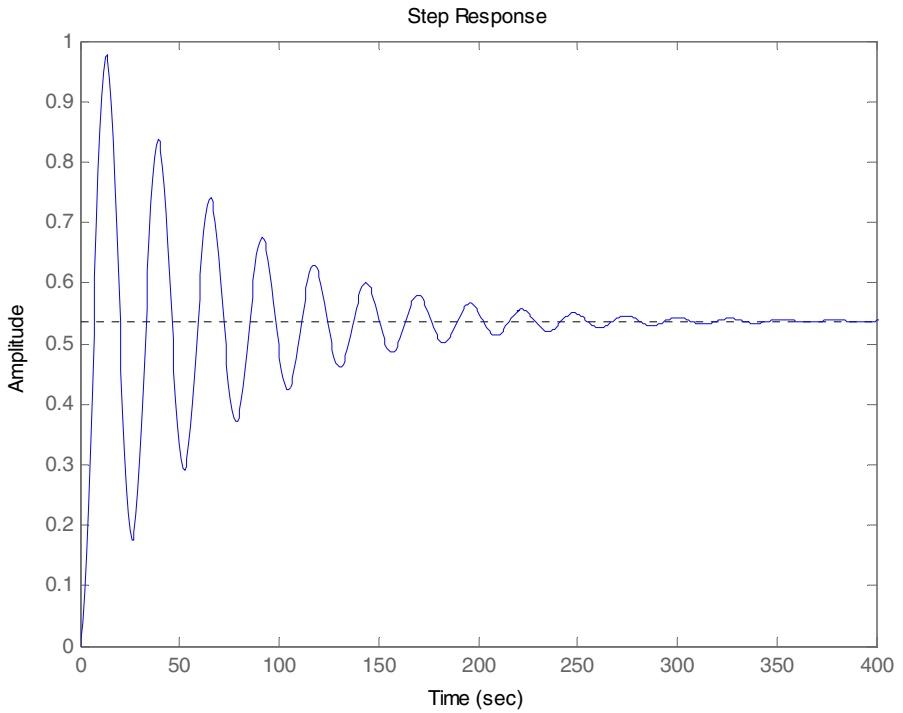


Fig. 4. Step response speed control system

4.2 Coefficient Diagram Method for Speed

As design example using CDM, the following section elaborates the procedure for developing u control and v control.

For denominator and numerator polynomials in the pitch cyclic channel for the longitudinal vertical model are calculated as the following:

$$\begin{aligned}\Delta_{(s)} &= s^5 + 31.65s^4 + 321.7s^3 + 41.4s^2 + 11.02s + 0.9 \\ (u \rightarrow \delta_{\text{Long}})_{(s)} &= -41.8s^4 - 840s^3 - 8919s^2 - 131290s - 12522 \\ (q \rightarrow \delta_{\text{Long}})_{(s)} &= 904s^4 + 13457s^3 + 1710s^2 + 4s \\ (\theta \rightarrow \delta_{\text{Long}})_{(s)} &= 901s^3 + 13417s^2 + 1705s + 4 \\ (w \rightarrow \delta_{\text{Long}})_{(s)} &= 0.67s^3 + 14.5s^2 + 214s + 6.85\end{aligned}\quad (15)$$

The corresponding coefficient diagrams for the above numerator and denominator polynomials are given in the following figures. The control design objective in this case is to change the coefficient of polynomial in order to stabilize the system using the appropriate feedback. By observation, it is more effective to use δ_{Long} to achieve the objective since δ_{Coll} is effective only when the vertical velocity feedback is used.

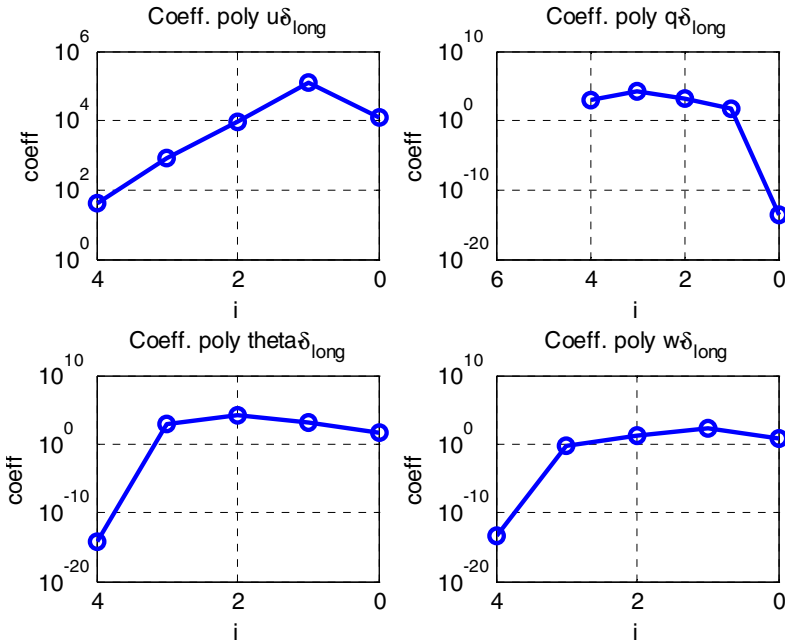


Fig. 5. Coefficient Diagrams for Numerator Polynomials $-\delta_{\text{Long}}$

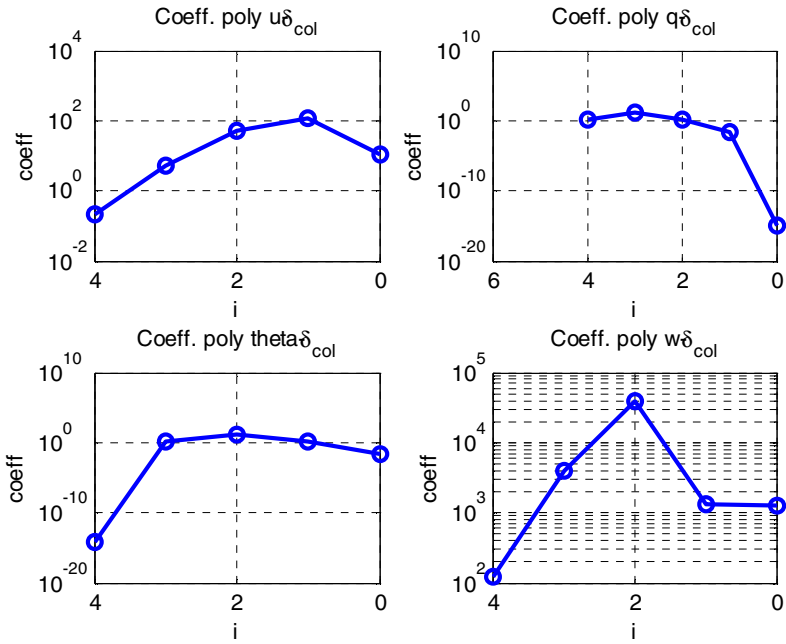


Fig. 6. Coefficient Diagrams for Numerator Polynomials $-\delta_{Col}$

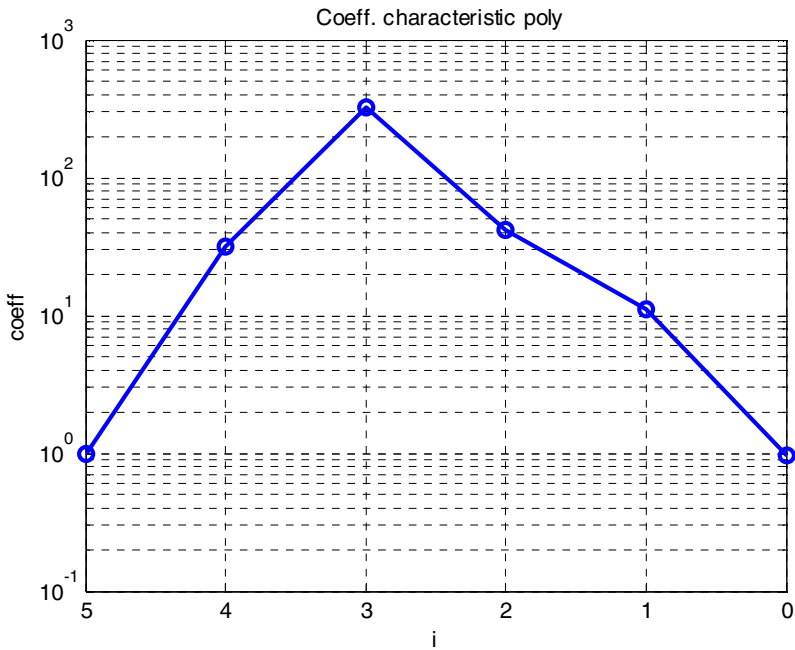


Fig. 7. Coefficient Diagram for Denominator Polynomials $-u$ Control

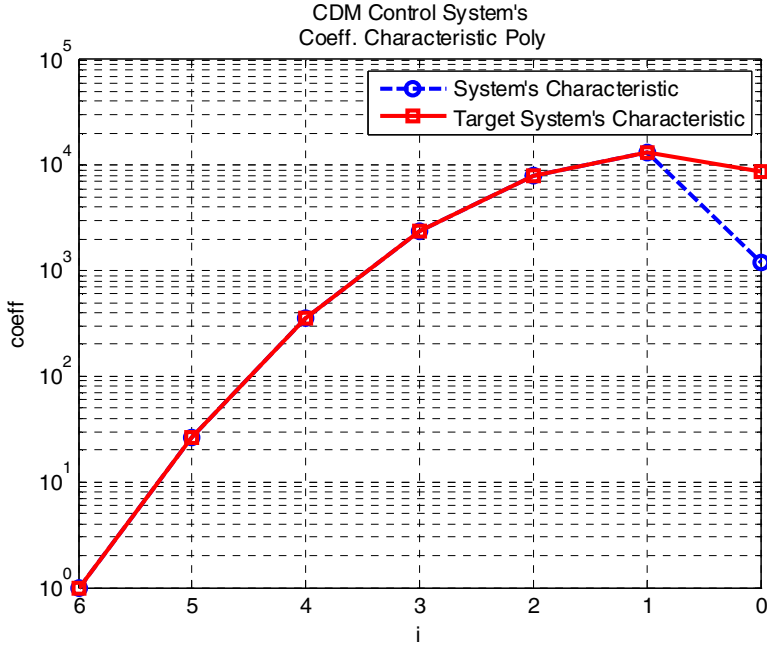


Fig. 8. Coefficient Diagram for Closed Loop Denominator Polynomials $-u$ Control

Using the CDM diagram, it can be observed that we can choose the PID controller such that:

$$s\delta_{\text{Long}} = k_0 u_r - \left[(k_0 + k_1 s)u + (k_2 + k_3 s)\theta + k_4 w \right] \quad (16)$$

The new characteristic polynomial $P(s)$ then becomes:

$$\begin{aligned} P_{(s)} &= s\Delta_{(s)} + (k_0 + k_1 s)(u \rightarrow \delta_{\text{Long}}) + (k_2 + k_3 s)(\theta \rightarrow \delta_{\text{Long}}) + k_4 (w \rightarrow \delta_{\text{Long}}) \\ &= s^6 + a_5 s^5 + a_4 s^4 + a_3 s^3 + a_2 s^2 + a_1 s + a_0 \end{aligned} \quad (17)$$

Solving the Diophantine equation,

$$\begin{aligned} -41.80k_1 + 31.65 &= a_5, \\ -41.80k_0 - 840.09k_1 + 901.2k_3 + 0.676k_4 + 321.74 &= a_4, \\ -840.09k_0 - 8918.95k_1 + 901.27k_2 + 13416.5k_3 + 14.53k_4 + 41.42 &= a_3, \\ -8918.9k_0 - 131287.6k_1 + 13.416.5k_2 + 1705.16k_3 + 214.61k_4 + 11.020 &= a_2, \\ -131287.6k_0 - 12522.15k_1 + 1705.16k_2 + 40.846k_3 + 6.85k_4 + 0.9583 &= a_1, \end{aligned} \quad (18)$$

we get the value for the gains as the following:

$$\begin{aligned} k_0 &= -0.0919 \\ k_1 &= 0.1193 \\ k_2 &= 1.4617 \\ k_3 &= 0.1343 \\ k_4 &= 13.4896 \end{aligned} \quad (19)$$

A similar procedure is implemented for the design of side velocity control. The result of the design is demonstrated in the following figures, including the test for the robustness due to an impulsive disturbance. The responses of a unit doublet in the input and to an impulse disturbance at $t = 35$ s are given. The controllers design using CDM all show a good disturbance rejection with zero steady-state error. The figures also show the robustness of control due to modeling uncertainty. For the longitudinal case, the control is tested by allowing the stability derivatives x_u , x_{a1s} and m_q to vary by $\pm 30\%$.

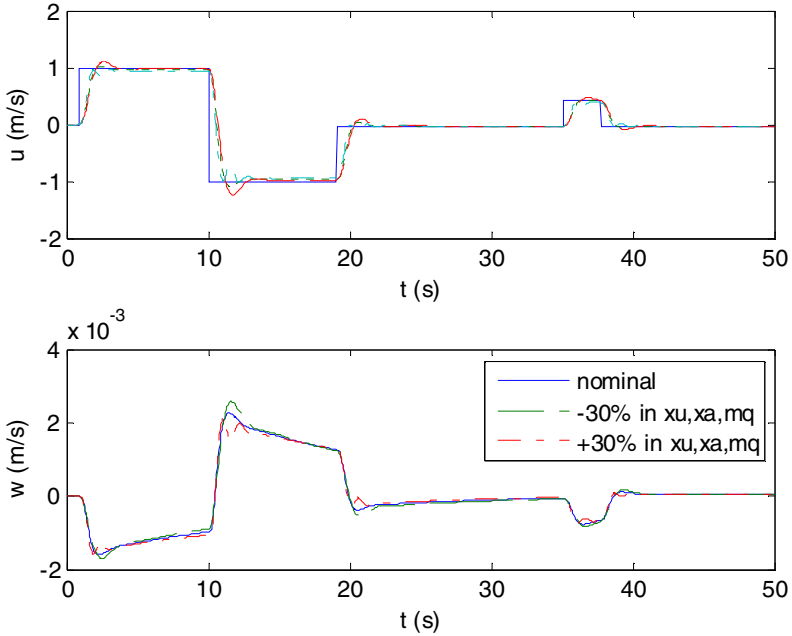


Fig. 9. Forward Speed Control Design with Uncertainty in x_u , x_{a1s} and m_q

The superiority of CDM design over classical approach has been demonstrated through results comparison of speed control design. The result is further extended for the design of MIMO control system. The following section details the implementation of CDM in the optimal control framework, using the so-called squared-Coefficient Diagram Method (s-CDM). The proposed technique is an extension from previous work by Manabe [7] where the implementation of s-CDM is given for a simple SIMO problem.

5 Squared-Coefficient Diagram Method (s-CDM) for Helicopter Control

The motivation behind this approach is the limitation of the existing LQR/LQG techniques. The primary concern for LQR/LQG designs has been the analytical weight selection for such techniques. Numerous efforts have been given in the literature and

the only workable solution to date is obtained through iteration. In addition to this problem, LQR and LQG sometimes fail to produce a robust controller for the plant with poles at the vicinity of the imaginary axis. As typical aerospace vehicles have this kind of behavior (i.e. the phugoid mode), the LQR or LQG should be used with caution. In what follows, s-CDM is proposed in conjunction with LQ design in which analytical weight selection is presented. The robustness of the control will be tested against parameter uncertainties and disturbances.

5.1 LQR Framework

The derivation is started by introducing the standard LQR formulation. In LQR framework, the plant is expressed in the state space expression:

$$\dot{\bar{\mathbf{x}}} = \mathbf{A} \cdot \bar{\mathbf{x}} + \mathbf{B} \cdot \bar{\mathbf{u}} \quad (20)$$

where $\bar{\mathbf{x}}$ is a vector of dimension n , and $\bar{\mathbf{u}}$ is an input vector. LQR design is made to minimize the performance index J given as

$$J = \int_0^{\infty} \left[\bar{\mathbf{x}}^T \cdot \mathbf{Q} \cdot \bar{\mathbf{x}} + \bar{\mathbf{u}}^T \cdot \mathbf{R} \cdot \bar{\mathbf{u}} \right] dt \quad (21)$$

where \mathbf{R} is positive definite, but \mathbf{Q} is not necessarily sign definite. The first term represents the regulation or tracking performance and the second term the minimization of control power. The closed-loop poles of the system with the feedback control are given by the stable eigen values of the Hamiltonian \mathbf{H} , where no eigen values lie on the imaginary axis.

$$\mathbf{H} = \begin{bmatrix} \mathbf{A} & -\mathbf{R}^{-1} \cdot \mathbf{B}^T \\ -\mathbf{Q}^T & -\mathbf{A}^T \end{bmatrix} \quad (22)$$

When the characteristic polynomial is given as in

$$\begin{aligned} P_{(s)} &= a_n s^n + a_{n-1} s^{n-1} + \dots + a_1 s + a_0 \\ &= \sum_{i=0}^n a_i s^i \end{aligned} \quad (23)$$

the following relation is obtained.

$$\frac{P_{(-s)} P_{(s)}}{a_n^2} = (-1)^n \det(s\mathbf{I}_{2n} - \mathbf{H}) \quad (24)$$

Therefore, if $P_{(s)}$ is designed by CDM such as done in the previous section, the weight \mathbf{Q} can be found. On the contrary, if \mathbf{Q} is specified and LQ design is made, $P_{(s)}$ can be obtained and it will be assessed in term of CDM.

5.2 Squared Polynomial in s-CDM

For a given polynomial $P_{(s)}$, $P_{(-s)}$ $P_{(s)}$ is a polynomial in $-s^2 = \Omega$, denoted as $PP_{(\Omega)}$. $PP_{(\Omega)}$ will be called the squared polynomial of $P_{(s)}$ hereafter, and $P_{(s)}$ will be called the original polynomial of $PP_{(\Omega)}$.

$$P_{(-s)}P_{(s)} = PP_{(-s^2)} = PP_{(\Omega)} \tag{25}$$

If $PP_{(\Omega)}$ has no positive real roots, there exists one original polynomial $P_{(s)}$ which is stable. This polynomial will be called the square-root polynomial of $PP_{(\Omega)}$. When $P_{(s)}$ is a characteristic polynomial, $P_{(s)}$ is the square-root polynomial of the squared polynomial $PP_{(\Omega)} = P_{(-s)}P_{(s)}$, because it is stable. The coefficients of these polynomials are selected as follows.

$$\begin{aligned} P_{(s)} &= a_n s^n + a_{n-1} s^{n-1} + \dots + a_1 s + a_0 \\ &= \sum_{i=0}^n a_i s^i \end{aligned} \tag{26}$$

$$\begin{aligned} PP_{(\Omega)} &= aq_n \Omega^n + aq_{n-1} \Omega^{n-1} + \dots + aq_1 \Omega + aq_0 \\ &= \sum_{i=0}^n aq_i \Omega^i \\ aq_n &= a_n^2 & aq_0 &= a_0^2 \\ aq_i &= a_i^2 - 2a_{i-1} \cdot a_{i+1} + 2a_{i-1} \cdot a_{i+1} + \dots \\ &= a_i^2 + 2 \sum_{i=j}^m (-1)^n a_{i-1} \cdot a_{i+1}, & m &= \min(i, n-1) \\ &= \mu a_i^2 \\ \mu &= 1 + 22 \sum_{i=j}^m \frac{(-1)^n}{\gamma_{ij}} \end{aligned} \tag{27}$$

In this way the coefficient aq_i of $PP_{(\Omega)}$ is expressed by the coefficient a_i and the stability index of high order γ_{ij} , which, in turn, is expressed by stability index γ_i .

5.3 Implementation of s-CDM for Hover Control

To implement s-CDM for the hover control the plant polynomial equations are rewritten as:

$$\begin{aligned} s^{nc} u &= u_{nc} \\ A_{p(s)} y &= B_{p(s)} u \end{aligned} \tag{28}$$

The LQR design for hover has the goal to minimize any deviation from hover trim condition with minimum control effort. It is formulated as the following cost function:

$$J = \int_0^{\infty} \left[\sum_{i=0}^{nc} qu_i u_i^2 + \sum_{i=0}^{np-1} qy_i y_i^2 \right] dt \quad (29)$$

where qu_i 's and qy_i 's are scalar constants and np is the order of $A_{p(s)}$. The weight of the tracking performance Q is expressed as

$$Q = \text{diag} \left(\left[qu_{nc-1} \quad \cdots \quad qu_0 \quad qu_{np-1} \quad \cdots \quad qy_1 \quad qy_0 \right] \right) \quad (30)$$

The weight for the control R can then be determined by considering the trade-off of tracking performance and control minimization.

The result of formulation for calculating the weight matrix Q is as follows.

$$\begin{aligned} PP_{(\Omega)} &= Q_{u(\Omega)} AA_{p(\Omega)} + Q_{y(\Omega)} BB_{p(\Omega)} \\ PP_{(\Omega)} &= P_{(-s)} P_{(s)} = \sum_{i=0}^{nc+np} aq_i \Omega^i \\ AA_{p(\Omega)} &= A_{p(-s)} A_{p(s)} = \sum_{i=0}^{np} apq_i \Omega^i \\ BB_{p(\Omega)} &= B_{p(-s)} B_{p(s)} = \sum_{i=0}^{mp} bq_i \Omega^i \\ Q_{u(\Omega)} &= \sum_{i=0}^{nc} qu_i \Omega^i \\ Q_{y(\Omega)} &= \sum_{i=0}^{np-1} qy_i \Omega^i \end{aligned} \quad (31)$$

Here mp is the order of the plant numerator polynomial $B_{p(s)}$. In this approach, if $PP_{(\Omega)}$ is obtained as the result of CDM design, the weight polynomials $Q_{u(\Omega)}$ and $Q_{y(\Omega)}$ can be obtained.

The calculated results for control design for hovering X-Cell 60 SE are presented as follows.

The helicopter's characteristic polynomials for are expressed for the longitudinal mode and lateral directional mode as follows:

$$\Delta_{\text{LongVer}(s)} = s^5 + 31.6547s^4 + 321.7496s^3 + 41.4357s^2 + 11.0203s + 0.9581 \quad (32)$$

$$\Delta_{\text{LatDir}(s)} = s^5 + 50.7248s^4 + 603.6828s^3 + 42.5467s^2 - 17.8504s + 0.6663 \quad (33)$$

The designed closed-loop system's characteristic polynomials (CDM design) are also given for both modes as:

$$P_{\text{LongVer}(s)} = s^6 + 26.6667s^5 + 355.5556s^4 + 2370.37s^3 + 7901.235s^2 \dots + 13168.72s + 1211.08 \tag{34}$$

$$P_{\text{LongVer}(s)} = s^6 + 26.6667s^5 + 355.5556s^4 + 2370.37s^3 + 7901.235s^2 \dots + 13168.72s + 1211.08 \tag{35}$$

In s-CDM framework, the expressions for the plant’s characteristic square polynomials are:

$$AP_{\text{LongVer}(s)} = \Omega^5 + 358.5208\Omega^4 + 100921.5997\Omega^3 \dots - 5313.9622\Omega^2 + 42.0507\Omega + 0.9179 \tag{36}$$

$$AP_{\text{LatDir}(s)} = \Omega^5 + 1365.6397\Omega^4 + 360080.9158\Omega^3 \dots + 23429.7538\Omega^2 + 261.9366\Omega - 0.4440 \tag{37}$$

Meanwhile, we have the expressions for the designed closed-loop system’s characteristic square polynomials:

$$PP_{\text{LongVer}(s)} = \Omega^6 + 15802.4691\Omega^4 + 684773.6626\Omega^3 \dots + 6242950.7697\Omega^2 + 34683058\Omega + 77073466.2926 \tag{38}$$

$$PP_{\text{LatDir}(s)} = \Omega^6 + 5000\Omega^4 + 121875\Omega^3 \dots + 625000\Omega^2 + 1953125\Omega + 2441406 \tag{39}$$

Plugging in the above polynomials into Eq.(31), we can obtain the weight of the CDM-LQ design. The weight matrices for the longitudinal and lateral directional mode are given as follows:

$$Q_{\text{LongVer}} = \begin{bmatrix} 237 & 0 & 0 & 0 & 0 \\ 0 & 24650646 & 0 & 0 & 0 \\ 0 & 0 & 4981280 & 0 & 0 \\ 0 & 0 & 0 & 34693042 & 0 \\ 0 & 0 & 0 & 0 & 77073684 \end{bmatrix} \tag{40}$$

$$Q_{\text{LatDir}} = \begin{bmatrix} 260 & 0 & 0 & 0 & 0 \\ 0 & 93723302 & 0 & 0 & 0 \\ 0 & 0 & 6716721 & 0 & 0 \\ 0 & 0 & 0 & 2021230 & 0 \\ 0 & 0 & 0 & 0 & 2441521 \end{bmatrix} \tag{41}$$

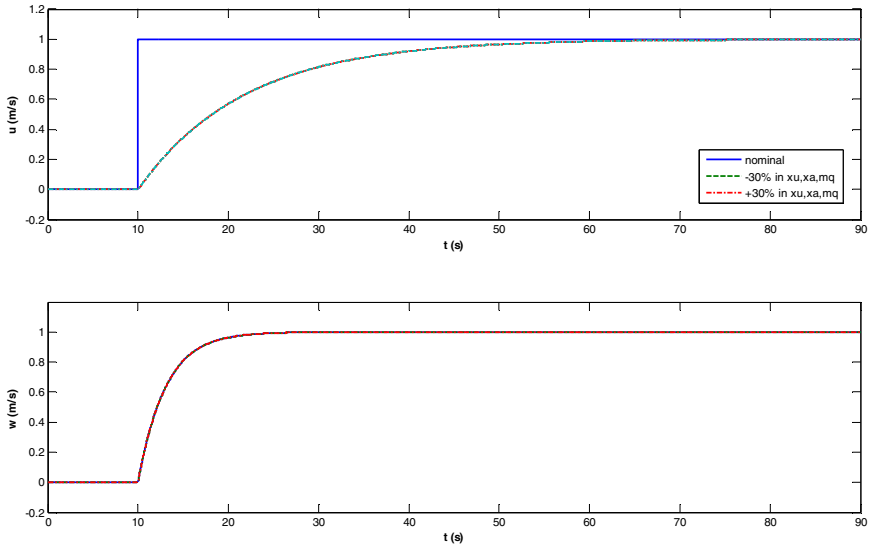


Fig. 10. Step Response Subjected to Parameter Variation

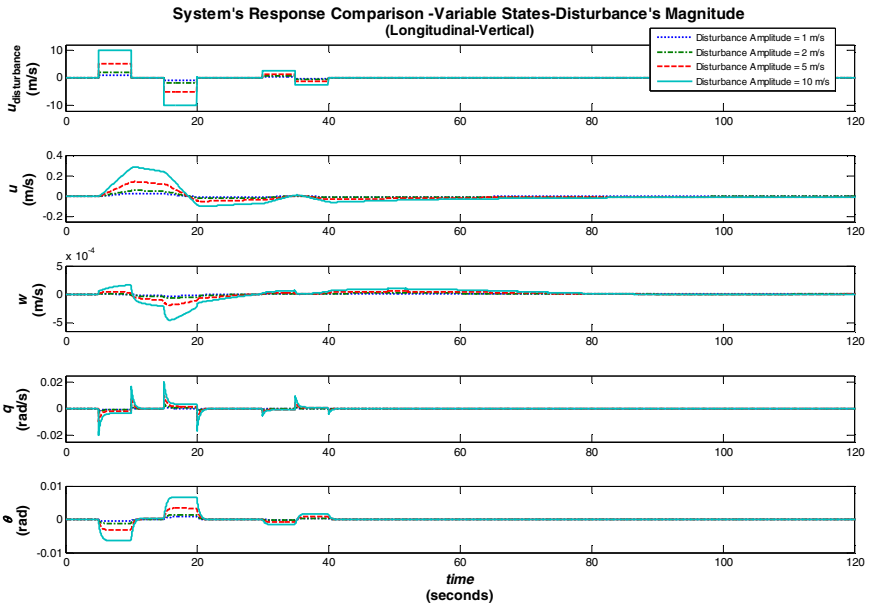


Fig. 11. System Response Comparison for Different Magnitude of Disturbance (Longitudinal Mode)

The corresponding CDM-LQ gain matrices are calculated as the following:

$$K_{\text{LongVer}} = \begin{bmatrix} -6.04073 \times 10^{-7} & -0.56477 & 2.4429 \times 10^{-4} & 5.2488 \times 10^{-4} & -3.4474 \times 10^{-4} \\ -5.3387 \times 10^{-4} & 5.4885 \times 10^{-4} & 0.23486 & 0.67320 & 0.17247 \end{bmatrix} \quad (42)$$

$$K_{\text{LatDir}} = \begin{bmatrix} -9.5475 \times 10^{-7} & -0.99923 & 2.1331 \times 10^{-4} & 4.0244 \times 10^{-6} & -1.1787 \times 10^{-4} \\ -1.114 \times 10^{-3} & 7.9840 \times 10^{-4} & 0.24553 & 0.16685 & 0.10143 \end{bmatrix} \quad (43)$$

Finally, the result of the design is presented in the above figures.

6 Conclusions

The paper presents the formulation of the control for small-scale helicopter in the algebraic approach framework. In this approach the characteristic polynomial and the controller are design simultaneously with due consideration to the performance specification and constraint imposed to the controller. In CDM, the performance specification is rewritten in a few parameters (stability indices γ_i 's, the stability limit indices γ_i^* 's and the equivalent time constant, τ). These design parameters determine the coefficients of the characteristic polynomial which are related to the controller parameters algebraically in explicit form. The control of small scale helicopter are designed by CDM is shown to be robust against model parameter uncertainties and external disturbances.

The elaboration in the paper includes the formal implementation of CDM for aerospace MIMO problem by using LQR framework. In the proposed framework, the considerations for stability, robustness and optimality are addressed simultaneously for a MIMO problem. Beyond the design examples available in the literature that are limited to SISO and SIMO applications, the work demonstrates a successful implementation of CDM-based LQR technique without the need of decomposing a MIMO problem into a series of SISO or SIMO problems.

Finally the extension of the use of Squared Coefficient Diagram Method (s-CDM) for MIMO problem is presented. To the best of author's knowledge, to date the application of s-CDM is limited to a simple SIMO problem. The work proposed the use of s-CDM in conjunction with LQ design in which analytical weight selection is presented. The designed control using s-CDM approach is demonstrated for hovering control of small-scale helicopter simultaneously subjected to plant parameter uncertainties and wind disturbances.

References

- [1] Gavrillets, V.: Autonomous Aerobatic Maneuvering of Miniature Helicopter, PhD thesis, Massachusetts Institute of Technology (2003)
- [2] Shim, D.: Hierarchical Control System Synthesis for Rotorcraft-Based Unmanned Aerial Vehicles, PhD thesis, University of California, Berkeley (2000)
- [3] Corban, J.E., Calise, A.J., Prasad, J.V.R., Hur, J., dan Kim, N.: Flight evaluation of adaptive high bandwidth control methods for unmanned helicopters. In: Proceedings of the AIAA Guidance, Navigation and Control, American Institute of Aeronautics and Astronautics (2002)
- [4] Manabe, S.: Application of Coefficient Diagram Method to MIMO Design in Aerospace. In: 15th Triennial World Congress, IFAC, Barcelona, Spain (2002)

- [5] Mettler, B., Tischler, M., dan Kanade, T.: System identification modeling of a small-scale unmanned rotorcraft for flight control design. *Journal of the American Helicopter Society* 47, 50–63 (2002)
- [6] Budiyono, A., Sudyanto, T., Lesmana, H.: First principle approach to modeling of small scale helicopter. In: *International Conference on Intelligent Unmanned Systems, ICIUS, Bali, Indonesia (2007)*
- [7] Manabe, S.: Analytic weight selection for LQ design. In: *8th Workshop on Astrodynamics and Flight Mechanics, ISAS, July 23-24 (1998)*
- [8] Budiyono, A.: Onboard Multivariable Controller Design for a Small Scale Helicopter Using Coefficient Diagram Method. In: *International Conference on Emerging System Technology, Seoul, Korea (2005)*

Discontinuous Control and Backstepping Method for the Underactuated Control of VTOL Aerial Robots with Four Rotors

Keigo Watanabe¹, Kouki Tanaka¹, Kiyotaka Izumi¹,
Kensaku Okamura¹, and Rafiuddin Syam²

¹ Department of Advanced Systems Control Engineering,
Graduate School of Science and Engineering, Saga University
{watanabe, izumi}@me.saga-u.ac.jp

² Manufacture Division, Department of Mechanical Engineering,
Hasanuddin University, Indonesia

Abstract. A control strategy is proposed here for four-rotor vertical take-off and landing (VTOL) aerial robot called X4-flyer. Since the X4-flyer has underactuated and nonholonomic features, a kinematics control law is first derived using Astolfi's discontinuous control. A backstepping method that is one of adaptive control methods based on Lyapunov methods, then provides the kinematic based inputs, to construct the torque control of X4-flyer. Finally, computer simulations are given to demonstrate the effectiveness of our approach.

1 Introduction

Unmanned vehicles are important when it comes to performing a desired task in a dangerous and/or inaccessible environment. Unmanned indoor and outdoor mobile robots have been successfully used for some decades. More recently, a growing interest in unmanned aerial vehicles (UAVs) has been shown among the research community. Being able to design a vertical takeoff and landing (VTOL)-UAV, which is highly maneuverable and extremely stable, is an important contribution to the field of aerial robotics since potential applications are tremendous (e.g., high buildings and monuments investigation, rescue missions, film making, etc.).

In practical applications, the position in space of the UAV is generally controlled by an operator through a remote-control system using a visual feedback from an onboard camera, while the attitude is automatically stabilized via an onboard controller. The attitude controller is an important feature since it allows the vehicle to maintain a desired orientation and, hence, prevents the vehicle from flipping over and crashing when the pilot performs the desired maneuvers.

Recently, in Europe, USA, and Australia, the study on VTOL type aerial robot attracts the attention of researchers, in which the robot is called "Draganflyer," "Quattrocopter," "X-4 Flyer," or "Quadrotor" and has four rotors in general [1], [2], [3].

As one reason for this research trend, the authors had pointed out [4] that such VTOL aerial robots with four rotors outperform in controllability and maneuverability over other VTOL vehicles with different rotor allocations, when controlling the rotor type VTOL vehicle by only increasing and decreasing the rotational speed of each rotor.

Note, however, that the control system for this VTOL type aerial robot can be regarded as an underactuated system [5] that deals with controlling six generalized coordinates with four inputs, and its control becomes complicated, compared to a nonholonomic control where any four states are controlled out of six generalized coordinates by using four inputs.

In this paper, we present a new control strategy for a VTOL aerial robot. We first derive the dynamics model of a VTOL aerial robot with four rotors using a Lagrange approach. A kinematics control law is first derived using Astolfi’s discontinuous control [6]. Backstepping, which is one of adaptive control methods based on Lyapunov methods, then combines the kinematics and dynamics, to achieve the torque control of the VTOL aerial robots.

Note here that Bouabdallah et al. [1] has considered a nonholonomic control for a VTOL aerial robot, called Quadrotor, using a backstepping, in which all attitudes and height position are controlled by using four inputs. Finally, computer simulations are demonstrated to show the effectiveness of our approach.

2 Dynamical Model of X4-Flyer

2.1 X4 Flyer

The coordinate system and construction of X4-flyer are shown in Fig. 1.

Let $E = \{E_x, E_y, E_z\}$ denote a right-hand inertial frame such that E_z denotes the vertical direction downwards into the earth. Let the vector $\xi = [x, y, z]^T$ denote the position of the centre of mass of the airframe in the frame E relative to a fixed origin $O \in E$.

Let c be a (right-hand) body fixed frame for the airframe. When defining the rotational angles $\eta = [\phi, \theta, \psi]^T$ around X -, Y -, and Z -axis in the frame c , the orientation

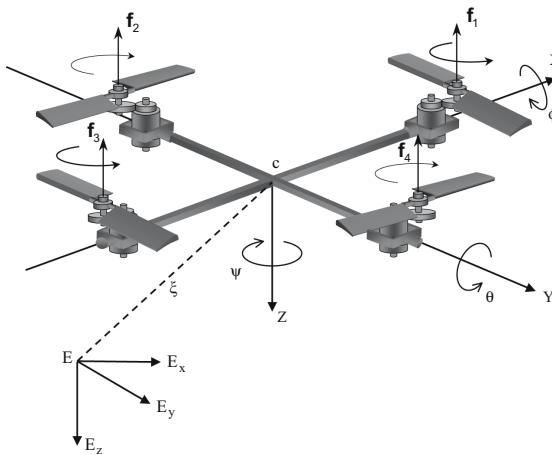


Fig. 1. Coordinate system of X4-Flyer

of the rigid body is given by a rotation $R : c \rightarrow E$, where $R \in \mathfrak{R}^{3 \times 3}$ is an orthogonal rotation matrix given by

$$R = \begin{bmatrix} c\theta c\psi & s\phi s\theta c\psi - c\phi s\psi & c\phi s\theta c\psi + s\phi s\psi \\ c\theta s\psi & s\phi s\theta s\psi + c\phi c\psi & c\phi s\theta s\psi - s\phi c\psi \\ -s\theta & s\phi c\theta & c\phi c\theta \end{bmatrix} \quad (1)$$

where $c\alpha$ denotes $\cos \alpha$ and $s\alpha$ implies $\sin \alpha$.

Let J denote the constant inertia matrix around the center of mass (expressed in the body fixed frame c), where the moment of inertia around each axis is given by I_x , I_y , and I_z . Moreover, let f_i denote the thrust generated by the rotor i in free air (expressed in c), m is the mass of the airframe, g denotes the acceleration due to gravity, and l denotes the distance from the rotors to the center of gravity of the airframe.

2.2 Dynamics of X4-Flyer

In this section, we present a dynamical model of the X4-flyer using a Lagrangian approach. The translational kinetic energy of the X4-flyer is

$$T_{trans} = \frac{1}{2} m \dot{\boldsymbol{\xi}}^T \dot{\boldsymbol{\xi}} \quad (2)$$

the rotational kinetic energy is

$$T_{rot} = \frac{1}{2} \dot{\boldsymbol{\eta}}^T J \dot{\boldsymbol{\eta}} \quad (3)$$

and the only potential energy which needs to be considered is the standard gravitational potential given by

$$U = -mgz \quad (4)$$

Since the Lagrangian is

$$\begin{aligned} L &= T_{trans} + T_{rot} - U \\ &= \frac{1}{2} m \dot{\boldsymbol{\xi}}^T \dot{\boldsymbol{\xi}} + \frac{1}{2} \dot{\boldsymbol{\eta}}^T J \dot{\boldsymbol{\eta}} + mgz \end{aligned} \quad (5)$$

when defining the generalized coordinate as $\mathbf{q} = [\boldsymbol{\xi} \ \boldsymbol{\eta}]^T$, the model for the full X4-flyer dynamics is obtained from the Euler-Lagrange equations with external generalized force \mathbf{F}

$$\frac{d}{dt} \frac{\partial L}{\partial \dot{\mathbf{q}}} - \frac{\partial L}{\partial \mathbf{q}} = \mathbf{F} \quad (6)$$

Partially or normally differentiating each term in left-hand side, it follows that

$$\frac{\partial L}{\partial \dot{\mathbf{q}}} = \begin{bmatrix} m \ddot{\boldsymbol{\xi}} \\ 0 \end{bmatrix} + \begin{bmatrix} 0 \\ J \dot{\boldsymbol{\eta}} \end{bmatrix} \quad (7)$$

$$\frac{d}{dt} \left(\frac{\partial L}{\partial \dot{\mathbf{q}}} \right) = \begin{bmatrix} m \ddot{\boldsymbol{\xi}} \\ J \ddot{\boldsymbol{\eta}} + \dot{J} \dot{\boldsymbol{\eta}} \end{bmatrix} \quad (8)$$

$$\frac{\partial L}{\partial \mathbf{q}} = \begin{bmatrix} mg \\ \frac{1}{2} \frac{\partial}{\partial \boldsymbol{\eta}} \left(\dot{\boldsymbol{\eta}}^T J \dot{\boldsymbol{\eta}} \right) \end{bmatrix} \quad (9)$$

so that

$$\begin{bmatrix} m\ddot{\xi} \\ J\ddot{\eta} + j\dot{\eta} \end{bmatrix} - \begin{bmatrix} mg \\ \frac{1}{2} \frac{\partial}{\partial \eta} (\dot{\eta}^T J \dot{\eta}) \end{bmatrix} = \mathbf{F} \quad (10)$$

Here, $\mathbf{F} = [F_{\xi} \ \boldsymbol{\tau}]^T$, where F_{ξ} is the translational force applied to the X4-flyer due to the control inputs and $\boldsymbol{\tau} = [\tau_{\phi} \ \tau_{\theta} \ \tau_{\psi}]^T$ is the generalized moments around the airframe. Letting the control input as the translational force be defined as $u_1 = f_1 + f_2 + f_3 + f_4$ and the unit vector of Z -direction in the airframe be $\mathbf{e}_3 = [0 \ 0 \ 1]^T$, it yields that

$$\begin{aligned} F_{\xi} &= -R\mathbf{e}_3 u_1 \\ &= -u_1 \begin{bmatrix} c\phi s\theta c\psi + s\phi s\psi \\ c\phi s\theta s\psi - s\phi c\psi \\ c\phi c\theta \end{bmatrix} \end{aligned} \quad (11)$$

and $\boldsymbol{\tau}$ becomes

$$\begin{aligned} \tau_{\phi} &= (f_2 - f_4)l \\ \tau_{\theta} &= (f_1 - f_3)l \\ \tau_{\psi} &= \sum_{i=1}^4 \tau_{M_i} \end{aligned}$$

where τ_{M_i} denotes the rotational torque due to each motor.

Since the Lagrangian contains no cross terms in the kinetic energy combining $\dot{\xi}$ and $\dot{\eta}$ in (5), the Euler-Lagrange equation can be partitioned into the dynamics for the ξ coordinates and the η dynamics. One obtains

$$\begin{aligned} m\ddot{\xi} + \begin{bmatrix} 0 \\ 0 \\ -mg \end{bmatrix} \\ = -[f_1 + f_2 + f_3 + f_4] \begin{bmatrix} c\phi s\theta c\psi + s\phi s\psi \\ c\phi s\theta s\psi - s\phi c\psi \\ c\phi c\theta \end{bmatrix} \end{aligned} \quad (12)$$

$$J\ddot{\eta} + \left(j - \frac{1}{2} \frac{\partial}{\partial \eta} (\dot{\eta}^T J) \right) \dot{\eta} = \begin{bmatrix} (f_2 - f_4)l \\ (f_1 - f_3)l \\ \sum_{i=1}^4 \tau_{M_i} \end{bmatrix} \quad (13)$$

The second term of the left-hand side in (13) is a Coriolis term, which is just equivalent to a term consisting of a Coriolis torque and a gyroscopic torque

$$\boldsymbol{\omega} \times J\boldsymbol{\omega} + \sum_{i=1}^4 J_r (\boldsymbol{\omega} \times \mathbf{e}_3) \boldsymbol{\omega}_i \quad (14)$$

where $\boldsymbol{\omega} = [\dot{\phi} \ \dot{\theta} \ \dot{\psi}]^T$, J_r denotes the moment of inertia for the rotor, $\boldsymbol{\omega}_i$ is the rotational speed of the rotor i .

Noting that

$$J\omega = \begin{bmatrix} I_x & 0 & 0 \\ 0 & I_y & 0 \\ 0 & 0 & I_z \end{bmatrix} \begin{bmatrix} \dot{\phi} \\ \dot{\theta} \\ \dot{\psi} \end{bmatrix} = \begin{bmatrix} I_x \dot{\phi} \\ I_y \dot{\theta} \\ I_z \dot{\psi} \end{bmatrix} \quad (15)$$

and $\omega \times$ is a skew symmetric matrix

$$\omega \times = \begin{bmatrix} 0 & -\dot{\psi} & \dot{\theta} \\ \dot{\psi} & 0 & -\dot{\phi} \\ -\dot{\theta} & \dot{\phi} & 0 \end{bmatrix} \quad (16)$$

Therefore, it follows that

$$\begin{aligned} \omega \times J\omega &= \begin{bmatrix} 0 & -\dot{\psi} & \dot{\theta} \\ \dot{\psi} & 0 & -\dot{\phi} \\ -\dot{\theta} & \dot{\phi} & 0 \end{bmatrix} \begin{bmatrix} I_x \dot{\phi} \\ I_y \dot{\theta} \\ I_z \dot{\psi} \end{bmatrix} \\ &= \begin{bmatrix} -\dot{\psi} I_y \dot{\theta} + \dot{\theta} I_z \dot{\psi} \\ \dot{\psi} I_x \dot{\phi} - \dot{\phi} I_z \dot{\psi} \\ -\dot{\theta} I_x \dot{\phi} + \dot{\phi} I_y \dot{\theta} \end{bmatrix} \\ &= \begin{bmatrix} -\dot{\theta} \dot{\psi} (I_y - I_z) \\ -\dot{\phi} \dot{\psi} (I_z - I_x) \\ -\dot{\phi} \dot{\theta} (I_x - I_y) \end{bmatrix} \end{aligned} \quad (17)$$

$$\begin{aligned} \omega \times e_3 &= \begin{bmatrix} 0 & -\dot{\psi} & \dot{\theta} \\ \dot{\psi} & 0 & -\dot{\phi} \\ -\dot{\theta} & \dot{\phi} & 0 \end{bmatrix} \begin{bmatrix} 0 \\ 0 \\ 1 \end{bmatrix} \\ &= \begin{bmatrix} \dot{\theta} \\ -\dot{\phi} \\ 0 \end{bmatrix} \end{aligned} \quad (18)$$

Thus, it is found that

$$\sum_{i=1}^4 J_r (\omega \times e_3) \omega_i = J_r \begin{bmatrix} \dot{\theta} \\ -\dot{\phi} \\ 0 \end{bmatrix} [\omega_2 + \omega_4 - \omega_1 - \omega_3] \quad (19)$$

Consequently, the final dynamics of X4 flyer can be reduced to

$$m\ddot{x} = -(\cos \phi \sin \theta \cos \psi + \sin \phi \sin \psi) u_1 \quad (20)$$

$$m\ddot{y} = -(\cos \phi \sin \theta \sin \psi - \sin \phi \cos \psi) u_1 \quad (21)$$

$$m\ddot{z} = -(\cos \phi \cos \theta) u_1 + mg \quad (22)$$

$$I_x \ddot{\phi} = \dot{\theta} \dot{\psi} (I_y - I_z) - J_r \dot{\theta} \Omega + l u_2 \quad (23)$$

$$I_y \ddot{\theta} = \dot{\phi} \dot{\psi} (I_z - I_x) + J_r \dot{\phi} \Omega + l u_3 \quad (24)$$

$$I_z \ddot{\psi} = \dot{\phi} \dot{\theta} (I_x - I_y) + u_4 \quad (25)$$

where $f_i = -b\omega_i^2$ (b is a thrust factor), $\tau_{Mi} = d\omega_i^2$ (d is a drag factor), and Ω , u_1 , u_2 , u_3 , and u_4 are respectively given by

$$\Omega = (\omega_2 + \omega_4 - \omega_1 - \omega_3) \quad (26)$$

$$u_1 = f_1 + f_2 + f_3 + f_4 = b(\omega_1^2 + \omega_2^2 + \omega_3^2 + \omega_4^2) \quad (27)$$

$$u_2 = f_2 - f_4 = b(\omega_2^2 - \omega_4^2) \quad (28)$$

$$u_3 = f_1 - f_3 = b(\omega_1^2 - \omega_3^2) \quad (29)$$

$$u_4 = \sum_{i=1}^4 \tau_{Mi} = d(-\omega_2^2 - \omega_4^2 + \omega_1^2 + \omega_3^2) \quad (30)$$

3 Controllability of X4-Flyer Based on Kinematics

3.1 Kinematic Equation

From the rotational matrix, the kinematic equation for X4-flyer, $\dot{\mathbf{q}} = S(\mathbf{q})\mathbf{v}$, can be reduced to

$$\begin{bmatrix} \dot{x} \\ \dot{y} \\ \dot{z} \\ \dot{\phi} \\ \dot{\theta} \\ \dot{\psi} \end{bmatrix} = \begin{bmatrix} \cos \phi \sin \theta \cos \psi + \sin \phi \sin \psi & 0 & 0 & 0 \\ \cos \phi \sin \theta \sin \psi - \sin \phi \cos \psi & 0 & 0 & 0 \\ \cos \phi \cos \theta & 0 & 0 & 0 \\ 0 & 1 & 0 & 0 \\ 0 & 0 & 1 & 0 \\ 0 & 0 & 0 & 1 \end{bmatrix} \begin{bmatrix} \dot{z}_b \\ \dot{\phi} \\ \dot{\theta} \\ \dot{\psi} \end{bmatrix} \quad (31)$$

where $\mathbf{v} = [\dot{z}_b \ \dot{\phi} \ \dot{\theta} \ \dot{\psi}]^T$, where \dot{z}_b denotes the Z -directional translational velocity and $[\dot{\phi} \ \dot{\theta} \ \dot{\psi}]^T$ is the rotational angular velocity vector in the airframe.

3.2 Lie Bracket

For two vectors $f(x)$ and $g(x)$, Lie bracket is defined as

$$[f, g] = \frac{\partial g}{\partial x} f - \frac{\partial f}{\partial x} g \quad (32)$$

This is also described as follows:

$$ad_f g = [f, g] \quad (33)$$

In addition, the higher-order Lie brackets are defined as

$$ad_f^0 g = g \quad (34)$$

$$ad_f^1 g = [f, g] \quad (35)$$

$$ad_f^2 g = [f, [f, g]] \quad (36)$$

$$ad_f^n g = [f, ad_f^{n-1} g] \quad (37)$$

3.3 Controllability of X4-Flyer

The kinematic model of X4-flyer is represented by a symmetric affine system with no drift terms such as

$$\dot{\mathbf{q}} = g_1(\mathbf{q})v_1 + g_2(\mathbf{q})v_2 + g_3(\mathbf{q})v_3 + g_4(\mathbf{q})v_4 \quad (38)$$

where $v_1 = \dot{z}_b$, $v_2 = \dot{\phi}$, $v_3 = \dot{\theta}$, $v_4 = \dot{\psi}$, and $g_i(\cdot)$ are given by

$$g_1(\mathbf{q}) = \begin{bmatrix} c\phi s\theta c\psi + s\phi s\psi \\ c\phi s\theta s\psi - s\phi c\psi \\ c\phi c\theta \\ 0 \\ 0 \\ 0 \end{bmatrix}, \quad g_2(\mathbf{q}) = \begin{bmatrix} 0 \\ 0 \\ 0 \\ 1 \\ 0 \\ 0 \end{bmatrix}$$

$$g_3(\mathbf{q}) = \begin{bmatrix} 0 \\ 0 \\ 0 \\ 0 \\ 1 \\ 0 \end{bmatrix}, \quad g_4(\mathbf{q}) = \begin{bmatrix} 0 \\ 0 \\ 0 \\ 0 \\ 0 \\ 1 \end{bmatrix}$$

Using any combinations among the above four vectors, the following Lie brackets are selected:

$$[g_1, g_2] = \begin{bmatrix} s\phi s\theta c\psi - c\phi s\psi \\ s\phi s\theta s\psi + c\phi c\psi \\ s\phi c\theta \\ 0 \\ 0 \\ 0 \end{bmatrix}, \quad [g_1, g_3] = \begin{bmatrix} -c\phi c\theta c\psi \\ -c\phi c\theta s\psi \\ c\phi s\theta \\ 0 \\ 0 \\ 0 \end{bmatrix}$$

A space $D(\mathbf{q})$ that is spanned by g_1, \dots, g_4 and their higher-order Lie brackets is called a reachable distribution. To assure that the system is locally controllable at the equilibrium point $\mathbf{q} = \mathbf{q}_0$, it is a necessary and sufficient condition for any symmetric affine system with $\mathbf{q} \in \mathbb{R}^n$ that the distribution $D(\mathbf{q}_0)$ spans \mathbb{R}^n .

If the reachable distribution is selected as $D(\mathbf{q}) = (g_1, g_2, g_3, g_4, [g_1, g_2], [g_1, g_3])$, then

$$D(\mathbf{q}) = \begin{bmatrix} c\phi s\theta c\psi + s\phi s\psi & 0 & 0 & 0 & s\phi s\theta c\psi - c\phi s\psi & -c\phi c\theta c\psi \\ c\phi s\theta s\psi - s\phi c\psi & 0 & 0 & 0 & s\phi s\theta s\psi + c\phi c\psi & -c\phi c\theta s\psi \\ c\phi c\theta & 0 & 0 & 0 & s\phi c\theta & c\phi s\theta \\ 0 & 1 & 0 & 0 & 0 & 0 \\ 0 & 0 & 1 & 0 & 0 & 0 \\ 0 & 0 & 0 & 1 & 0 & 0 \end{bmatrix} \quad (39)$$

has rank 6 at $\mathbf{q} = 0$, so that the system is locally controllable. Note also that this system is globally controllable except for a singular case where the above determinant is to be zero.

4 Kinematic Control

4.1 Astolfi's Discontinuous Control

For a nonlinear system with continuous parameters, Astolfi [6] proposed a method that a discontinuous coordinate transformation was performed at the origin to make the controlled object discontinuous in advance, so that the origin was stabilized by a continuous feedback law.

4.2 Discontinuous Feedback Control of X4-Flyer

In equation (31), exchanging \dot{x} and \dot{z} gives

$$\dot{z} = \cos \phi \cos \theta \dot{z}_b \quad (40)$$

$$\dot{y} = (\cos \phi \sin \theta \sin \psi - \sin \phi \cos \psi) \dot{z}_b \quad (41)$$

$$\dot{x} = (\cos \phi \sin \theta \cos \psi + \sin \phi \sin \psi) \dot{z}_b \quad (42)$$

$$\dot{\phi} = \dot{\phi} \quad (43)$$

$$\dot{\theta} = \dot{\theta} \quad (44)$$

$$\dot{\psi} = \dot{\psi} \quad (45)$$

Here, new control inputs are defined as follows:

$$u_1 = (\cos \phi \cos \theta) v_1 \quad (46)$$

$$u_2 = v_2 \quad (47)$$

$$u_3 = v_3 \quad (48)$$

$$u_4 = v_4 \quad (49)$$

and, as a σ -process to make the present system discontinuous, the following coordinate transformation is applied:

$$y_1 = z \quad (50)$$

$$y_2 = \frac{y}{z} \quad (51)$$

$$y_3 = \frac{x}{z} \quad (52)$$

$$y_4 = \phi \quad (53)$$

$$y_5 = \theta \quad (54)$$

$$y_6 = \psi \quad (55)$$

When defining the coordinates before a transformation as $Z_1 = z$ and $Z_2 = [y \ x \ \phi \ \theta \ \psi]^T$, the above transformation is equivalent to the situation that $\sigma = z$ and $\Phi = [y \ x \ \phi z \ \theta z \ \psi z]^T$ are chosen in $Y_1 = z$ and $Y_2 = \Phi(Z_1, Z_2)/\sigma(Z_1)$, which are the coordinates after the transformation. Note here that $\sigma(0) = 0$ and $\Phi(0, Z_2) = [y \ x \ 0 \ 0 \ 0]^T \neq 0$ are satisfied.

Differentiating these with respect to time yields

$$\begin{aligned}\dot{y}_1 &= \dot{z} \\ &= u_1\end{aligned}\quad (56)$$

$$\begin{aligned}\dot{y}_2 &= \frac{\dot{y}z - \dot{z}y}{z^2} \\ &= \frac{(\cos \phi \sin \theta \sin \psi - \sin \phi \cos \psi) v_1 z - u_1 y}{z^2} \\ &= \frac{(\cos \phi \sin \theta \sin \psi - \sin \phi \cos \psi) v_1 - \left(\frac{y}{z}\right) u_1}{z} \\ &= \left(\frac{\cos \phi \sin \theta \sin \psi - \sin \phi \cos \psi}{\cos \phi \cos \theta} - y_2\right) \frac{u_1}{y_1}\end{aligned}\quad (57)$$

$$\begin{aligned}\dot{y}_3 &= \frac{\dot{x}z - \dot{z}x}{z^2} \\ &= \frac{(\cos \phi \sin \theta \cos \psi + \sin \phi \sin \psi) v_1 z - u_1 x}{z^2} \\ &= \frac{(\cos \phi \sin \theta \cos \psi + \sin \phi \sin \psi) v_1 - \left(\frac{x}{z}\right) u_1}{z} \\ &= \left(\frac{\cos \phi \sin \theta \cos \psi + \sin \phi \sin \psi}{\cos \phi \cos \theta} - y_3\right) \frac{u_1}{y_1}\end{aligned}\quad (58)$$

$$\begin{aligned}\dot{y}_4 &= \dot{\phi} \\ &= u_2\end{aligned}\quad (59)$$

$$\begin{aligned}\dot{y}_5 &= \dot{\theta} \\ &= u_3\end{aligned}\quad (60)$$

$$\begin{aligned}\dot{y}_6 &= \dot{\psi} \\ &= u_4\end{aligned}\quad (61)$$

and arranging it gives the following transformed system:

$$\frac{d}{dt} \begin{bmatrix} y_1 \\ y_2 \\ y_3 \\ y_4 \\ y_5 \\ y_6 \end{bmatrix} = \begin{bmatrix} 1 & | & 0 & 0 & 0 \\ \left(\frac{\cos \phi \sin \theta \sin \psi - \sin \phi \cos \psi}{\cos \phi \cos \theta} - y_2\right) \frac{1}{y_1} & | & 0 & 0 & 0 \\ \left(\frac{\cos \phi \sin \theta \cos \psi + \sin \phi \sin \psi}{\cos \phi \cos \theta} - y_3\right) \frac{1}{y_1} & | & 0 & 0 & 0 \\ 0 & | & 1 & 0 & 0 \\ 0 & | & 0 & 1 & 0 \\ 0 & | & 0 & 0 & 1 \end{bmatrix} \begin{bmatrix} u_1 \\ u_2 \\ u_3 \\ u_4 \end{bmatrix}\quad (62)$$

Then, the transformed coordinates $Y_1 = y_1$ and $\mathbf{Y}_2 = [y_2 \ y_3 \ y_4 \ y_5 \ y_6]^T$ are reduced to

$$\dot{Y}_1 = g_{11}(Y_1, \mathbf{Y}_2)u_1\quad (63)$$

$$\dot{\mathbf{Y}}_2 = g_{21}(Y_1, \mathbf{Y}_2)u_1 + g_{22}(\mathbf{Y}_2) \begin{bmatrix} u_2 \\ u_3 \\ u_4 \end{bmatrix}\quad (64)$$

where

$$\begin{aligned}
 g_{11}(\mathbf{Y}_1, \mathbf{Y}_2) &= 1 \\
 g_{21}(\mathbf{Y}_1, \mathbf{Y}_2) &= \begin{bmatrix} \left(\frac{\cos \phi \sin \theta \sin \psi - \sin \phi \cos \psi}{\cos \phi \cos \theta} - y_2 \right) \frac{1}{y_1} \\ \left(\frac{\cos \phi \sin \theta \cos \psi + \sin \phi \sin \psi}{\cos \phi \cos \theta} - y_3 \right) \frac{1}{y_1} \\ 0 \\ 0 \\ 0 \end{bmatrix} \\
 g_{22}(\mathbf{Y}_2) &= \begin{bmatrix} 0 & 0 & 0 \\ 0 & 0 & 0 \\ 1 & 0 & 0 \\ 0 & 1 & 0 \\ 0 & 0 & 1 \end{bmatrix}
 \end{aligned}$$

When using the input $u_1 = -ky_1$, it is easy to find that

$$g_{21}u_1 = -k \begin{bmatrix} \frac{\cos \phi \sin \theta \sin \psi - \sin \phi \cos \psi}{\cos \phi \cos \theta} - y_2 \\ \frac{\cos \phi \sin \theta \cos \psi + \sin \phi \sin \psi}{\cos \phi \cos \theta} - y_3 \\ 0 \\ 0 \\ 0 \end{bmatrix} \triangleq f(\mathbf{Y}_2) \tag{65}$$

Partially differentiating $f(\mathbf{Y}_2)$ with respect to \mathbf{Y}_2 and evaluating the Jacobian matrix at the origin gives the following approximation:

$$f(\mathbf{Y}_2) \simeq \left. \frac{\partial f(\mathbf{Y}_2)}{\partial \mathbf{Y}_2} \right|_{\mathbf{Y}_2=0} \mathbf{Y}_2 \tag{66}$$

Therefore, the linearization about the origin ($y_2 = y_3 = y_4 = y_5 = y_6 = 0$) becomes

$$\dot{\mathbf{Y}}_2 = f(\mathbf{Y}_2) + g_{22} \begin{bmatrix} u_2 \\ u_3 \\ u_4 \end{bmatrix} \tag{67}$$

$$\simeq \begin{bmatrix} k & 0 & k & 0 & 0 \\ 0 & k & 0 & -k & 0 \\ 0 & 0 & 0 & 0 & 0 \\ 0 & 0 & 0 & 0 & 0 \\ 0 & 0 & 0 & 0 & 0 \end{bmatrix} \begin{bmatrix} y_2 \\ y_3 \\ y_4 \\ y_5 \\ y_6 \end{bmatrix} + \begin{bmatrix} 0 & 0 & 0 \\ 0 & 0 & 0 \\ 1 & 0 & 0 \\ 0 & 1 & 0 \\ 0 & 0 & 1 \end{bmatrix} \begin{bmatrix} u_2 \\ u_3 \\ u_4 \end{bmatrix} \tag{68}$$

which is apparently controllable, so that it is easy to find a linear state feedback (as a continuous function) that stabilizes the system asymptotically.

5 Dynamical Control

5.1 Backstepping Method

In the field of nonlinear control and nonlinear adaptive control, a backstepping method was developed to construct an adaptive system using output errors, where the relative-order of the system is two or more. For such a backstepping method, the error system is

divided into subsystems in hierarchical structure, up to the number of the relative-order, where a virtual input is generated step by step for each subsystem whose relative-order is one.

5.2 Dynamical Model of X4-Flyer

The dynamical model of X4-flyer is described in the following matrix form:

$$M(\mathbf{q})\ddot{\mathbf{q}} + V_m(\mathbf{q}, \dot{\mathbf{q}})\dot{\mathbf{q}} + G(\mathbf{q}) = B(\mathbf{q})\boldsymbol{\tau} \quad (69)$$

where

$$M(\mathbf{q}) = \begin{bmatrix} m & 0 & 0 & 0 & 0 & 0 \\ 0 & m & 0 & 0 & 0 & 0 \\ 0 & 0 & m & 0 & 0 & 0 \\ 0 & 0 & 0 & I_x & 0 & 0 \\ 0 & 0 & 0 & 0 & I_y & 0 \\ 0 & 0 & 0 & 0 & 0 & I_z \end{bmatrix}$$

$$V_m(\mathbf{q}, \dot{\mathbf{q}}) = \begin{bmatrix} 0 & 0 & 0 & 0 & 0 \\ 0 & 0 & 0 & 0 & 0 \\ 0 & 0 & 0 & 0 & 0 \\ 0 & 0 & 0 & J_r\Omega + I_z\dot{\psi} & -I_y\dot{\theta} \\ 0 & 0 & -J_r\Omega - I_z\dot{\psi} & 0 & I_x\dot{\phi} \\ 0 & 0 & 0 & I_y\dot{\theta} & -I_x\dot{\phi} & 0 \end{bmatrix}$$

$$G(\mathbf{q}) = \begin{bmatrix} 0 \\ 0 \\ -mg \\ 0 \\ 0 \\ 0 \end{bmatrix}$$

$$B(\mathbf{q}) = \begin{bmatrix} -(c\phi s\theta c\psi + s\phi s\psi) & 0 & 0 & 0 \\ -(c\phi s\theta s\psi - s\phi c\psi) & 0 & 0 & 0 \\ -c\phi c\theta & 0 & 0 & 0 \\ 0 & l & 0 & 0 \\ 0 & 0 & l & 0 \\ 0 & 0 & 0 & 1 \end{bmatrix}$$

5.3 Degenerate State-Space Model

To generate a degenerate state-space model, the following kinematic and dynamical models are combined:

$$\dot{\mathbf{q}} = S(\mathbf{q})\mathbf{v} \quad (70)$$

$$M(\mathbf{q})\ddot{\mathbf{q}} + V_m(\mathbf{q}, \dot{\mathbf{q}})\dot{\mathbf{q}} + G(\mathbf{q}) = B(\mathbf{q})\boldsymbol{\tau} \quad (71)$$

To do so, differentiating (70) with respect to time gives

$$\ddot{\mathbf{q}} = \dot{S}(\mathbf{q})\mathbf{v} + S(\mathbf{q})\dot{\mathbf{v}} \quad (72)$$

Substituting equations (70) and (72) into (71) and premultiplying both sides by $S^T(\mathbf{q})$ yields

$$\begin{aligned} & S^T(\mathbf{q}) \left[M(\mathbf{q}) \left\{ \dot{S}(\mathbf{q})\mathbf{v} + S(\mathbf{q})\dot{\mathbf{v}} \right\} \right. \\ & \left. + V_m(\mathbf{q}, \dot{\mathbf{q}})S(\mathbf{q})\mathbf{v} \right] + S^T(\mathbf{q})G(\mathbf{q}) = S^T(\mathbf{q})B(\mathbf{q})\boldsymbol{\tau} \end{aligned} \quad (73)$$

Here, when defining

$$\bar{M}(\mathbf{q}) = S^T(\mathbf{q})M(\mathbf{q})S(\mathbf{q}) \quad (74)$$

$$\bar{V}_m(\mathbf{q}, \dot{\mathbf{q}}) = S^T \left(M(\mathbf{q})\dot{S}(\mathbf{q}) + V_m(\mathbf{q}, \dot{\mathbf{q}})S(\mathbf{q}) \right) \quad (75)$$

$$\bar{G}(\mathbf{q}) = S^T(\mathbf{q})G(\mathbf{q}) \quad (76)$$

$$\bar{B}(\mathbf{q}) = S^T(\mathbf{q})B(\mathbf{q}) \quad (77)$$

the degenerate state-space model can be described in

$$\dot{\mathbf{q}} = S(\mathbf{q})\mathbf{v} \quad (78)$$

$$\bar{M}(\mathbf{q})\dot{\mathbf{v}} + \bar{V}_m(\mathbf{q}, \dot{\mathbf{q}})\mathbf{v} + \bar{G}(\mathbf{q}) = \bar{B}(\mathbf{q})\boldsymbol{\tau} \quad (79)$$

where

$$\begin{aligned} \bar{M}(\mathbf{q}) &= \begin{bmatrix} m & 0 & 0 & 0 \\ 0 & I_x & 0 & 0 \\ 0 & 0 & I_y & 0 \\ 0 & 0 & 0 & I_z \end{bmatrix} \\ \bar{V}_m(\mathbf{q}) &= \begin{bmatrix} 0 & 0 & 0 & 0 \\ 0 & 0 & J_r\Omega + I_z\dot{\psi} & -I_y\dot{\theta} \\ 0 & -J_r\Omega - I_z\dot{\psi} & 0 & I_x\dot{\phi} \\ 0 & I_y\dot{\theta} & -I_x\dot{\phi} & 0 \end{bmatrix} \\ \bar{G}(\mathbf{q}) &= \begin{bmatrix} -mg \cos \phi \cos \theta \\ 0 \\ 0 \\ 0 \end{bmatrix}, \bar{B}(\mathbf{q}) = \begin{bmatrix} -1 & 0 & 0 & 0 \\ 0 & l & 0 & 0 \\ 0 & 0 & l & 0 \\ 0 & 0 & 0 & 1 \end{bmatrix} \end{aligned}$$

5.4 Partial Linearization of Degenerate State-Space Model

To partially linearize the dynamical model, the following nonlinear feedback

$$\boldsymbol{\tau} = \bar{B}^{-1}(\mathbf{q}) \left\{ \bar{M}(\mathbf{q})\mathbf{a} + \bar{V}_m(\mathbf{q}, \dot{\mathbf{q}})\mathbf{v} + \bar{G}(\mathbf{q}) \right\} \quad (80)$$

is applied to (79), where \mathbf{a} is an acceleration vector. From this nonlinear feedback, equations (78) and (79) can be reduced to

$$\dot{\mathbf{q}} = S(\mathbf{q})\mathbf{v} \quad (81)$$

$$\dot{\mathbf{v}} = \mathbf{a} \quad (82)$$

When defining the state vector as $\mathbf{x} = [\mathbf{q} \ \mathbf{v}]^T$ and the input vector as $\mathbf{u} = \mathbf{a}$, from equations (81) and (82), the state-space model in closed-loop system can be described by

$$\dot{\mathbf{x}} = f(\mathbf{x}) + g(\mathbf{x})\mathbf{u} = \begin{bmatrix} S(\mathbf{q})\mathbf{v} \\ 0 \end{bmatrix} + \begin{bmatrix} 0 \\ I \end{bmatrix} \mathbf{u} \quad (83)$$

where I is a unit matrix.

5.5 Application of Backstepping Method

In equation (81), if \mathbf{v} can be regarded as an input, then the system can be controlled by the discontinuous control of Astolfi. Here, assume that \mathbf{v} is a virtual input, its desired value \mathbf{v}_{des} is a stabilizing function, and $\mathbf{r}_b = \mathbf{v} - \mathbf{v}_{des}$ is an error variable.

Using the error variable in the equation (81) of kinematic model gives

$$\dot{\mathbf{q}} = S(\mathbf{q})(\mathbf{v}_{des} + \mathbf{r}_b) \quad (84)$$

When selecting the Lyapunov energy function such as

$$V = \frac{1}{2} \mathbf{r}_b^T \mathbf{r}_b \quad (85)$$

the time derivative of (85) becomes

$$\begin{aligned} \dot{V} &= \mathbf{r}_b^T \dot{\mathbf{r}}_b \\ &= \mathbf{r}_b^T (\dot{\mathbf{v}} - \dot{\mathbf{v}}_{des}) \\ &= \mathbf{r}_b^T \left(\mathbf{u} - \frac{\partial \mathbf{v}_{des}}{\partial \mathbf{q}} \frac{d\mathbf{q}}{dt} \right) \\ &= \mathbf{r}_b^T \left(\mathbf{u} - \frac{\partial \mathbf{v}_{des}}{\partial \mathbf{q}} S(\mathbf{q})(\mathbf{v}_{des} + \mathbf{r}_b) \right) \end{aligned} \quad (86)$$

Here, the control input \mathbf{u} is defined as

$$\mathbf{u} = -C\mathbf{r}_b + \frac{\partial \mathbf{v}_{des}}{\partial \mathbf{q}} S(\mathbf{q})(\mathbf{v}_{des} + \mathbf{r}_b) \quad (87)$$

where $C \in \Re^{4 \times 4}$ is a positive definite matrix. Therefore, equation (86) can be reduced to

$$\dot{V} = -\mathbf{r}_b^T C \mathbf{r}_b \leq 0 \quad (88)$$

so that the system can be asymptotically stable.

The dynamical control for a case when applying a backstepping method is shown in Fig. 2

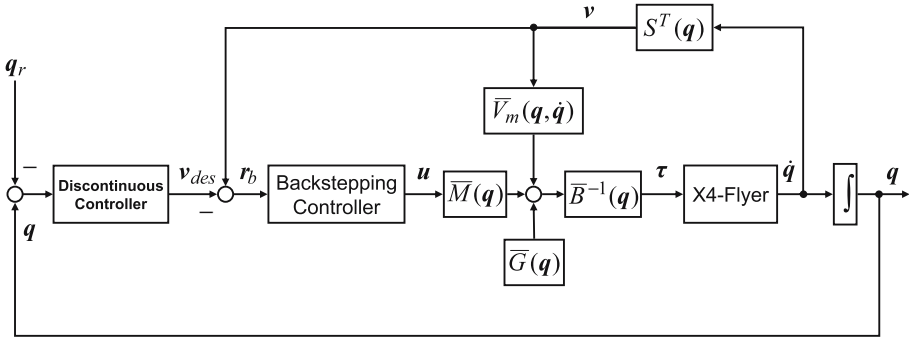


Fig. 2. Block diagram of dynamical control using a backstepping method

6 Simulations

6.1 Simulations Based on Kinematic Control

Here, the kinematic control of X-4 flyer is performed by using the discontinuous control law of Astolfi.

When $k = 1$ and the closed-loop poles are determined as $(-1, -2, -3, -4, -5)$ for equation (68), the feedback coefficient matrix is obtained by

$$F = \begin{bmatrix} 19 & -5 & 8 & 1 & 0 \\ 4 & -20 & 1 & 8 & 0 \\ 0 & 0 & 0 & 0 & 1 \end{bmatrix} \tag{89}$$

so that $[u_2 \ u_3 \ u_4]^T$ is represented by

$$\begin{bmatrix} u_2 \\ u_3 \\ u_4 \end{bmatrix} = - \begin{bmatrix} 19 & -5 & 8 & 1 & 0 \\ 4 & -20 & 1 & 8 & 0 \\ 0 & 0 & 0 & 0 & 1 \end{bmatrix} \begin{bmatrix} y_2 \\ y_3 \\ y_4 \\ y_5 \\ y_6 \end{bmatrix} \tag{90}$$

Fig. 3 and Fig. 4 show the simulation results of the case where the initial condition is set to $q_0 = [1.5 \ 1.5 \ -2.0 \ \pi/10 \ \pi/10 \ \pi/10]^T$ and the desired value is $q_r = [0 \ 0 \ 0 \ 0 \ 0 \ 0]^T$.

It is found from this result that the objective points of horizontal positions x and y are first controlled, the orientations of ϕ , θ , and ψ are secondly controlled, and the component of vertical position z is finally controlled. Additionally, Fig. 5 shows the control input to the corresponding case.

6.2 Simulations Based on Dynamical Control

Here, the simulation of X4-flyer is demonstrated by using the backstepping method. The physical parameters used in the simulation are shown in Table 1.

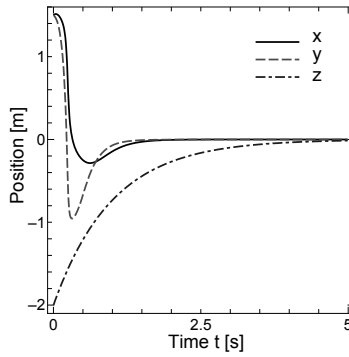


Fig. 3. Position control via discontinuous controller

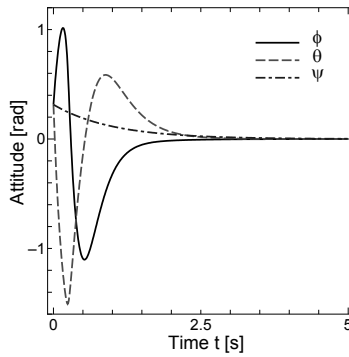


Fig. 4. Attitude control via discontinuous controller

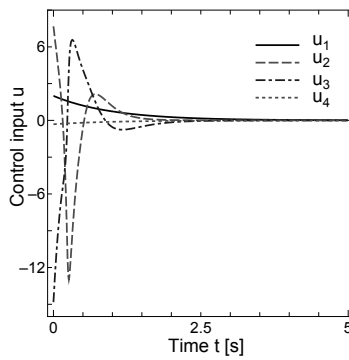
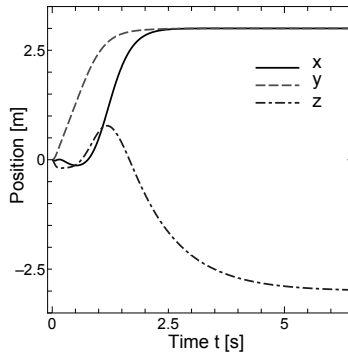
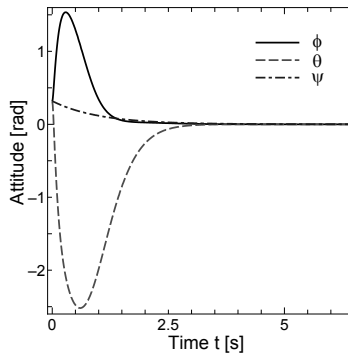


Fig. 5. Control inputs due to kinematic controller

Table 1. Model parameters for X4-flyer

Parameter	Description	Value	Units
g	Gravity	9.80665	m/s^2
m	Mass	0.468	kg
l	Distance	0.225	m
I_x	Roll Inertia	4.9×10^{-3}	$\text{kg} \cdot \text{m}^2$
I_y	Pitch Inertia	4.9×10^{-3}	$\text{kg} \cdot \text{m}^2$
I_z	Yaw Inertia	8.8×10^{-3}	$\text{kg} \cdot \text{m}^2$
J_r	Rotor Inertia	3.4×10^{-5}	$\text{kg} \cdot \text{m}^2$
b	Thrust Factor	2.9×10^{-5}	
d	Drag Factor	1.1×10^{-6}	

**Fig. 6.** Position control via dynamical controller**Fig. 7.** Attitude control via dynamical controller

The design parameters associated with the kinematic control part are assumed to be set as the same as those of the simulations based on kinematic control. The positive definite matrix in Lyapunov function is set to $C = \text{diag}(50, 50, 50, 50)$. In

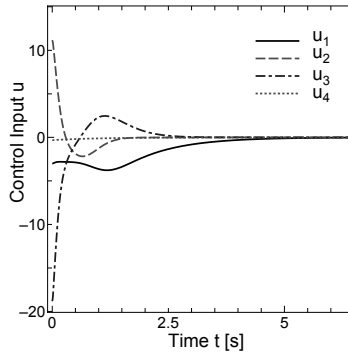


Fig. 8. Control inputs due to backstepping method

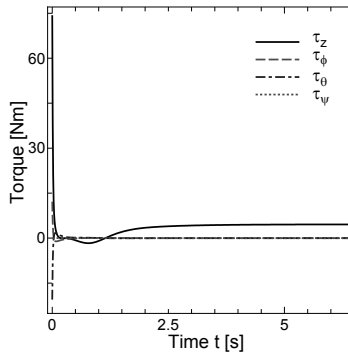


Fig. 9. Torque inputs due to total dynamical model

addition, assume that the initial value of generalized coordinates is set to $\mathbf{q}_0 = [0 \ 0 \ 0 \ \pi/10 \ \pi/10 \ \pi/10]^T$ and the desired value is $\mathbf{q}_r = [3 \ 3 \ -3 \ 0 \ 0 \ 0]^T$.

The simulation results are shown in Fig. 6 and Fig. 7. It is seen from this result that all the generalized coordinates are converged to the desired values smoothly. The corresponding inputs due to the kinematics are shown in Fig. 8 and the torque inputs due to the dynamics are depicted in Fig. 9.

7 Conclusion

For a VTOL-type aerial robot, called X4-flyer that is an underactuated system, a kinematic controller based on the Astolfi's discontinuous control has been derived and then it has been used to realize a dynamical-based controller according to the so-called backstepping method. Their validity was proved by several simulations.

The Astolfi's discontinuous control assured only a local stability if the chained form was not applied. From this fact, it may be possible to extend the present results so as to guarantee the system stability globally by applying the transformation of chained form.

References

- [1] Bouabdallah, S., Siegwart, R.: Backstepping and Sliding-mode Techniques Applied to an Indoor Micro Quadrotor. In: Proc. of IEEE Int. Conf. on Robotics and Automation, pp. 2259–2264 (2005)
- [2] Tayebi, A., McGilvray, S.: Attitude Stabilization of a VTOL Quadrotor Aircraft. *IEEE Trans. on Control Systems Technology* 14(3), 562–571 (2006)
- [3] Castillo, P., Dzul, A., Lonazo, R.: Real-time stabilization and tracking of a four-rotor mini rotorcraft. *IEEE Trans. on Control System Theology* 12(4), 510–516 (2004)
- [4] Watanabe, K., Izumi, K.: On the controllability of rotor-type flying robots: Why is the drive of four rotors effective for X4-flyer? In: Proc. of 7th SICE System Integration Division, Annual Conference (SI 2006), pp. 820–821 (2006)
- [5] Mita, T.: *Introduction to Nonlinear Control*, Shokodo, Tokyo (2000)
- [6] Astolfi, A.: Discontinuous control of nonholonomic systems. *System and Control Letters* 27(1), 37–45 (1996)

An Insect-Like Flapping-Wing Device Actuated by a Compressed Unimorph Piezoelectric Composite Actuator

Quoc Viet Nguyen¹, Hoon Cheol Park^{1,*}, Nam Seo Goo¹, and Doyoung Byun²

¹ Department of Advanced Technology Fusion
{qvnguyen, hcparck, nsgoo}@konkuk.ac.kr

² Department of Aerospace Information Engineering
Artificial Muscle Research Center & Smart Robot Center
Biomimetics and Intelligent Microsystem Laboratory
Konkuk University, Seoul 143-701, South Korea
Tel.: +82-2-450 3531; Fax: +82-2-444 6670
dybyun@konkuk.ac.kr

Abstract. In this work, we have introduced an insect-inspired flapper mimicking typical general characteristics of flying insects such as wing corrugation and wing clap-fling as well as wing rotation. The flapper was actuated by a unimorph piezoelectric composite actuator and a compressed one, respectively, for force generation comparison. Flapping tests were conducted both in the air and in a vacuum chamber to measure total vertical force and vertical inertia force, and then the vertical aerodynamic force was calculated by subtracting the vertical inertia force from the total vertical force. Further, the wing kinematics of the flapper was figured out by examining high-speed camera images taken from front and top views at the same time. The experimental results confirmed that the flapper could optimally operate at flapping frequency of 9 Hz and applied voltage of 300 voltage peak-to-peak (V_{pp}). In addition, the results also showed that we could increase the flapping angle 22 % and improve the average of vertical aerodynamic force 19 % by using the compressed piezoelectric composite actuator.

1 Introduction

Flying insects are the only group of invertebrates to have evolved powered flight over the past several million years of evolution. They have many fascinating features of flight and maneuverable abilities that are superior to any man-made flying vehicles in many ways: flying insects have capability of long-time hovering, quick maneuver, instantly dart sideways or backward, and effectively discontinuous changes of direction, etc. Typically, the flapping frequency of insects ranges from a few hertz to hundreds hertz; as flapping frequency increases their body weight increases and their wing area decreases. From the viewpoint of aerodynamics, flying insects can produce relatively high lift and thrust and fly in the low Reynolds number regime ranging from 5 to 10,000 [1], where effect of the viscous force is dominant. In engineering

* Corresponding author.

application, if these outstanding characteristics can be somehow mimicked and implemented in micro air vehicles (MAVs), the performance of the next generation of flying vehicles can be greatly innovated. Therefore, many researchers have involved in doing reverse-engineering [2] and revealing the secret of insect flight [3,4].

Due to the fast response as well as relative high actuation force, piezoelectric materials are widely used for insect-mimicking research. One of the most significant works of flying insect mimicking was made by Fearing et al. [5]. They introduced an micromechanical flying insect (MFI) which can produce flapping angle of 120° at flapping frequency of 150 Hz. Nguyen et al. [6] used a four-bar linkage to mimic thorax of a flying insect and developed a full three-dimensional prototype of flapping wing device actuated by a piezoceramic actuator named LIPCA (Light-weight piezoceramic composite actuator) [7]. This flapping-wing device was successfully demonstrated in terms of force and vortex generation. The most recent work is a 60 mg flapping-wing system introduced by Wood et al. [8]. They have successfully enabled their flapping-wing system to generate sufficient thrust to take off with an external power supply and constrained body degrees of freedom.

This work is an extended work of reference [6]. According to [6], the flapping device still needs improvement due to the limited actuation displacement and force of the LIPCA actuator. Recently, the LIPCA actuator under compression has been proven to show better performance than the original one without compression in terms of actuation displacement and force generation [9,10]. As expected, we achieve a better flapping performance of the flapper when we simply replace the actuation part in the flapping device with the compressed LIPCA.

For demonstration of the performance improvement in terms of aerodynamic force generation and flapping angle, two flappers actuated by the original LIPCA and the compressed LIPCA, respectively, have been experimentally examined. The flapping tests were conducted at various flapping frequencies varied from 6 Hz to 15 Hz to search for the best flapping frequency at which the maximum aerodynamic force is obtained. At the optimum flapping frequency of the flapper, the flapping tests were also undertaken both in the air and in a vacuum chamber to measure total force and inertia force. Then the aerodynamic force could be calculated by subtracting the inertia force from the total force. In addition, the kinematics of the flapping wing during upstroke and downstroke could be figured out by examining the high-speed camera images.

2 Description of the Flapper

2.1 Overview of Biomimetic Inspirations

Flying insects have utilized special techniques for flight, as the result, they can hover unlike most of birds. In this work, we have mimicked some important mechanisms of insect flight, which are wing rotation [11], wing corrugation [12], and wing clap-fling [13], and implemented these features into a flapping device. Figure 1 shows the full flapper after assembly.

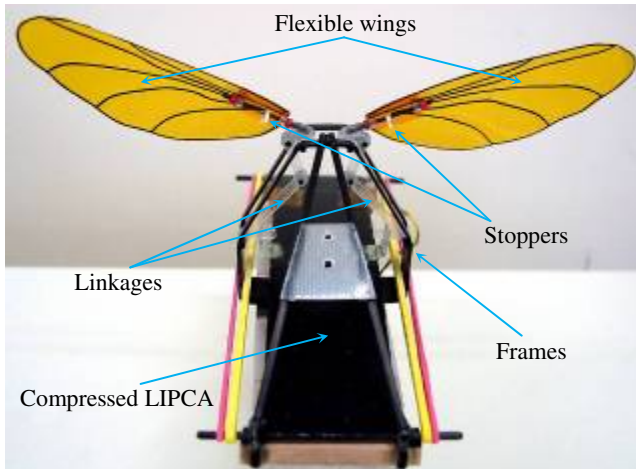


Fig. 1. Full flapping device

We used light-weight materials such as balsa wood, acrylic sheet, kapton film, carbon rod and carbon/epoxy composites to make all components of the flapper including four-bar linkage systems, hinges, wings, stoppers and supporting frame. The engineering data of the flapper are summarized in Table 1.

Table 1. Dimension and weight of the flapper

Dimension	Length (cm)	10.00
	Width (cm)	12.50
	Height (cm)	6.50
	Wing area (cm ²)	27.50
Weight (gram)	LIPCA	6.10
	Wings	0.15
	Structures	4.13
	Total weight	10.38

2.2 Actuator and Linkage System

Actuator is one of the most important parts as an artificial muscle in the flapper to create the wing stroke motion. For this purpose, we used both original LIPCA and compressed LIPCA to excite the flapper. To apply a compressive load to the LIPCA, at first, two carbon rods were glued to both ends of the original LIPCA. The compressive load was then applied to the LIPCA using rubber bands whose stiffness and length were selected so that a compressive load of approximately 9 N could be applied, which improved the actuation performance of the LIPCA as previously proven in reference [10].

The LIPCA shown in Figure 2 comprises of a piezoceramic wafer encapsulated by carbon/epoxy and glass/epoxy layers as shown in Figure 2(a). The whole stack then is cured in an autoclave with a suitable temperature profile to bond the layers together.

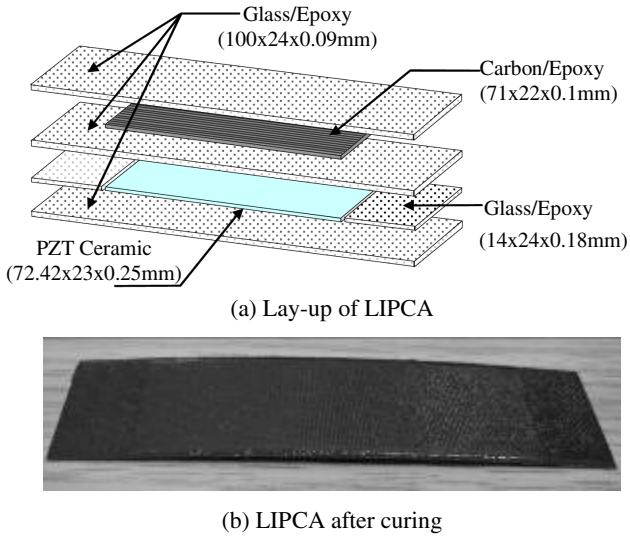


Fig. 2. LIPCA actuator

The slightly curved shape of the LIPCA after curing, Figure 2(b), is due to the mismatch between the coefficients of thermal expansion of the layers [7].

When the LIPCA is under electric field, it produces displacement in bending mode. However, it can produce only a few millimeters of displacement even when it is under critical electric field. Therefore, the induced bending displacement must be amplified and converted to flapping motion by a 4-bar linkage system [14] shown in Figure 3.

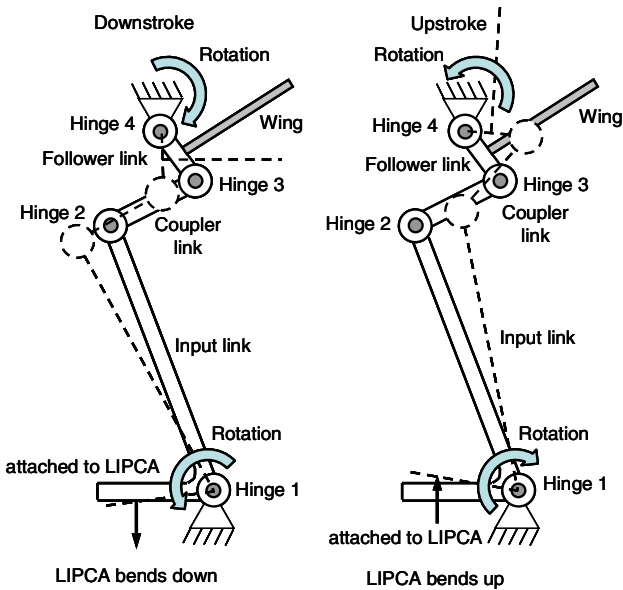


Fig. 3. Working principle of linkage system

2.3 Linkage System

The linkages play an important role not only to amplify the limited bending actuation displacement of the LIPCA to large flapping angle, but also to transmit the actuation force from the LIPCA to the wings and vice versa. They should be light weight and stiff enough to sustain the periodic forces caused by the reciprocating motion of the wings and the LIPCA during operation. The acrylic sheet with 1 mm thickness was suitably used for machining the linkages by a laser cutting machine (LaserPro Mercury, L-40V, GCC American Inc., USA). This is to make the flapper as precisely and symmetrically as possible to avoid undesirable vibration during flapping test.

Figure 3 describes the right part of the 4-bar linkages in the flapper when the flapper is viewed from front (Figure 1). Hinge 1 and hinge 4 are fixed hinges mounted on the supporting frame, and hinge 2 and hinge 3 are freely moving hinges. The input link directly receives the motion from the LIPCA and transfers the motion to the follower link through the coupler link.

Under the variation of the applied voltage, the LIPCA bends up and down, and creates upstroke and downstroke of wings, respectively (Figure 3). In this flapper, the LIPCA was installed in a simply supported configuration to provide a larger actuation displacement at higher flapping frequency.

2.4 Artificial Wing

In flapping flight, wings not only change their movement direction and their angle of attack relative to the airflow, but they undergo deformation, which may actually be necessary for the generation of sufficient aerodynamic force. Most insect wings are flexible and corrugated, which consist of membrane stiffened by veins. The veins are extended from the wing root to the wing tip and also along the chord of the wing resulting in a zigzag cross section of the wing. The corrugation greatly increased both the stiffness and strength of insect wings [12]. Newman and Wootton [15] have shown that in such corrugations the membrane itself may have a structural role, further stiffening the wing by means of a 'stressed skin' effect. Rees [16] and Tamai et al. [17] further demonstrated that a corrugated wing made a good aerofoil for force generation at low Reynolds numbers.

We fabricated the wings by using carbon/epoxy fibers and kapton film with 30 micrometer in thickness. The wing shape and vein structure was taken from wings of horse botfly (*Gasterophilus*) shown in Figure 4(a). The carbon/epoxy fibers were laid out on the kapton film by following the wing vein structure. The whole stack of artificial wings were then vacuum bagged and cured in an autoclave at high temperature (177 °C) at where the epoxy resin melts and glue the carbon fibers to kapton film. After cooling down to the room temperature (25 °C), the epoxy resin helps the carbon fibers adhere to the kapton film, and the artificial wing is slightly deformed due to thermal deformation as shown in Figure 4(b). It should be noticed that only wing shape and main wing structure were mimicked and wing flexibility is not mimicked and investigated at this stage.

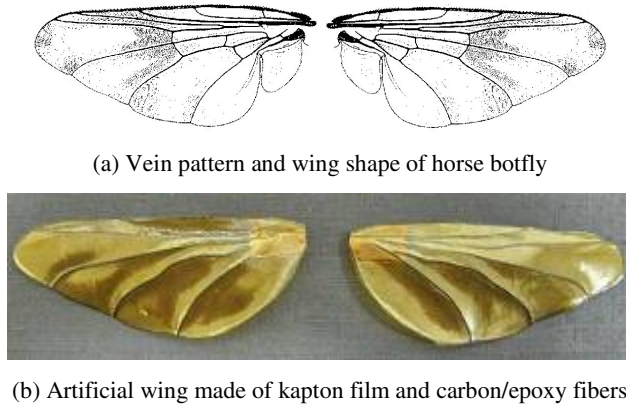


Fig. 4. Vein pattern and shape of horse botfly’s wing and artificial wing

2.5 Passive Wing Rotation

Insects fly by actively rotating their wings during flapping to adjust the angle of attack in such a way the wings can capture the vortex sheet and produce additional lift and thrust even during upstroke. The wing rotation is supposed to create additional circulation causing rotational forces that add to or subtract from the force produced by translation of the wing depending on the direction of rotation [18].

Mimicking the active wing rotation of insect requires a lot of efforts and additional complex mechanism resulting in weight increase and flapping frequency reduction. Instead of that, we mimicked the wing rotation by using a passive wing rotation mechanism induced by resultant aerodynamic forces shown in Figure 5. We located the rotational axis at the leading edge of the wing; the rotational axis is as far as possible from the axis of aerodynamic center of the wing. During flapping, the wing flaps up and down along the flapping path and creates the aerodynamic forces on the

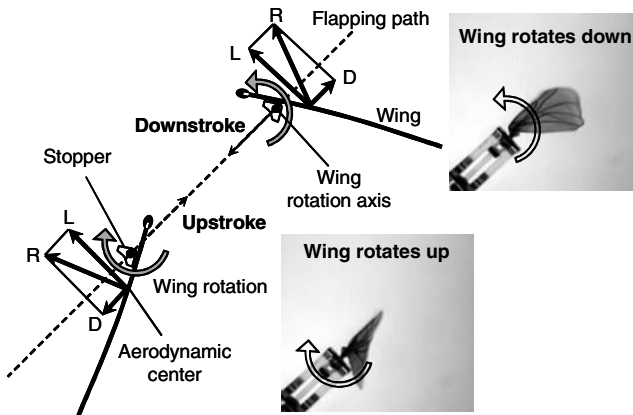
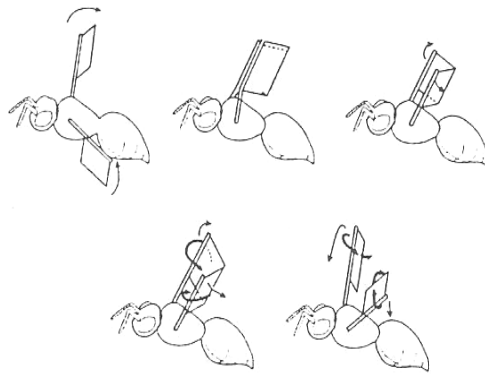


Fig. 5. Working principle of passive wing rotation (L = Lift, D = Drag, R = Resultant force)

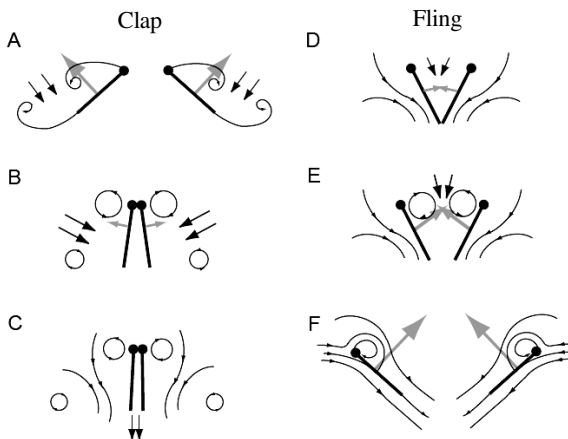
wing. The resulting aerodynamic force at the aerodynamic center makes the wing passively rotate about the rotational axis in clockwise direction for upstroke and counter-clockwise direction for downstroke. The rotation wing angle was limited by the shape of the stopper installed at the rotational axis of the wing. The wing rotation angle can be easily adjusted by changing the shape of the stopper.

2.6 Wing Clap-Fling Mechanism

Clap-fling mechanism proposed by Weis-Fogh [13] is a method of insect flight. In this process, the wings clap together above the insect’s body and then fling apart. As the wings fling open, the air gets sucked into the gap between the wings and creates a vortex over each wing. This bound vortex then moves across the wing and, in the clap, acts as the starting vortex for the other wing. In most cases, this method increases circulation or lift to the extent of being higher than the typical leading edge vortex method. The process of the clap and fling is graphically described in Figure 6(a).



(a) Sequence of clap and fling [13]



(b) Stream line created by clap and fling [18]

Fig. 6. Clap-fling mechanism

Figure 6(b) shows stream line of air flow and aerodynamic forces created by clap and fling, which is taken from reference [18]. More details on the clap and fling mechanism can be found in [18, 19, 20].

In this present flapper, the wing clap-fling mechanism of the flapper could be created at the end of upstroke by adjusting the applied voltage and the connecting point between the actuator and the input link, shown in Figure 2. The flapping angle was calculated by taking angle difference between the beginning of downstroke and the end of downstroke.

Figure 7 shows flapping angles captured by a high-speed camera (Photron FASTCAM APX-120K, Photron, Japan) at 2000 frames per second. The flapper was operated by 300 V_{pp} with square wave input at frequency of 9 Hz. The flapping angle of the wing was about 110° for the flapper actuated by compressed LIPCA and 90° for the flapper actuated by original LIPCA. Thus, the use of the compressed LIPCA resulted in about 22 % increase in the flapping angle. It can be noticed that the wing is almost vertically placed at the end of upstroke, which will create clap of the two wings.

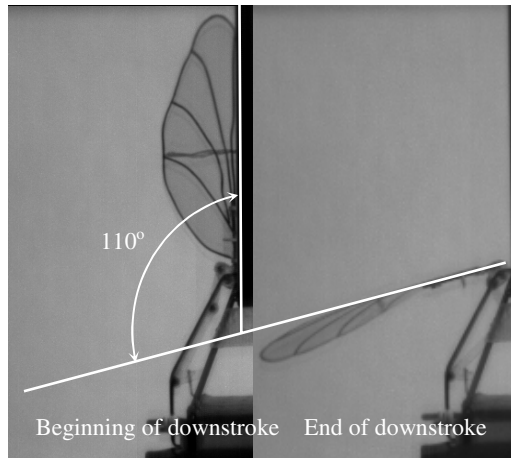


Fig. 7. Flapping angle with clap captured by a high-speed camera for the flapper actuated by the compressed LIPCA

3 Experimental Test

3.1 Experimental Setup

The apparatuses for the flapping test are composed of a high voltage power supply (AMT-1.5B40, Matsusada Precision Inc., Japan), a function generator (Agilent 33120A, Agilent Technologies, USA), an oscilloscope (Tektronix TDS 2024, Tektronix Inc., USA), a high sensitive multi-axis force/torque load cell (Nano17, resonant frequency of 7.2 kHz, resolution of 1/1280 N, ATI Industrial Automation, USA) with interface power supply and DAQ card, and a PC as shown in Figure 8.

The high voltage amplifier provides driving voltage of 300 V_{pp} in a square wave form generated by the function generator to the compressed LIPCA that activates the

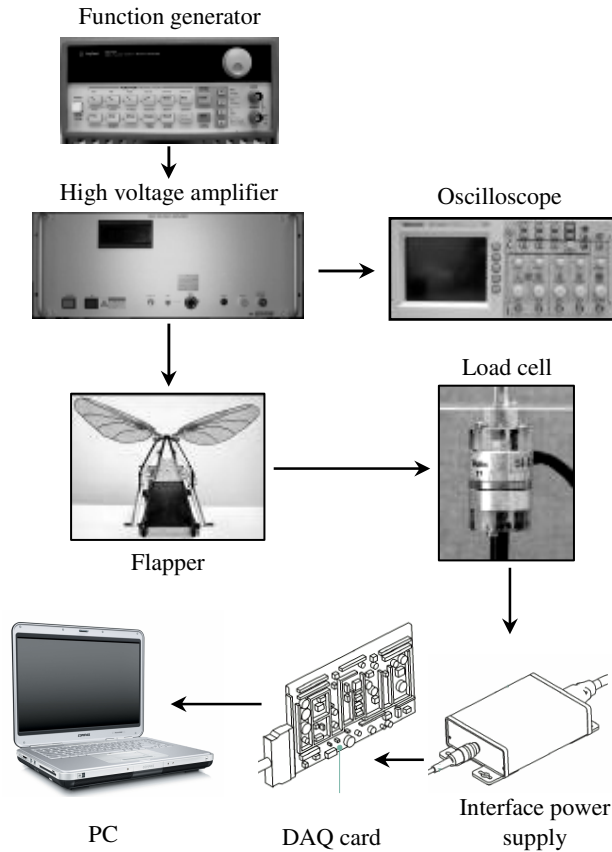


Fig. 8. Experimental set-up for force measurement

flapper to make the wing stroke motion. Frequency of driving voltage measured by the oscilloscope can be varied by the function generator, so that flapping test can be easily conducted at different flapping frequency for force measurement. Signals from the load cell were acquired by the DAQ card and stored in a computer for data analysis.

3.2 Force Measurement in the Air

For the force measurement, the load cell was firmly mounted on an acrylic stand as shown in Figure 9. The flapper was connected to the load cell by a carbon rod, and the signal wires of the load cell were connected to the data acquisition system. One end of the carbon rod was fixed at the mounting adapter of the load cell; the other end was tightly attached to the flapper tilted about 40° with respect to the horizontal line, which mimics the posture of insects that tilt their flapping plane about 30° to 60° during their flight [21]. The output signals, which resulted from the produced force, were acquired from the load cell using the DAQ card and then directly inverted to the force data by using an integrated software installed in the computer.

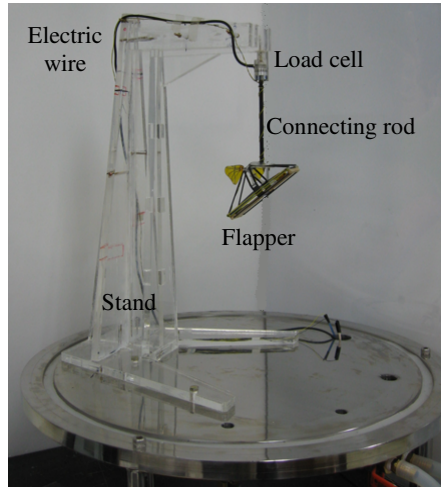


Fig. 9. Force measurement in the air



Fig. 10. Force measurement in the vacuum

In this test, the LIPCA was driven at voltage of $300 V_{pp}$ and various frequencies from 6 Hz to 15 Hz. The total vertical forces generated by the flapper in the air were measured for the various frequencies to find the optimal flapping frequency at which the flapper can generate maximum vertical force. Further, the effect of the compressed LIPCA has been examined by comparing the vertical force generated by the two flappers actuated by the original LIPCA and compressed LIPCA.

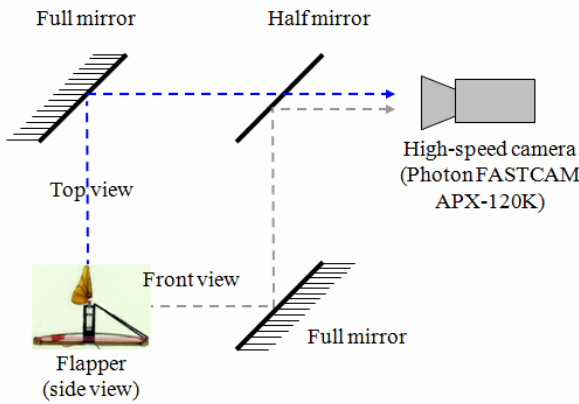
3.3 Force Measurement in the Vacuum

Inertia forces induced by vibration and wing stroke motion are the main source affecting the total forces measured in the air, which include both aerodynamic force and inertia force. In order to separating them, flapping tests in the vacuum must be conducted. Because there is almost no air in the vacuum, the measured forces are only inertia forces.

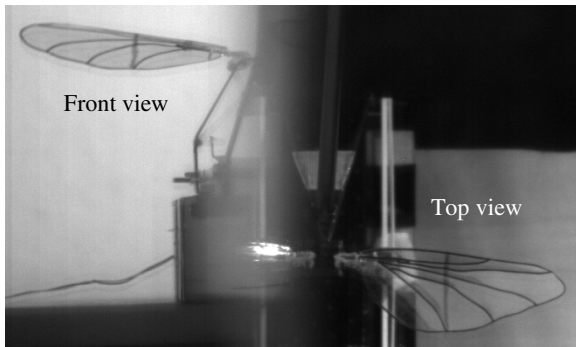
The flapping tests with the same configuration as flapping tests in the air were conducted in a vacuum chamber, as shown in Figure 10, at vacuum level of 95% to measure the inertia force induced by flapping wing motion of the flapper. This inertia force was then subtracted from the total vertical force measured in the air to get the vertical aerodynamic force.

3.4 Wing Kinematics Capture

To capture the passive wing rotation angle and wing flapping angle at the same time, we used a high-speed camera (Photon FASTCAM APX-120K) and a mirror system arranged as in Figure 11(a). Motions of the wing in the front view and top view are



(a) Set-up for capturing wing kinematics



(b) Image captured by a high speed camera and a mirror system

Fig. 11. Set-up for wing kinematics capture

synchronized by the mirror system and captured by the high-speed camera operated at 2000 frames per second. Figure 11(b) shows one of the images taken by the high-speed camera. The wing kinematics was determined in terms of the wing rotation and wing flapping angles with respect to the reference axis as shown in Figure 12. In this flapper, the limits of nose-down rotation angle and nose-up rotation angle are 10° and 60° , respectively.

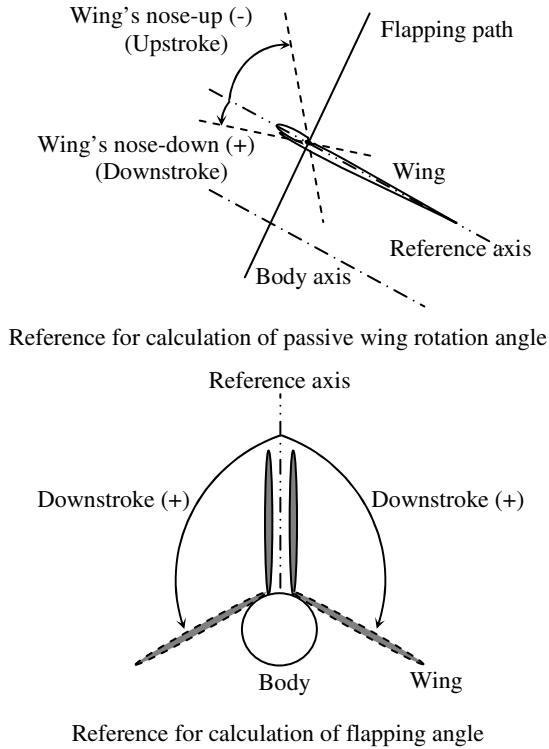


Fig. 12. Reference for calculation of rotation angle and flapping angle

4 Result and Discussion

4.1 The Optimum Flapping Frequency

By prescribing voltage of $300 V_{pp}$ to the flapper and varying flapping frequency over the range from 6 Hz to 15 Hz with increment of 1Hz, the measured data enable us to determine the optimum flapping frequency, at which the largest average vertical force is generated. Figure 13 shows the vertical forces measured at the various flapping frequencies.

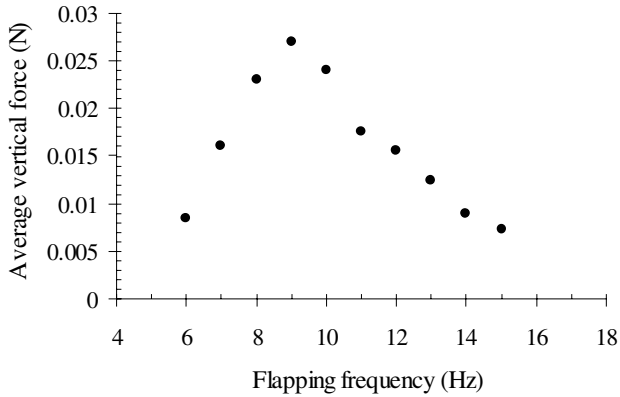


Fig. 13. Measured vertical force at various flapping frequencies

The vertical force reached the maximum value at around flapping frequency of 9 Hz that can be named the optimum flapping frequency of the flapping system. Obviously, flapping angle keeps changing as flapping frequency was varied. The maximum flapping angle is obtained when the flapper is operated at around 9 Hz, where the LIPCA produces maximum actuation displacement. For lower flapping frequency than 9 Hz, the vertical force was smaller due to the low flapping-wing speed. For higher flapping frequency than 9 Hz, the vertical force decreased as the flapping frequency increased, because the time spent for the passive wing rotation during upstroke and downstroke was not enough to fully complete the wing rotation, i.e., the wing's nose-down and wing's nose-up angles can not reach 10° and 60° , respectively. Thus, the flapping system was operated at 9 Hz for all flapping tests in the vacuum chamber to measure inertia forces. The same phenomenon was observed for the flapper actuated by the original LIPCA [6].

4.2 Aerodynamic Force

At the best flapping frequency of 9 Hz and prescribed voltage of $300 V_{pp}$, we measured the vertical forces generated by two flappers actuated by the compressed LIPCA and the original LIPCA both in the air and in the vacuum chamber, and then we plotted the data in Figure 14 and Figure 15, respectively. For a clear investigation, the graphs were plotted within three periods. The aerodynamic force was calculated by subtracting the inertia force from the total force.

The average vertical aerodynamic force of the flapper actuated by the compressed LIPCA was 0.025 N, while that of the flapper actuated by the original LIPCA was 0.021 N (19% increase). These average values were calculated and represented by the horizontal dash lines as shown in Figures 14-15. The average vertical inertia forces for both cases were relatively small. The inertia force did not significantly contribute to the average value of total force, but it is vital to determine the aerodynamic force profile.

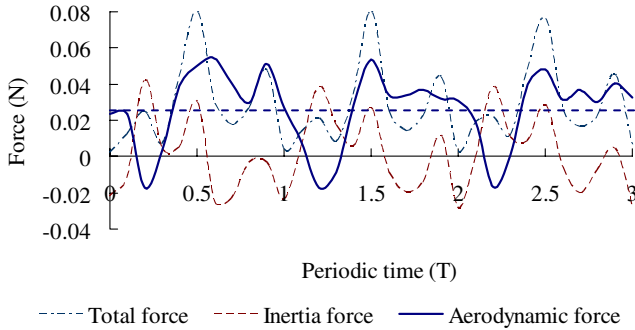


Fig. 14. Vertical force at 300 V_{pp} and 9 Hz with square wave input for the flapper actuated by the compressed LIPCA

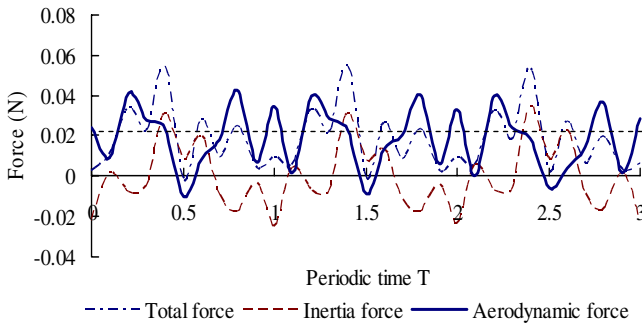


Fig. 15. Vertical force at 300 V_{pp} and 9 Hz with square wave input for the flapper actuated by the original LIPCA

Table 2 summarizes the experimental results obtained by the flapping tests in the air and in the vacuum chamber. The average aerodynamic force could be improved 19 % when the flapper was actuated by the compressed LIPCA. The improvement is mainly due to the improved actuation displacement and force of the compressed LIPCA. The improved actuator performance contributed to 22 % larger flapping angle and subsequently to 19% increase in the average aerodynamic force. The difference in the two inertia force profiles mainly came from different actuation mechanisms of the two flappers.

Table 2. Experimental results

Flapper	Average vertical force		
	Total force	Inertia force	Aerodynamic force
Original flapper	0.022 N	0.001 N	0.021 N
New flapper	0.027 N	0.002 N	0.025 N

4.3 Wing Kinematics

By examining the high speed camera images of front and top view at the same time, the flapping angle and the passive wing rotation angle were figured out and plotted in Figure 16. Due to the passive wing rotation produced by the aerodynamic force, at the beginning of downstroke (or at the end of upstroke) the wing's nose is up at 60° , and then it starts to flap down and rotate about the rotational axis in the counter-clockwise direction and reaches a full nose-down rotation angle of 10° at $0.125 T$. After that, the wing rotation angle of 10° is maintained until the end of downstroke at $0.53 T$. For the upstroke, as the wing starts to flap up, it also begins rotating about the rotational axis in the clockwise direction and reaches a full rotation angle of 60° at $0.708 T$ (within $0.178 T$). Afterward the rotation angle is kept constant to the end of upstroke (Figure 16). The same sequence of wing rotation is repeated for the next cycles. During one cycle (T), the duration of the downstroke was about $0.53 T$, which is slightly longer than the duration of the upstroke ($0.47 T$). The time ratio between downstroke and upstroke of the flapper is 1.13. This kinematics exactly reflects the design we made for the passive wing rotation, and it can be used for a computational fluid dynamics simulation [22].

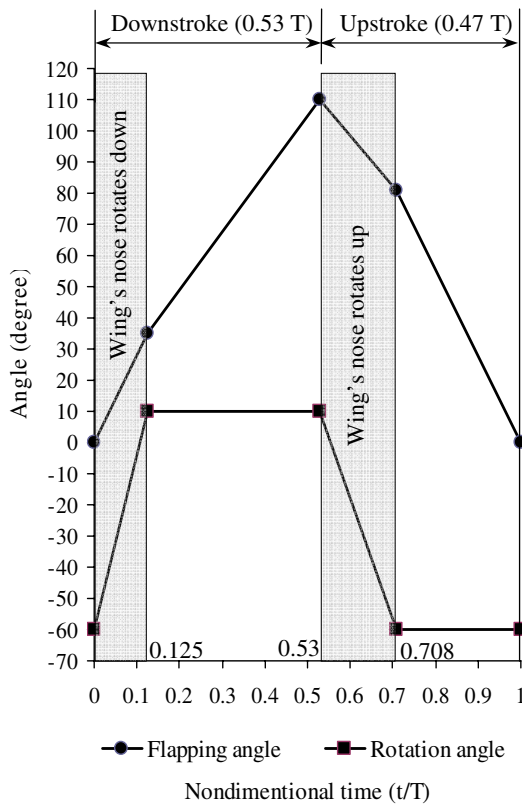


Fig. 16. Flapping angle and passive wing rotation angle of the flapper

5 Conclusions

In this paper, we have experimentally investigated characteristics of a flapping-wing device actuated by both compressed and uncompressed unimorph piezoceramic actuators in terms of wing kinematics and vertical aerodynamic force generation. The flapper can passively create wing rotation as well as flapping motion mimicking flapping motion of insects. From the experimental examination, we could conclude that the flapper actuated by the compressed LIPCA can generate a larger aerodynamic force than the flapper actuated by the original LIPCA. The use of the compressed LIPCA contributed to 22% larger flapping angle, and subsequently, to 19% increase in the average vertical aerodynamic force. However, it could not increase the flapping frequency of the flapper: it is suggested that the geometry of the linkages should be modified to increase the optimum flapping frequency. Flapping tests in the vacuum confirmed that the average inertia force is relatively small compared to the average total force. Further computational fluid dynamics simulations and smoke visualization are required to investigate the effect of the wing flexibility and wing clap on enhancement of the lift.

Acknowledgment

This research was supported by Korea Research Foundation Grant (KRF-2006-005-J03301) and Korea Science and Engineering Foundation Grant (National Research Laboratory Program, R0A-2007-000-20012-0). Authors appreciate the financial support.

References

- [1] Ellington, C.P.: The novel aerodynamics of insect flight: Applications to microair vehicles. *J. Exp. Biol.* 202, 3439–3448 (1999)
- [2] Bandyopadhyay, P.R.: Trends in Biorobotic Autonomous Undersea Vehicles. *IEEE J. Oceanic Eng.* 30, 109–139 (2005)
- [3] Alexander, D.E.: *Nature's flyers*, Baltimore. The Jonh Hopkins University Press (2002)
- [4] van den Berg, C., Ellington, C.P.: The three dimensional leading-edge vortex of a 'hovering' model hawkmoth. *Phil. Trans. R. Soc. Lond. B* 352, 329–340 (1997)
- [5] Fearing, R.S., et al.: A micromechanical flying insect thorax. In: *Neuro-technology in Biomimetic Robot*. MIT Press, Cambridge (2002)
- [6] Nguyen, Q.V., Park, H.C., Syaifuddin, M., Byun, D.Y., Goo, N.S.: Characteristics of an insect-mimicking flapping system actuated by a unimorph piezoceramic actuator. *J. Intell. Mater. Syst. Struct.* (online on February 2008)
- [7] Yoon, K.J., Park, K.H., Lee, S.K., Goo, N.S., Park, H.C.: Analytical design Model for piezo-composite unimorph actuator and its verification using LIPCA's. *Smart Mater. Struct.* 13, 459–467 (2004)
- [8] Wood, R.J.: Lifftoff of a 60mg flapping-wing MAV. In: *Proc. of IEEE/RSJ International Conference on Intelligent Robots and Systems*, San Diego, CA, USA (November 2007)

- [9] Mossi, K., Smith, B., Mouhli, M., Bryant, R.G.: Characteristics of carbon reinforced piezoelectric composite. In: Proc. of International Conference on Emerging System Technology, Konkuk University, Seoul (2005)
- [10] Nguyen, Q.V., Park, H.C., Goo, N.S.: Performance analysis of a piezoceramic unimorph actuator under compressive mechanical load and electric field. *J. Korean Phys. Soc.* 51, S56–S61 (2007)
- [11] Dickinson, M.H., Lehmann, F.O., Sane, S.P.: Wing rotation and the aerodynamics basis of insect flight. *Science* 284, 1954–1960 (1999)
- [12] Rees, C.J.C.: Form and function in corrugated insect wings. *Nature* 256, 200–203 (1975)
- [13] Weis-Fogh, T.: Unusual mechanisms for the generation of lift in flying animals. *Scientific America* 233, 80–87 (1975)
- [14] Syaifuddin, M., Park, H.C., Yoon, K.J., Goo, N.S.: Design and evaluation of LIPCA-actuated flapping device. *Smart Mater. Struct.* 15, 1225–1230 (2006)
- [15] Newman, D.J.S., Wootton, R.J.: An approach to the mechanics of pleating in dragonfly wings. *J. Exp. Biol.* 126(1), 361–372 (1986)
- [16] Rees, C.J.C.: Aerodynamic properties of an insect wing section and a smooth airfoil compared. *Nature* 258, 141–142 (1975)
- [17] Tamai, M., Wang, Z., Rajagopalan, G., Hu, H., He, G.: Aerodynamic Performance of a Corrugated Dragonfly Airfoil Compared with Smooth Airfoils at Low Reynolds Numbers. In: 45th AIAA Aerospace Sciences Meeting and Exhibit, Reno, Nevada (January 2007)
- [18] Sane, S.P.: The aerodynamics of insect flight. *The J. of Exp. Bio.* 206, 4191–4208 (2003)
- [19] Lighthill, M.: On Weis-Fogh mechanism of lift generation. *J. Fluid Mech.* 60, 1–17 (1973)
- [20] Maxworthy, T.: Experiments on the Weis-Fogh mechanism of lift generation by insects in hovering flight. Part 1. Dynamics of the ‘fling’. *J. Fluid Mech.* 93, 47–63 (1979)
- [21] Grodnitsky, D.L.: Form and Function of Insect Wings. The John Hopkins University Press, Baltimore (1999)
- [22] Nguyen, Q.V., Truong, Q.T., Park, H.C., Goo, N.S., Byun, D.Y.: A study on the flapping performance of an insect-inspired flapper actuated by a compressed unimorph piezoelectric composite actuator. *IEEE Trans. on Automation Science and Engineering* (submitted)

Designing Cicada-Mimetic Flapping Wing with Composite Wing Structure and Application to Flapping MAV

Joon Hyuk Park and Kwang-Joon Yoon

Department of Aerospace Information System
Artificial Muscle Research Center,
Smart Robot Center in Institute of Intelligent Vehicle & System Tech Engineering
Konkuk University
#1 Hwayang-dong Kwangjin-gu Seoul, Korea
Joonpark1025@hanmail.net, kjyoon@konkuk.ac.kr

Abstract. This paper represents of the successful development on bio-mimetic wing design inspired from cicada. Since we have already developed the flapping MAVs with different scale having different performance, the attempts to design the wing structure similar to the insect wing, which expected to bring improvement of performance, were made. In this research, the cicada was chosen for the insect model and 36cm flapping MAV selected for wing application. The carbon fiber prepreg composite material was used for wing structure. The aerodynamic force measurement, wing kinematics observation and wind tunnel test were conducted to evaluate the performance between normal wing and bio-mimetic wing. It was proved that the bio-mimetic wing is superior to the normal wing in terms of not only force generation but also the aspect of appropriate wing kinematics. The force measurement of bio-mimetic wing in various wind flow velocity and operating power was also resulted to have better flight performance in lift and thrust coefficient comparing to the normal wing.

1 Introduction

Flapping flight of the nature's flyer, especially insect has fascinated humans for many centuries, since its flapping technique remains unsurpassed in many aspects of aerodynamic performance and maneuverability. Experimental studies on the configuration with more decreased sizes of flapping MAV's are being conducted mainly by some enterprises and colleges. We also have been researching on flapping MAVs from 2004 and successfully performed the mission on two times of IMAVC (International Micro Air Vehicle Competition : 2005,2006) and we have succeeded in flying 15cm flapping MAV composed of electric pager motor weighs less than 10gram in MAV07 conference held in France Sep, 2007.

Bio-mimetic flapping vehicle should follow the flight principles of insect wing and should perform very complicated flapping mechanisms in order to have more capability and maneuverability such as taking-off backwards, flying sideways, and landing upside-down [1] as insects. However, there are many difficulties to build an efficient flapping mechanism as well as fabricating bio-mimetic wings due to the limited materials and actuator realization [2]. Recently, there has been tremendous

progress in the observation of insect’s flapping flight, since there is possibility for adopting its excellent technique for micro aerial vehicle (MAV) that can fly by flapping wing [3-4]. and sustained flight. Since our flapping system is unable to perform the wing rotation actuation as seen in insect, so the deformation of wing during flapping is affecting to the performance mostly. It is, therefore, very important to concentrate and study on the efficient wing design which could perform proper passive deformation. By designing, fabricating and testing on bio-mimetic wing expected to bring the most efficient flapping wing design for our flapping system.

2 Characteristics of Low-Reynolds Number Aerodynamics Applied to Flapping MAV

As many researches and studies about flight aspects of low-Reynolds regime especially the flapping flight area, there are many remarkable results that could prove the advantages of unsteady aerodynamics [5-6]. It has shown that flapping wings benefit from unsteady aerodynamics at insect scale to generate lift than steady-state aerodynamics as well as high maneuverability and agility as seen in insects and hummingbirds [7]. Biological flight systems, known as the most efficient flight mechanism, are also superior to engineering flight systems at all small scales for their better power supply, better stability and control system, fly in atmospheric dynamics and low Reynolds number aerodynamics [5].

Refers to the well-known features of natural flyers, small insects has a wing chord Reynolds number between 100 to below 1000 which uses unsteady effects to stay aloft with corrugated, curved plates wings. For the large insects to small bird, it has wing chord Reynolds number between 1000 to 15000 which uses conventional airfoil circulation and sensitive to transition and separation [8].

As the size of vehicle decreases with having higher wing beat frequency, features of unsteady flight regime affects more critically. In order to fulfill those characteristics, we focused on analyzing flight mechanisms including wing structures of insect and adopt those characteristics to our flapping vehicle. Moreover, we intended to improve our flapping vehicles by comparing flight mechanism of insect and tried to find the differences in order to specify the necessities in improving vehicle’s performance which would be the final purpose of our research.

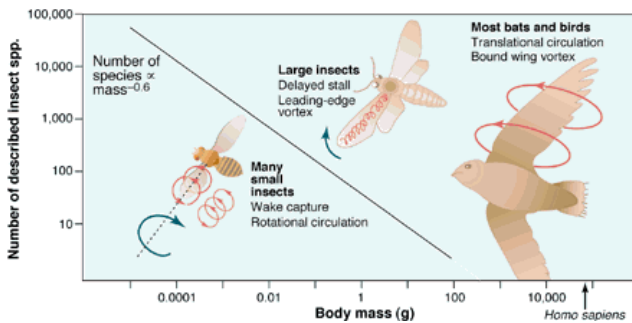


Fig. 1. Flight mechanisms of natural flyers[8]




Most small insects 100<Re<1000	Large insects to small birds 1000<Re<15000	Birds 15000< Re
		
-Delayed stall -Wake capture -Rotational circulation	-Dynamic stall -Delayed stall -Wake capture	-Bound circulation -Quasi-Steady mechanisms

Fig. 2. Comparison of flight characteristics over different Reynolds number

As shown in Figure 2, flight mechanisms and aerodynamic characteristics vary by the different Reynolds number regime. We have studied on recent papers about insect and flapping MAV especially papers on insect flight mechanism and development of flapping MAVs which gives great help to understand basic principles of flapping mechanisms and ideas of wing structural design. From Pennycuick [9] the relation between flight speed and the mass of a bird can be given by

$$U = 4.77m^{1/6} \tag{1}$$

where U is the flight speed in m/s and m is the mass in grams. Greenewalt [10] computed from statistical data the correlation between wing flapping frequency f (Hz), vs. wing length l (cm), to be

$$fl^{1.16} = 3.54 \tag{2}$$

while Azuma [11] showed that the correlations for wing flapping frequency (Hz) vs. mass, m (g), for large birds and small insects are

$$f(\text{largebirds}) = 116.3m^{-1/6} \tag{3}$$

$$f(\text{smallinsects}) = 28.7m^{-1/3} \tag{4}$$

From Equations. (1)–(4), relationships between wingtip speed and mass can be derived. These relations are

$$\text{Wingtip Speed (large bird)} = 11.7m^{-0.065} \tag{5}$$

$$\text{Wingtip Speed (small insects)} = 9.7m^{-0.043} \tag{6}$$

For larger flyers, their flights can be approximated by quasi-steady-state assumptions because their wings flap at low frequency during cruising. Hence the

wingtip speed is low compared to the flight speed. So larger birds, such as eagles and seagulls, tend to have soaring flight and their wings behave like fixed wings. On the other hand, smaller birds and insects fly in an unsteady state, e.g., flies and mosquitoes flap their wings at several hundred hertz. As the results of other researches and papers [12], we assume that our flapping MAVs would operate in an unsteady-state flow regime in which the wingtip speed is faster than the flight speed and fluid motion is complicated also not constant over time.

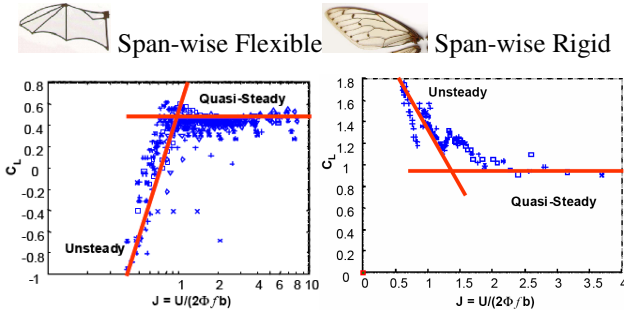


Fig. 3. Stiffness distribution effects on lift performance

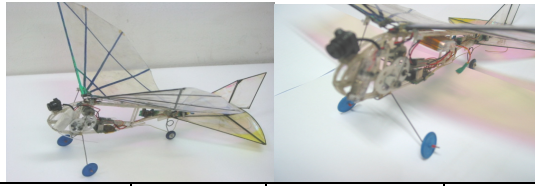
Reference attached in figure 3 also shows the aerodynamic performance of natural insect wings, carbon fiber wings, and MEMS wings tested and it also proves that spanwise stiffness is an important factor in lift production in flapping flight. [13] For the same size of wings, cicada wings with rigid leading edge produce larger lift coefficients according to the result shown in this experiment. We are going to discuss about this in following chapter with comparison data of advance ratio J in different size of flapping MAVs.

Therefore because the lift coefficient of the spanwise rigidity is higher than that of the spanwise flexibility in unsteady-state flight, we used carbon to make the span structure of mechanical flapping wing be rigid. The flapping mechanism is designed such that the left and right wings move up and down and produce flapping along the wing chord due to the wing’s elasticity. That means the structural elasticity along the wing chord direction is an important factor. The wing frame is an important part producing the elasticity of whole wing and thus the structure of the wing frame would affect the wing efficiency and feature variance.

3 Bio-inspired Mechanism Development

3.1 Flapping Model for Bio-inspired Mechanism Application

For application of bio-mimetic wing design, the 36cm flapping MAV was chose. The design procedures are introduced in reference [14], and specification of vehicle is shown in Figure 4.



Component Part	Mass	Wing Span	36 cm
Motor	6.09 g	Wing Area	432 cm ²
Battery	10.2 g	Weight	50 g
Speed Controller	1.22 g	Wing loading	0.115g/cm ²
R/C Receiver	2.04 g	Fuselage	25 cm
Fuselage and Gear Box	20.71 g	Gear Ratio	28:1 reduction
Wing	4.35 g	Frequency	20 Hz
Camera & transmitter	+6.05 g	Up Stroke	35°
Total Mass	44.60 g(+6.05g)	Down Stroke	0°
		Flight Duration	15 min

Fig. 4. Specification of 36cm ornithopter

3.2 Selection of Insect Model for 36cm Bio-mimetic Wing

There's no such insect which can fly only by their flapping motion. They can fly only through complex flight mechanism such as delayed stall, rotational circulation, and wake capture. But there hasn't developed such flapping mechanism which can perform those performances of insect at the same time, it is recommended to make wings which mimic the wings of insects which expected to improve its flight efficiency through applying those wings to our vehicle.

For selecting insect model to design the wing similar to insect, investigations on several insect for their total weight(g), wing span(cm), wing area(mm²) were conducted as shown in Figure 5. On this basis, selection on appropriate insect model for our vehicle was carried out. The selection was done based on the insect having lower flapping frequency with larger wing area compare to its total weight because the developed flapping MAV is quiet heavy and also with very low flapping frequency. In fact, it is improper to compare the parameters between flapping MAVs and insects, for the aspect of size of 36cm, but since the flight mechanism was based more on the insect so the conceptual design of wing structure should follow as same. Cicada was selected for our model because it satisfies the previous conditions.

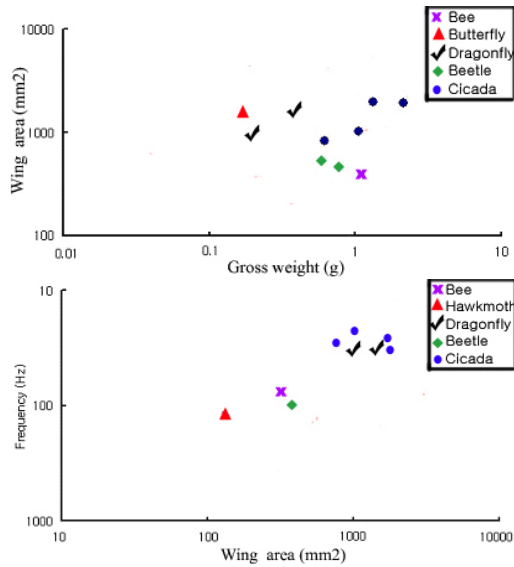


Fig. 5. Comparison of wing area versus gross weight and frequency

After analyzing wings of cicada, we found that it is a cambered wing divided into many cell-type membranes formed with veins throughout the whole wing area as shown in Figure 6 [16].

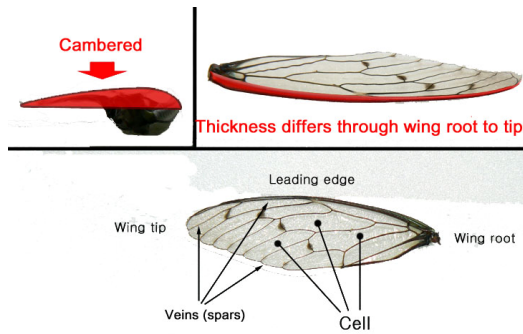
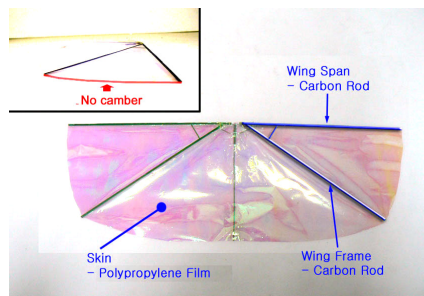


Fig. 6. Characteristics of insect wing (cicada)

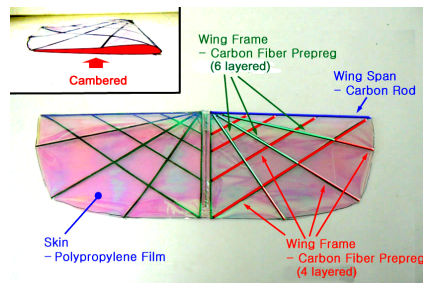
It was also observed that the leading edge vein has more thickness related to other veins and the thickness reduced from wing root to wing tip. This can show that the insect wing has an efficient wing structure for the unsteady flight by differences in thickness of veins and the size of cells surrounded by those veins. It was also observed that camber on both span-wise and chord direction, it can efficiently control the wing deformation during flapping motion.

3.3 Cell-Type Wing

Keeping the features of insect wing in Fig. 6 in mind, attempts at adding more frames with cell-type wing design instead of 2 frame wing design and adopting camber on span-wise direction design was made. In order to compare the flight characteristics between bio-mimetic wing and normal wing, we set two types of wings on experiment. Wing spars of both wings have the same thickness made of carbon prepreg, and PET was used for skins. Type A, the wing designs of prototype, has only one wing frame crossing the wing area and plane surface. But type B, the wing section is divided into many cells by many frames and also has camber along the chord line. We used carbon fiber to form main spar and each sub frames. To reinforce the rigidity through the wing span direction, we placed additional thickness to the main spar.



Type A (Proto-type : 2frames)



Type B (Bio-mimetic Wing)

Fig. 7. Cell-type wing made up with composite material

3.4 Cambered Wing

The thin airfoil was used to minimize drag, suitable for characteristics of the low Reynolds number. As in Fig. 8, by using X-foil software, the EH3012 airfoil was cut from the leading edge by 7.7% and only the airfoil with the upper surface was designed.



Fig. 8. Aifroil EH3012 1

3.5 Fabricating

We formed mold to fabricate the cambered and cell-type wing. The procedures of fabrication are shown in figure 9. For fabrication, the carbon/epoxy fibers were placed on the steel mold having camber then vacuum bagged and cured in an autoclave at high temperature, 177 C, to properly form the wing frame. The amount of time and temperature in curing will determine the stiffness, therefore suitable curing time and temperature was precededly experimented. After frame curing, attaching PET(Polyethylene terephthalate) to frame using cyanoacrylate adhesive followed assure perfect bonding each other.

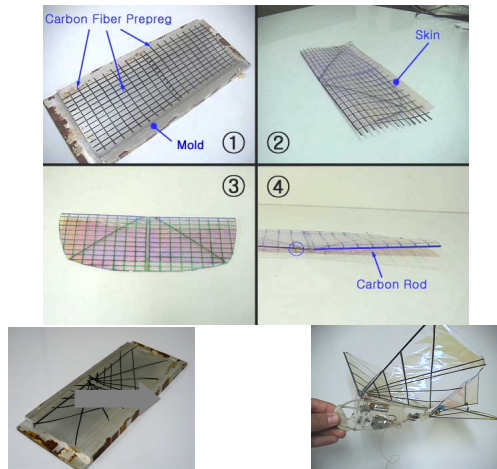


Fig. 9. Procedures of bio-mimetic wing fabrication

4 Experimental Methodology

4.1 References in Calculation of Wing Kinematics

Wing kinematics is one of the significant parameters in flapping because the flapping angle plays great role in the flight mechanism of insect. To analyze the pitching angle, plunging displacement and flapping displacement, motions of the wing in the front view, side view and top view was captured by the high speed camera operated at 2000 fps as shown in Figure 10. In this test, the wing kinematics with phase calculations of prototype wing and bio-mimetic wing, both wingspan length of 36cm, were investigated. The references of calculation of flapping angle, wing rotational angle and plunging displacement are shown in Figure 11-13.

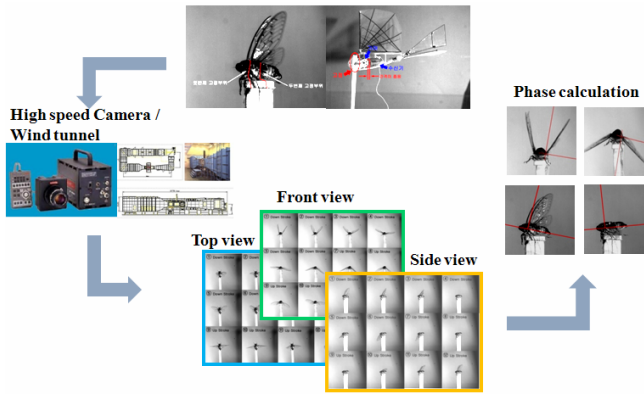


Fig. 10. Schematic for capturing wing kinematics

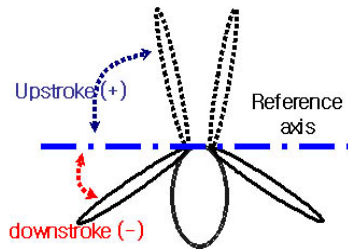


Fig. 11. Reference for calculation of flapping angle

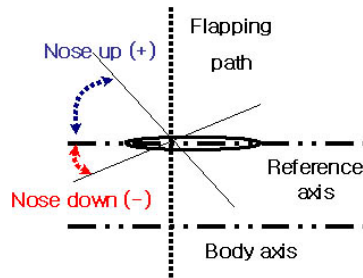


Fig. 12. Reference for calculation of wing rotation angle

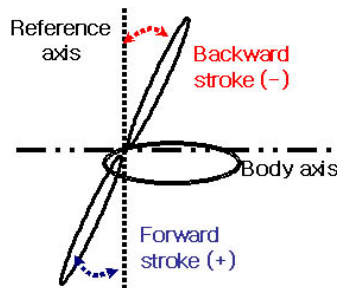


Fig. 13. Reference for calculation of plunging displacement

4.2 Observation on Flapping Motion of Cicada

To compare the morphology of cicada and 36cm bio-mimetic wing, the wing kinematics analysis was conducted based on the image captured every 1/2000 second by high speed camera. Every testing period, taking image of both front and side view and synchronize each frame in order to calculate its flapping displacement, plunging motion, pitching angle. Cicada was placed to the experimental frame with two fixing point tied up with wires to properly attached horizontally. Figure 14 shows the placement of cicada and kinematics calculation.

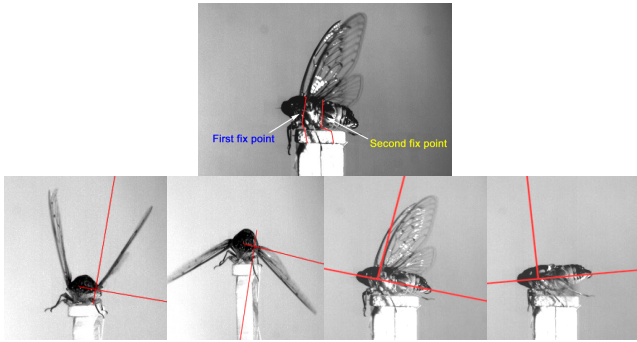


Fig. 14. Experiment on wing kinematics of cicada

Flapping displacement was based on its wing root, displacement of upward to be positive value and displacement of downward to be negative. Likely the plunging displacement we set basis on its wing root. Displacement of forward, we set to positive value and backward we set negative. For the pitching angle we chose the mean value of wing twisting angle.

4.3 Aerodynamic Performance Test

The lift and thrust coefficients can be expressed as follows:

$$C_L = \frac{2L}{\rho AU^2} \quad C_T = \frac{2T}{\rho AU^2} \quad (6)$$

where L, T, U, A are lift, thrust, flight speed, wing area, and air density, respectively[6]. To analyze the flight performance with various wind condition, the wind tunnel experiment conducted under different flow velocity and operating power. In this test, measurement on lift and thrust force generation with every 1V difference ranging 1V~4V and every 1m/s difference ranging 1m/s~5m/s. The calculation on lift coefficient and thrust coefficient were based on the equation above and flow velocity was considered as flight speed. The angle of attack at this test was set to be 0 degree constantly. The wind tunnel and experimental devices are shown in Figure 15.

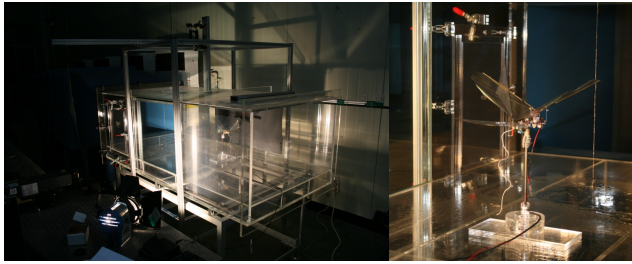


Fig. 15. Experiment on aerodynamic performance of normal and bio-mimetic wings

5 Experimental Results and Discussion

5.1 Result of Wing Kinematics of Cicada

Flapping motion, plunging motion and pitching motion of cicada's wing in one flapping cycle are shown in Figure 14. As the result shows, at the beginning of

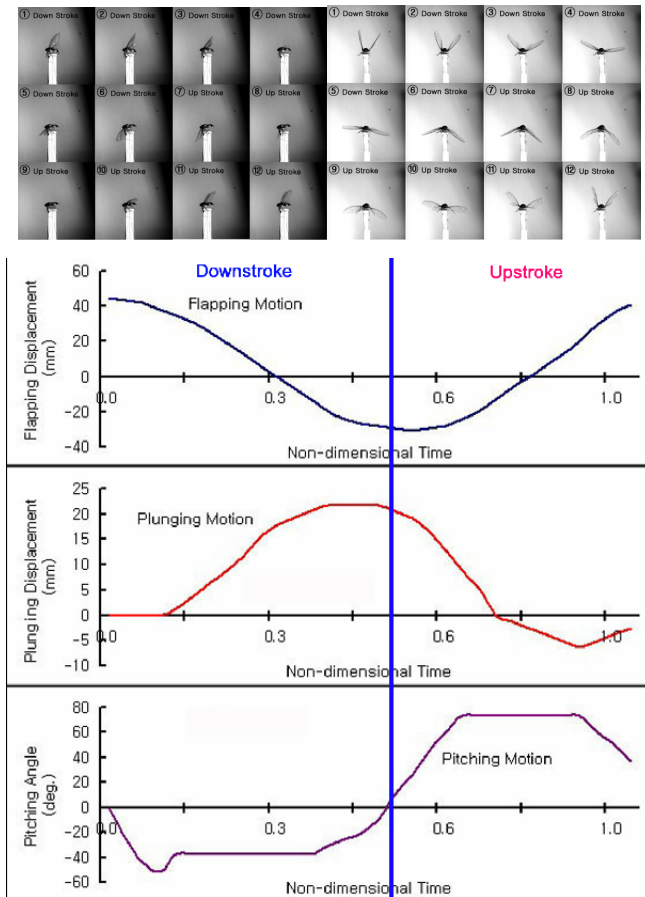


Fig. 16. Wing kinematics of cicada wing

down-stroke, wing moves its pitch downward and when it reaches the maximum down-stroke point it automatically makes wing rotation so as to transverse its pitch to upward at the beginning of the upstroke motion. For the plunging motion it makes forward stroke during down-stroke and makes backward stroke during the upstroke motion, known as pronation and supination. But this doesn't mean that flapping and plunging motion has same phase. Flapping motion occurs later than plunging motion relatively.

5.2 Result of Wing Kinematics of Prototype and Bio-mimetic Wing

Similar to the wing kinematics calculation of cicada, same methodology was used to result the flapping and wing rotational angle with plunging displacement shown in Figure 15. This graph shows that both cicada and testing wing have similar flight statistics in some point of view which will be discussed later.

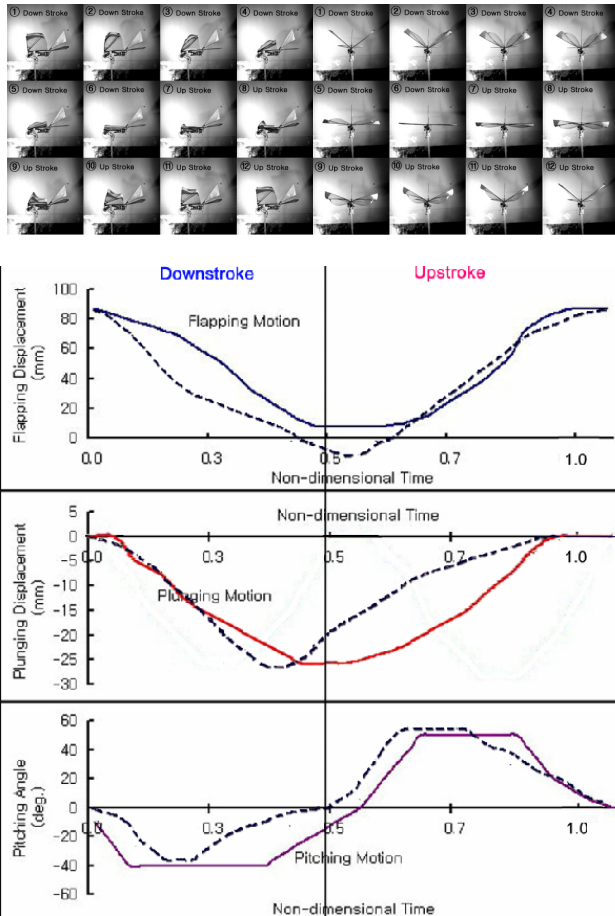


Fig. 17. Wing kinematics of prototype and bio-mimetic wing

The result of wing kinematics of bio-mimetic wing is plotted in dash and prototype wing is plotted in lines. Prototype wing and bio-mimetic wing both made pitch down angle during down-stroke and pitch up angle during upstroke. Although there isn't any mechanical link systems to operate pitching motion, our vehicle could perform a pitching motion due to the passive deformation. There are several differences in performance between normal wing and insect imitating wing compare to the cicada's wing.

Firstly, type A has almost same phase in both flapping and plunging motion but type B shows a clear different point of reversing point.

Secondly, they differs the wing rotation point. Type A shows its wing rotation after starting upstroke but type B shows its wing rotation at the end of down-stroke. In other word, the point of wing rotation is between phase changing point of flapping motion and that of plunging motion which has much similarity to cicada's according to Figure 7-2. This proves that cambered and cell-type wing can perform more likely to the cicada's compare to the normal wing based on stated reasons.

5.3 Aerodynamic Force Analysis of 36cm Bio-mimetic Wing

The aerodynamic force measurements of prototype wing and bio-mimetic wing was conducted to prove the efficiency of application of flapping wing structures of insects. According to the previous chapter, bio-mimetic wing has superior performance in wing kinematics comparing to the original wing but to assure its better efficiency, force generation should also be larger. For this experiment, wing type A, the prototype wing, and bio-mimetic wing were prepared having wing length of 36cm and wingbeat amplitude to be 35 degree equally. The data from the force measured in the air and vacuum were averaged and subtracted to calculate pure aerodynamic force. The experiment devices and scene of aerodynamic force measurement is shown in Figure 18.

Average aerodynamic lift produced by prototype wing was measured 0.075N and thrust 0.018N. For bio-mimetic wing, the average aerodynamic lift was 0.088N and thrust 0.020N. Result shows that both lift and thrust generation of bio-mimetic wing is

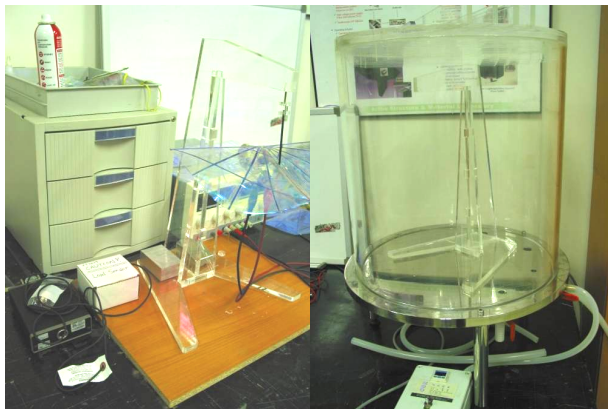


Fig. 18. Experiment devices and scene of aerodynamic force measurement of 36cm bio-mimetic wing

higher than that of prototype wing obtaining 17% improvement in lift force generation and 11% improvement in thrust generation.

5.4 Aerodynamic Performance Analysis under Various Wind Flow Velocity and Power Condition

As the result from wind tunnel test also proved the efficient performance of bio-mimetic wings with better aerodynamic coefficient. As shown in Figure 19, the bio-mimetic wing has higher Lift coefficient through all Power and Velocity variation and also the drag coefficient of bio-mimetic wing shows better performance comparing to the normal wing.

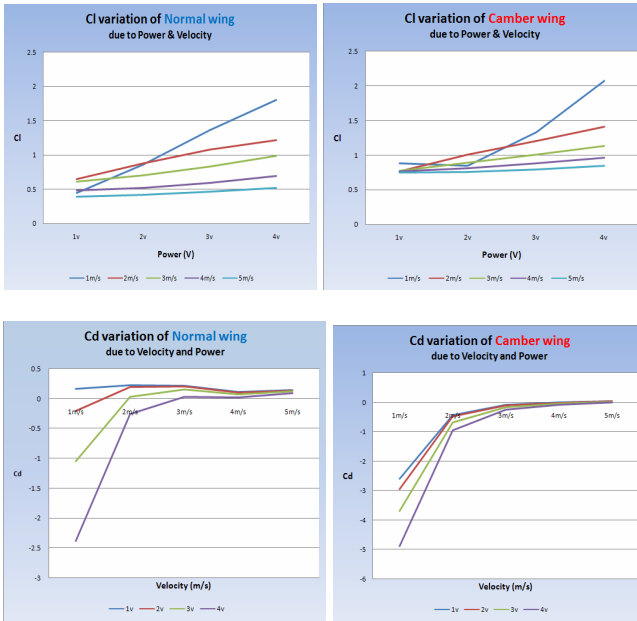


Fig. 19. Results of wind tunnel test

6 Conclusions

In this research, design, fabricating and performance analysis of 36cm bio-mimetic wing inspired from cicada were conducted. It was observed that, by the aspect of the force generation and wing kinematics, the developed cicada mimetic wing has better flapping performances and characteristics comparing to the original wing. The wing kinematics analysis, force generation analysis and aerodynamic performance analysis were conducted with high speed camera, vacuum chamber and wind tunnel. By the actual flight test, the bio-mimetic also operated to have higher stability throughout all kinds of AOA. It was proved to be a best solution to make the flapping wing followed the characteristics of insect wing regarding to the higher flapping performance, thus we expect future flapping MAV can be optimized and improved on this basis.

Acknowledgment

This work also has been supported by a grant of Brain Korea of the Ministry of Education. The authors gratefully acknowledge the financial support.

References

- [1] Dickinson, M.H., Lehmann, F.O., Sane, S.P.: Wing rotation and the aerodynamics basis of insect flight. *Science* 284, 1954–1960 (1999)
- [2] McMichael, J., Francis, M.: *Micro Air Vehicles – Toward a New Dimension in Flight*. DARPA (1997)
- [3] Ansari, S.A., Zbikowski, R., Knowles, K.: Aerodynamic modelling of insect-like flapping flight. for micro air vehicles. *Progress in Aerospace Sciences* 42(2), 129–172 (2006)
- [4] Lentink, D., Bradshaw, N.L., Jongerius, S.R.: Novel micro aircraft inspired by insect flight. *Comparative Biochemistry and Physiology - Part A: Molecular & Integrative Physiology* 146(4, suppl. 1), S133–S134 (2007)
- [5] Alexander, D.E.: *Nature's flyers*. Hopkins University Press, Baltimore (2002)
- [6] Ellington, C.P.: The novel aerodynamics of insect flight: Applications to micro air vehicles. *The Journal of Experimental Biology* 202, 3439–3448 (1999)
- [7] Ho, S., Nassef, H., Pornsinsirirak, N., Tai, Y.-C., Ho, C.-M.: Unsteady aerodynamics and flow control for flapping wing flyers. *Progress in Aerospace Sciences* 39(8), 635–681 (2003)
- [8] Lentink, D., Bradshaw, N.L., Jongerius, S.R.: Novel micro aircraft inspired by insect flight. *Comparative Biochemistry and Physiology - Part A: Molecular & Integrative Physiology* 146(4, suppl. 1), S133–S134 (2007)
- [9] Pennycuik, C.J.: The mechanics of bird migration. *Ibis* 111, 525–556 (1969)
- [10] Greenewalt, C.H.: Dimensional relationships for flying animals. *Smithson Misc. Collect.* 144, 1–46 (1962)
- [11] Azuma, A.: *The biokinetics of flying and swimming*. Springer, Tokyo (1992)
- [12] Ho, S.: Unsteady aerodynamics and flow control for flapping wing flyers. *Progress in Aerospace Sciences* 39, 635–681 (2003)
- [13] MEMS technology for a battery-powered ornithopter. In: *The 13th IEEE Annual International Conference on MEMS*, Miyazaki, Japan, pp. 709-804, January 23-27 (2000)
- [14] Park, J.H.: Designing Biomimetic Ornithopter Capable of Sustained and Controlled Flight. *Journal of Bionic Engineering* 5, 39–47 (2008)
- [15] Soh, A.K.: Experimental studies of the material properties of the forewing of cicada (*Homoptera*, *Cicadidae*). *The Journal of Experimental Biology* 207, 3035–3042 (2004)
- [16] Nick Pornsin-sirirak, T.: Titanium-alloy MEMS Wing Technology for A Micro Aerial Vehicle Application
- [17] Vogel, S.: *Life in Moving Fluids*, 2nd edn. Princeton University Press, Princeton (1994)
- [18] Usherwood, J.R.: *Aerodynamics and animal flight based on propeller models*. Queens' College (2001)
- [19] Pornsin-Sirirak, T.N.: Unsteady-State Aerodynamic Performance of MEMS Wings

Robot-System for Management of Environmental Conditions Using Multiple Mobile Robot Types

- Sample Application for Position Estimation -

N. Hashimoto, H. Adachi, S. Kato, and K. Komoriya

National Institute of Advanced Industrial Science and Technology
{naohisa-hashimoto,h.adachi,shin.kato,komoriya.k}@aist.go.jp

Abstract. This study describes a system that allows robots to manage environmental conditions. The proposed system consists of a database center and various autonomous robots, each with different functions. The robots' functionality differs in mobility due to differences in their locomotion mechanisms, and information acquisition capability, which is defined by the sensors they are equipped with, correspondent ability to an incident, and so on. This study describes the overall concept and some important features of the proposed system. In addition, we propose a position estimation method and explain the experiments conducted to evaluate it. Future tasks are also mentioned.

1 Introduction

A variety of mobile robots have been developed for specific applications, such as entertainment, work support and transportation. There has been much research into autonomous mobile robots with various sensors and actuators depending on the purpose and environments. Various sensors, such as RTK-GPS, RFID, gyro sensor, vision system, magnetic marker, ultrasonic sensor, laser larder sensor, and millimeter-wave sensor have been evaluated for autonomous locomotion [1,2].

The sensor specifications depend on the environment conditions the mobile robot travels in. Many researchers have attempted to improve the system performance and robustness by using sensor fusion.

In this study, we propose a high-efficiency robot-system for effective environmental management. The system employs different types of mobile robots, each with different features and specifications.

This study focuses on the environmental-recognition capability of mobile robots. Here, environmental recognition is defined as accurately detecting and estimating the position of obstacles. For mobile robots, environmental recognition must be reliable, and this study addresses this issue by enabling data sharing among robots.

The concept and necessary functions of the proposed system and a sample application are described. In addition, future enhancements are also discussed.

2 Concept and Functions of the Proposed System

The objective of the proposed system is to manage a certain site by using robots having different features and specifications. In this study, it is assumed that the environment

where the proposed system is applied is a company or school facility, which includes buildings interiors, area around the buildings, walkways and roads. It is difficult for single-species mobile robots to manage such a complex environment. Therefore, we determine that the system requires a mixture of robot types capable of cooperating and collaborating among each other. The system and the individual robots require knowing the capability of other robots in advance. Figure 1 illustrates the concept of the proposed system.

The proposed system consists of different types of mobile robots and an administration system with a monitoring function. A human operator can get on one mobile robot, and control it directly, if necessary. Each mobile robot is able to travel automatically and autonomously execute pre-determined task.

The headquarter comprises the administration system, the operator of the system, the robot operator, and an unmanned robot depending on the situation. The location of the headquarter of the system can be varied to accommodate changes in environment and situation. This strategy enables both flexibility and quick response for the system. Each mobile robot reports its position and environment information to the administration system.

The administration system maintains information on the activity state and positions of each robot. Each mobile robot is able to comprehend the overall situation and make decisions by receiving all necessary information and instructions. In this study, all mobile robots are not fully automated but operated by a human, depending on the situation. Therefore, a study of the Human machine interface (HMI) which displays information and is used to operate the system is essential. The proposed system utilizes the following as methods:

- Method to effectively manage each mobile robot
- Method to implement a wide-area ad hoc wireless network
- Method to construct a database.

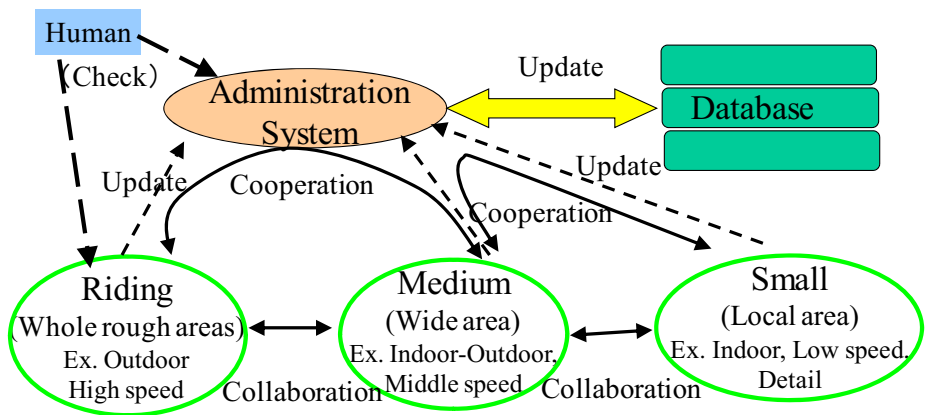


Fig. 1. Concept of Proposed System

3 Cooperation among Mobile Robots

3.1 Overview

We have proposed a method using a RTK-GPS to develop an automatic driving system uses the vehicle position and specific course information [3]. This system does not require new infrastructure, which reduces costs. It can obtain specific course information in advance, and then reconstruct the course and adapt accordingly. The only disadvantage is that, it is difficult to improve the reliability of environmental recognition of the Automatic Driving System because the GPS information reception is hindered by the surroundings. We proposed an environmental recognition method that uses detailed position data of objects that are in the track of the vehicles, such as white lines, road shape, light poles, and road signs [4]. There has been a great deal of research into SLAM [5,6].

This section describes a method for improving the positioning reliability that applies the cooperation property of the mobile robots. In this study, a mobile robot supported by the other robots is called a supported robot, and a mobile robot that supports the other robots is called a supporting robot.

The concept of the proposed method is shown in Fig. 2. The supported robot travels along the specified course. The supported robot has its own sensors; however, if due to some reasons the position accuracy of the supported robot is found to be too low, it would have trouble staying the specified course. In this situation, a supporting robot with more reliable sensors estimates the relative position of the supported robot, and calculates its absolute position. Subsequently, the supporting robot sends the position data to the supported robot. Using this data, the supported robot can correct the position error and continue traveling.

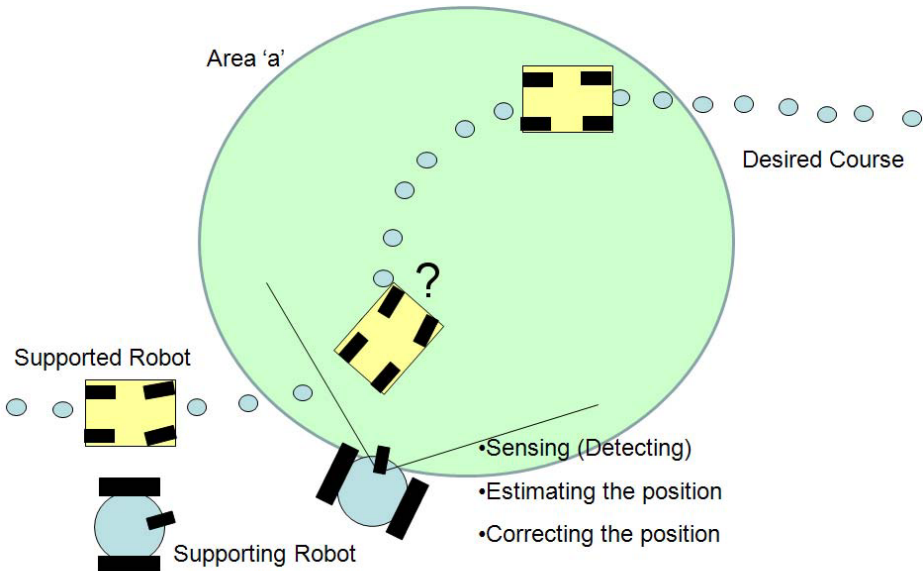


Fig. 2. Proposed Method

This method requires the following: the measurement of the state variables of the supported robot for correcting the position error (the state variables are mentioned later.), a way of aggregating position estimations by considering the time stamp and accuracy, and a control algorithm for the supporting robot. This proposed method can be also used for obstacle detection by sharing information about the existence of obstacles.

3.2 Measurement Algorithm

The state variables of the supported robot are position, heading, velocity, and yaw rate. In this study, all state variables are measured with a laser range finder which detects the existence of an object, and measures the distances to the object. We use high reflectance tapes for measurement. Three pairs of high reflectance tapes (width =0.1 [m], length = 0.5[m]) are placed on the supported robot. One pair on its back 0.4 [m] apart, and the others pairs are placed on the left and right sides 0.7 [m] apart. In this study, only a pair on its back is used. The data processing from the laser range finder is as follows:

- 1) The measurement system searches the data from the laser range finder.
- 2) The system determines that two tapes are part of a pair by checking the distances between the tapes (0.4 [m] or 0.7[m]).
- 3) The robot heading is calculated with the gradients the tape pair.
- 4) The robot's center position through the positions and gradients of two tapes of a pair.

There are many kinds of sensors for measuring relative position between a sensor and a robot, such as, stereo vision, and mill-wave sensor. In this study, since our purpose is to investigate the feasibility of the system, we use a single sensor of a laser range finder. The measurement of the state variables with a laser range finder has sufficient accuracy of ± 0.2 [m] [7].

3.3 Estimation Algorithm

The supporting robot estimates the relative position of the supported robot by the method described in section 3.2 and converts the relative position into the absolute position of the supported robot. The conversion equation is

$$\begin{pmatrix} xsa \\ ysa \\ w \end{pmatrix} = \begin{pmatrix} 1 & 0 & xsb \\ 0 & 1 & ysb \\ 0 & 0 & 1 \end{pmatrix} \cdot \begin{pmatrix} \sin(\theta sb) & \cos(\theta sb) & 0 \\ -\cos(\theta sb) & \sin(\theta sb) & 0 \\ 0 & 0 & 0 \end{pmatrix} \cdot \begin{pmatrix} X_1 \\ Y_1 \\ 1 \end{pmatrix}$$

$$\theta sa = \theta sb + \phi$$

where,

X_1 : Relative position (x) of supported robot (in Fig. 3)

Y_1 : Relative position (y) of supported robot

ϕ : Relative angle of supported robot

xsa : Absolute position (x) of supported robot

ysa : Absolute position (y) of supported robot

θsa : Absolute angle of supported robot

x_{sb} : Absolute position (x) of supporting robot
 y_{sb} : Absolute position (y) of supporting robot
 θ_{sb} : Absolute angle of supporting robot
 w : Parameter (not used)

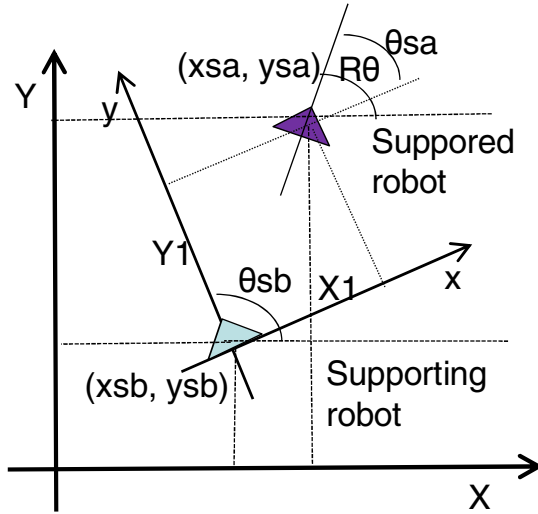


Fig. 3. Method for Converting from Relative Position to Absolute Position

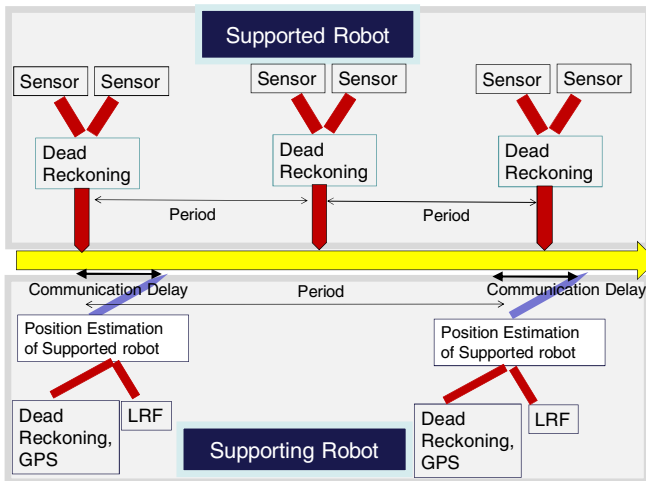


Fig. 4. Position Estimation (time-line)

In this study, the absolute position of the supported robot is calculated and transmitted by the supporting robot through a wireless LAN(WLAN). The position estimation-fusion is based on the algorithm[8] which considers communication delay with a

Kalman filter [9]. In this study, the position data sent from the supporting robot is used as observation data. The flow of position estimation is shown in Fig.4. The communication delay is set to 0.1[s] in this experiment.

3.4 Supporting Robot Control Algorithm

In this study, the travel path of the supporting robot is bounded by the state variables of the supported robot. A laser range finder is used in this study. The system can estimate the position and yaw angle of the supported robot by detecting the pairs of tapes. Therefore, the supporting robot has to maintain its position from where it can detect at least one pair of tapes on the supported robot. In addition, the supporting robot also stays the distance within 6[m] of the supported robot due to the sensor's performance limitation. The control algorithm shown in Fig.5 is based on the mobile guidance algorithm [10,11]. The supporting robot is controlled along the desired track for the supporting robot and remains 1[m] to the side and 4[m] behind the supporting robot and moves parallel to the supported robot.

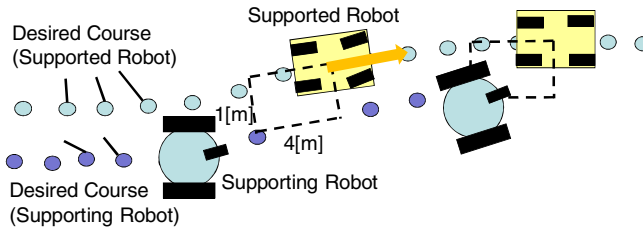


Fig. 5. Control Algorithm

3.5 Supported Robot Control Algorithm

The supported robot travels along the desired course. The robot controls the steering, throttle and brake by referring the relating data of the desired course and its position using the control method[8]. However that system estimated the robot's position with a RTK-GPS whereas this experiment estimates the robot's position by the proposed method. The velocity of the vehicle is set to approximately 0.5[m/s] on the straight line, about 0.4[m/s] on other corners.

4 Experiments

4.1 Configuration of the Experiments

This study evaluated the proposed system by experimentations. Two experimental robots were used a wheel chair which is used as the supporting robot, and a small electric one-seater vehicle which is the supported robot. Figure 6 shows the supporting robot and Figure 7 shows the supported robot. A laser range finder on the supporting robot provides the measurements, and provides distance data to an object within 180 [deg] with a resolution of 0.5 [deg]. A laser range finder has also been used for

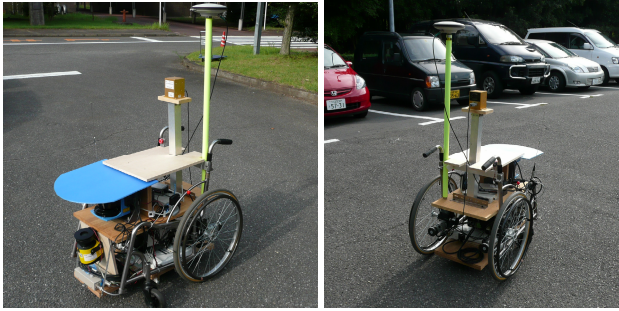


Fig. 6. A supporting Robot

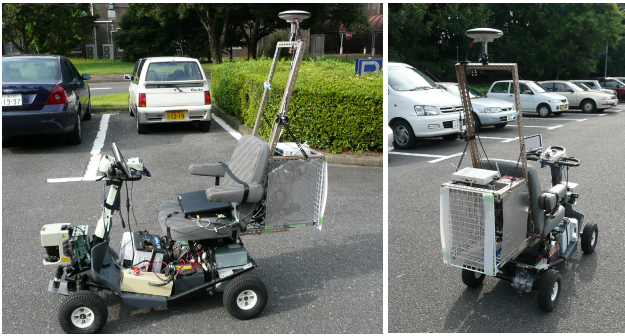


Fig. 7. A supported Robot

obstacle detection on the supported robot. In this experiment, the supporting robots used the RTK-GPS for localization; however other localization methods can be employed. A laptop on each robot served as an on-board computer. Both robots had the data for the specified course in advance. It was assumed that obstacles do not exist in the experimental place and there is no sensor blind area. To evaluate the algorithm for allowing the supporting robot to estimate the supported robot's position, the RTK-GPS system (Novatel OEM4-G2) having localization accuracy within ± 0.02 [m] is loaded on the supported robot. Since the RTK-GPS measurement includes the communication delay, it is not completely accurate, and data from the RTK-GPS on the supported robot were used for comparison. This sensor on the supported robot cannot be used for position estimation for control in area "a". A WLAN (2.4[GHz]) system provided communication between the robots with a time lag of 50 [ms]. We use User Datagram Protocol (UDP) for WLAN communication, since the system needs high communication speeds. In this experiment, the supported robots can estimate their own position by the RTK-GPS, using dead reckoning until it enters in area "a" (Fig. 2). While the supported robot travels through area "a", it estimates its position with data which it receives from the supporting robot and by dead reckoning. The supporting robot travels near the supported robot, estimating its position while the supported robot is in area "a". The system configuration is shown in Fig. 8. The experiments were conducted on the periphery road and in the parking lot.

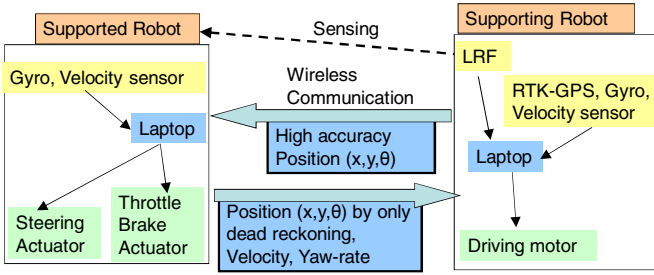


Fig. 8. System Configuration



Fig. 9. Scenes of Experiments

4.2 Experimental Result and Discussion

Figure 9 shows scenes of the experiments. Some experimental results of automated guidance are shown in Figs. 10 and 11. Figure 10 shows the four types of trajectories. The first is the center of the supported robot's track as estimated by the proposed system; the second is the center of the supported robot's track as measured by the RTK-GPS, the third track is the position of the supporting robot and the fourth is the desired

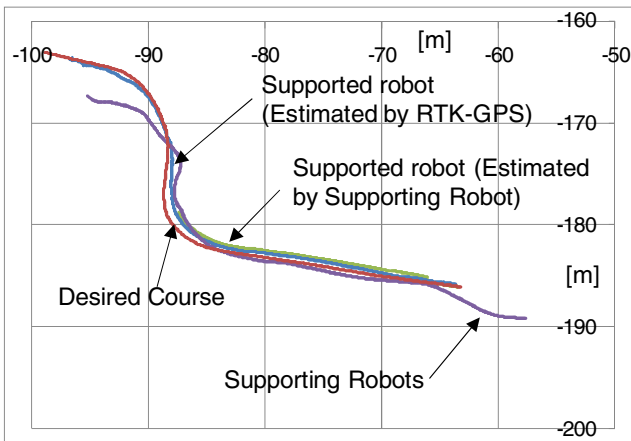


Fig. 10. Experimental Result 1 (Trajectories)

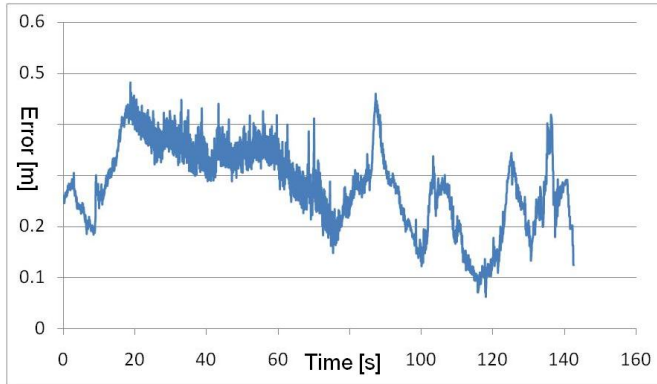


Fig. 11. Experimental Result 2 (Estimation Error)

(planned) course for the supported robot. In Fig.10 the origin is set at the RTK-GPS base point in our laboratory. Figure 11 shows the error between the system's estimated position and the RTK-GPS data. These results show that the proposed system can consecutively estimate the position of the supported robot with high accuracy. Each error of the result is within about 0.45[m] and, therefore, the measurement algorithm can provide localization data without discontinuities, and with sufficient accuracy for robot control.

Considering the supporting robot, it is controlled while maintain a suitable position relative to the supported robot, and the desired course. When a system estimates the position of an object with a sensor such as a laser range finder, however the further an object is from the system, the larger the estimation error becomes. As long as the supporting robot is within about 6 [m] of the supported robot, the system provides precise measurements of the supported robot's location.

5 Conclusions

This study describes the concept of a proposed robot system that provides efficient and effective environmental management using mobile robots with a variety of features. This study describes an application of the proposed robot system and evaluates the method by experimentation, proving the validity of the method.

We are considering testing the system in other situations, such as determining the existence of obstacles.

References

- [1] Hermosillo, J., Pradalier, C., Sekhavat, S., Laugier, C.: Machine Intelligence and Robotic Control Journal 5(3), 95–102 (2004)
- [2] Scheuer, A., Laugier, C.: Planning: Sub-Optimal and Continuous Curvature Paths for Car-Like Robots. IEEE-RSJ, Intelligent Robots and Systems (1998)

- [3] Omae, M., Hashimoto, N., Fujioka, T., Shimizu, H.: A study on automated control algorithm in local area with parking lot. *JSAE Transaction* 35(3), 235–240 (2004) (in Japanese)
- [4] Hashimoto, N., Omae, M., Komoriya, K., Shimizu, H.: Improvement of Reliability of Environmental Recognition on Automatic Driving System by Using Data of Objects. *International Journal of ITS Research* 3(1) (2005)
- [5] Hara, Y., Kawata, H., Ohya, A., Yuta, S.: SLAM for Large Environments using Scan Data with Received Light Intensity of a SOKUIKI Sensor, SI-3C2-4, pp. 1014–1015 (2006) (in Japanese)
- [6] Ekvall, S., Jensfelt, P., Kragic, D.: Integrating Active Mobile Robot Object Recognition and SLAM in Natural Environments. *IEEE/RSJ IROS* (2006)
- [7] Hashimoto, N., Kato, S., Minobe, N., Tsugawa, S.: Guidance System to Target Spot for Charging by Communications. *WEVA Journal* 1 (2007)
- [8] Omae, M., Fujioka, T.: DGPS-Based Position Measurement and Steering Control for Automatic Driving. In: *Proceedings of 1999 American Control Conference*, pp. 3686–3690 (1999)
- [9] Kagami, S., Ishikawa, M.: A Sensor Slection Method Considering Communication Delays. *Journal of IEICE J88-A* (5), 577–587 (2005) (in Japanese)
- [10] Hashimoto, N., Kato, S., Minobe, N., Tsugawa, S.: Autonomous Vehicle Guidance through Cooperation between Vehicles. In: *13th ITS-World-Congress* (2006)
- [11] Hashimoto, N., Kato, S., Minobe, N., Tsugawa, S.: Automated Vehicle Mobile Guidance System for Parking Assistance. In: *IEEE-Intelligent Vehicle Symposium* (2007)

Locomotion Elicited by Electrical Stimulation in the Midbrain of the Lizard *Gekko gekko*

Wang Wenbo¹, Guo Ce¹, Sun Jiurong², and Dai Zhendong¹

¹ Institute of Bio-inspired Structure and Surface Engineering
Nanjing University of Aeronautics and Astronautics, Nanjing, China
{wwb523, guozc, zddai}@nuaa.edu.cn

² College of Life Sciences
Peking University, Beijing, China
sjr@pku.edu.cn

Abstract. Locomotor behaviors evoked by stimulating the midbrain were studied in anesthetized and freely moving, awaking lizard *Gekko gekko*. Twenty *Gekko gekko* males were used in the anesthetized brain stimulation experiments; twenty were for microelectrode implantation. In the acute studies, four locomotor modes (lateral curvature of vertebral column, 's' shape curvature of vertebral column, limbs moving and walking or crawling manner, phonation reaction) were elicited successfully by normal electrical stimulation in anesthetized gekkos. The research show most effective points of stimulation for induced locomotion were located at the midbrain tegmentum. In the awake experiment, electrical stimulation was delivered through implanted electrode of certain regions (the regions were decided by the results of the acute experiments) of the midbrain in 20 gekkos. Locomotor modes, such as right and left turn, even the combined locomotion (going forward then turning around) was successfully elicited. Results suggested that it is possible to carry out artificial induction on *Gekko gekko* through electrical stimulation on the related nucleus in their brain.

Keywords: *Gekko gekko*, electrical stimulation, midbrain, mesencephalic tegmentum, locomotion induce.

1 Introduction

Animals have wonderful locomotion abilities, especially those that can move on 3-dimensional, complex terrain. The remarkable motion capability of geckos has made them the hot spot for research, such as the investigations on the adhesion mechanism in gecko setae (Autumn, 2000; Gao, 2005; Rizzo, 2006; Sun, 2005; Sitti, 2002; Geim, 2003). The motion ability of a modern mobile robot system in an unstructured environment lags far behind animals in stability, flexibility, robust, environmental adaptation and efficiency of energy sources (Dickinson, 2000). Since the 1990s, bio-robotics has become one of the main directions for robotics research (Dai, 2007; Guo, 2005). The lizard *Gekko gekko*, located in Southwest China, North Vietnam, Northeast India and the Indo-Australian Archipelago (Holzer, 1979) was chosen as the target animal and was studied for developing a bio-robot, since it is big enough for investigating and for load-carrying. If we can modulate gekkos' locomotion just like the robo-rats (Talwar, 2002), it will be a revolution of Three Dimensional Obstacle-Free (TDOF) robots! As is commonly known among biological scientists, the

midbrain in mammals contains circuits that modulate locomotion. Modern research on the brain mechanisms for the initiation of locomotion has discovered a site in the midbrain known as the mesencephalic locomotor region (MLR), and such a region has been detected in all species that have been examined (Adams, 1968 and 2006; Terry, 1978; McClellan, 1984; Jordan, 1998; Jean, 2003). However, there is no research on the *Gekko*'s midbrain for locomotion control. Most research on *gekko* has been on its forebrain, especially the neuroanatomical functions (Smeets, 1986; Hoogland, 1995; Bruce, 1995; Fokje, 1988; Gonzalez, 1990; Li, 2001), although there has been some research on *gekko*'s vocalization (Kennedy, 1975; Lan, 1982) and locomotion mechanism of the toes controlled by peripheral nerve (Guo, 2006). In this study, we applied the electrical stimulation technique to locate the nerve corpuscle in *Gekko*'s middle brain that is responsible for *Gekko*'s locomotion.

2 Methods

2.1 Subjects

Adult *Gekko gekko* males (n=40), snout-to-vent length from 150 to 165 mm, body weight from 65 to 100 g, were bought from Nanning, Guangxi Province in China and were housed in a special room used for raising *gekko*s. In that facility, *gekko*s were raised for at least two weeks. Twenty were used in the anesthetized brain stimulation experiments; the remainders were for microelectrode implantation.

2.2 Surgery Procedures

2.2.1 Gekkos for Anesthetized Test

*Gekko*s in the acute experiment were lightly anesthetized with Nembutal (30 mg/kg). After the *gekko*s were anesthetized, they were placed in the stereotaxic apparatus and their heads were held firmly by the cranium holder (Model IBSS-*Gekko*-01, designed for *Gekko* used only and which was compatible with standard stereotaxic devices, Appl. 200610086008. X) (Wang, 2007). Opening the skull, cutting off the dura, and removing off the arachnoid, the craniotomy was carried out to expose the selected brain area for electrical stimulation.

2.2.2 Gekkos for Freely Moving, Awake Test

*Gekko*s for the freely moving, awake experiment did not perform the craniotomy. Instead, we used the micro dental motor handpiece which can be fixed on the stereotaxic apparatus to drill holes (diameter 600 μ m) on the skull of the *gekko*s' heads. And we used needle to penetrate the dura and arachnoid of the *gekko*s' brain. Then a number of bipolar stainless stimulating microelectrodes (Teflon coated for isolation) were chronically implanted into the *gekko*s' brain. Once the electrodes were lowered to the selected point they were fixed to the skull with dental cement. And a connector was used to connect the electrode for the next stimulation.

2.3 Stimulation Procedures and Behavioral Testing

In the acute experiments, a constant-current (negative pulses, 10-100 μ A) was delivered through a electrical stimulator (Chengdu instrument factory, model YC-2-S). The

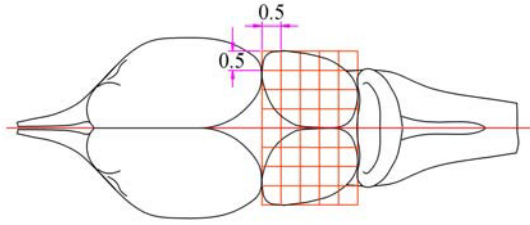


Fig. 1. Stimulation sites of the mesencephalon

brain was stimulated at various points on a grid of sites (Fig. 1) across the midbrain with a bipolar stainless electrode (diameter $100\mu\text{m}$). And at each point, the electrode was lowered into the brain tissue by $50\mu\text{m}$ steps. The stimuli were 2-5 sec trains of monophasic square waves, and the stimulus duration was shortened when the responses became too violent. The stimulus intensity was varied between $10\text{-}60\mu\text{A}$. At each stimulated site, the current was increased by steps of $10\mu\text{A}$. Response reproducibility was tested at three stimulus intensities. A rest period of 10 min was allowed between successive tests.

In the chronic experiment, the geckos were tested in an open field (on which the grid of $38\text{ mm}\times 38\text{ mm}$ was drawn) after recovery from surgery one weeks later. The stimuli consisted of biphasic pulses no more than $100\mu\text{A}$. Response reproducibility was tested at three times. A rest period of 5 min was allowed between two tests. We tested these stimulation points once a day after 5 o'clock P.M. and gave another two experiments in the following two days.

In the tunnel test, a cage with tunnel (Fig. 2) was made for the experimentation. In which, the geckos were made to crawling along the tunnel.

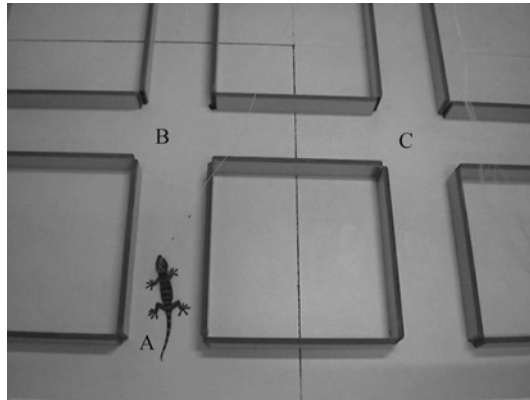


Fig. 2. The gecko was made to move from A to B then to C along the tunnel (The width of the tunnel is 20 cm, the distance form A to B is 50 cm—the same as that of B to C). In the test, Electrical stimulation was delivered to the gecko's brain through soft fine wire. gecko was made to start form A on the forward command; when the gecko got to B , the forward stimulation stop and the stimulation for right turn began; when the gecko turning the suitable angle, the turning command stopped and the forward crawling command was given.

2.4 Histology

On completion of the studies for acute stimulation, a direct current (80 μ A, 30 s) was passed between alternate electrode pairs to provide an anatomic referent for stimulation sites. The animals were sacrificed with Pentobarbital Sodium and perfused through the heart with 0.8% NaCl solution followed by 1% potassium ferrocyanide and a buffered 4% paraform solution. Their heads were detached and placed in a 4% paraform solution for at least 2 days. The fixed brains were removed and cut in 30 μ m coronal frozen sections. The sections were stained with Neutral Red for light microscopy localization of the electrolytic lesions.

As to the awake studies, an electrolytic lesion (n=10) was also made at the stimulation site using DC current applied at the end of experiments for later histological identification.

3 Results

3.1 Results of Acute Studies

We defined four locomotor modes: lateral curvature of vertebral column(LCVC), 's' shape curvature of vertebral column(SCVC), limbs moving and walking or crawling manner(LM&CM), phonation reaction(PR). These motion modes exhibited by gekkos were evoked by electrical stimulation (Fig. 3). The schematic distribution of the effective site to electrical stimulation was shown in Fig. 4. For the sake of modulation on *Gekko's* locomotion, we pay more attention to the curvature of vertebral column. The research shows the curvature of vertebral column was often accompanied with limbs movement such as the limbs adduction and stretching. And there are two forms for the

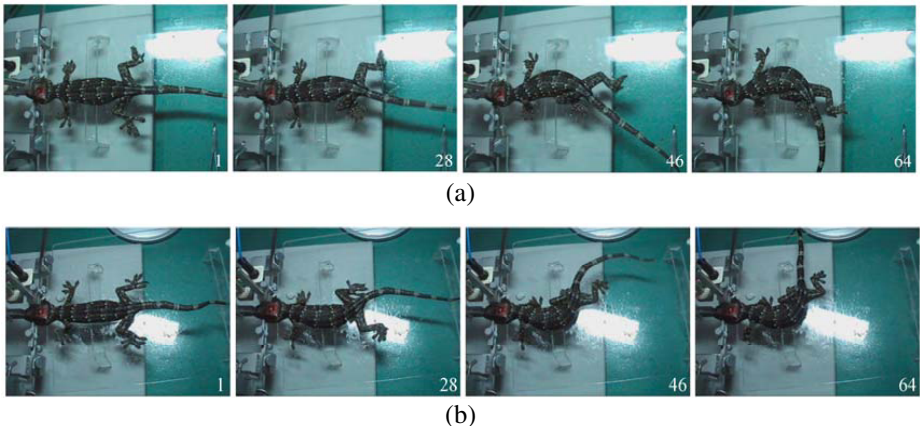


Fig. 3. Locomotion of lateral curvature of vertebral column (bending toward the contralateral side of stimulation sites) induced by midbrain electrical stimulation of the lightly anesthetized gekkos. From right to left, the recording pictures arrange on time successively (the number on which represents the serial number of the frame in the tape). (a) Vertebral column bent to the right and (b) to the left.

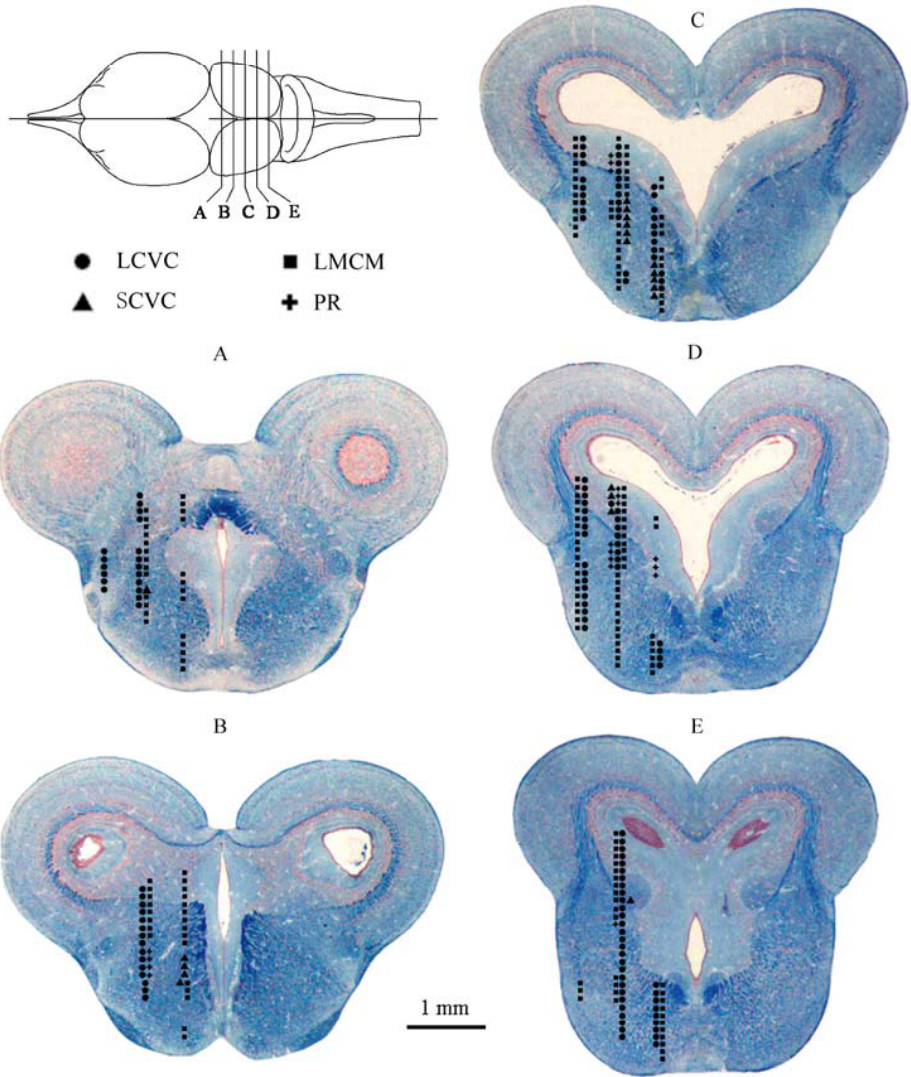


Fig. 4. Locomotion evoked by electrical stimulation in the midbrain of the gecko. Corresponded to the brain areas indicated by lines on the the dorsal view of the gecko's brain at the left-top, the right part of five brain maps were selected to show the positive sites to evoke locomotion.

lateral curvature of vertebral column: bending toward the ipsilateral or contralateral side of stimulation sites. According the *Gekko's* crawl gait we presume that the 's' shape curvature of vertebral column is correlated with the movement of crawling forward.

And the anatomic study show most effective points of stimulation for induced locomotion were located at the mesencephalic tegmentum near the midline (Fig. 5).

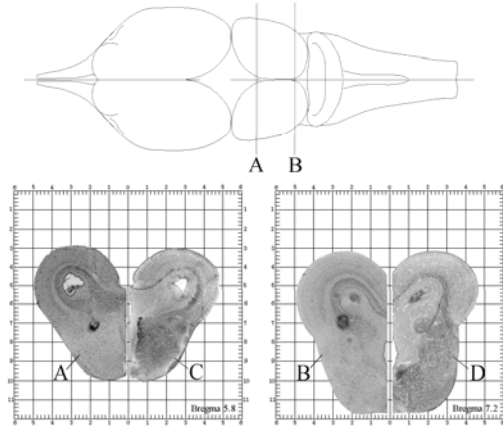


Fig. 5. Anatomic referent for stimulation sites in the midbrain of the gekko. A, B: Coronal section (frozen section, neutral red staining). C, D: Corresponding brain atlas (paraffin section, HE staining).

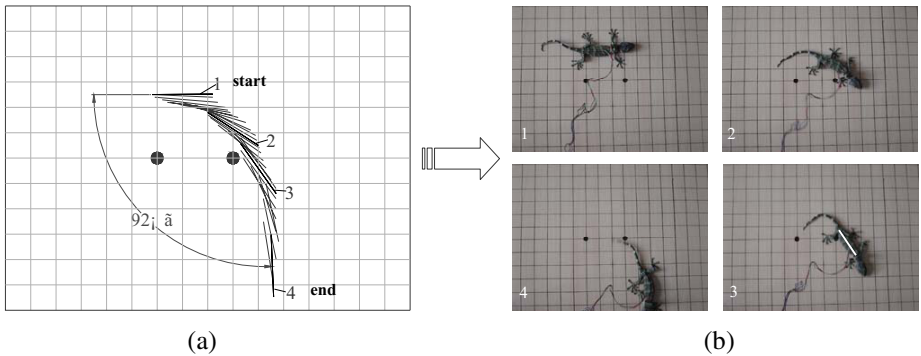


Fig. 6. Right turning motion induced by midbrain electrical stimulation in the awake *Gekko gekko*. (a) Schematic of the *Gekko*'s motion route. (b) Recording pictures of the specified position in the left route schematic diagram. The white line (the midline of the body between the forelimbs and hindlimbs of the animal) in the picture 3 indicates the gekko's position.

3.2 Results of Awake Studies

According to the results of acute studies, electrical stimulation was delivered through implanted electrodes of certain regions of the midbrain in 20 *Gekko gekkos*. Locomotor modes, such as right and left turn and forward crawling were successfully elicited. Fig. 6 shows the right turning of the gekko in the awaking test. The stimulus duration is about 3.72 s (93 frame total, 25 frames/s for the recording). We selected 28 frames of the recording to draw the route schematic diagram, and the midpoint of the gekko's forelimbs and hindlimbs were chosen as the two reference point. The line between the two reference points represents the position of the *Gekko* in each selected frame. From the Schematic of the gekko's motion route, we calculated that the turning angle was about 88°. Results show that the turning angle increases with the duration for electrical stimulation.

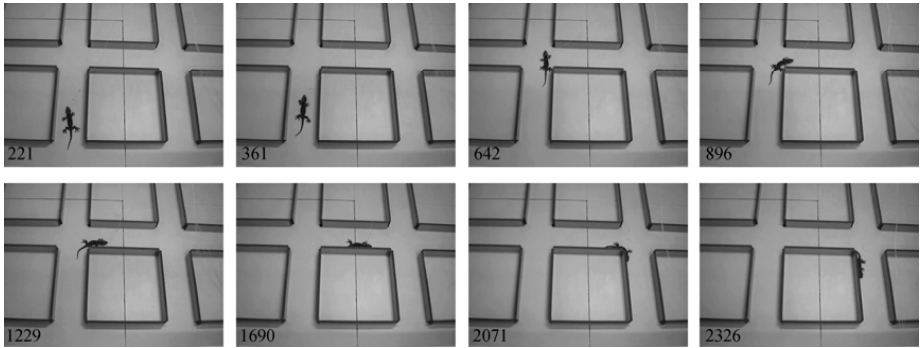


Fig. 7. Combined locomotion was induced successfully in a setting tunnel (forward going and right turning; the number in the picture indicate the serial number of the frame in the tape)

Furthermore, the experiment of combined locomotion which to combine the forward crawling and right turning was conducted successfully in a setting tunnel (Fig. 7).

4 Discussion

Our electrical stimulation study suggests that there are areas for locomotion control in gecko's midbrain. Anatomical studies revealed that the region might included the medial longitudinal fasciculus (FLM), medial longitudinal fasciculus□medial and lateral forebrain bundle (MFB), nucleus profundus mesencephali (PMI), stratum album periventriculare (SAP) and the red nucleus (Nrb).

The ongoing experiments of chemical microstimulation (L-glutamic acid microinjection) of gecko's midbrain have given some tentative confirmation to this conclusion. Locomotion of lateral curvature of vertebral column could be induced through chemical stimulation to the midbrain tegmentum. Whether there is MLR in the mesencephalic tegmentum is still to be identified.

The response reproducibility in awake studies is not as good as that of anesthetized stimulation. This was caused by several difficulties.

Geckos lack the tightly adhering brain cases of mammals and birds and, instead they possess an enormous subarachnoid space (Distel, 1978); the brain tissue is supported mostly by the cartilage and connective tissue. So the shape and position of the brain tissue is easy to change when it is pressed by electrodes. And most important, there was no midbrain atlas for *Gekko gekko*. For this reason, we carried out the preliminary preparation of the geckos' brain atlas and engaged in the work now. However, it has a long road to go to set up a set of precise stereotaxic brain atlas for the *Gekko*.

In order to increase the accuracy markedly, we should perform the experiments on a larger sample of animals and improve the technique to implant the stimulated microelectrodes.

5 Conclusions

The present results imply a crucial role of *Gekko*'s midbrain neurons in the initiation of locomotion. And stimulation in freely moving, awake gekkos suggested that it is possible to carry out artificial induction on the *Gekko gekko*.

Acknowledgment

The authors wish to acknowledge Mr. Cai L, Ma S J, and Ma G L, for their participation in the experiment and the histology work.

This work was supported by the National Natural Science Foundation of China (Grant No. 60535020, 30400086), 863 Program (Grant No. 2007AA04Z201).

References

- [1] Autumn, K., Liang, Y.A., Flsieh, S.T., et al.: Adhesive force of a single gecko foot-flair. *Nature* 405, 681–685 (2000)
- [2] Gao, H.J., Wang, X., Yao, H.M., et al.: Mechanics of hierarchical adhesion structures of geckos. *Mech. Mater* 37(2, 3), 275–285 (2005)
- [3] Rizzo, N.W., Gardner, K.H., Walls, D.J., et al.: Characterization of the structure and composition of gecko adhesive setae. *J. R. Soc. Interface* 3, 441–451 (2006)
- [4] Sun, J.R., Guo, C., Cheng, H., et al.: Comparison of the setae between the dung beetle *Copris ochus* and the gecko *Gekko gekko* and the effects of deformation on their functions. *Acta Zoo Sin* 51(4), 761–767 (2005) (in Chinese)
- [5] Geim, A.K., Dubonos, S.V., Grigorieva, I.V., et al.: Microfabricated adhesive mimicking gecko foot-hair. *Nat. Mat.* 2(7), 461–463 (2003)
- [6] Sitti, M., Fearing, R.S.: Nanomolding based fabrication of synthetic gecko foot-hairs. In: *Proceedings of the IEEE Nanotechnology Conference*, Washington DC, USA, pp. 137–140 (2002)
- [7] Geim, A.K., Dubonos, S.V., Grigorieva, I.V., et al.: Microfabricated adhesive mimicking gecko foot-hair. *Nat. Mat.* 2(7), 461–463 (2003)
- [8] Dickinson, M.H., Farley, C.T., Full, R.J., et al.: How animals move: an integrative view. *Science* 288(7), 100–106 (2000)
- [9] Dai, Z.D., Sun, J.R.: Research progress in gecko locomotion and biomimetic gecko-robots. *Prog. Nat. Sci.* 17(1), 1–5 (2007) (in Chinese)
- [10] Guo, C., Dai, Z.D., Sun, J.R.: Current status and prospect of research on bio-robots. *Robot* 27(2), 188–192 (2005) (in Chinese)
- [11] Talwar, S.K., Xu, S.H., Hawley, E.S., et al.: Rat navigation guided by remote control. *Nature* 417(2), 37–38 (2002)
- [12] Adams, D.B.: Cells related to fighting behavior recorded from midbrain central gray neuropil of cat. *Science* 159, 894–896 (1968)
- [13] Adams, D.B.: Brain mechanisms of aggressive behavior: An updated review. *Neurosci. Biobehavi. Revi.* 30, 304–318 (2006)
- [14] Robinson, T.E.: Electrical stimulation of the brain stem in freely moving rats: I. Effects on behavior. *Physiol. Behav.* 21(2), 223–231 (1978)

- [15] Robinson, T.E., Vanderwolf, C.H.: Electrical stimulation of the brain stem in freely moving rats: II. Effects on hippocampal and neocortical electrical activity, and relations to behavior. *Exp. Neurol.* 61(3), 485–515 (1978)
- [16] McClellan, A.D., Grillner, S.: Activation of 'fictive swimming' by electrical microstimulation of brainstem locomotor regions in an in vitro preparation of the lamprey, central nervous system. *Brain Res.* 300, 357–361 (1984)
- [17] Jordan, L.M.: Initiation of Locomotion in Mammals. *Annals of the New York Academy of Sciences* 860, 83–93 (1998)
- [18] Jean, M.C., Céline, B.L., Réjean, D.: Bimodal locomotion elicited by electrical stimulation of the midbrain in the salamander *Notophthalmus viridescens*. *J. Neurosci.* 23(6), 2434–2439 (2003)
- [19] Smeets, W.J.: A forebrain atlas of the lizard *Gekko gekko*. *J. Comp. Neurol.* 254, 1–19 (1986)
- [20] Hoogland, P.V., Vermeulen-Vanderzee, E.: Efferent connections of the lateral cortex of the lizard *Gekko gekko*: evidence for separate origins of medial and lateral pathways from the lateral cortex to the hypothalamus. *J. Comp. Neurol.* 352(3), 469–480 (1995)
- [21] Bruce, L.L., Neary, T.J.: Afferent projections to the lateral and dorsomedial hypothalamus in a lizard, *Gekko gekko*. *Brain Behav. Evol.* 46(1), 30–42 (1995)
- [22] Russchen, F.T., Jonker, A.J.: Efferent connections of the striatum and the nucleus accumbens in the lizard *Gekko gekko*. *J. Comp. Neurol.* 276(1), 61–80 (1988)
- [23] Gonzalez, A., Russchen, F.T., Lohman, A.H.: Afferent connections of the striatum and the nucleus accumbens in the lizard *Gekko gekko*. *Brain Behav. Evol.* 36(1), 39–58 (1990)
- [24] Li, G.F., Meng, S.Q., Jiang, S.Y.: Connections of rostrallateral area of the anterior dorsal ventricular ridge in lizards *Gekko gekko*. *Zoological Res.* 22(1), 74–77 (2001) (in Chinese)
- [25] Kennedy, M.C.: Vocalization elicited in a lizard by electrical stimulation of the midbrain. *Brain Res.* 97, 321–325 (1975)
- [26] Lan, S.C., Zhang, G.Q.: A study of the production of phonation reaction in *Gekko gekko* by stimulation of the midbrain. *Acta Zoo Sin* 28(1), 15–21 (1982) (in Chinese)
- [27] Guo, C., Dai, Z.D., Ji, A.H., et al.: Study on the regulation and control mechanism of the gecko's toes. *Chin. J. Biomed. Engin.* 25(1), 100–104 (2006) (in Chinese)
- [28] Wenbo, W., Zhendong, D., Hua, T., Ce, G., Juirong, S.: A stereotaxic method and apparatus for the *Gekko gekko*. *Chinese Science Bulletin* 53(7), 1107–1112 (2008)
- [29] Distel, H.: Behavior and electrical brain stimulation in the green iguana, *Iguana iguana* L. 11. Stimulation effects. *Exp. Brain Res.* 31, 353–360 (1978)

How Does “Intelligent Mechanical Design Concept” Help Us to Enhance Robot’s Function?

Amir A.F. Nassiraei and Kazuo Ishii

Graduate School of Life Science and Systems Engineering
Kyushu Institute of Technology
2-4 Hibikino, Wakamatsu-ku,
Kitakyushu City, Fukuoka 808-0196, Japan
{nassiraei, Ishii}@brain.kyutech.ac.jp

Abstract. As the study of autonomous mobile robots grows in popularity in recent years, the demand for designing simple, suitable, and reliable robot mechanics has also increased. However, a survey through literature reveals little about the mechanical design process or unified methodology to actually design proper mechanics for mobile robots. The mechanical design for the mobile robots is rather different from conventional industrial robots/manipulators used in automation of industrial process. There are limits on, among other things, the size and weight, the number and type of actuators/sensors, the power supply, the robot functions, and the constraint of environment where robots will be used. Therefore, we aim to share our experiences in the mechanical design process, especially to those new in this area. This is done through outlining the considerations and exploration new mechanical design concept, called “Intelligent Mechanical Design (IMD)”. The IMD is the concept on which the “Mecha-Telligence Principles (MTP)” and “Mecha-Telligence Methodology (MTM)” for the mechanical design of autonomous mobile robots are based. The MTM, involves seven mechanical design principles (MTP), is employed to maximize the designer’s creativity and lead to simpler, more suitable, mechanically superior solutions for complex problems. In this article we show, not only, how the MTP/MTM can be applied in design process of whole robot mechanics, but also, how they satisfy the designer perspective in investigating issues concerning what mechanism or mechanical parts are required to enhance the robot’s function. This approach is accomplished by exploring the definition of environmental niche and its related constraints which form the first-constituent principle in MTP. After defining all necessary terms, a practical mechanical design is considered to investigate the feasibility of the presented design methodology.

Keywords: Mechanical design, Intelligent design, Mobile robot, Autonomous robot.

1 Introduction

Early development of robotics research in the 1960s and 1970s was focused on industrial robots/manipulators for the automation of industrial processes [1]. Mechanical manipulators resemble human arms are deployed in the factories for various automation tasks. In the 1980s, robots started walking out of the manufacturing floors in the form of wheeled or legged mobile mechatronic systems

and underwater autonomous vehicles. The roles of robots are no longer limited to automated factory workers but are changing into exploration for hazardous, human-unfriendly, extreme environments, and servants [2] to provide surveillance, security, and cleaning tasks. Ingenious autonomous robotic systems that equipped with artificial intelligence capability resemble biological counterparts which were emerging in the late 1990s, such as Sonys Aibo robotic dog [3, 4, 5], and Hondas humanoid robots from P2, P3, to Asimo [6, 7]. These systems not only walked out of factories and service sector but also walked into our everyday life and households. Eventually these robots are going to co-habit with humans to provide assistance and cares.

Thereby, it is expected that robots with different degrees of autonomy and mobility will play an increasingly important role in all aspects of human life. To do this, robots must become much more complex than they are today in their hardware, software and mechanical structures. The drawbacks of increasing robot complexity may lead to low reliability and increasing size, weight, cost, power consumption, and motion limitation. To solve these problems, the simplification of robots mechatronics is critical to their design. The field of robotic mechanical design has advanced so far based on intuition, creativity and human ingenuity. However, a survey through literature reveals little about the mechanical design process or unified methodology to actually design such systems. Therefore, this article aims to share our experiences in the mechanical design process, especially to those new in this area. As it has been described in our previous paper [8], the robot design is done through outlining the considerations and exploration new mechanical design concept, called “Intelligent Mechanical Design (IMD)”. Exploring this concept produces landmarks in the territory of mechanical designing in the form of seven design principles. The design principles, named “Mecha-Telligence Principles (MTP)”, provide guidance on how to design mechanics for autonomous mobile robots. To show how MTP can be applied in the design process we proposed a novel methodology, we named this the “Mecha-Telligence Methodology (MTM)”. This methodology assists the designer to create and design simple, and sufficient mechanical solutions for problems with different degrees of complexity [8, 9]. In this methodology suitable optimum mechanics are designed by considering the robots tasks, behaviors, morphology, and analysis of the environmental and physical-morphological constraints within the design process.

This paper is divided into three main parts. In the section 2, to enhance the readers understanding, some of the important points regards to the IMD, MTP, and MTM, which are excerpted from our previous paper, will be briefly described [8]. In the third section, the extend-definition of environmental niche and its related constraints are introduced to show how the MTP/MTM can be implemented, not only, in design process of whole robot mechanics, but also, in design of mechanism or mechanical parts which are required to enhance the robot’s function. Finally in the last section, we investigate the feasibility of the proposed methodology by applying it to the mechanical design of an autonomous

mobile soccer robot. In this educational project we show how a novel ball-kicking-lifting-holding device can be designed by employing MTM in the design process.

2 Mechanics and Intelligence

One of the fundamental question in the field of mechanics related to design of an autonomous mobile robot is that: “What is the ideal mechanical design for an autonomous mobile robot which can perform the defined desired behavior(s) in an environment where it will be used?”

Thinking deeply about this basic question reveals two main problems. First one is, the exact meaning of the term of “ideal” in relation to a robot being reliable, robust, simple, suitable, *etc.* And second one is, the lack of exact definitions for these terms when are applied in the mechanical design of an autonomous mobile robot. In this paper we tackle these problems and propose a methodology to integrate all such terms with one: “Intelligent mechanical design (IMD)”. Note that the meaning of “Intelligent” as presented here, is not the same as in common phrases such as “Intelligent design”, “Intelligent mechanics”, “Mechanical intelligence”, and “Intelligent designer”. “Intelligence” is used here as an umbrella term for similar and related concepts.

2.1 What Is Intelligence?

“Intelligence is a large field and the human being is not yet ready to even understand its fundamentals. Maybe he will never ever understand what it’s all about. We are living in a huge complex environment and nature is just too complex to explain in three to four sentences. Intelligence is something that was created by nature and sure not by us humans ourselves” [10]. Many leading experts in their fields have attempted to define and describe intelligence. The results have been a myriad of definitions with none of these experts seeming be sure about even their own definition. One wonderful approach not only to meaning of “intelligence”, but also to use of the term in the design process for autonomous agents is found in a book by the title “Understanding Intelligence” [11]. The authors use the concept of intelligence to define what they call complete agents and, in turn, they use this concept to form one of their design principles (the complete agent principle) for the design of autonomous agents” [1].

¹ Note that all selected terms to describe the concept of “intelligent mechanical design” and also seven mechanical design principles (except the first principle) are our original. Only the way to the description the term of “intelligent mechanical design” and the idea to establish the landmarks of the territory of mechanical designing in the form of different principles are inspired from the description of “intelligence” term and the design principles of “Autonomous agent” presented in the book of Understanding Intelligence .While Pfeife discusses the definition of “Intelligence” and design process of “autonomous agents”, here the concept of “Intelligent mechanical design” and design process of “Mechanics of autonomous mobile robots” are proposed.

2.2 Intelligent Mechanical Design: IMD

Following Pfeifer’s approach in attempting to create an acceptable definition of “intelligence” we will briefly discuss the related terms necessary to produce a suitable definition of IMD.

Intelligent Mechanical Design (IMD): This term is used to describe complete mechanical designs (designs that are self-controllable, reliable, feasible, and compatible) that resolve the functionality- usability trade-off in an optimal way. Mechanical design must always be considered with respect to a particular environmental niche.

Self-controllable: A mechanical design is self controllable, if the robot can be controlled by a set of internal hardware, independent of external motive forces. Self-controllability should always be considered with respect to a specific system.

Reliable: A mechanical design is reliable, if, in the majority of cases, the robot fulfills its design specification.

Feasible: A mechanical design is feasible, if the robot can be manufactured as a real mechanical structure using current manufacturing methods and commercial materials. Feasible mechanical design is influenced by a number of requirements, such as cost, size, weight, water tightness, dust resistance, etc.

Compatible: A mechanical design is compatible, if the design of the sensory-motor architecture has compatibility with the size, weight and shape of the hardware. Compatibility should always be considered with respect to a specific system.

The functionality-usability trade-off: Represents a compromise between, on the one hand, adding new functionality, and on the other, achieving usability conditions [12].

Environmental niche: This term will be explained in detail in the next section.

2.3 Mecha-Telligence Principle: MTP

The concept of IMD described above is the basis of the seven design principles which form the MTP. MTP guides us to ask the right questions when designing self-controllable, reliable, feasible, and compatible mechanics for autonomous mobile robots (see Fig. 1). The definition of robot environment, behaviors and tasks is highlighted as Meta principles to underscore their centrality to the mechanical design process for autonomous mobile robots. Also, note that using the term IMD to describe complete mechanical designs, is the landmark as second principle. This section describes the seven design principle.

(1) The Three-constituent principle: In the approach presented here robot design forms a compromise between “Robot Environment” and “Robot Desired Behavior”. Designing mechanical parts for autonomous mobile robots always

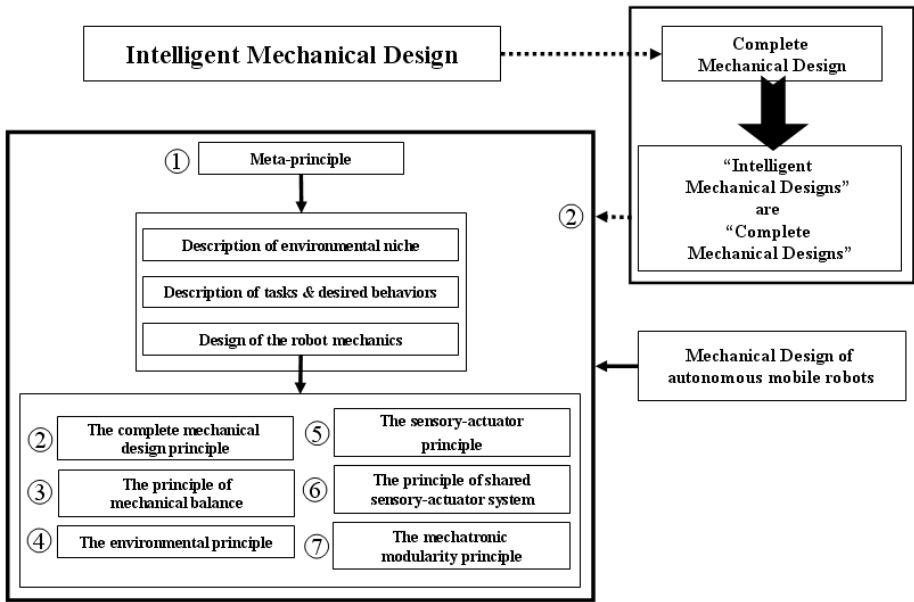


Fig. 1. Overview of design principles of mechanical design of autonomous mobile robots, MTP

involves three constituents: (I) definition of environmental niche; (II) definition of desired behaviors and tasks; (III) design of robot mechanics [11]. Constituent (III) has been split into design principles 2 through 7.

(2) The complete-mechanical design principle: This principle states that intelligent mechanical designs are complete, that is, from sub-section 2.2, complete mechanical designs are self-controllable, reliable, feasible, and compatible.

(3) The principle of mechanical balance: This principle has two aspects. (1) The complexity of the mechanical design has to match the complexity of the robot’s desired behaviors, (2) Robot mechanics should not be designed “in a vacuum” but rather must take the sensory system and hardware architecture into account.

(4) The environmental principle: This principle states two things: that the physics of the system-environment interaction and constraints of the environmental niche should be exploited [11]. The environmental principle is significant in that it has direct effect on the simplicity and reliability of a mechanical design.

(5) The sensory-actuator principle: This principle states that the type and position of the sensors and actuators in a system has a direct effect on robot functionality, performance, simplicity, and reliability. By designing or selecting suitable and sufficient sensors and actuators, and correctly fixing their position

in the system, the performance and functionality of the robot is enhanced. This principle interacts strongly with the principle 6.

(6) Shared sensory-actuator system principle: The principle requires sparing use of actuators and sensors numbers. The number of actuators and sensors used for a system is a significant mechanical design parameter that has a direct influence on system reliability.

(7) The mechatronics modularity principle: This principle states that a robot should have a modular architecture in its electronics and mechanics. This principle can play a significant role in both the mechanical reliability mentioned in the second principle and ease of maintenance.

2.4 Mecha-Telligence Methodology: MTM

To show how MTP can be applied in designing an autonomous mobile robot, we propose a novel methodology: the MTM (see Fig. 2). Mechanical design in the proposed methodology is based on preference classification of the robot specification. This specification is created by describing the interaction of the robot with its environment and the physical parameters of the robot mechatronics (principle 1). In this approach the robot specification is grouped into high- and low-level specifications which can be expressed as tasks (desired behaviors) and the physical parameters of the robot. The high-level-specification has two layers:

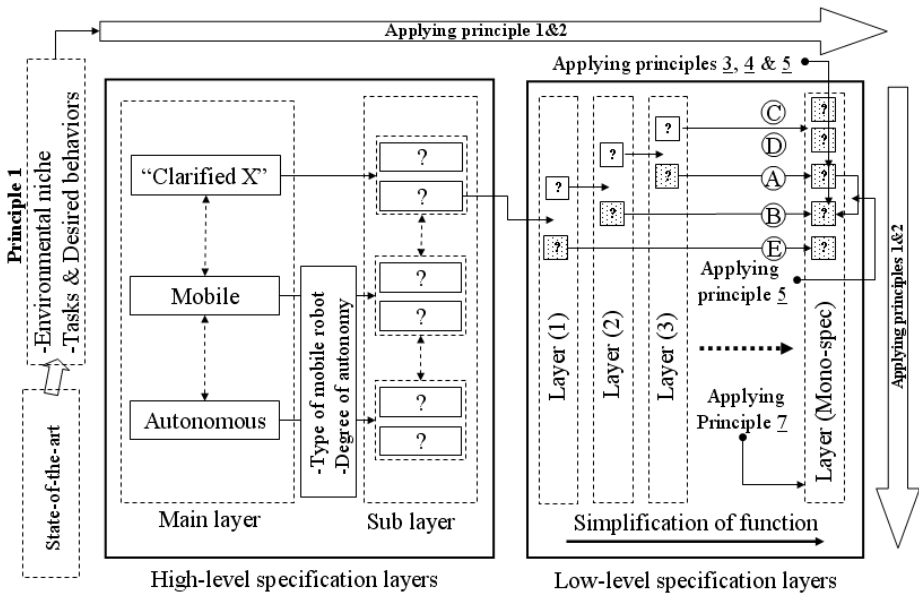


Fig. 2. Overview of MTM for mechanical design of autonomous mobile robots. Robot task is variable “X”.

main and sub, and is derived from the robot’s tasks and its interaction with the environment in which the robot will be used. A low-level-specification consists of a set of layers explaining the physical setup of the robot, its body, sensory, and motor systems. The main goal of this analytical process is to produce a mono-spec layer (the last layer of low-level-specification) defining a basic function and selecting a sensor for a single task or behavior. The mechanical design is started from these crucial mono-specs, then the mono-spec design is extended by adding the minimum actuators and sensors to the design (principle 6). In each step we attempt to produce a suitable solution by considering robot morphology and actuator design, by applying the description of environmental and physical-morphological constraints, and by employing passive mechanisms which have inherent intelligence characteristics (principle 3 and 4). Mechanical design is finalized by considering the suitable and sufficient positioning of the sensory-motor system (principle 5) and modularity of the robot’s mechatronics (principle 7). Note that the designer must consider principles 1 and 2 simultaneously in whole design process.

3 Environmental Niche and the Related Constraint

The environmental niche for a robot can be thought of as the range in each variable in its environment. We use the term of “environment” here to mean essentially two things: first, the direct-physical meaning: the area or space where the robot is used, including natural and artificial objects; second, the indirect-physical meaning: the artificial parameters governing its function. These terms requires some explanation, here we describe some examples for for better understanding. Figures 3 to 6 show four examples of can-collecting robot with different particular environment.

First example: In this example, a robot is designed to collect the cans in its environment and brings them to the corner of the room (see Fig. 3). The environmental niche and its constraints can be itemized as follows:

Environmental niche:

- A flat surface (Direct)
- Indoor environment (Direct)
- A set of cylindrical can (Direct)
- A ledge (Direct)

Environmental niche constraint:

- Can size (D, H) (Direct)
- Ledge height (H1) (Direct)

Second example: In the second example, the task of the robot is to collect objects in its environment and bring them to a can-room located in the corner of the room, (see Fig. 4). In this example the cost for making the robot is also limited. By adding a can room and the cost limitation to the environment of

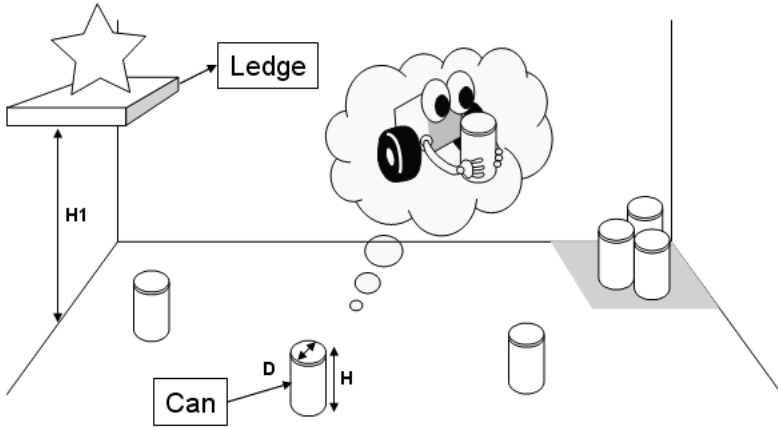


Fig. 3. First example of can-collecting robot

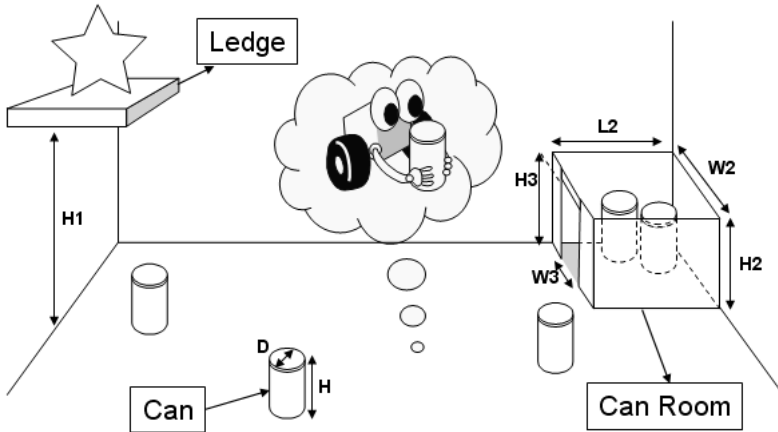


Fig. 4. Second example of can-collecting robot

the robot, the environmental niche and relative constraints will be changed as follows:

Environmental niche:

- A flat surface (Direct)
- Indoor environment (Direct)
- A set of cylindrical can (Direct)
- A ledge (Direct)
- A can room (Direct)
- Cost limitation (Indirect)

Environmental niche constraint:

- Can size (D, H) (Direct)
- Ledge height (H1) (Direct)
- Can room size (L2, W2, H2) (Direct)
- Can room door size (W3, H3) (Direct)
- Cost (cost < X \$) (Indirect)

In this example "cost limitation", which mean be considered as a user request, illustrates the second aspect of environmental niche.

Third example: Third example shows the case to consider a robot which is designed to compete in a can-collecting competition (see Fig. 5). The task of the robot is the same as the previous example. The rules of the game include limitations in size of the robot and the robot should fit in a box with specific dimensions. In this case, the environmental niche and the related constraint can be defined as follows:

Environmental niche:

- A flat surface (Direct)
- Indoor environment (Direct)
- A set of cylindrical can (Direct)
- A ledge (Direct)
- A can room (Direct)
- Size limitation (it is considered based on the game rules) (Indirect)

Environmental niche constraint:

- Can size (D, H) (Direct)
- Ledge height (H1: if $H4 > H1$) (Direct)
- Can room size (L2, W2, H2) (Direct)

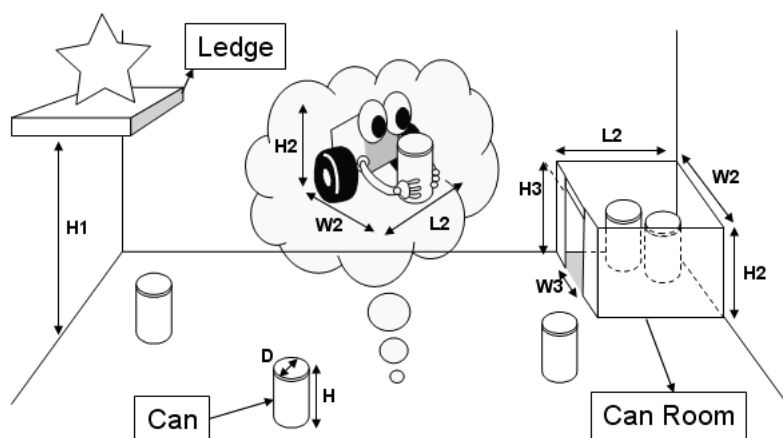


Fig. 5. Third example of can-collecting robot

- Can room door size ($W3$: if $W3 < W4$, $H3$: if $H3 < H4$) (Direct)
- Maximum robot size ($L4$, $W4$, $H4$) (Indirect)

Note, because of the robot size limitation, some environmental niche constraints should be considered to be conditional constraints. As an example, the height of the ledge ($H1$) is a constraint, if the ledge is lower than the maximum height of the robot ($H4 > H1$).

Forth example: In the last example, it is assumed that we already have a robot with a particular architecture. The aim is to enhance the robot task performance by designing mechanism or mechanical parts which are required to rotate the camera (see Fig. 6). The environmental niche and relative constraint can be recognized as follows:

Environmental niche:

- A flat surface (Direct)
- Indoor environment (Direct)
- A set of cylindrical can (Direct)
- A ledge (Direct)
- A robot (Indirect)
- Robot size limitation (it is considered based on the game rules) (Indirect)

Environmental niche constraint:

- Can size (D , H) (Direct)
- Ledge height ($H1$: if $H3 < H1$) (Direct)
- Robot size without camera ($L2$, $W2$, $H2$) (Indirect)
- Maximum size of robot ($L3$, $W3$, $H3$) (Indirect)

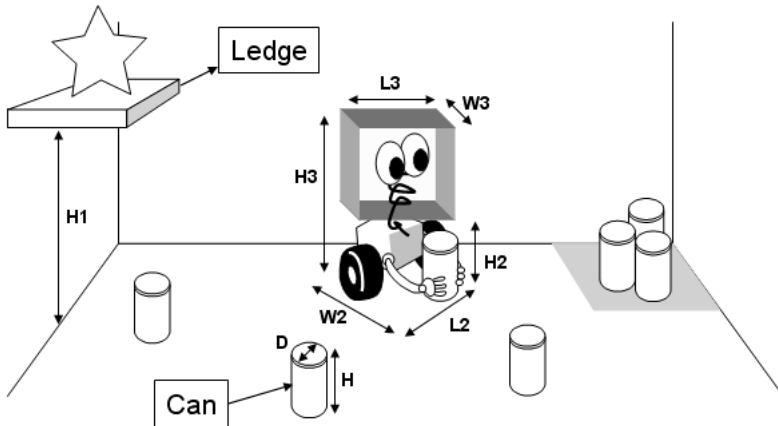


Fig. 6. Forth example of can-collecting robot

In this example, since the size of robot has direct effect to the design of the camera mechanism, the "existing robot" is considered as an environmental niche. Also any limitations in the robot hardware, such as number of sensors/actuators which can be added to the robot system, are recognized as the environmental niche. This example described here to show the MTP/MTM can be applied not only in design process of whole robot mechanics but also in the case where necessary parts should be installed to the existing robot to enhance its function and task performance. In this approach all design parameters that influence the mechanical design can be counted as a part of environmental niche and must be considered in the forth principle of MTP presented in previous section.

4 Design Process of an Autonomous Soccer Mobile Robot

RoboCup is one of grand challenges to promote AI and Robotics related research [13]. In RoboCup games, many robots rush around on the field and each robot must be tough and robust to physical collisions and breakdowns in hardware system. RoboCup robot requires high reliability and easy-maintenance, moreover, adaptability to new regulations. RoboCup robot is the good subject to show how our new methodology works. This section is divided into two parts. First, we introduce our approach in realization of a simple, robust, and valuable platform for "Musashi robots" [14] designed based on MTP/MTM. "Musashi" robots are series of autonomous mobile soccer robots which have fully mechatronics modular architecture including an omni-directional moving mechanism and an omni-vision system, aiming to participate in RoboCup Middle size League. Second, we investigate the feasibility of the presented design methodology by applying MTP/MTM in design process of strong ball-kicking device including ball-lifting and -holding mechanisms for our “Musashi” robot.

4.1 Design Process of “Musashi” Robot

The first step in MTM is to describe the tasks, desired behaviors, environmental niche, and environmental niche constrain, as shown in Fig. 2. To extract the sub-layer from main-layer, it is necessary that the type of robot and its degree of autonomy are also specified. Let us start with a basic question: "what is ROBOCUP?"

RoboCup is an international joint project to promote AI, robotics, and related field. It is an attempt to foster AI and Intelligent robotics research by providing a standard problem where wide range of technologies can be integrated and examined. RoboCup chose to use *soccer game* as a central topic of research, aiming at innovations to be applied for socially significant problems and industries [13, 15].

Robot task

By considering the aim of RoboCup, "playing soccer" is the robot's main task.

Desired behavior

Based on "RoboCup Middle size League" rules and common sense about soccer, the desired behaviors can be described to five following items:

- Put the robot in the field
- Robot gets the desired commands (such as start the game, corner kick, throw in, and etc.) sent by a referee from a host computer via wireless communication.
- Robot moves autonomously in the field, detects object in its environment (Object detection), and avoids them (Obstacle avoidance).
- Robot closes to the ball and carries it into the goal (play with ball)
- Robot communicates with other robots based on the team strategy algorithm.

Environmental niche and the relative constraints

Alternatively, regard to "RoboCup Middle size League" rules, the environmental niche and the relative constraints can be defined and itemized as follows (Fig. 7):

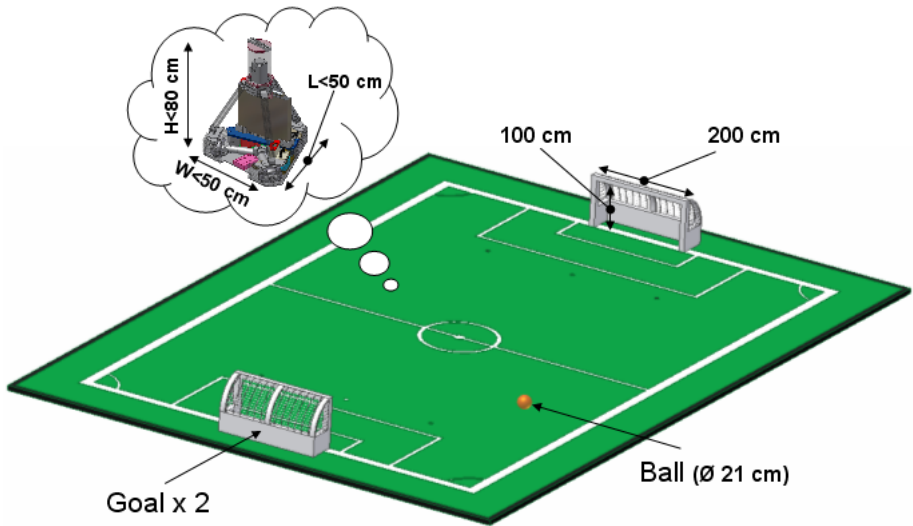


Fig. 7. Environmental niche (Designing soccer robot, "Musashi")

Environmental niche:

- A flat surface (Direct)
- Indoor environment (Direct)
- RoboCup field (a flat surface) (Direct)
- RoboCup rules (Indirect)

Environmental niche constraint:

- Two goals (White) (Direct)
- One ball (Orange, D=21 cm) (Direct)
- Robot size (L<50, W<50, H<80 cm) (Indirect)
- Robot weight (< 80 kg) (Indirect)
- Robot color (Black) (Indirect)

In this case, since the height of robot is limited to 80 cm, the goal size is not counted as a environmental niche constraint.

Degree of autonomy and mobility: Robots should autonomously perform all actions necessary to play soccer, without human intermediary. Only the start, stop, and desired commands will be sent via wireless communication to the robots by a side-referee. Robot needs to be designed as a wheeled-untethered robot (Fig. 8).

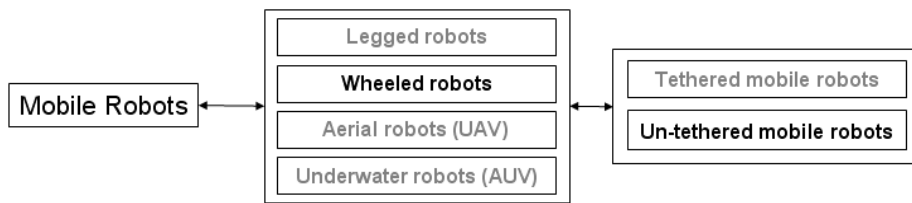


Fig. 8. “Musashi” robot is designed as a wheeled-untethered mobile robot

4.1.1 Simplification of the “Musashi” Robot Design Functions: Applying MTM

For the steps above, the high-level specification layers including the main- and sub-layer are seen in the left columns in Fig. 9. The variable “X” in the main-layer in Fig. 2, the robot task, is clarified to “Play soccer” term. Alternatively, the sub-layer is derived from the main-layer based on description of the robot desired behaviors and its degree of autonomy and mobility. The right columns indicates the generation of layer-1, -2, and mono-spec layer, respectively. In these columns the dash-arrows and -horizontal boxes show the terms which are on the process of simplification and the black ones indicate the terms which are recognized as a simple basic-function (e.g. robot moving mechanism illustrates in mono-spec layer) or sensor-selecting for a single task or behavior (e.g. the type and position of sensors which are required for object detection, obstacle avoidance, and etc., as shown in layer-2). Figure 9 (A to D alphabets show in right side of figure) also illustrates the functional design priority from a mechanical parts design point of view.

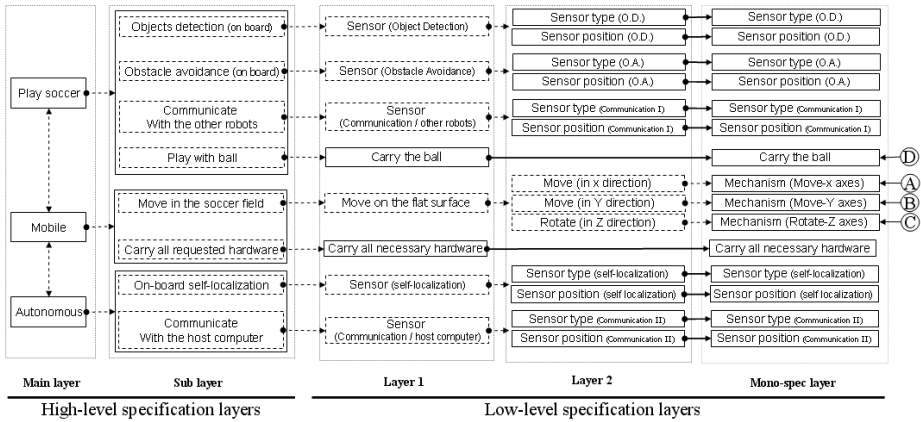


Fig. 9. Mecha-Telligence methodology applied in designing an autonomous mobile soccer robot

4.1.2 Design Process of “Musashi” Robot: Applying MTP

This sub-section provides an overview of our robot design and its architecture. It also shows how the MTP are applied in the design process. Figure 10 shows some popular moving mechanisms to satisfy the functions (A) to (C). The drive wheels are usually placed on each side of the robot. A non-driven wheel, often a castor wheel, forms a three- or four-support structure for the body of the robot (Mechanism-I to -V, Fig. 10). In fact, castors can cause problems if the robot reverses its direction. Then the castor wheel must turn half a circle and, in the process, the offset swivel can impart an undesired motion vector to the robot. This may result in to a translation heading error [16]. Straight line motion is

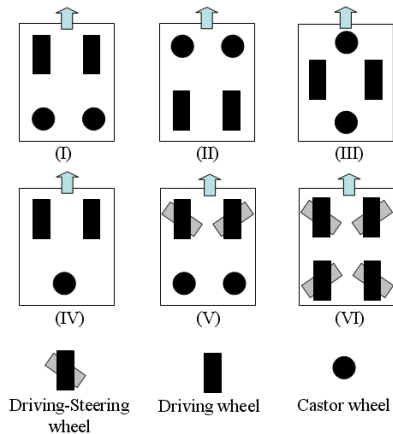


Fig. 10. Different types of differential moving mechanism

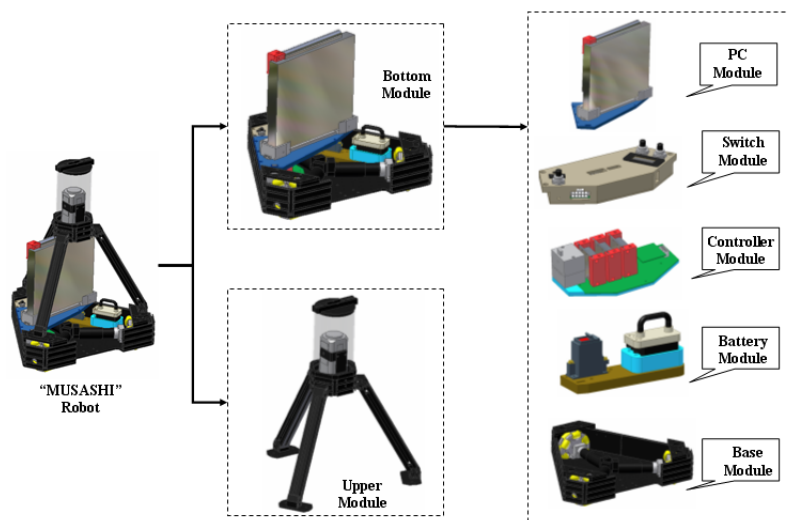


Fig. 11. “Musashi” robot modular architecture

accomplished by turning the drive wheels at the same rate in the same direction however that is not as easy as it sounds. Moving mechanism-VI has four driving-steering wheels that it causes stable motion, but based on the third principle of MTP, the complexity of its mechanical design does not satisfy the complexity of the robot’s desired behavior.

As the result of survey in the existing moving mechanism and consideration of the Principal 3 (*The principle of mechanical balance*), we designed an omnidirectional platform including three set of drive units arranged in the shape of triangle into the robot base as shown in Fig. 11 (*considering principle 5 and 6*). The dynamical and kinematic characteristics of the design allows a high maneuverability in the field, easy controllable for programing, and expected reliability and compatibility for the robot (*Principle 2: The complete-mechanical design principle*). Robots have been designed in such a way to satisfy the three environmental constraints, size, weight and color (*Considering principle 4*). In addition, “Musashi” robot is designed based on mechatronics modularity concept (*Applying principle 7*) [17, 18]. Regarding “Musashi” modular architecture, we designed and divided the robot into two main modules, a bottom module and an upper module (Fig. 11). The bottom module consists of five modules, PC-, Switch-, controller-, Battery-, and base-module. Using this approach, we could realize a simple, reliable, and robust robot, for which troubleshooting would be relatively easy and manufacturing could be done at low cost.

Object detection, collision avoidance, and self localization were performed by selecting an omni-directional camera as a robot’s vision sensor, installed in the top of the robot (*Applying principle 5 & 6*). An on-board wireless network device installed on the robot’s PC is used for robot communication with a host computer and also other robots. Note, all functions illustrated in the right column in Fig. 9

are realized, only, by designing the simple moving mechanism (Omni-directional mechanism), employing the suitable vision system (Omni vision), and selecting a proper PC including an on-board wireless network.

4.2 Design Process of a Kicking Device for “Musashi” Robot

In 1997, RoboCup MSL robots had no kicking device. One year later at the second RoboCup tournament, the Freiburg team introduced the first kicking device to be used, and were champions for that year [19]. After 1998, the development of kicking devices became a key consideration for all participating teams [20, 21, 22]. In this section the design process of a novel ball-kicking-lifting-holding device, designed based on MTM, is described in detail.

As it is pointed out in the process design of “Musashi” robot, the first step in MTM is to define the robot tasks, desired behaviors, environmental niche/environmental niche constrain, and the type of robot and its degree of autonomy. Those definitions must be clarified, not only, for designing of whole robot mechanics, but also, for investigating issues concerning what mechanism or mechanical parts are required for expanding the functions of existing robot. In case of designing a kicking device for “Musashi” robot, all the above terms have similar definition as our previous example, except the forth item of desired behavior and the description of environmental niche/environmental niche constrain. The forth item of the robot desired behaviors can be considered as follow: “Robot catches the ball, carries the ball, and *kicks it* into the goal (play with ball)”

Desired behavior

In this example, since the kicking device is installed in “Musashi” robot, only the forth item of the robot desired behaviors will be different comparing with our previous example:

- Put the robot in the field. (no change)
- Robot gets the desired commands. (no change)
- Robot autonomously moves, detects object, and avoids them. (no change)
- Robot closes to the ball, *holds the ball*, carries the ball, and *kicks/loop shoot it* into the goal (play with ball). (new)
- Robot communicates with other robots. (no change)

Environmental niche and the relative constraints

In this case we have a robot with a particular architecture (“Musashi” robot) and a fix low-level hardware (we do not want to modify the low-level hardware). Then, the environmental niche and the relative constraints can be defined and itemized as follows (see Fig. 12):

Environmental niche:

- A flat surface (Direct)
- Indoor environment (Direct)

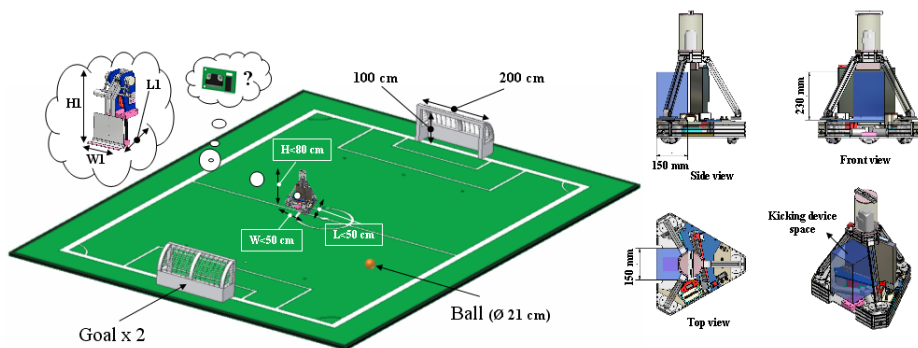


Fig. 12. Environmental niche (Designing kicking device)

- RoboCup field (a flat surface) (Direct)
- RoboCup rules (Indirect)
- A robot (Indirect)
- Hardware limitation (Indirect)

Environmental niche constraint:

- Two goals (Direct)
- One ball (D=21 cm) (Direct)
- Robot size (L<50, W<50, H<80 cm) (Indirect)
- Robot weight (< 80 kg) (Indirect)
- Robot color (Black) (Indirect)
- Kicking device/Position limitation (see Fig. 12-Right side) (Indirect)
- Kicking device/Size limitation (L1~150, W1~150, H1~230 cm) (Indirect)
- Hardware limitation (we do not want to modify the low-level hardware) (Indirect)

**4.2.1 Simplification of the Kicking Device Design Functions:
Applying MTM**

Figure 13 indicates the simplification process of the design functions regard to developing a strong kicking device. The description of the high-level specification layer refers to the previous example (Fig. 9). In such cases that the robot has already a particular structure, the terms relative to the target desired behavior will be only selected and simplified for the low-level specification layers. In this example the term of “play with ball” is considered and exploded to the more basic simple behavior and the function is finally split to six mono-functions, A to F alphabets show in the right side of Fig. 13. In general, three mechanisms are necessary to use the energy of storage energy elements or devices (such as spring, elastic, pneumatic and solenoid): (a) a mechanism to store energy, (b) a mechanism to maintain energy, and (c) a mechanism to release energy. This general principle is indicated in driving process of the layer-2 from the layer-1.

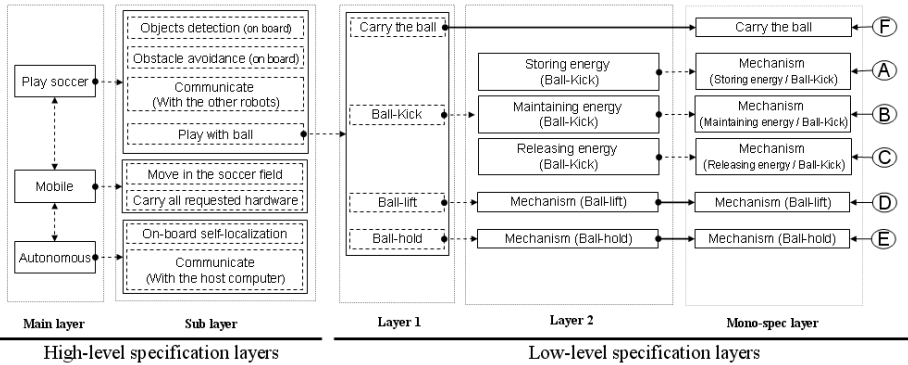


Fig. 13. Mecha-Telligence methodology applied in designing an autonomous mobile soccer robot

4.2.2 Design Process (Kicking Device): Applying MTP

Regards to the sixth environmental niche constraint (*applying principle 4*), three alternative can be considered for designing kicking device mechanism as shown in Fig. 14. Since the actuators which they can generate the force F require more space (*applying principle 4 considering the seventh environmental niche constraint*), we selected the third alternative as a start point to realize a compact, strong, and simple shooting mechanism.

Storing energy (Function A): A cam mechanism is used to charge the torsion springs installed in joint A and store energy (*applying principle 4: exploiting the*

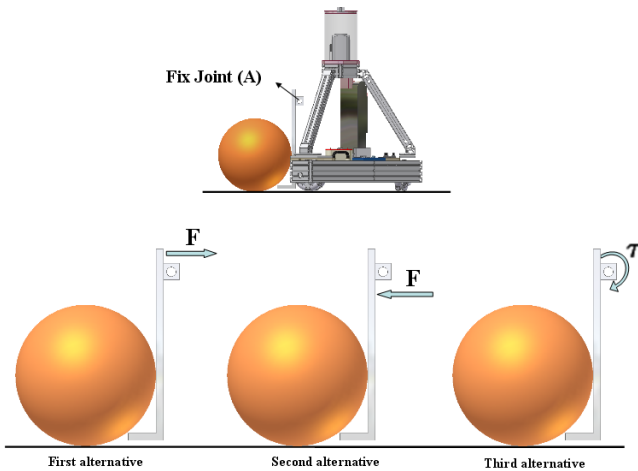


Fig. 14. Three alternative for kicking device mechanism

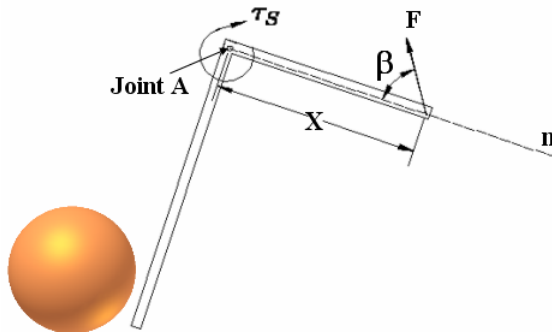


Fig. 15. Illustrate basic concept of cam charger mechanism. Joint A is fixed and the torsion springs, as a resistance torque, are installed in this joint. τ_s = spring torque (resistant torque), F = Motive force , X = distance between joint A and the point where force F is applied, and β = angle between force F and the direction of n .

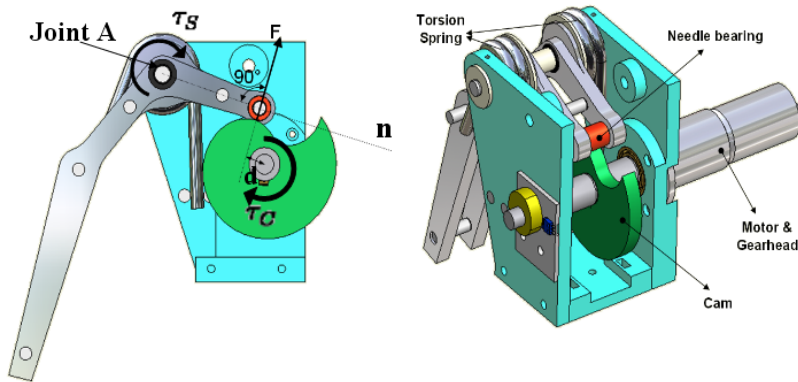


Fig. 16. This figure shows the relation between the cam and the torsion spring

eighth environmental niche constraint). The basic concept of this mechanism is shown in Fig. 15. With regard to Eqs. (1) and (2), the motive force F to charge the torsion spring is minimized while the force F is perpendicular to the n axis ($\beta = 90$ degrees) under the condition that the torque τ_s and X take certain values.

$$F = \frac{\tau_s}{X \cdot \sin \beta} \tag{1}$$

$$\beta = 90^\circ \Rightarrow F_{min} = \frac{\tau_s}{X} \tag{2}$$

The main function of the specially designed cam is keeping the angle β equal to 90 degrees during the spring charging process (see Fig. 16). The torque of a motor needed to charge the spring will be minimized as in the following equation. (3).

$$\tau_C (min) = F_{min} \cdot d \tag{3}$$

Here, d is the perpendicular distance between the direction of the contact force F and the center of the cam C . In this mechanism, during the charging time, the perpendicular distance between the direction of the contact force F and the center of the cam (d in Fig. 16) decreases when the spring torque and the contact force F increase. The important point is that the more the spring is charged, the less the required motor torque is in the second half of the charging process [23].

Maintaining energy (Function B): At the completion of charging, the direction of force F is towards the center of the cam. The mechanism has an inherent characteristic to lock without any motor torque as shown in Fig. 17.

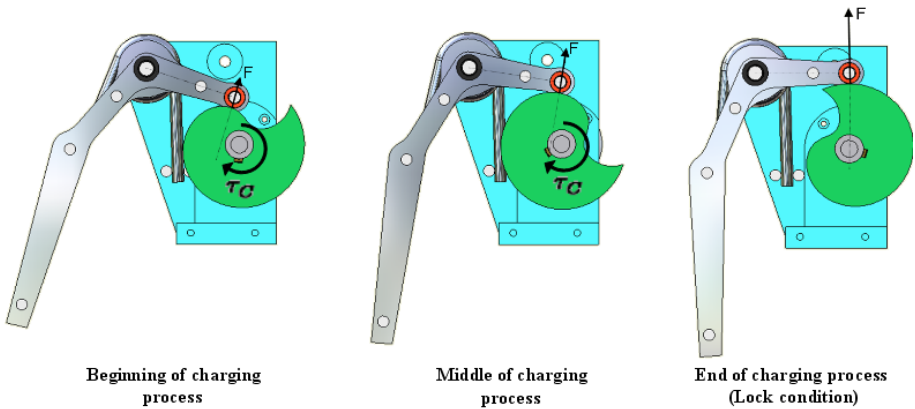


Fig. 17. Shows the sequence of charging of springs in beginning, middle, and end of the charging process

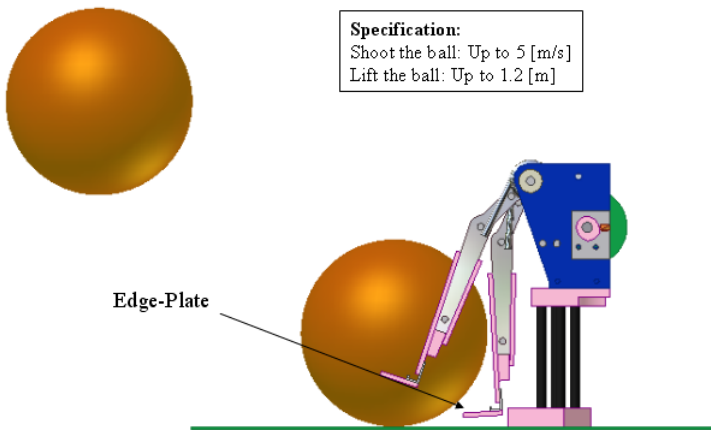


Fig. 18. Ball-lifting mechanism

Releasing energy (Function C): It is clear that when the motor continues to rotate after the locking process, the spring will be released rapidly.

Ball-lifting mechanism (Function D): Figure 18 indicates our simple solution to lift the ball (*Applying the principles 4 and 6*). By changing the width of the edge-plate we can adjust the parameter of lifting the ball up to 120 [cm].

Ball-holding mechanism (Function E): Figure 19 illustrates our simple linkage mechanism, installed inside of the cam charger mechanism using for ball-holding (*Applying the principle 6*). This linkage mechanism is activated and controlled by the same motor and limit switch used for ball-kicking as shown in Fig. 20. The key point is using the death area used for locking the "Cam Charger"

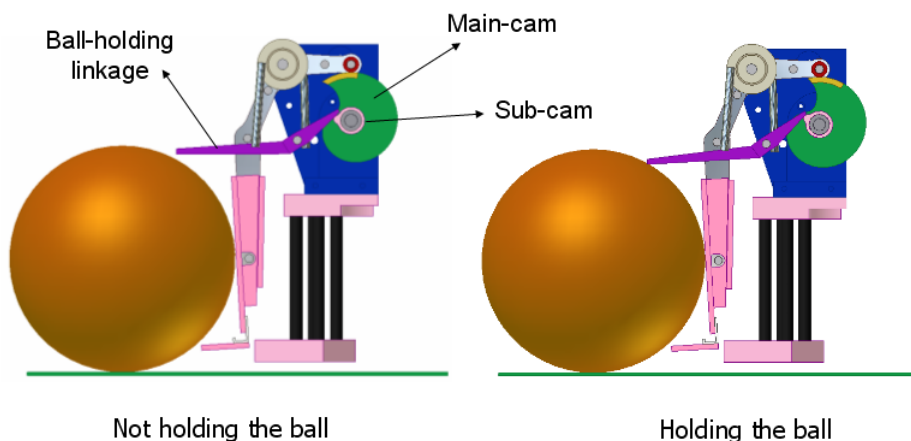


Fig. 19. Ball-holding mechanism

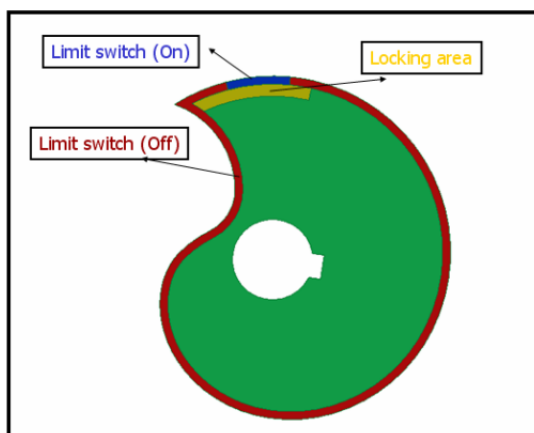


Fig. 20. Control sequences of the ball-holding mechanism

mechanism. In locking area, if the motor is rotating the kicking plate does not move but the linkage mechanism will be activated by pushing the sub-cam fixed to the main-cam.

5 Conclusion

In this article, the concept of “Intelligent Mechanical Design (IMD)” is presented to show how a mechanical structure can be designed to affect robot controllability, simplification and task performance. Based on the IMD concept, we propose a novel methodology (“Mecha-Telligence Methodology/MTM”) including seven design principles (“Mecha-Telligence Methodology/MTP”) for the mechanical design of autonomous mobile robot. Alternatively, we show the MTP/MTM can be implemented, not only, in design process of whole robot mechanics, but also, in design of mechanism or mechanical parts which are required to enhance the robot’s function. This approach is accomplished by exploring the definition of environmental niche and its related constraints which form the first-constituent principle in MTP. The feasibility of the proposed methodology was demonstrated by applying it to the mechanical design of a mobile autonomous soccer robot (“Musashi” robot) and the design process of a strong kicking device. In the first example, we discuss how MTP/MTM can lead the designer to realize a simple, robust, and valuable platform for “Musashi robots” which is done by selecting a proper moving mechanism, a suitable vision system, and designing fully mechatronics modular architecture. The second example introduces our approach in implementation of a compact-strong kicking device having the capability of shooting (up to 5.0 m/sec), lifting (up to 120 cm), and holding a ball, designed based on MTP/MTM. One of the features of developed kicking mechanism is that charging, maintaining and releasing the spring energy including kicking-, lifting-, and holding- a ball are realized by only employing a simple DC motor gearhead and controlling using a limit switch. Employing the developed Musashi robots, the Hibikino-Musashi team was ranked among the eight best teams at the RoboCup 2006 world championships in Bremen, was placed fourth at the RoboCup 2007 world champion ship in Atlanta, the second place in the RoboCup Japan Open in 2007, and was the champion and awarded the Most Valuable Player award at the RoboCup Japan Open in 2006 and 2008.

Acknowledgment

This work was partially supported by a grant of Knowledge Cluster Initiative and Kyutech 21st COE project by Ministry of Education, Culture, Sports, Science and Technology (MEXT).

References

- [1] Crisman, J.D., Bekey, G.: The Grand challenge for robotics and automation. *IEEE Robotics & Automation Magazine* 3, 10–16 (1996)
- [2] Engelberger, J.F.: *Robotics in Service*. The MIT Press, Cambridge (1989)

- [3] Friedman, B., Kahn Jr., P.H., Hagman, J.: Hardware companions?: What online AIBO discussion forums reveal about the human-robotic relationship. In: Proc. of CHI 2003, pp. 273–280. ACM Press, New York (2003)
- [4] Melson, G.F., Kahn Jr., P.H., Beck, A.M., Friedman, B., Roberts, T., Garrett, E.: Robots as Dogs?: Children’s Interactions with the Robotic Dog AIBO and a Live Australian Shepherd. In: Proc. in conference on Human Factors in Computing Systems, pp. 1642–1659 (2005)
- [5] Bartneck, C., Forlizzi, J.: Shaping human-robot interaction: Understanding the social aspects of intelligent robot products. In: Ext. Abstracts CHI 2004, pp. 1731–1732. ACM Press, New York (2004)
- [6] Hirai, K., Hirise, M., Haikawa, Y., Takenaka, T.: The development of Honda Humanoid Robot. In: Proc. of the IEEE International Conference on Robotics & Automation, Leuven, Belgium, pp. 1321–1326 (1998)
- [7] Honda Motor Co., Ltd, Asimo year, model (2000),
<http://world.honda.com/ASIMO/technology/spec.html>
- [8] Nassiraei, A.A.F., Ishii, K.: Concept of Intelligent Mechanical Design for Autonomous Mobile Robots. *Journal of Bionic Engineering* 4(4), 217–226 (2007)
- [9] Nassiraei, A.A.F.: Concept of Intelligent Mechanical Design for Autonomous Mobile Robots, PhD Dissertation, Kyushu Institute of Technology, Fukuoka (2007)
- [10] AI - Classwork Assignment 1. © Philip Izzy/s997143 (2001)
- [11] Fifer, R., Schemer, C.: Understanding Intelligence. Massachusetts Institute of Technology (1999)
- [12] Wu, Y., Van Slyke, C.: Interface complexity and elderly users: Revisited. In: Southern Association of Information Systems Conference, Savannah, Georgia, USA, pp. 289–294 (2005)
- [13] Matsubara, H., Asada, M., Kuniyoshi, Y., Noda, I., Osawa, E.: The RoboCup: The Robot World Cup Initiative. In: Proceedings of the First International Conference on Autonomous Agents, Marina del Rey, California, USA, pp. 340–347 (1997)
- [14] Ichinose, T., Takemura, Y., Azeura, K., Godler, I.: Hibikino- Musashi. In: CD-ROM Proc. of RoboCup 2006 (2006)
- [15] RoboCup homepage, <http://www.robocup.org/>
- [16] Goris, K.: Autonomous Mobile Robot: Mechanical Design, PhD Dissertation, Vrije University Brussel, Brussels, Belgium (2004-2005)
- [17] Nassiraei, A.A.F., Takemura, Y., Sanada, A., Kitazumi, Y., Ogawa, Y., Godler, I., Miyamoto, H., Ghaderi, A.: Concept of Mechatronics Modular Design for an Autonomous Mobile Soccer Robot. In: Proc. of IEEE International Symposium on Computational Intelligence in Robotics and Automation, USA, pp. 178–183 (2007)
- [18] Takemura, Y., Ogawa, Y., Nassiraei, A.A.F., Sanada, A., Kitazumi, Y., Godler, I., Ishii, K., Miyamoto, H.: A System Design Concept based on Omni-direction, Safety and Modularity for an Autonomous Mobile Soccer Robot. *Journal of Bionic Engineering* 5, 121–129 (2008)
- [19] Asada, M., Veloso, M.M., Tambe, M., Noda, I., Kitano, H., Kraetzschmar, G.K.: Overview of roboCup-98. In: Asada, M., Kitano, H. (eds.) *RoboCup 1998*. LNCS, vol. 1604, pp. 1–21. Springer, Heidelberg (1999)
- [20] Bredenfeld, A., Barakova, E., Vecanovic, B., Christaler, T.: GMD-Musashi team description. In: *Proceeding of RoboCup 2003*, Italy (2003)

- [21] Peijnenburg, A.T.A., Veldhuis, G.P., Warmerdam, T.P.H.: Philips CFT RoboCup Team Description. In: Preliminary proceedings of 2002 RoboCup conference (2002)
- [22] Riberio, F.A., Braga, P., Monterio, J., Moutinho, I., Silva, P., Silva, V.: New improvements of MINHO Team for RoboCup Middle Size League in 2003. In: CD-ROM Proceedings of RoboCup, Padova (2003)
- [23] Nassiraei, A.A.F., Ishii, K., Masakado, S., Matsuo, T., Ichikawa, K., Fukushima, H., Murata, M., Sonoda, T., Takahira, I., Miki, T.: Realization of Rapid Movement for Legged Entertainment Robots Using Two New Actuators, the Inertia Actuator and the Cam Charger. *Journal of Advanced Computational Intelligence and Intelligent Information* 11(8), 979–988 (2007)

Multiple Moving Obstacles Avoidance for Wheeled Type Robots Using Neural Network

Tomohiro Yamaguchi and Yoshio Watanabe

Department of Electronics and Informatics Frontiers, Kanagawa University
3-27-1 Rokkakubashi, Kanagawa-ku, Yokohama 221-8686, Japan

Abstract. Mobile robot path planning in a movement environment is an important problem. We studied acquisition of a path to a destination and multiple moving obstacles avoidance of a wheeled type robot. The paper proposes a method of path planning based on neural network and genetic algorithm. The avoidance action of a wheeled type robot is determined from the obstacle configuration, the robot's self-state and destination information using a neural network. The design parameter of neural network is adjusted by using genetic algorithm.

1 Introduction

As robots extend their application areas from factory to office or home, various functions are needed for robots. In mobile robots, function to avoid obstacle is one of the necessary condition [1]. A mobile robot must be able to avoid both static and moving obstacles in its path. In the case where a robot cannot communicate with moving obstacles, the robot needs to predict the future motion of them. An obstacle avoidance of mobile robots with consideration to a moving obstacle is treated by some researches [2]-[4].

Moreover, two or more obstacles exist in the real-world. For this reason, obstacle avoidance of mobile robot needs to consider two or more obstacles.

This paper examines the multiple moving obstacle avoidance problem in a mobile robot. As a mobile robot, a wheel type robot with two independent drive wheels and one steering is used. For this reason, spin turn is included in action of a robot. In the obstacle avoidance problem of a wheel type robot, it is necessary to avoid all of obstacles by only turning.

Wheeled type robot actions, i.e., the velocity and turning angle, are determined from the position of the destination, obstacles dimensions, and the relative velocity of an obstacle to the robot using a neural network (NN), and multiple moving obstacles avoided. In order to avoid obstacles with the minimum movement time, the design parameters of the NN are optimized by genetic algorithm (GA), using the data collected from several environments, in which each environment has different destinations and obstacles configuration. The effectiveness of present method is proved through a simulation.

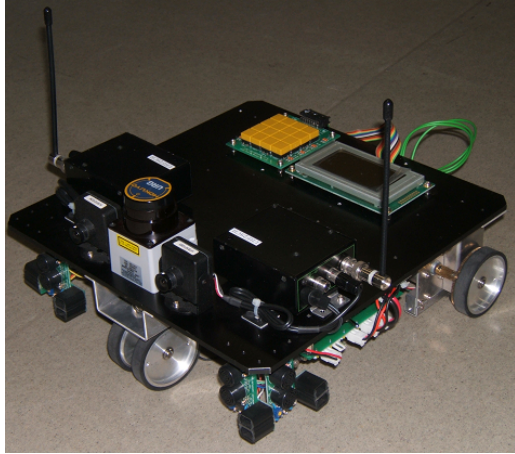


Fig. 1. Plat-F1

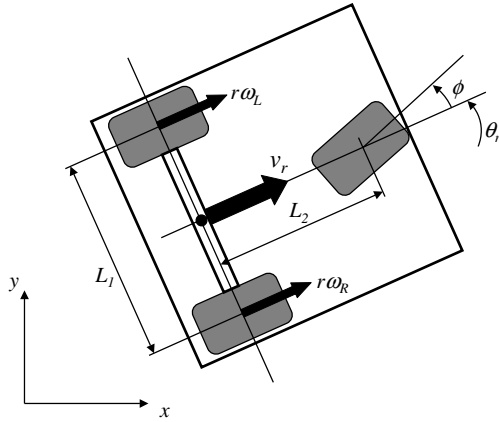


Fig. 2. Kinematics of wheeled type robot

2 Wheeled Type Robot

Plat-F1 (see Fig. 1) is the wheeled type robot. Size of Plat-F1 is 300 [mm] square. Plat-F1 has two independent drive wheels and one steering wheel. Potentiometer is attached in the steering shaft and steering angle can be measured. Rotary encoders are attached in the each drive wheel and rotation angle of drive wheel can be measured.

In order to recognition environment, ultrasonic sensors are attached in front and side direction of the robot. Furthermore, stereo camera and leaser range sensor are attached in the robot. Leaser range sensor can be measured from 0.02 to 4.0 [m], and scanning angle is 240 [degrees].

Kinematics model of wheeled type robot shown in Fig. 2. When the rotational speeds of right wheel and left wheel are assumed to be ω_R and ω_L , the turning angular velocity of robot $\dot{\theta}_r$ is obtained by

$$\dot{\theta}_r = \frac{r}{L_1}(\omega_R - \omega_L) \quad (1)$$

Here, L_1 denotes interval of right and left wheels ($L_1 = 290$ [mm]), and r is radius of wheel ($r = 30$ [mm]). Orientation of the robot θ_r is calculated by

$$\theta_r = \theta_{r0} + \frac{1}{L_1} \int_0^t r(\omega_R - \omega_L) dt \quad (2)$$

Moreover, the velocity of robot v_r is obtained by

$$v_r = \frac{r}{2}(\omega_R + \omega_L) \quad (3)$$

Velocity of the x- and y-direction are obtained by

$$\dot{x}_r = \frac{r \cos \theta_r}{2}(\omega_R + \omega_L) \quad (4)$$

$$\dot{y}_r = \frac{r \sin \theta_r}{2}(\omega_R + \omega_L) \quad (5)$$

Then, positions of the robot (x_r, y_r) are calculated by

$$x_r = x_{r0} + \frac{r}{2} \int_0^t \cos \theta_r (\omega_R + \omega_L) dt \quad (6)$$

$$y_r = y_{r0} + \frac{r}{2} \int_0^t \sin \theta_r (\omega_R + \omega_L) dt \quad (7)$$

Here, when we give the velocity and turning angle of the robot, the rotation speeds of right wheel and left wheel are obtained by

$$\omega_R = \frac{2v_r + L_1 \dot{\theta}_r}{2r} \quad (8)$$

$$\omega_L = \frac{2v_r - L_1 \dot{\theta}_r}{2r} \quad (9)$$

Moreover, steering angle ϕ is given by

$$\phi = \tan^{-1} \frac{L_2 \dot{\theta}_r}{v_r} \quad (10)$$

where L_2 denotes interval of front wheel and rear wheel, $L_2 = 235$ [mm].

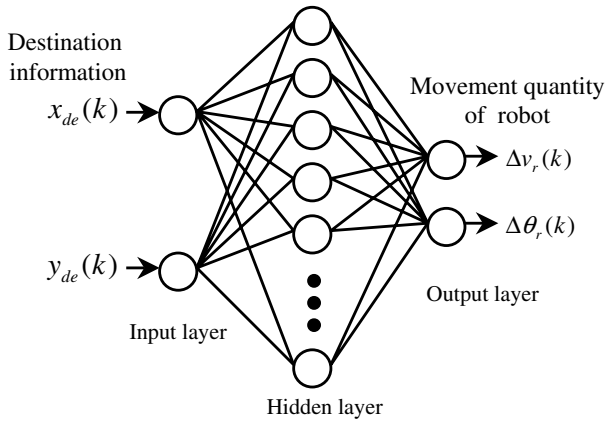


Fig. 3. Neural network for moving to destination

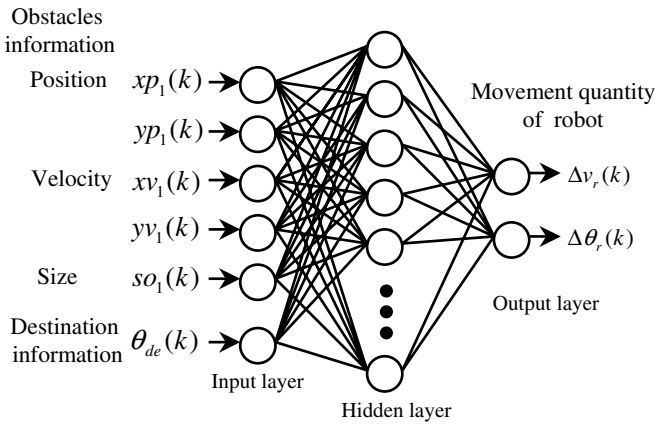


Fig. 4. Neural network for avoiding obstacle

3 Detrmination of Robot Actions

To move the wheeled type robot to destination, we use NN shown in Fig. 3. Inputs to the NN are assumed to be the distance error, i.e., x-directional distance between the center-of-gravity of the robot and destination $x_{de}(k)$, and y-directional distance error $y_{de}(k)$. Output of the NN is the velocity of the robot $\Delta v_r(k)$ and the turning angle of the robot $\Delta \theta_r(k)$.

Moreover, to avoid an obstacle, we add NN shown in Fig. 4. Inputs to the NN are assumed to be the position of obstacles $\{x_{p_i}(k), y_{p_i}(k)\}$, the relative velocity of an obstacle to the robot $\{x_{v_i}(k), y_{v_i}(k)\}$, the size of an obstacle $so_i(k)$, and forward direction of the robot $\theta_{de}(k)$.

In this research, an action of the wheeled type robot to avoid multiple moving obstacles is provided by a three-layered NN shown in Fig. 5.

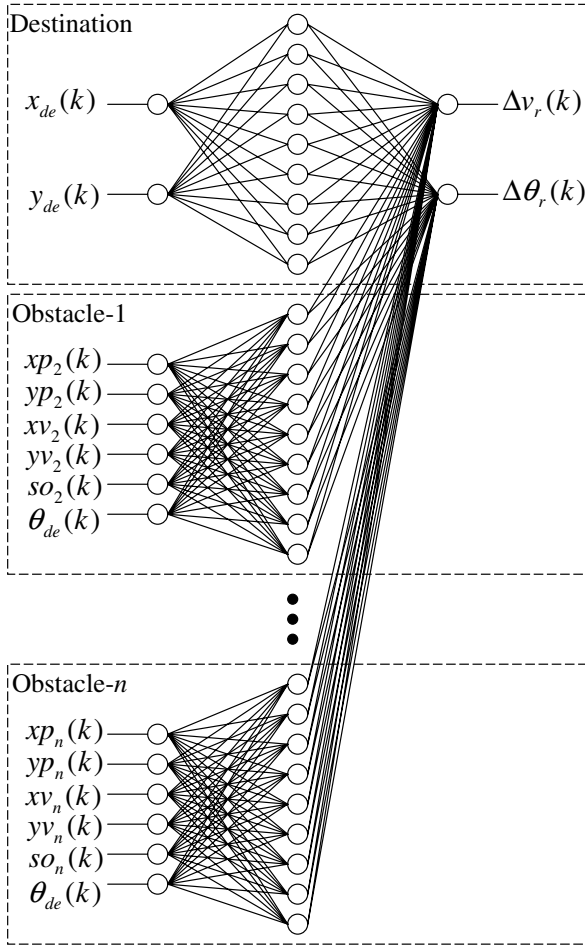


Fig. 5. Neural network for avoiding multiple obstacles

Since the NN is changed with the number of obstacles, NN is prepared to each obstacle. In the input of NN shown in Fig. 5, Obstacle-1 is obstacle information that is the nearest position to a robot. Here, the maximum number of obstacle is set to 10 and the order of input information to NN is changed by near the position of obstacles.

A radial basis function neural network (RBFNN) [5], known as an NN that realizes various approximation functions, is used in the control system. With an RBFNN, a nonlinear function is expanded by any basis function having a circular contour, and is used as function approximation or pattern recognition. Unit functions at the hidden (or intermediate) layer of RBFNNs are given by

$$\psi_{li}(\mathbf{x}_l) = \exp \left\{ - \frac{\| \mathbf{x}_l(k) - \mathbf{c}_i \|^2}{\sigma_i^2} \right\} \quad (11)$$

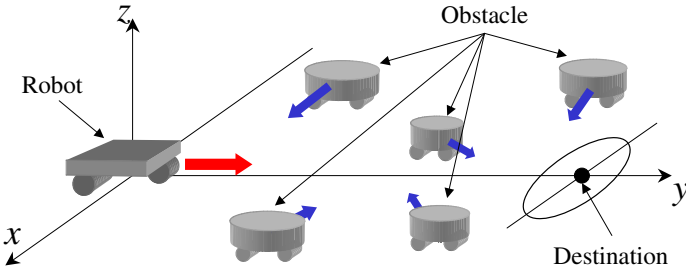


Fig. 6. Setup of environment

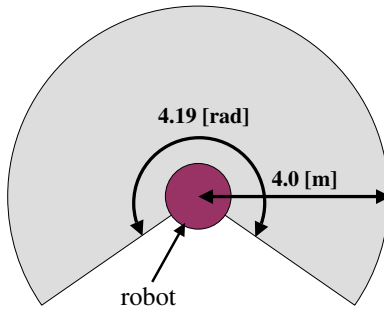


Fig. 7. Serch renge of obstacles

where ψ_{li} denotes i th unit output at the hidden layer of obstacle number l , design parameters of RBF are center c_i , and standard deviation σ_i for each input. j th unit output at output layer o_j is given by

$$o_j(k) = \sum_{l=1}^n \sum_{i=1}^m w_{lij} \psi_{li}(\mathbf{x}_l) \tag{12}$$

calculated by a linear combination of outputs of the hidden layer. w_{lij} denotes the connection weight between the i th hidden unit and the j th output unit of obstacle number l , and m denotes the number of units at the hidden layer, where the number of units is determined by trial and error. The number of units was set to $m = 20$, because a good result was obtained when m was three times the number of inputs.

Using this RBFNN, an action of the wheeled type robot is determined from the information of the obstacles, the robot's self-state, and the destination information.

4 Acquisition of Obstacle Avoidance Action

The simulation acquires action of multiple obstacles avoidance for wheeled type robot. The simulated environment is shown in Fig. 6 in which the y -axis is set to the forward direction of the robot. The robot is assumed to start from the center-of-gravity point

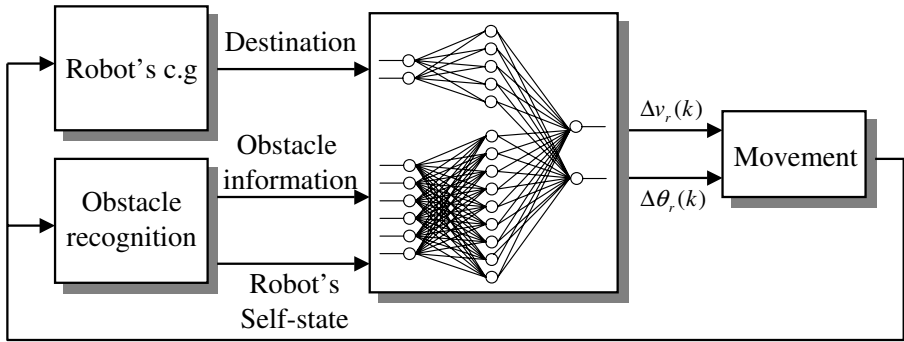


Fig. 8. Obstacle avoidance control system

of (0.0, 0.0) [m] and approach the goal, a circle having radius 0.5 [m], centered on the destination point. Simulation is performed nine times by setting distance error to $(x_{de}, y_{de}) = (0.0, 10.0), (2.0, 10.0), (-2.0, 10.0), (0.0, 12.0), (2.0, 12.0), (-2.0, 12.0), (0.0, 8.0), (2.0, 8.0), (-2.0, 8.0)$ [m]. Here, a robot's size is set to 350 [mm] and the maximum velocity is set to 1.5 [m/s]. Obstacle information is updated from the amount of movements and the forward direction of the robot and obstacles. In this research, a robot has two independent drive wheels and one steering. For this reason, spin turn is included in action of a robot.

Moreover, the search range of the obstacles is shown in Fig. 7. Action of the wheeled type robot is determined using the information of obstacles that exists in the search range.

The block diagram of the present obstacle avoidance control system is shown in Fig. 8. RBFNN determines each amount of movements of the robot from the position of obstacles and robot's self-state.

Obstacle information is updated from the amount of movements and the forward direction of the robot and obstacles.

The initial configuration of obstacles, i.e., position, velocity, forward direction and size, are determined at random. 450 kinds of environments with different initial configuration are prepared, and RBFNN is optimized. Moreover, the number of obstacle is set to 15 in one environment. Furthermore, obstacle is assumed to be going straight.

In simulation, connection weights of the NN and parameters (center and standard deviations) of RBFs are optimized by a GA [6] so that the robot avoids obstacles and reaches the destination with a minimum movement time. Table 1 shows design parameters for the GA used in simulation. The associated fitness function of an individual is defined by

$$fitness = \sum_{i=1}^{ob_n} (fitness_o + fitness_c) \quad (13)$$

whose solution is searched for as a minimization problem. ob_n is the number of environments considered in optimization. $fitness_o$ is an evaluation function associated with penalty for collision with an obstacle. $fitness_o$ is given by

Table 1. Design parameters for GA

The number of individuals	100
Crossover rate	0.6 (uniform crossover)
Selection strategy	tournament selection (3 individuals)
Elitist preserving strategy	10

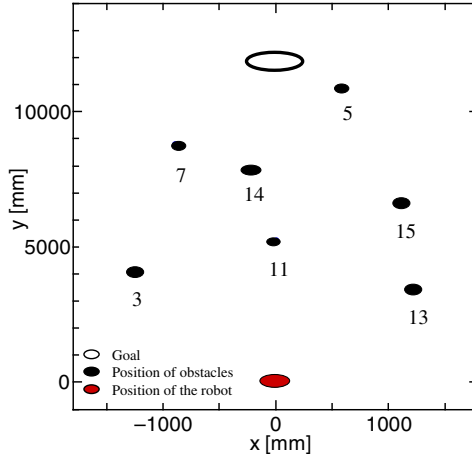


Fig. 9. Initial position of obstacles and robot

$$fitness_o = \begin{cases} 0.0, & \text{if there is no collision} \\ 10.0, & \text{otherwise} \end{cases} \quad (14)$$

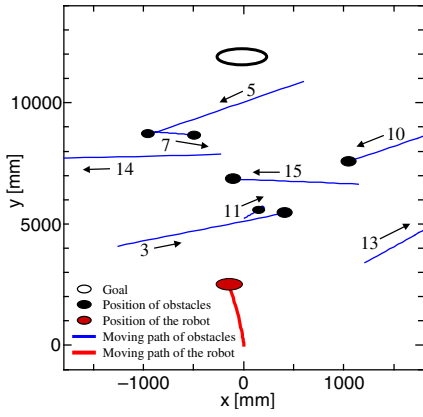
$fitness_c$ is an evaluation function related to movement time required to reach the destination, and given by

$$fitness_c = [x_{de}^2(k) + y_{de}^2(k)] \times T \times 10^{-3} \quad (15)$$

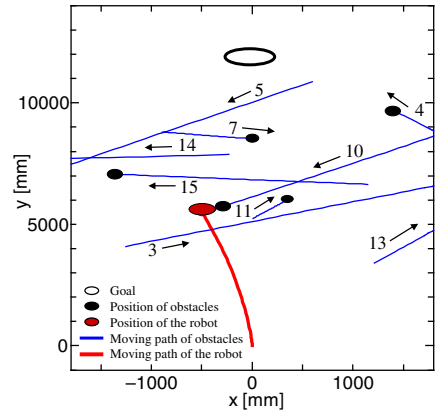
T denotes movement time required to move from the starting point to the destination while avoiding obstacles. The maximum number of movement time T_{max} in one environment is set to 60 [s] and moving stops if movement time exceed T_{max} .

5 Multiple Moving Obstacles Avoidance for Wheeled Type Robot

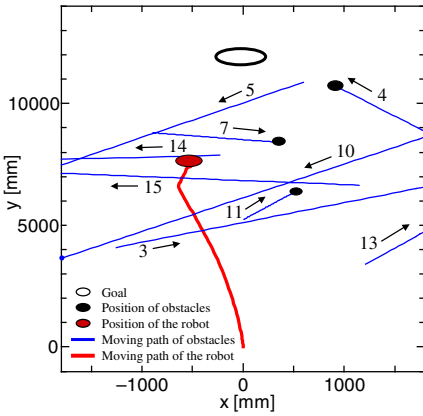
We set the initial distance errors at $(x_{de}, y_{de})=(0.0, 12.0)$ [m]. The initial configurations of 15 obstacles in this simulation are shown in Table 2. Here, x_p and y_p denotes the x- and y-directional coordinates of obstacles, v_o denotes the velocity, θ_o denotes the forward direction, and s_o denotes the size. Fig. 9 shows the initial position of obstacles and wheeled type robot. Here, the circle in Fig. 9 denotes the size of obstacles and wheeled type robot. Fig. 10 shows the movement path of the wheeled type robot and multiple



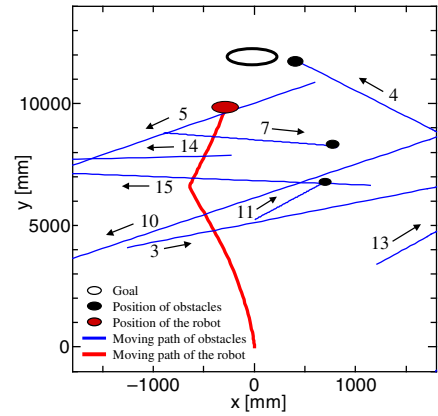
(a) $t=2$ [s]



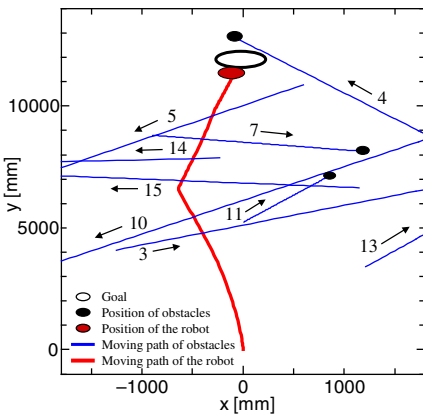
(b) $t=4$ [s]



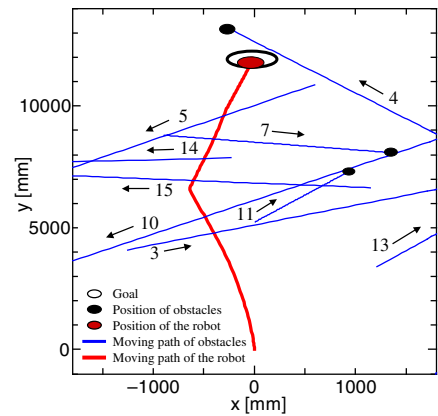
(c) $t=6$ [s]



(d) $t=8$ [s]



(e) $t=10$ [s]



(f) $t=10.7$ [s]

Fig. 10. Movement path of the robot and multiple obstacles

Table 2. The initial configuration of obstacles

No	x_p [mm]	y_p [mm]	v_o [m/s]	θ_o [rad]	s_o [mm]
1	4149.0	4727.0	0.75	4.39	176.0
2	-3056.0	11855.0	0.77	1.86	106.0
3	-1254.0	4094.0	1.01	5.39	155.0
4	2430.0	7521.0	0.58	0.44	166.0
5	594.0	10873.0	1.26	2.52	53.0
6	2063.0	7889.0	0.66	4.20	80.0
7	-888.0	8800.0	0.21	4.40	52.0
8	2384.0	4578.0	0.94	3.03	55.0
9	-3865.0	9681.0	1.52	3.09	186.0
10	2513.0	9609.0	1.20	2.51	162.0
11	6.0	5241.0	0.21	5.86	149.0
12	3114.0	11819.0	1.26	3.47	145.0
13	1211.0	3397.0	1.03	5.87	117.0
14	-231.0	7874.0	1.69	1.67	192.0
15	1144.0	6647.0	0.61	1.40	159.0

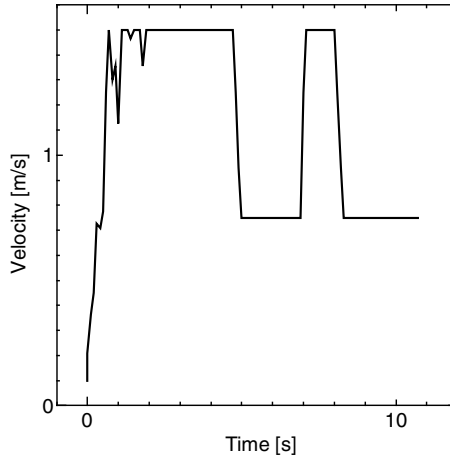


Fig. 11. Velocity of robot for avoiding obstacles

moving obstacles. The positions of obstacles and wheeled type robot after two seconds is shown in Fig. 10-(a), after four seconds shown in (b), after six seconds shown in (c), after eight seconds shown in (d), and after ten seconds shown in (e), respectively. Here, the arrow in Fig. 10 denotes the forward direction of moving obstacle. The wheeled type robot has avoided multiple moving obstacles. Velocity of the wheeled type robot for avoiding obstacles is shown in Fig. 11. Furthermore, turning angle of the wheeled

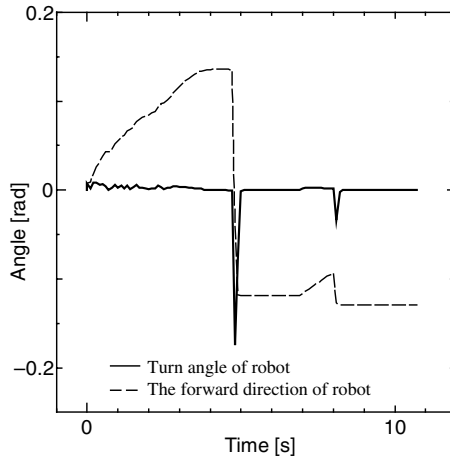


Fig. 12. Turning angle of robot for avoiding obstacles

type robot for avoidance obstacles is shown in Fig. 12. Moreover, the movement time to the goal is 10.7 [s] and final distance error was $(x_{de}, y_{de})=(0.032, 0.247)$ [m].

6 Conclusion

In order to avoid multiple moving obstacles, the action of wheeled type robot has been determined through an RBFNN, whose inputs were the position of the destination, obstacles dimensions, and the relative velocity of an obstacle to the robot. Using the training data on several environmental conditions, the design parameters of the RBFNN were optimized using GA so that the obstacles could be avoided with the minimum movement time.

For the simulation result, we found that the RBFNN was useful for acquiring multiple moving obstacles avoidance action of wheeled type robot. However, since it realized in the decided environment, the obstacle of the environment that differed extremely may be unavoidable. Therefore, the effectiveness of the proposed system needs to be verified by using the actual system. Moreover, the obstacle configuration was assumed to be so simple, i.e., a complicated one was not considered here. Thus, the present technique should be extended to deal with any complicated configuration.

References

- [1] Miura, J., Shirai, Y.: Probabilistic uncertainty modeling of obstacle motion for robot motion planning. *Journal of Robotics and Mechatronics* 14(4), 349–356 (2002)
- [2] Tsubouchi, T., Rude, M.: Motion Planning for Mobile Robots in a Time-Varying Environment. *Journal of Robotics and Mechatronics* 8(1), 15–24 (1996a)
- [3] Fiorini, P., Shiller, Z.: Motion planning in dynamic environments using velocity obstacles. *International Journal of Robotics Research* 17(7), 760–772 (1998)

- [4] Inoue, A., Inoue, K., Okawa, Y.: On-line motion planning of an autonomous mobile robot to avoid multiple moving obstacles based on the prediction of their future trajectories. *Journal of Robotics Society of Japan* 15(2), 249–260 (1997)
- [5] Elanayar, V.T.S., Shin, Y.C.: Radial basis function neural network for approximation and estimation of nonlinear stochastic. *IEEE Transactions on Neural Networks* 5(4), 594–603 (1994)
- [6] Michalewicz, Z.: *Genetic Algorithms + Data Structure = Evolution Programs*, 3rd revised and extended edn. Springer, Germany (1996)

Virtual Reality Simulation of Fire Fighting Robot Dynamic and Motion

Joga D. Setiawan¹, Mochamad Subchan¹, and Agus Budiyo²

¹ Mechanical Engineering Department
Diponegoro University, Semarang, Indonesia
joga@mesin.ft.undip.ac.id

² Department of Aerospace Information Engineering
Konkuk University, Korea
budiyo@alum.mit.edu

Abstract. This paper presents one approach in designing a Fire Fighting Robot which has been contested annually in a robotic student competition in many countries following the rules initiated at the Trinity College. The approach makes use of computer simulation and animation in a virtual reality environment. In the simulation, the amount of time, starting from home until the flame is destroyed, can be confirmed. The efficacy of algorithms and parameter values employed can be easily evaluated. Rather than spending time building the real robot in a trial and error fashion, now students can explore more variation of algorithm, parameter and sensor-actuator configuration in the early stage of design. Besides providing additional excitement during learning process and enhancing students understanding to the engineering aspects of the design, this approach could become a useful tool to increase the chance of winning the contest.

1 Introduction

Fire fighting robot (FFR) is an autonomous ground vehicle that has been popularly known to engineering students around the world. It has been contested annually in a robotic student competition in many countries following the rules initiated at the Trinity College, USA. The contest requires advanced mechatronics technology and knowledge using a handy robot as an educational tool [2].

The task of an FFR is to simulate a real-world operation of an autonomous robot performing a fire protection function in a real house. Starting from a home noted by “H” circle, an FFR has to find its way through an arena that represents a model house, find a lit candle that represents a fire in the house, extinguish the fire in the shortest time, and return to its home within a specified time.

This paper presents one approach in designing an FFR using computer animation in a virtual reality environment including one configuration example that consists of the mechanical design of the vehicle, the choice and arrangement of sensors and actuators, and the artificial intelligence of its controller.

The FFR has been developed to meet contest rules in [2]. As shown in Fig. 1, it is designed as a tracked vehicle with differential drive controlled by a unique algorithm embedded in its microcontroller. The control system the FFR shown in Fig. 2 will be mathematically modeled including its environment, which is the arena used in the competition shown in Fig 3.

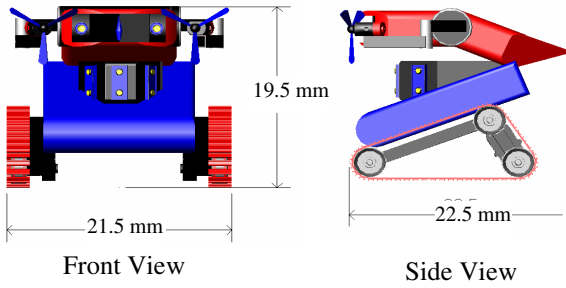


Fig. 1. Fire Fighting Robot as a Tracked Vehicle

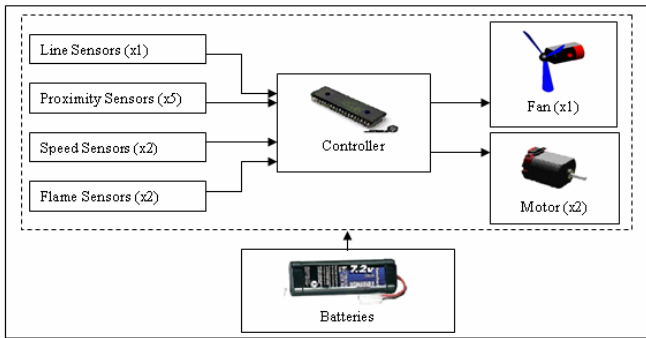


Fig. 2. Control System of Fire Fighting Robot

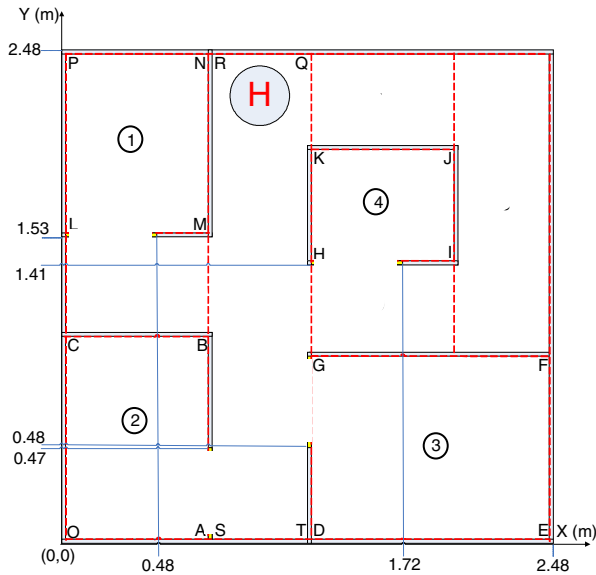


Fig. 3. Contest Arena of Fire Fighting Robot

2 Mathematical Model

The FFR moving autonomously in the contest arena can be mathematically modeled according to three main groups: environment, kinematics and dynamics.

2.1 Environment

The mathematical model for the environment is built by determining the coordinates of walls that look like a labyrinth having four separated rooms as shown in Fig 3. All walls are assumed to have the same thickness.

According to the contest rules [1], white lines are available at the doorway of each room such that they can be used by FFR to determine whether it has moved to a room. In addition, white circumferential lines on the floor are provided around the home "H" and the only-one targeted candle. Thus, the coordinates of these circles are also noted since they can be used by FFR to determine whether to stop or not knowing it is at home or near a target.

The coordinates for the candle's location are set to be varied such that the candle can be anywhere in the four rooms. However, some contest rules are applied. For example, the candle will not be placed in a hallway, but it might be placed just inside a doorway of a room. The candle circle will not touch the doorway line, at least 33 cm into the room before it encounters the candle [1].

2.2 Kinematics

Fire Fighting Robot moves on X-Y plane with the velocity vector $V = [u \ v \ 0]^T$ at its center of mass (COM) shown in Fig. 4, where u is the longitudinal speed and v is the lateral speed. Since the motion is nonholonomic, $v=0$. However, it may rotate with an angular speed $\omega = [0 \ 0 \ r]^T$. If $q = [X \ Y \ \theta]^T$ is the state vector representing robot's X-Y position measured at the COM relative to the origin, where θ is robot's orientation, thus $\dot{q} = [\dot{X} \ \dot{Y} \ \dot{\theta}]^T$ is its velocity vector.

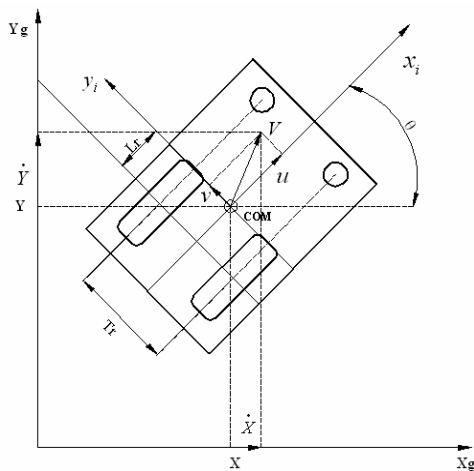


Fig. 4. Robot's Position, Orientation and Geometry on X-Y Plane Coordinate System

The lateral and angular speeds, u and r can be determined by having angular speeds on the left and right drive wheels, ω_l and ω_r

$$u = (\omega_r + \omega_l) \frac{R_t}{2} \quad (1)$$

$$\omega = r = (\omega_r - \omega_l) \frac{R_t}{T_r} \quad (2)$$

where R_t is the radius of drive wheels and T_r is the distance between the left and the right drive wheels. Therefore, the velocity vector can be expressed as

$$\dot{q} = \begin{bmatrix} \dot{X} \\ \dot{Y} \\ \dot{\theta} \end{bmatrix} = \begin{bmatrix} \frac{1}{2} R_t \cos \theta & \frac{1}{2} R_t \cos \theta \\ \frac{1}{2} R_t \sin \theta & \frac{1}{2} R_t \sin \theta \\ \frac{R_t}{T_r} & -\frac{R_t}{T_r} \end{bmatrix} \begin{bmatrix} \omega_r \\ \omega_l \end{bmatrix} \quad (3)$$

2.3 Dynamics

2.3.1 Tracked Vehicle

The robot has one drive wheel and two sprockets on each side as shown in Fig 5. The normal force on the drive wheel noted as N_c is

$$N_c = \frac{k}{2(L_r + k)} m.g \quad (4)$$

The friction force acting on the drive wheel F_{si}

$$F_{si} = \mu.N_c \quad (5)$$

where μ is the effective friction coefficient. Since the total moment required to accelerate the wheels consisting one drive wheel, two sprockets and a belt is

$$\sum M_c = I_{wheels} \alpha \left(2 + \frac{L_2}{R_t} \right) \quad (6)$$

where I_{wheels} is the effective wheel rotational inertia, thus the motor will need to overcome the torsional load

$$T_L = \sum M_c + F_{si}.R_t \quad (7)$$

2.3.2 Sensors

All sensors installed on the FFR as shown in Fig. 2 are assumed to have relatively very high bandwidth such that there is no need to model their dynamics. However, for the proximity sensors, the characteristic of GP2D12 infrared sensor is used [6]. Its calibration curve that relates the distance and the resulting voltage is incorporated to the simulation in order to reveal the effect of its nonlinear characteristic. The location of five proximities sensors from the top view of the FFR are shown in Fig 6. One proximity sensor is facing forward of the FFR noted as CF while four others are

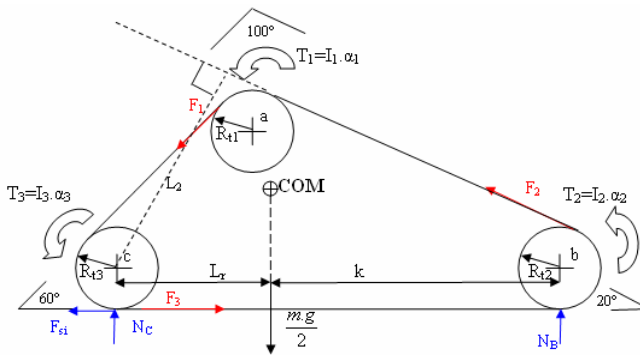


Fig. 5. Forces and Torsion on One Side of Robot

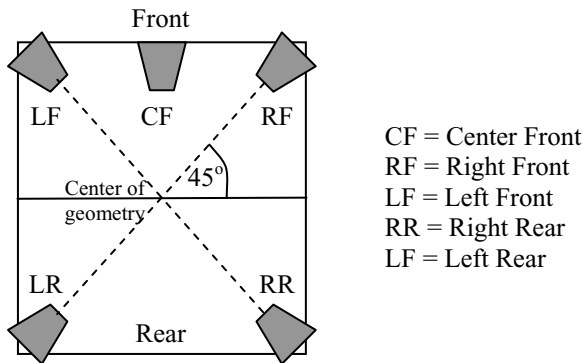


Fig. 6. Location of Five Proximity Sensors

looking outward at each corner. Using simple geometric distance equations, the effect of the location and orientation of these sensors are included besides the effect of FFR location and orientation in order to navigate in the arena without hitting walls.

One line sensor is placed facing down to detect the white lines on the arena floor. The signal from this sensor can be modeled as a digital value 1 as soon as the sensor coordinate is at the location of white floors mentioned in section 2.1, otherwise the value is 0. An example of sensor used for this is a photo-reflector Hamamatsu P5587 [7].

Besides for detecting the existence of home and candle circles, the information from the white line sensors are useful for determining the zone or room of the FFR is currently located. This is done by having the controller to record the number of white line has been encountered.

The two flame sensors are installed at top center facing forward focusing at a specified distance from the FFR as shown in Fig. 7. FFR. The relative distance R of the candle flame is determined by the following equation

$$R = \sqrt{(X_C - X_R)^2 + (Y_C - Y_R)^2} \tag{8}$$

where (X_C, Y_C) is the candle location coordinate in m and (X_R, Y_R) is the FFR location coordinate in m, in order to mathematically modeled the output signal in term of light intensity I in footcandle shown in Eq. 9.

$$I = \frac{0.0125}{R^2} K, \quad R > 0 \tag{9}$$

where $K = f(d\theta)$ is the light intensity coefficient modeled in Fig. 8.

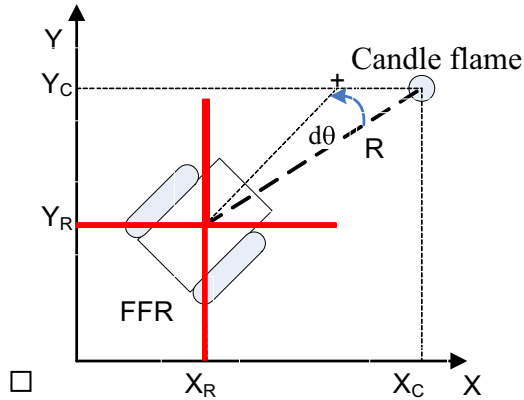


Fig. 7. Relative Distance and Orientation of FFR for Flame Detection

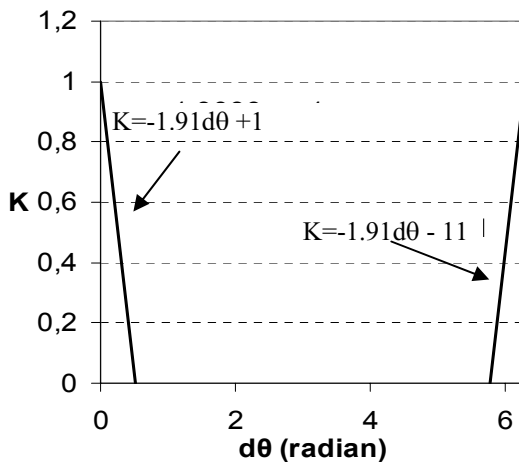


Fig. 8. The Effect of FFR Relative Orientation to the Light Intensity Coefficient K

2.3.3 Actuators

Two equivalent DC motors are assumed to propel the robot. Each DC motor is connected to the drive wheel on each side. The motor generates torsion

$$T_m(s) = K_t I_a(s) \quad (10)$$

where K_t is torsion coefficient in N-m/A and I_a is the armature current. This armature current depends on the applied voltage E_a and back emf E_b which are popularly known in many control textbooks [3]. For the sake of brevity, the discussion of the DC motor model is thus omitted here, even though the model is included in the simulation.

Using Eqs. 6, 7 and 10, the dynamic equation of each wheel can therefore be summarized as

$$(J_m + I_{wheels} \left(2 + \frac{L_2}{R_t} \right)) \frac{d\omega_m(t)}{dt} + B_m \cdot \omega_m(t) = T_m(t) \quad (11)$$

where the rotor inertia of the DC motor is represented by J_m , and other viscous friction on the motor bearing, gearbox and wheels bearings are lumped to B_m .

Other actuators are the two DC motors to drive two fans. These fans are turned-on only to the destroy the candle flame. It is assumed that after the FFR approaches the flame and the fans are activated for 4 seconds, then the flame is put off. Thus, there is no need to model the dynamic of these fans. However, for animation purposes, the fans are shown to rotate during this action in the virtual reality environment.

2.4 Controller

The controller used is assumed to have high enough sampling rate relative to the traveling speed of the FFR so that the controller dynamic can be neglected. Moreover, the controller is modeled to have sufficient input and output channels that are compatible with all sensors and actuators utilized by the FFR. Furthermore the controller is modeled to be capable of performing counting operation.

3 Navigation Algorithm

A navigation algorithm used for the FFR to move efficiently in the arena has been uniquely developed. The algorithm can be separated into three main tasks:

1. Navigation going through corridors
2. Navigation in rooms
3. Navigation to return home

3.1 Navigation through Corridor

There are three basic motions that the FFR can perform in this task [5]:

1. Moving forward that depends on the readings from the proximity sensors.
2. Turning that is determined by the odometry of encoders connected to the right and left drive wheels. The odometry reading is used to estimate how many degrees the FFR has rotated during turning. When to turn to the left or to the right depends on the six identified cases shown in Fig. 9.

3. Wall Following. This motion is needed to make sure the FFR is always moving in parallel with detected side walls as shown in Fig. 10.

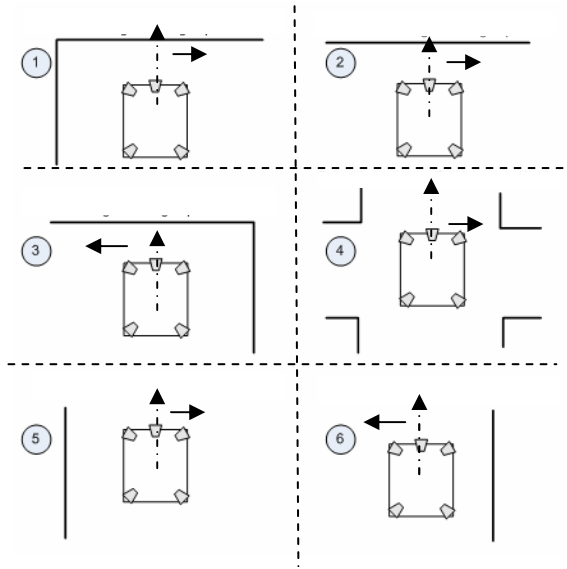


Fig. 9. FFR Turns due to Encountered Wall Cases

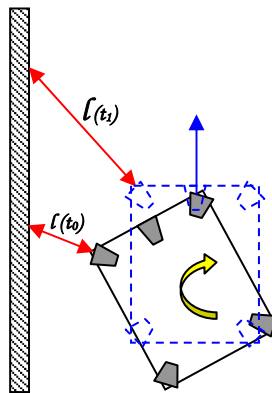


Fig. 10. Wall Following using Information from at Least Two Proximity Sensors

3.2 Navigation in Rooms

Once the FFR identifies that it has been in a room and had few distance passing a white line on a doorway, the controller will switch to the task noted as the Navigation in Rooms as shown in Fig 11.

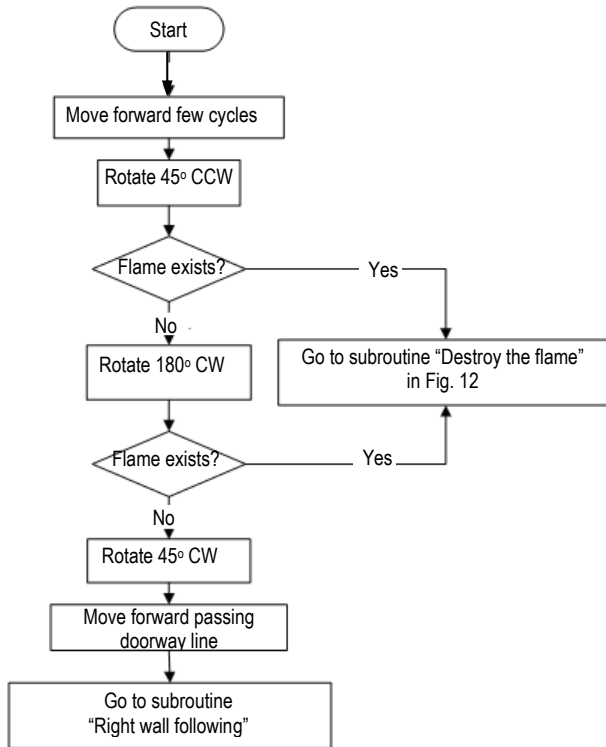


Fig. 11. Task of Navigation in Rooms

3.3 Navigation to Destroy the Flame

The FFR may detect existence of a flame during rotating and scanning a room and therefore the controller will switch the task to the Navigation to Destroy the Flame as shown in Fig. 12.

3.4 Navigation to Return Home

The controller will switch to the task Navigation to Return Home after the flame has been extinguished. This task is basically use Wall Following motion explained in section 3.1. At the end the FFR is set to stop after few distance passing the white circle of the Home.

4 Virtual Reality Simulation

The algorithm of FFR navigation is implemented on State Flow of MATLAB/SimulinkTM from Mathworks as shown in Fig. 13. To travel along the corridor, the subsystem “To_Room” is used in which it has two subroutines: Wall Following and and Turn Program.

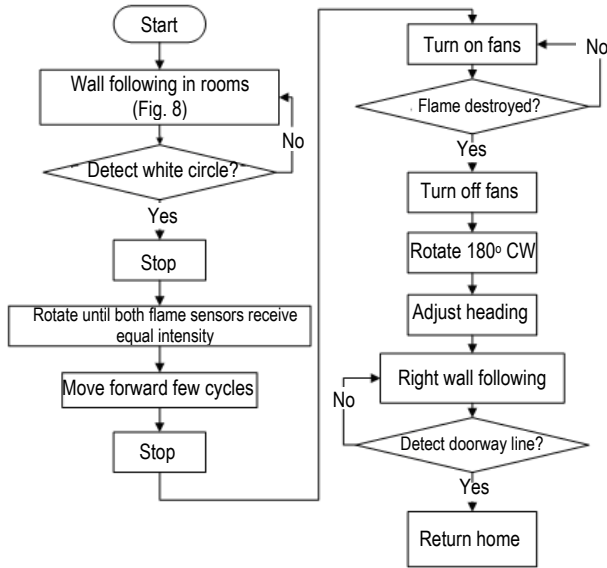


Fig. 12. Task of Navigation to Destroy the Flame

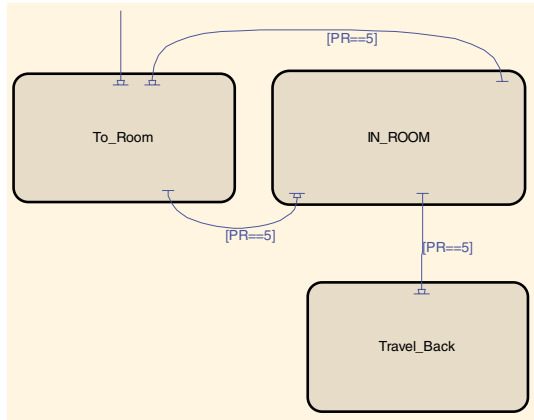


Fig. 13. State Flow of Main Algorithm

Fire Fighting Robot virtual reality is created using Virtual Reality Toolbox in MATLAB/Simulink. The result of the virtual reality environment can be seen in Fig. 14. The FFR trajectories of four cases are provided in Fig. 15 and the elapsed times required to destroy the flame and the total time until the FFR returns home are shown in Table 1. The Simulink block diagram of the overall FFR mathematical model and algorithm is shown in Figure 16. Simulation parameters are obtained in [4].



Fig. 14. View of Virtual Reality Environment

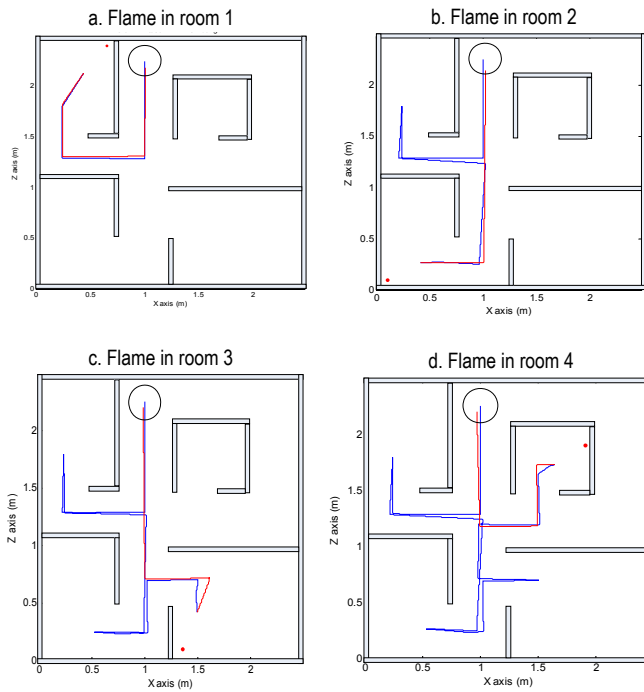


Fig. 15. Example of Four Trajectories of FFR

The animation results shown in Figure 15 reveal that the robot can successfully find the candle in four cases and navigate through the arena without hitting walls. The elapsed time performance of robot seen in Table 1 satisfies time limits of the contest

Table 1. Example of four cases showing the elapsed time required to destroy the flame and return home

Flame location	Room 1	Room 2	Room 3	Room 4
Time to destroy the flame (s)	40.8	84.2	120.6	156.8
Total time until return home (s)	82.6	123.6	161.1	196.3

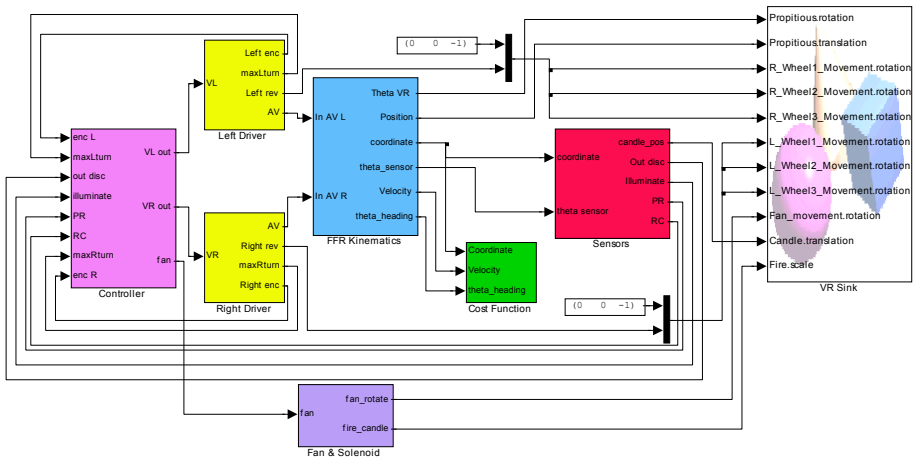


Fig. 16. Simulink Block Diagram of FFR Model and Algorithm

regulation; maximum 5 minutes to find the candle and maximum 2 minute in return trip mode [2].

5 Conclusions

This paper describes the viability of simulation and animation of Fire Fighting Robot in order to evaluate the performance of the robot design in meeting some of the contest rules such as navigating in a labyrinth arena without hitting walls, quickly extinguishing a flame in a room and return home.

This work shows the benefit of virtual reality tool that enables students to quickly evaluate and clearly visualize the dynamic and motion of Fire Fighting Robot and the interaction between the robot and its environment before spending too much time in building the robot. The present model gives a reasonably accurate analytical representation of an example Fire Fighting Robot and its contest arena. In turn,

students can become more familiar with the analytical models. This model can give the basis of a model that could be used by students to explore more innovative design for their robot.

References

- [1] Nawash, N.: H-infinity Control of an Autonomous Mobile Robot, Master of Science Thesis, Cleveland State University, Cleveland (2005)
- [2] Panitia Kontes Robot Cerdas Indonesia, 2005. Panduan KRCI-2006: Kontes Robot Cerdas Indonesia. Jakarta:Universitas Indonesia (2006)
- [3] Phillips, C.L., dan Royce, D.H.: Feedback Control Systems, 4th edn. Prentice Hall, New Jersey (2000)
- [4] Schworer, I.: Navigation and Control of an Autonomous Vehicle. Master of Science Thesis, Virginia Polytechnic Institute and State University, Blacksburg, Virginia (2005)
- [5] Subchan, M.: Development of Algorithm and Dynamic Simulation of Fire Fighting Robot Using MatLab, Simulink and Virtual Reality. Undergraduate Final Project Report, Mechanical Engineering Department, Diponegoro University, Semarang (2007)
- [6] http://www.acroname.com/robotics/parts/c_sensor.html (February 14, 2007)
- [7] <http://www.perkinelmer.com/opto> (May 2, 2006)

Monotonic Decreasing Energy and Switching Control for Underactuated Manipulators

Kiyotaka Izumi, Keisuke Ichida, Keigo Watanabe, and Yuichi Kamada

Department of Advanced Systems Control Engineering,
Graduate School of Science and Engineering, Saga University
{watanabe,izumi}@me.saga-u.ac.jp

Abstract. The fuzzy-energy regions based switching method was proposed to control underactuated systems. The switching rule of this method was designed on error energy region with some boundary curves described by fuzzy rules. This method was validated by some simulations. The number of switching times for partly stable controllers increased according to initial conditions and design parameters. This paper discusses about the novel energy definition and the switching rules with the defined energy, in order to decrease the number of switching times. The effectiveness of the present approach energy is verified through some simulations for a 2-link underactuated manipulator.

1 Introduction

Normal manipulators have one actuator at least for each joint, so the degrees of freedom are equal to the number of actuators. On the other hand, underactuated manipulators have any passive or free joints, which can not generate any torques. From this fact, it must control the joints more than the number of actuators and its control law becomes complicated, but any light-weight, energy saving and cost cutting are expectable.

It is well known for us that such control systems can be reduced to a system with second-order nonholonomic constrains, and recently a second-order chained form is often adopted as a canonical form in order to use the conventional several control approaches such as invariant manifold method, discontinuous control law, etc. developed in the field of underactuated control systems. Such canonical transformation needs the knowledge of Lee algebra, such as Lee bracket, Lee derivative, etc.

On the contrary, in our laboratory a switching computed torque method has been proposed up to now [1, 2, 3, 4, 5], in which we need no any transformation of the system into a canonical form. However, on how to switch partly stabilizing controllers, we must discuss the switching rules based on fuzzy reasoning or neural networks, etc. In addition, the energy definition used there was not necessarily to be monotonic decreasing, so that there was an increasing problem of the number of switching times [6, 7, 8].

In this research, a method based on the switching of fuzzy energy regions is applied to an underactuated manipulator with two links. In particular, we discuss about the novel energy definition and the switching rules with the monotonic decreasing energy, to reduce the number of switching times. The effectiveness of the present approach is verified through some simulations for a 2-link underactuated manipulator, compared to the existing approach with the conventional Euclidean norm.

2 Switching Control with Fuzzy Energy Regions

In a fuzzy energy region based switching control, the control objective is controlled by switching several partly stable controllers, where the energy region is divided into sub-regions according to several regional curves, which are described by a fuzzy representation, so that the partly stable controller will be adopted depending on the condition that the current energy is within the corresponding sub-region assigned in advance.

2.1 Partly Stable Controller

The dynamical equation of two-link underactuated manipulators is given by

$$\ddot{\theta}_1 = -\frac{M_{22}(\boldsymbol{\theta})}{D}h_1(\boldsymbol{\theta}, \dot{\boldsymbol{\theta}}) + \frac{M_{12}(\boldsymbol{\theta})}{D}h_2(\boldsymbol{\theta}, \dot{\boldsymbol{\theta}}) + \frac{M_{22}(\boldsymbol{\theta})}{D}\tau_1 \quad (1)$$

$$\ddot{\theta}_2 = \frac{M_{12}(\boldsymbol{\theta})}{D}h_1(\boldsymbol{\theta}, \dot{\boldsymbol{\theta}}) - \frac{M_{11}(\boldsymbol{\theta})}{D}h_2(\boldsymbol{\theta}, \dot{\boldsymbol{\theta}}) - \frac{M_{12}(\boldsymbol{\theta})}{D}\tau_1 \quad (2)$$

where M_{ij} denotes the element of i th row and j th column for the inertia matrix, h_i is the i th component of vector for the centrifugal force and the Coriolis force, and D denotes the determinant of the inertia matrix.

Using the computed torque method, a partly stable controller for the first link, i.e., PSC1 can be designed by

$$\tau_1 = \frac{D}{M_{22}(\boldsymbol{\theta})} \left(\ddot{\theta}_1^* + \frac{M_{22}(\boldsymbol{\theta})}{D}h_1(\boldsymbol{\theta}, \dot{\boldsymbol{\theta}}) - \frac{M_{12}(\boldsymbol{\theta})}{D}h_2(\boldsymbol{\theta}, \dot{\boldsymbol{\theta}}) \right) \quad (3)$$

$$\ddot{\theta}_1^* = \ddot{\theta}_{d1} + K_{v1}(\dot{\theta}_{d1} - \dot{\theta}_1) + K_{p1}(\theta_{d1} - \theta_1)$$

Similarly, a partly stable controller for the second link, i.e., PSC2 can be reduced to

$$\begin{aligned}
 \tau_1 &= -\frac{D}{M_{12}(\boldsymbol{\theta})} \left(\ddot{\theta}_2^* - \frac{M_{12}(\boldsymbol{\theta})}{D} h_1(\boldsymbol{\theta}, \dot{\boldsymbol{\theta}}) \right. \\
 &\quad \left. + \frac{M_{11}(\boldsymbol{\theta})}{D} h_2(\boldsymbol{\theta}, \dot{\boldsymbol{\theta}}) \right) \\
 \ddot{\theta}_2^* &= \ddot{\theta}_{d2} + K_{v2}(\dot{\theta}_{d2} - \dot{\theta}_2) + K_{p2}(\theta_{d2} - \theta_2)
 \end{aligned} \tag{4}$$

where $\boldsymbol{\theta}$ is the joint angle vector; $\boldsymbol{\theta}_d = [\theta_{d1} \ \theta_{d2}]^T$ is a desired vector; and K_{pi} and K_{vi} are proportional and derivative gains for the i th link.

2.2 Switching Rule Using Error Energy Regions

There are several definitions for the energy in a feedback controlled system. First, a squared sum of inputs is considered, but any energy plane can not be constructed for an underactuated system with only one input. Next, a kinetic energy for each link can be expected to be used, but the second link can not be considered independently because it includes the angular velocity for the first link from a constraint that the second link is connected to the first link. From these reasons, references [6]~[8] used each link error

$$\begin{aligned}
 \mathbf{e}_i &= \boldsymbol{\theta}_{di} - \boldsymbol{\theta}_i \\
 \boldsymbol{\theta}_{di} &= [\theta_{di} \ \dot{\theta}_{di}]^T \\
 \boldsymbol{\theta}_i &= [\theta_i \ \dot{\theta}_i]^T
 \end{aligned}$$

to define the error energy in discrete-time:

$$E_i(k) = \|\mathbf{e}_i(k)\|^2 \tag{5}$$

for the construction of energy region. Figure 1 shows the energy plane for a two-link underactuated manipulator, where PSC1 should be applied in the region R_1 , whereas PSC2 should be used in the region R_2 . Here, the shadowed region denotes an overlapped region of R_1 and R_2 , in which a partly stable controller used in one-step delayed instant should be used successively. Approximating regional division curves π_1 and π_2 by two straight lines respectively and introducing a fuzzy representation for the boundary lines, the switching rule can be described by

- Rule 1: If $E_2 = S$ then $s_1 = 1$
- Rule 2: If $E_2 = M$ and $\hat{I}(k-1) = 1$ then $s_2 = 1$
- Rule 3: If $E_2 = M$ and $\hat{I}(k-1) = 2$ then $s_3 = 2$
- Rule 4: If $E_2 = B$ then $s_4 = 2$

where s_i denotes the index number of a partly stable controller at the i th fuzzy rule. That is, the number 1 means the PSC1 and similarly the number 2 denotes the PSC2. The membership function is shown in Fig. 2 for the part approximated

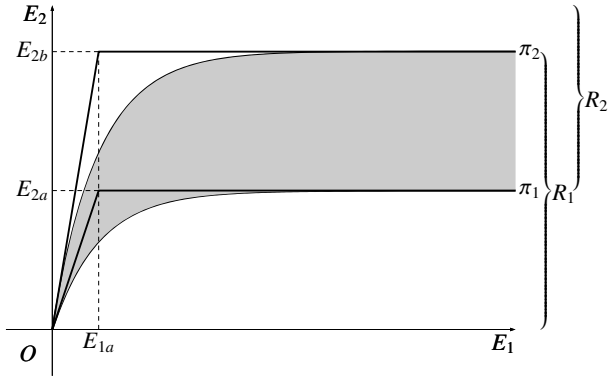


Fig. 1. Energy plane of 2-link underactuated manipulator

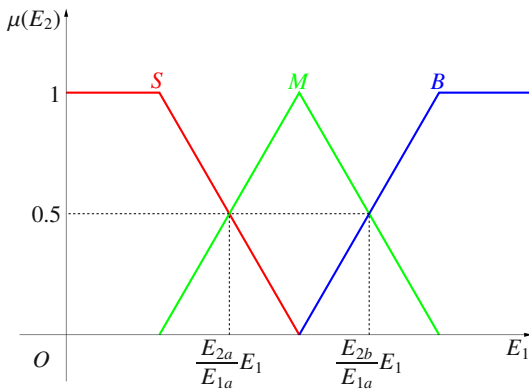


Fig. 2. Membership functions for $E_1 \leq E_{1a}$

by a ramp function, whereas it is shown in Fig. 3 for the part approximated by using a line parallel in E_1 axis. Note here that the index number of a partly stable controller is output as an integer $\hat{I}(k)$, because the fuzzy reasoning results in a real number.

2.3 Simulations

The conventional method was simulated using the condition tabulated in Table 1. Keeping the gains of partly stable controllers as $K_{pi} = 25$ and $K_{vi} = 10$, the regional parameters were determined as $E_{1a} = 4$, $E_{2a} = 1$ and $E_{2b} = 8$ through manual adjustments.

The time response of each joint angle is shown in the left-side of Fig. 4, while showing the energy state in the right-side of Fig. 4. Here, the time response of the first link is designated by a solid line in the left-side figure, whereas that of the second link is depicted by a broken line. The energy state due to PSC1

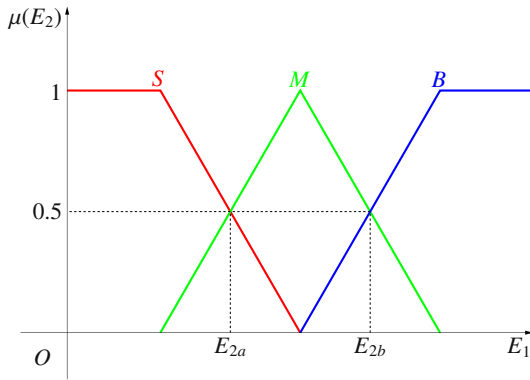


Fig. 3. Membership functions for $E_1 > E_{1a}$

Table 1. Simulation conditions

Sampling interval	0.01 [s]
Initial value	$\theta = [0 \ \pi/4]^T, \dot{\theta} = [0 \ 0]^T$
Desired value	$\theta_d = [0 \ 0]^T, \dot{\theta}_d = [0 \ 0]^T$
Link length	$l_1 = 0.4, l_2 = 0.22$
Link COG	$l_{g1} = 0.2, l_{g2} = 0.11$
Link mass	$m_1 = 0.582, m_2 = 0.079$
Link inertia	$I_1 = 0.023, I_2 = 9.5 \times 10^{-4}$
Damping coefficient	$\mu_1 = 0, \mu_2 = 0.02$

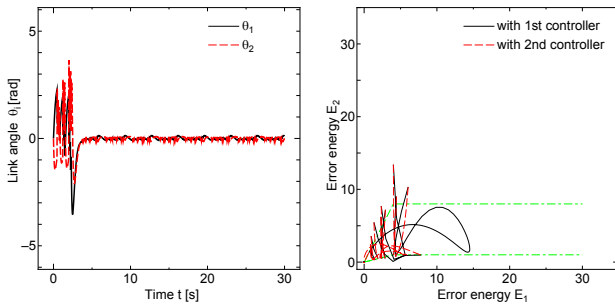


Fig. 4. Simulation results with a conventional approach

is shown by a solid line in the right-side figure, whereas that due to PSC2 is depicted by a broken line. It is seen from these figures that the time response of each joint angle converged around the desired value, though the energy state did not necessarily decrease monotonically under the condition that two partly stable controllers were applied.

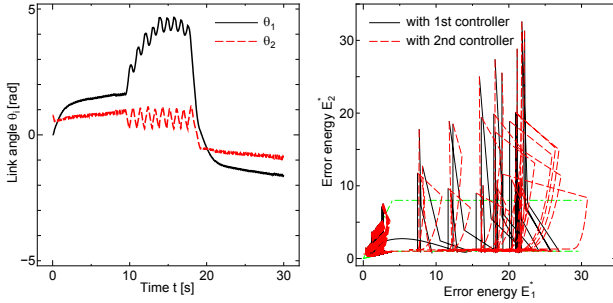


Fig. 5. Simulation results with the proposed energy

3 Energy Definition Using Monotonic Decreasing Property

When designing partly stable controllers by the computed torque method, it is not assured that the energy defined by Eq. (5) decreases monotonically. From this fact, a new energy definition $E_i^*(k)$ is proposed:

$$E_i^*(k) = \begin{cases} \min(E_i^*(k-1), E_i(k)) & \text{if PSC for } i\text{th link} \\ & \text{is selected} \\ E_i(k) & \text{otherwise} \end{cases} \quad (6)$$

where k_s is the discrete-time index at which a partly stable controller switches to PSC i , where the energy is updated as $E_i^*(k_s) := E_i(k_s)$. The proposed energy $E_i^*(k)$ decreases monotonically while the PSC i is selected. Figure 5 shows the simulation result using the proposed energy. The time responses of link angles oscillate, though they do not diverge.

4 Switching Rule That Realizes Monotonically Decreasing Energy

The constraint of a switching rule described by

$$\hat{I}^*(k) = \begin{cases} \hat{I}(k) & \text{if } E_i^*(k) < E_i(k_s) \\ \hat{I}(k-1) & \text{otherwise} \end{cases} \quad (7)$$

is appended to the output of fuzzy reasoning. It is expected that PSC i will be selected until $E_i^*(k)$ is less than $E_i(k_s)$. The monotonically decreasing energy is generated by Eq. (7). The simulation result is plotted in Fig. 6. Link angles are converged to around the desired values. The maximum amplitude of energy becomes smaller than those of Fig. 4 and Fig. 5.

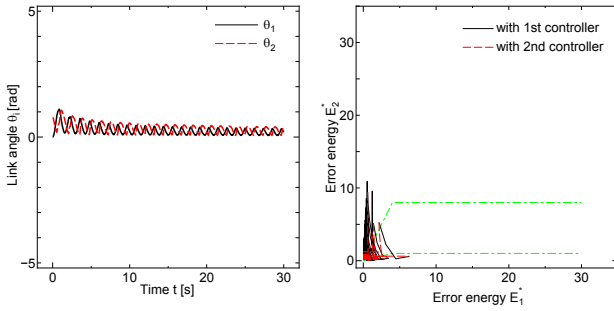


Fig. 6. Simulation results with the proposed energy and switching

Table 2. Initial tip position and posture

Index of condition	Tip position	Posture
1st con.	(0.4, 0.4)	right-handed
2nd con.	(0.4, 0.4)	left-handed
3rd con.	(-0.4, 0.4)	right-handed
4th con.	(-0.4, 0.4)	left-handed

Table 3. Switching times for each initial condition

	Conventional method	Proposed energy	Proposed energy and switching
1st con.	238	230	56
2nd con.	218	254	61
3rd con.	235	257	55
4th con.	226	253	54
Ave.	229	249	57

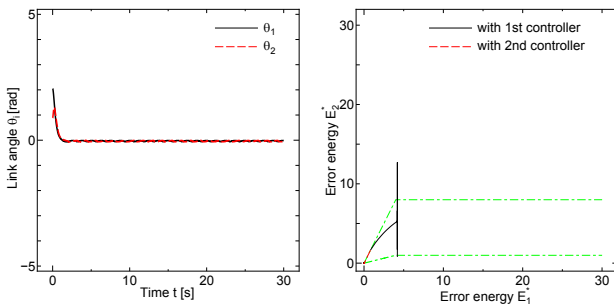


Fig. 7. Simulation results for the 3rd initial condition using the proposed energy and switching

5 Discussions

Some simulations were executed with four different initial states, which were also different from Table 1. These initial states are listed in Table 2. The number of switchings for each condition is shown in Table 3. It is found that the average number of switchings are independent of initial conditions. Applying the proposed energy definition and the switching rule, the corresponding number of switchings is the least, compared to those of other methods.

For example, the simulation result using the 3rd condition is illustrated in Fig. 7. Observe that link angles converge to the desired values with small oscillations.

6 Conclusions

In this paper, we have proposed the definition of monotonically decreasing energy and the switching method using the defined energy. The proposed method was applied to an underactuated manipulator. It was verified from some simulations that the number of switchings decreased when the proposed method was applied. When the design parameter could be adjusted suitably, we would expect the improvement of the controlled performances.

References

- [1] Udawatta, L., Watanabe, K., Izumi, K., Kiguchi, K.: Obstacle Avoidance of Three-DOF Underactuated Manipulator by Using Switching Computed Torque Method. *Trans. on Control, Automation and Systems Engineering* 4(4), 347–355 (2002)
- [2] Udawatta, L., Watanabe, K., Izumi, K., Kiguchi, K.: Evolution of Underactuated Robots and Control Techniques. *Machine Intelligence and Robotic Control* 4(3), 127–134 (2002)
- [3] Udawatta, L., Watanabe, K., Izumi, K., Kiguchi, K.: Control of Underactuated Robot Manipulators Using Switching Computed Torque Method: GA Based Approach. *Soft Computing* 7(8), 51–60 (2003)
- [4] Udawatta, L., Watanabe, K., Izumi, K., Kiguchi, K.: Control of Underactuated Manipulators Using Fuzzy Logic Based Switching Controller. *J. of Intelligent and Robotic Systems* 38, 155–173 (2003)
- [5] Udawatta, L., Watanabe, K., Izumi, K., Kiguchi, K.: Control of 3-DOF Underactuated Manipulator Using Fuzzy Based Switching. *Artificial Life and Robotics* 8(2), 153–158 (2004)
- [6] Izumi, K., Watanabe, K.: Switching Fuzzy Energy Method Optimized by Genetic Algorithm for Controlling Underactuated Manipulators. In: *Proc. of Joint 2nd International Conference on Soft Computing and Intelligent Systems and 5th International Symposium on Advanced Intelligent Systems (SCIS&ISIS 2004) FE-1-4* (2004)
- [7] Ichida, K., Izumi, K., Watanabe, K., Uchida, N.: Switching Rules Based on Fuzzy Energy Regions for a Switching Control of Underactuated Robot Systems. In: *Proc. of the Int. Conf. on Control, Automation and Systems (ICCAS 2005)*, pp. 1949–1964 (2005)
- [8] Ichida, K., Izumi, K., Watanabe, K., Uchida, N.: Control of Three-Link Underactuated Manipulators Using a Switching Method of Fuzzy Energy Regions. In: *Proc. of the 12th Int. Symposium on Artificial Life and Robotics*, pp. 764–767 (2007)

Positive Real Synthesis of Networked Control System: An LMI Approach

Riyanto Bambang and Imam Arifin

School of Electrical Engineering and Informatics
Institut Teknologi Bandung, Bandung, Indonesia
briyanto@lskk.ee.itb.ac.id, arifin-i@ee.its.ac.id

Abstract. This paper presents positive real synthesis for Networked Control Systems (NCS) in discrete-time to render closed-loop positive realness (passivity). The synthesis is based on the definition of passivity for discrete Markovian jump linear systems, whose sufficient condition is given by stochastic Lyapunov functional. The controller via state feedback is designed to guarantee the stability of NCS and closed-loop positive realness by taking into account packet losses. A periodic communication scheme is utilized among sensor, controller and actuator. It is shown that a mode-dependent positive real controller exists if a set of coupled linear matrix inequalities have positive definite solutions. The controller can then be constructed in terms of the solutions. A numerical example is presented to show how the desired passivity performance of NCS is achieved.

1 Introduction

The recent advancement of computing, communication and sensing has spurred the development of Networked Control Systems (NCS). NCS are spatially distributed systems in which communication between plants, sensors, actuators and controllers occurs through a shared band-limited digital communication networks [3,4,11]. These networks are usually shared by a number of feedback loops. In traditional control systems, these connections are established via point-to-point cable wiring. Compared with the point-to-point wiring, the introduction of communication networks has many advantages, such as high system testability and resource utilization, as well as low weight, space, power, and wiring requirements and easy system diagnosis and maintenance. The increasingly fast convergence of sensing, computing and (wireless) communication on cost effective, low power, small-size devices, is also quickly enabling a surge of new control applications. Consequently NCS has finding application in a broad range of areas such as mobile sensor networks, remote surgery, multiple mobile autonomous robotics, multiple unmanned aerial vehicles (UAV) formation, large scale distributed industrial processes and automation, computer integrated manufacturing systems, tele-operation and tele-control, intelligent vehicle systems, satellite clusters, etc [8]. In an NCS, it also makes it possible to distribute processing functions and computing loads into several relatively small computing power units.

Recently, modeling, analysis and control of networked control systems with limited communication capability has emerged as a topic of significant interest to

control community. There are a number of key issues that make control over communication networks distinct from traditional control systems : limited packet rate, sampling and network delay, packet dropout and system architecture. The traditional point-to-point feedback control theory should be extended for feedback control system for which connections among sensors, actuators, and controllers are shared through band-limited communication networks. With the advent of cheap, small, low-power processors with communication capabilities, it has become possible to endow sensors and actuators with processing power and ability to communicate with remote controllers through shared/multi-purpose networks [9].

Most of the results on performance control synthesis for NCS deal with H_∞ norm constraints [2,3,16 and references therein]. As far as the authors concern, [15] is the only work dealing with passivity constraint in NCS framework. In this paper we propose a control design method for networked control system which satisfies positive-real (passivity) requirements, in addition to stability. Important aspects of networked control systems, namely random delays and packet losses, are taken into consideration in the passive control design. We assume, however, that if the arrival of the messages is delayed then they are regarded as loss. Moreover, an acknowledgement message is assumed to be provided from the receiver to the sender to acknowledge whether a message is sent successfully or not. Communication between sensor and controller (input side) and between controller (output side) and actuator is performed in a periodic way. The networked control system is modeled using Markov Jump Linear System, where packet loss is modeled as two-state **Bernoulli** process [3]. Compared to the approach used in [15], the present paper employs periodic Markov Jump Systems representation, while [15] utilizes sampled-data representation of NCS and Lyapunov-Krasovskii functional.

The concept of passivity or positive realness plays an important role in system, signal and control theory, and arises naturally in many areas of science and engineering [12]. The idea originates in traditional circuit theory. In general, positive realness corresponds to passivity for linear time-invariant dynamical systems. The main motivation for studying passivity comes from robust, adaptive and nonlinear control problems. Parallel to small gain theorem, passivity of certain closed-loop transfer functions will ensure the overall stability of feedback systems [1]. Therefore, if a certain closed-loop transfer function matrix can be made passive by using some controllers, then the closed-loop system will be guaranteed to be robust with respect to all passive uncertainties. The passivity requirements are also important in a number of practical cases where the control designer has information about phase uncertainties [14].

The synthesis problem considered in this paper is how to construct a state feedback controller for a networked control system such that the resulting closed-loop system satisfies passivity (see also [13] for output feedback case). Based on the definition of passivity under state-space representation of jump linear systems, the passivity condition is firstly obtained using stochastic Lyapunov functional technique. It is shown that the passivity condition of jump systems guarantees the stability. A kind of mode-dependent controllers suited for a networked control system is proposed via

state feedback to ensure the passivity of the resulting closed-loop systems. By adopting similar algebraic manipulation techniques as in H_∞ control synthesis for NCS [3,5,6,10], the existence conditions and the synthesis methods for the mode-dependent controllers can be formulated in terms of a set of solutions of coupled linear matrix inequalities, which can be effectively solved using available LMI-solver.

The remainder of the paper proceeds as follows: In Section 2, networked control analysis and synthesis problems are formulated. In Section 3, a new approach for stabilization is presented for networked control system to ensure closed-loop passivity. Section 4 illustrates effectiveness of this approach through a numerical example. Finally, we conclude the result of this paper in Section 5.

2 Networked Control System Problem Statement and Analysis

The problem of networked control system is formulated as a remote control system. Formulation of the networked control system as a Markov jump linear systems follows closely from [2,3]. The plant is remotely controlled by the controller connected via a shared communication channel. It is assumed that there are multiple sensors and actuators communicating with the controller; however, as a result of the sequential nature of the channel, only one of them can transmit a message at any discrete-time instant. To meet this requirement efficiently, we employ a periodic communication scheme [3].

Consider the remote control system for NCS model in Figure 1. Generalized plant P is described in the form of discrete-time system and has a state space equation as follow:

$$\begin{aligned} x(k+1) &= Ax(k) + B_1w(k) + B_2u(k) \\ z(k) &= C_1x(k) + D_{11}w(k) + D_{12}u(k) \\ y(k) &= x(k) \end{aligned} \tag{1}$$

where $x(k) \in \mathfrak{R}^n$ is the state, $w(k) \in \mathfrak{R}^{m_1}$ is the exogenous input, $u(k) \in \mathfrak{R}^{m_2}$ is the control input, $z(k) \in \mathfrak{R}^{p_1}$ is the controlled output and $y(k) \in \mathfrak{R}^{p_2}$ is the measurement output.

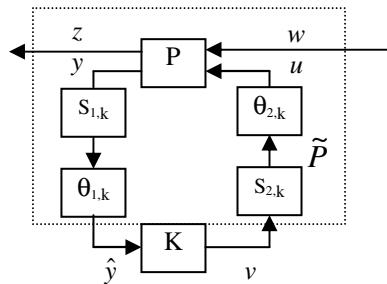


Fig. 1. Remote Control System [3]

The periodic communication scheme is performed as follows [2]. Suppose there are p_2 sensors and m_2 actuators, then the period be $N \geq m_2 + p_2$. If each sensor is capable to transmit messages, then the *switching pattern* for the sensor side defined by a vector $s_1 \in I_{p_1+1}^N$. This specifies that at time k , the sensor indexed as $s_1(\text{mod}(k,N)+1)$ is allowed to send a message. If $s_1(\text{mod}(k,N)+1)$ is zero, it means there is no communication takes place. For example, let $N = 4$, $p_2 = 2$, and $s_1 = [2, 1, 0, 2]$. In this case, sensor 1 transmits at $k = 1, 5, \dots$ while sensor 2 transmits at $k = 0, 3, \dots$, and there is no communication at $k = 2, 6, \dots$. Similarly, the switching pattern $s_2 \in I_{m_2+1}^N$ for the m_2 actuators that determines the periodic transmission from the controller to the actuators with the same period N . We assume that, at any given time, at most only one message can be transmitted by the sensors or the controller. In terms of the switching patterns, this means that $s_i(k) \neq 0$ iff $s_j(k) = 0$ for $i \neq j$ and all k .

To define periodic switchings strategy in communication between sensors and controllers and between controller and actuator, we need some notation [2]. Let $\{s_{1i}\}$ and $\{s_{2j}\}$ be two sets of vectors given as follows :

$$s_{1i} = [0\dots 010\dots 0] \in \mathfrak{R}^{1 \times p_2} \quad ; i = 1, \dots, p_2$$

$$s_{2j} = [0\dots 010\dots 0]^T \in \mathfrak{R}^{m_2 \times 1} \quad ; j = 1, \dots, m_2$$

where s_{1i} and s_{2j} have the i^{th} and j^{th} elements equal to 1, respectively, and the rest are zero. The N -periodic matrices $S_1(k)$ and $S_2(k)$ in Figure 1 are defined as :

$$S_1(k) := s_{1i} \quad ; s_1(\text{mod}(k, N) + 1) = i$$

$$S_2(k) := s_{2j} \quad ; s_2(\text{mod}(k, N) + 1) = j$$

for $k \in \mathbb{Z}_+$. We refer to them as the switches.

A lossy communication channel is assumed in this paper. Due to network congestion or network delay, the messages transmitted randomly are lost. Let $\theta_1(k)$, $\theta_2(k) \in \{0, 1\}$ be the stochastic processes that represent the message losses, from the sensors to the controller and from the controller to the actuators. If $\theta_i(k) = 0$, then the message at time k is lost; otherwise, it arrives. We assume that these are independent and identically distributed (i.i.d.) **Bernoulli** processes specified by

$$\alpha_1 := \text{Prob}\{\theta_1(k) = 0\}$$

$$\alpha_2 := \text{Prob}\{\theta_2(k) = 0\} \quad ; k \in \mathbb{Z}_+$$

Note that the overall plant including the switches S_1 and S_2 and the message loss processes θ_1 and θ_2 is periodically time varying with period N and with random switchings.

The state space equation of the overall plant \tilde{P} including the switches S_1 and S_2 and the message loss processes θ_1 and θ_2 , can be expressed as :

$$\begin{aligned}
 x(k+1) &= Ax(k) + B_1w(k) + \theta_2(k)B_2S_2(k)v(k) \\
 z(k) &= C_1x(k) + D_{11}w(k) + \theta_2(k)D_{12}S_2(k)v(k) \\
 \hat{y}(k) &= \theta_1(k)S_1(k)x(k)
 \end{aligned} \tag{2}$$

In Figure 1, K is the controller to be designed. The controller K is allowed to be N -periodic. An acknowledgement is received by the controller from the actuator regarding the arrival of control input $u(k)$.

The controller takes a form as follows:

$$v(k) = K(k) \hat{y}(k) \tag{3}$$

In this paper, we employ the following notion of stability.

Definition 1 [2]: For the periodically time-varying system with random switchings given by

$$\begin{aligned}
 x(k+1) &= A(k, \theta(k))x(k) + B(k, \theta(k))w(k) \\
 z(k) &= C(k, \theta(k))x(k) + D(k, \theta(k))w(k)
 \end{aligned} \tag{4}$$

with $w \equiv 0$, the equilibrium point at $x=0$ is

1. mean square stable if for every initial state $(x(0), \theta(0))$

$$\lim_{k \rightarrow \infty} E \|x(k)\|^2 | x(0), \theta(0)] = 0$$

2. stochastically stable if for every initial state $(x(0), \theta(0))$,

$$\sum_{k=0}^{\infty} E \|x(k)\|^2 | x(0), \theta(0)] < \infty. \text{ In other words, } \|x\|_2 < \infty \text{ for every initial state.}$$

3. exponentially mean square stable if for every initial state $(x(0), \theta(0))$, there exists constants $0 < \alpha < 1$ and $\beta > 0$ such that

$$\forall k \geq 0, \quad E \|x(k)\|^2 | x(0), \theta(0)] < \beta \alpha^k \|x(0)\|^2$$

4. almost surely stable if for every initial state $(x(0), \theta(0))$, $\Pr \left[\lim_{k \rightarrow \infty} \|x(k)\| = 0 \right] = 1$

It is known that the first three definitions of stability are actually equivalent for an MJLS. We refer to the equivalent notions of mean square, stochastic, and exponential mean square stability as second moment stability. Moreover, Second Moment Stability (SMS) is sufficient but not necessary for almost sure stability. In the remainder of this paper, references to stability will be in the sense of second moment stability. The major motivation for this choice is that straightforward necessary and sufficient conditions, given later, exists to check for SMS but not for almost sure stability [2].

Lemma 1 [3]. For the system (4), the origin is stochastically stable if and only if there exists an N -periodic matrix $P(k) \in R^{n \times n}$ such that $P(k) = P^T(k) > 0$ and

$$\sum_{i \in I_M} \alpha_i A^T(k, i) P(k+1) A(k, i) - P(k) < 0 \quad ; k \in I_N$$

where $I_N := \{0, 1, \dots, N-1\}$

The theorem states that SMS is equivalent to finding N positive definite matrices which satisfy N coupled, discrete Lyapunov equations. It is interesting to note that stability of each mode is neither necessary nor sufficient for the system to be SMS. The condition simplifies under an additional assumption on the Markov process.

Definition 2 [1]: The Markovian jump linear system (4) with $u(k)=0$, is said to be strictly passive, if every $T>0$, with zero initial condition $x(0)=0$, it satisfies

$$E\left\{\sum_{k=0}^T w(k)^T z(k)\right\} > 0 \tag{5}$$

Furthermore, it is said to be strictly passive with dissipation η if

$$E\left\{\sum_{k=0}^T (w(k)^T z(k) - \eta w(k)^T w(k))\right\} > 0 \tag{6}$$

Remark 1. If the notation ‘>’ is replaced by ‘≥’, the above strictly passive definition is referred to as passive definition. This paper focuses on strictly passive problems, and often the strictly passivity is referred to as passivity wherever no confusion arises.

Following analysis result is related to passivity of Markovian jump systems.

Asumption 1. $D(k,i) + D^T(k,i) > 0 ; i \in I_M$

Lemma 2. For $\eta \geq 0$, the markovian jump linear systems (4) is said to be strictly passive with dissipation η , if there exists a set of positive definite symmetric matrices, $P(k)$ such that

$$\Theta_i = \left(\sum_i \alpha_i \begin{bmatrix} A^T(k,i)P(k+1)A(k,i) - P(k) & A^T(k,i)P(k+1)B(k,i) - C^T(k,i) \\ B^T(k,i)P(k+1)A(k,i) - C(k,i) & B^T(k,i)P(k+1)B(k,i) + 2\eta I - D(k,i) - D^T(k,i) \end{bmatrix} \right) \tag{7}$$

$\Theta_i < 0$

Proof. Based on Lemma 1, the Markovian jump system (4) is stochastically stable, if there exists a set of positive definite symmetric matrices $P(k)$ such that

$$A^T(k,i)\bar{P}(k+1)A(k,i) - P(k) < 0 \tag{8}$$

with

$$\bar{P}(k+1) = \sum_{i,j=1}^N \alpha_{ij} P(k+1)$$

For given positive definite symmetric matrices $P(k) \in R^{nm}$, set up the stochastic Lyapunov functional as

$$V(k, x) = x^T(k)P(k)x(k) \tag{9}$$

and considering Markov jump system (4), we have

$$\begin{aligned}
& E \left\{ \sum_{k=0}^T V(k+1, x(k+1)) - V(k, x(k)) \right\} \\
&= E \left\{ \sum_{k=0}^T x^T(k+1)P(k+1)x(k+1) - x^T(k)P(k)x(k) \right\} \\
&= E \left\{ \sum_{k=0}^T (A(k, \theta(k))x(k) + B(k, \theta(k))w(k))^T P(k+1)(A(k, \theta(k))x(k) + B(k, \theta(k))w(k)) \right. \\
&\quad \left. - x^T(k)P(k)x(k) \right\} \\
&= E \left\{ \sum_{k=0}^T x^T(k) [A^T(k, \theta(k))P(k+1)A(k, \theta(k)) - P(k)] x(k) \right. \\
&\quad + x^T(k) [A^T(k, \theta(k))P(k+1)B(k, \theta(k))] w(k) + w^T(k) [B^T(k, \theta(k))P(k+1)A(k, \theta(k))] x(k) \\
&\quad \left. + w^T(k) [B^T(k, \theta(k))P(k+1)B(k, \theta(k))] w(k) \right\} \\
&= E \left\{ \sum_{k=0}^T \begin{bmatrix} x(k) \\ w(k) \end{bmatrix}^T \begin{bmatrix} A^T(k, \theta(k))P(k+1)A(k, \theta(k)) - P(k) & \\ & B^T(k, \theta(k))P(k+1)A(k, \theta(k)) \\ & & A^T(k, \theta(k))P(k+1)B(k, \theta(k)) \\ & & & B^T(k, \theta(k))P(k+1)B(k, \theta(k)) \end{bmatrix} \begin{bmatrix} x(k) \\ w(k) \end{bmatrix} \right\} \tag{10} \\
&= E \left\{ \sum_{k=0}^T \begin{bmatrix} x(k) \\ w(k) \end{bmatrix}^T \left(\sum_i \alpha_i \begin{bmatrix} A^T(k, i)P(k+1)A(k, i) - P(k) & \\ & B^T(k, i)P(k+1)A(k, i) \\ & & A^T(k, i)P(k+1)B(k, i) \\ & & & B^T(k, i)P(k+1)B(k, i) \end{bmatrix} \begin{bmatrix} x(k) \\ w(k) \end{bmatrix} \right) \right\}
\end{aligned}$$

Following condition is constructed to satisfy the Definition 2 above.

$$\begin{aligned}
& E \left\{ \sum_{k=0}^T V(k+1, x(k+1)) - V(k, x(k)) - z^T(k)w(k) - w^T(k)z(k) + 2\eta w^T(k)w(k) \right\} \\
&= E \left\{ \sum_{k=0}^T (A(k, \theta(k))x(k) + B(k, \theta(k))w(k))^T P(k+1)(A(k, \theta(k))x(k) + B(k, \theta(k))w(k)) \right. \\
&\quad - x^T(k)P(k)x(k) - (C(k, \theta(k))x(k) + D(k, \theta(k))w(k))^T w(k) \\
&\quad \left. - w^T(k)(C(k, \theta(k))x(k) + D(k, \theta(k))w(k)) + 2\eta w^T(k)w(k) \right\} \\
&= E \left\{ \sum_{k=0}^T \begin{bmatrix} x(k) \\ w(k) \end{bmatrix}^T \begin{bmatrix} A^T(k, \theta(k))P(k+1)A(k, \theta(k)) - P(k) & \\ & B^T(k, \theta(k))P(k+1)A(k, \theta(k)) - C(k, \theta(k)) \\ & & A^T(k, \theta(k))P(k+1)B(k, \theta(k)) - C^T(k, \theta(k)) \\ & & & B^T(k, \theta(k))P(k+1)B(k, \theta(k)) + 2\eta I - D(k, \theta(k)) - D^T(k, \theta(k)) \end{bmatrix} \begin{bmatrix} x(k) \\ w(k) \end{bmatrix} \right\} \\
&= E \left\{ \sum_{k=0}^T \begin{bmatrix} x(k) \\ w(k) \end{bmatrix}^T \left(\sum_i \alpha_i \begin{bmatrix} A^T(k, i)P(k+1)A(k, i) - P(k) & \\ & B^T(k, i)P(k+1)A(k, i) - C(k, i) \\ & & A^T(k, i)P(k+1)B(k, i) - C^T(k, i) \\ & & & B^T(k, i)P(k+1)B(k, i) + 2\eta I - D(k, i) - D^T(k, i) \end{bmatrix} \begin{bmatrix} x(k) \\ w(k) \end{bmatrix} \right) \right\} \tag{11} \\
&= E \left\{ \sum_{k=0}^T \zeta^T(k) \Theta_i \zeta(k) \right\} < 0
\end{aligned}$$

where $\zeta(k) = [x^T(k) \ w^T(k)]^T$, obviously, condition (11) holds if $\Theta_i < 0$. The necessity is proved along similar lines as those of Bounded Real Lemma for periodic systems with random switching stated in Theorem 3.3 of [3] under additional weak controllability assumption. This completes the proof. \square

Lemma 3 [7]. The block matrix $\begin{bmatrix} P & M \\ M^T & Q \end{bmatrix}$ is negative definite if and only if

$$\begin{aligned} Q &< 0 \\ P - MQ^{-1}M^T &< 0 \end{aligned} \tag{12}$$

In the sequel, $P - MQ^{-1}M^T$ will be referred to as the Schur complement. This lemma will be used for controller synthesis in the next section.

3 Positive Real Synthesis of Networked Control System

In this section, we present the solution to the remote control synthesis problem formulated in Section 2.

For the system (2) and controller (3), we have the state space equation for the closed loop system $F_l(\bar{P}, K)$

$$\begin{aligned} \bar{x}(k+1) &= \bar{A}(k, \theta_1(k), \theta_2(k))\bar{x}(k) + \bar{B}(k, \theta_1(k), \theta_2(k))w(k) \\ z(k) &= \bar{C}(k, \theta_1(k), \theta_2(k))\bar{x}(k) + \bar{D}(k, \theta_1(k), \theta_2(k))w(k) \end{aligned} \tag{13}$$

where $\bar{x}(k) \in R^{2n}$ is state given by $\bar{x}(k) := [x^T(k) \quad \hat{x}^T(k)]^T$ and ;

$$\begin{aligned} \bar{A}(k, \theta_1(k), \theta_2(k)) &:= [A + \theta_2(k)B_2S_2(k)K(k)\theta_1(k)S_1(k)] \\ \bar{B}(k, \theta_1(k), \theta_2(k)) &:= B_1 \\ \bar{C}(k, \theta_1(k), \theta_2(k)) &:= [C_1 + \theta_2(k)D_{12}S_2(k)K(k)\theta_1(k)S_1(k)] \\ \bar{D}(k, \theta_1(k), \theta_2(k)) &:= D_{11} \end{aligned}$$

Notice that \bar{A} and \bar{C} system matrices depend on both θ_1 and θ_2 . As mentioned earlier, this system consists of 4 modes determined by the original process pairs $(\theta_1(k), \theta_2(k))$. Let $\theta(k) := (\theta_1(k), \theta_2(k))$ be associated with the probability $\alpha_{i,j} := Prob\{\theta(k) = (i, j)\}$, $i, j \in \{0,1\}$, where [3]

$$\begin{aligned} \alpha_{0,0} &= \alpha_1\alpha_2 & \alpha_{1,0} &= (1-\alpha_1)\alpha_2 \\ \alpha_{0,1} &= \alpha_1(1-\alpha_2) & \alpha_{1,1} &= (1-\alpha_1)(1-\alpha_2) \end{aligned} \tag{14}$$

We can apply Lemma 2 to this system to obtain the synthesis result.

The following is the main result of the paper which provides a solution to the synthesis of state feedback controller for NCS to render closed-loop passivity using periodic communication scheme and taking into consideration network random delays and packet losses.

Theorem 1. For closed loop system (13) and dissipation $\eta \geq 0$, there exists a set of $P(k)$ satisfying condition $\Theta_l < 0$, if and only if there exists a set of positive definite symmetric matrices $X(k) \in R^{n \times n}$ and matrices $Y(k) \in R^{m \times n}$ satisfying

$$\begin{bmatrix} -X(k) & ()^T & ()^T & ()^T & ()^T & ()^T \\ -[C_1 X(k) + \hat{D}_2 Y(k)] & 2\eta I - (D_{11})^T - D_{11} & ()^T & ()^T & ()^T & ()^T \\ \sqrt{\alpha_{00}}[AX(k) + \hat{B}_2 Y(k)] & B_1 & -X(k+1) & 0 & 0 & 0 \\ \sqrt{\alpha_{01}}[AX(k) + \hat{B}_2 Y(k)] & B_1 & 0 & -X(k+1) & 0 & 0 \\ \sqrt{\alpha_{10}}[AX(k) + \hat{B}_2 Y(k)] & B_1 & 0 & 0 & -X(k+1) & 0 \\ \sqrt{\alpha_{11}}[AX(k) + \hat{B}_2 Y(k)] & B_1 & 0 & 0 & 0 & -X(k+1) \end{bmatrix} < 0 \quad (15)$$

By manipulation of matrix and change of controller variables, the existence conditions and the synthesis methods for the mode-dependent controllers can be formulated in terms of a set of solutions of coupled linear matrix inequalities, which can be effectively solved using LMI-software. Furthermore, the mode-dependent state feedback passive controller is given by $v(k) = K(k)\hat{y}(k)$, where $K(k) = Y(k)(S_1(k)X(k))^{-1}$.

Proof. Suppose there exists a set of positive definite symmetric matrices $P(k)$, satisfying condition $\Theta_i < 0$ to follows that the closed-loop system is stochastically stable and passive in equality (7), i.e.

$$\Theta_i = \left(\sum \alpha_i \begin{bmatrix} A^T(k, i)P(k+1)A(k, i) - P(k) & A^T(k, i)P(k+1)B(k, i) - C^T(k, i) \\ B^T(k, i)P(k+1)A(k, i) - C(k, i) & B^T(k, i)P(k+1)B(k, i) + 2\eta I - D(k, i) - D^T(k, i) \end{bmatrix} \right) \quad (16)$$

$\Theta_i < 0$

Applying Schur complements, above inequality (16) is equivalent to the following inequality

$$\begin{bmatrix} -P(k) & ()^T & ()^T & ()^T & ()^T & ()^T \\ -C_{cl} & 2\eta I - (D_{cl})^T - D_{cl} & ()^T & ()^T & ()^T & ()^T \\ \sqrt{\alpha_{00}}A_{cl} & B_{cl} & -P^{-1}(k+1) & 0 & 0 & 0 \\ \sqrt{\alpha_{01}}A_{cl} & B_{cl} & 0 & -P^{-1}(k+1) & 0 & 0 \\ \sqrt{\alpha_{10}}A_{cl} & B_{cl} & 0 & 0 & -P^{-1}(k+1) & 0 \\ \sqrt{\alpha_{11}}A_{cl} & B_{cl} & 0 & 0 & 0 & -P^{-1}(k+1) \end{bmatrix} < 0$$

Then, substitute $A_{cl}, B_{cl}, C_{cl}, D_{cl}$ using matrices $\bar{A}(k, \theta_1(k), \theta_2(k)), \bar{B}(k, \theta_1(k), \theta_2(k)), \bar{C}(k, \theta_1(k), \theta_2(k)), \bar{D}(k, \theta_1(k), \theta_2(k))$ in (13) to obtain

$$\begin{bmatrix} -P(k) & ()^T & ()^T & ()^T & ()^T & ()^T \\ -[C_1 + \theta_2(k)D_2 S_2(k)K\theta_1(k)S_1(k)] & 2\eta I - (D_{11})^T - D_{11} & ()^T & ()^T & ()^T & ()^T \\ \sqrt{\alpha_{00}}[A + \theta_1(k)B_2 S_2(k)K\theta_1(k)S_1(k)] & B_1 & -P^{-1}(k+1) & 0 & 0 & 0 \\ \sqrt{\alpha_{01}}[A + \theta_1(k)B_2 S_2(k)K\theta_1(k)S_1(k)] & B_1 & 0 & -P^{-1}(k+1) & 0 & 0 \\ \sqrt{\alpha_{10}}[A + \theta_1(k)B_2 S_2(k)K\theta_1(k)S_1(k)] & B_1 & 0 & 0 & -P^{-1}(k+1) & 0 \\ \sqrt{\alpha_{11}}[A + \theta_1(k)B_2 S_2(k)K\theta_1(k)S_1(k)] & B_1 & 0 & 0 & 0 & -P^{-1}(k+1) \end{bmatrix} < 0$$

To simplify the last inequality, define term $\hat{K}(k) = K(k)S_1(k)$ and $\hat{B}(k) = B_2 S_2(k)$, and it becomes

$$\begin{bmatrix} -P(k) & ()^T & ()^T & ()^T & ()^T & ()^T \\ -[C_1 + \theta_1(k)\theta_2(k)\hat{D}_2 \hat{K}] & 2\eta I - (D_{11})^T - D_{11} & ()^T & ()^T & ()^T & ()^T \\ \sqrt{\alpha_{00}}[A + \theta_1(k)\theta_2(k)\hat{B}_2 \hat{K}] & B_1 & -P^{-1}(k+1) & 0 & 0 & 0 \\ \sqrt{\alpha_{01}}[A + \theta_1(k)\theta_2(k)\hat{B}_2 \hat{K}] & B_1 & 0 & -P^{-1}(k+1) & 0 & 0 \\ \sqrt{\alpha_{10}}[A + \theta_1(k)\theta_2(k)\hat{B}_2 \hat{K}] & B_1 & 0 & 0 & -P^{-1}(k+1) & 0 \\ \sqrt{\alpha_{11}}[A + \theta_1(k)\theta_2(k)\hat{B}_2 \hat{K}] & B_1 & 0 & 0 & 0 & -P^{-1}(k+1) \end{bmatrix} < 0$$

Pre- and post-multiplying the inequality by block-diagonal matrix $\text{diag}\{P^{-1}(k), I, I, I, I, I\}$, letting $X(k) = P^{-1}(k)$, $Y(k) = K(k)X(k)$, the coupled linear matrix inequalities (15) are obtained. \square

Based on Theorem 1, the controller is constructed as follows. First, solve LMI (15) for positive definite symmetric matrices $X(k)$ and $Y(k)$ using available LMI solver. Then, using these solutions the controller is obtained via

$$K(k) = Y(k)(S_1(k)X(k))^{-1}$$

assuming that the required inverse exists. A more relaxed condition on nonsingularity can be obtained by using the concepts of generalized inverse of a matrix.

4 Numerical Example

In this section, we show through a numerical example, how the the LMI-based synthesis method presented in this paper can be used to synthesize a controller for NCS which render closed-loop passivity. The example is adapted from [14] with modification on the state matrix.

Consider the generalized plant of a system described by:

$$\begin{aligned}
 x(k+1) &= \begin{bmatrix} 0 & 1 & 0 \\ 0 & 0 & 1 \\ 0 & 0 & 1.8 \end{bmatrix} x(k) + \begin{bmatrix} 0 \\ 0 \\ 1 \end{bmatrix} w(k) + \begin{bmatrix} 0 \\ 0 \\ 2 \end{bmatrix} u(k) \\
 z(k) &= [0.018 \quad 0.114 \quad 0.47]x(k) + 0.1w(k) + 0.5u(k) \\
 y(k) &= [0.9 \quad -1.2 \quad -0.8]x(k) + 1.8w(k)
 \end{aligned}
 \tag{17}$$

According to the equation in (17), we can see that number of sensor $p_2 = 1$ and number of actuator $m_2 = 1$. Therefore, this system can be formulated as a periodic system with period $N=2$.

The impulse response of the generalized plant in open loop configuration is shown in Figure 2. As shown, the open loop systems is unstable.

First, state feedback controller which renders closed-loop passivity is constructed in point-to-point connection. Impulse response of this system is shown in Figure 3 (in the case without uncertainty).

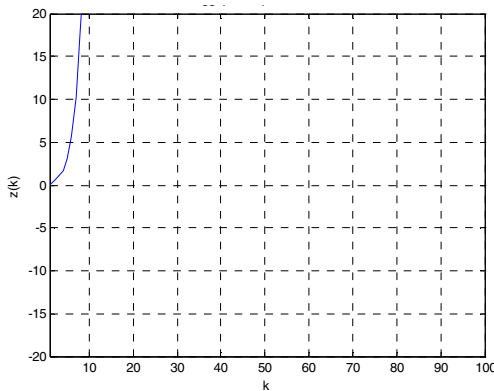


Fig. 2. Impulse response of open loop system

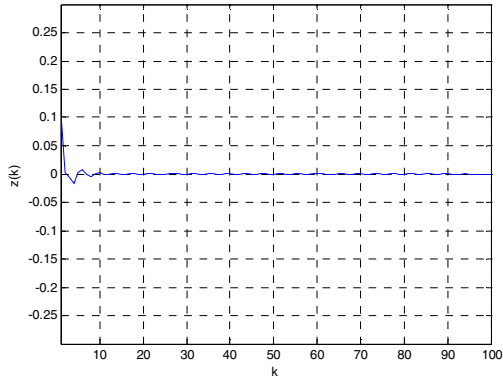


Fig. 3. Impulse response of closed-loop system without uncertainty

Robustness of this system is evaluated by applying parametric uncertainty to the system matrix. We found that the closed-loop system has certain robustness with respect to such uncertainty. However, when the size of uncertainty becomes sufficiently large, the system tends to be unstable, as shown by impulse response of the closed-loop perturbed system in Figure 4.

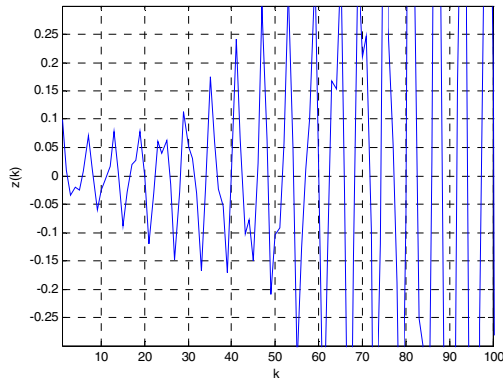


Fig. 4. Impulse response of the system with uncertainty

Then, a state feedback controller for system (17) in NCS configuration is synthesized using the LMI-based synthesis of Theorem 1. It is assumed that the loss probability of communication network from the sensor to the actuator and from the actuator to the sensor are $\alpha_1=0.5$ and $\alpha_2=0.5$, respectively. Figure 5 shows impulse response of NCS without uncertainty in system matrix. We can see that the system is stabilized by the proposed approach.

Similarly to the point-to-point case, the robustness evaluation of networked control system is carried out by applying uncertainty to the system matrix. Stable condition of NCS with uncertainty is shown in Figure 6. Figure 7 shows impulse response of

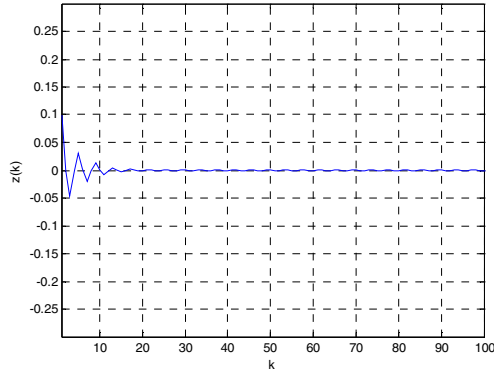


Fig. 5. Impulse Response of NCS without uncertainty

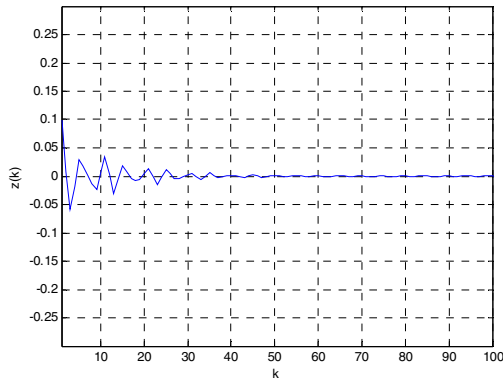


Fig. 6. Impulse Response of NCS with uncertainty: Stable

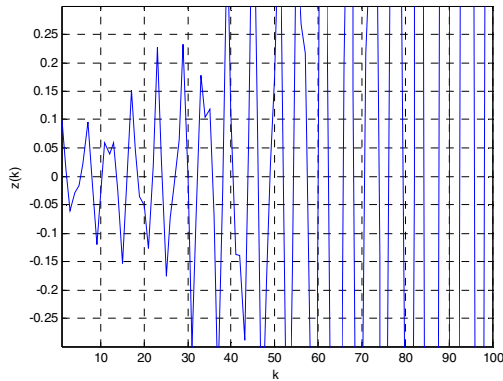


Fig. 7. Impulse Response of NCS with uncertainty: Unstable

networked control system when sufficiently large size of uncertainty is applied such that the closed-loop system becomes unstable. It is found, as expected, that the robustness margin of the point-to-point configuration is larger than that of NCS.

5 Conclusions

In this paper we have presented analysis and synthesis problems for networked control systems in discrete-time to render closed-loop positive-realness. The networked control system is modeled using discrete-time periodic Markov Jump Linear System. The state feedback controller synthesis was constructed using the solutions of a set of coupled linear matrix inequality. The results are extended for output feedback case in [13].

References

- [1] Liu, F.: Passive Analysis and Synthesis of Uncertain Markovian Jump Systems in Discrete Time. In: Proceedings of the American Control Conference Denver, Colorado, June 4-6, 2003, pp. 4875-4880 (2003)
- [2] Seiler, P., Sengupta, R.: An H_∞ Approach to Networked Control. IEEE Trans. on Automatic Control 50(3), 356-364 (2005)
- [3] Ishii, H.: An H_∞ Control with Limited Communication and Message Losses. In: Proceedings of the 2006 American Control Conference, Minnesota-USA, FrC04.1, June 14-16 (2006)
- [4] Zhang, W., Branicky, M.S., dan Phillips, S.M.: Stability of networked control systems. IEEE Control Systems Magazine 21, 84-99 (2001)
- [5] Gahinet, P., Apkarian, P.: A Linear matrix Inequality Approach to H_∞ Control. Int. Journal Robust and Nonlinear Control 4, 421-448 (1994)
- [6] Seiler, P., dan Sengupta, R.: A Bounded Real Lemma for Jump Systems. IEEE Trans. Autom. Control 48, 1651-1654 (2003)
- [7] Boyd, S., El Ghaoui, L., Feron, E., Balakrishnan, V.: Linear Matrix Inequalities in Systems and Control Theory. SIAM, Philadelphia (1994)
- [8] Seiler, P.: Coordinated Control of Unmanned Aerial Vehicles. Ph D dissertation. University of California, Berkeley (2001)
- [9] Zhang, W., Branicky, M.S., dan Phillips, S.M.: Stability of networked control systems. IEEE Control Systems Magazine 21, 84-99 (2001)
- [10] Seiler, P., Sengupta, R.: Analysis of Communication Losses in Vehicle Control Problems. In: Proceedings of the American Control Conference, Arlington, VA, June 25-27 (2001)
- [11] Hristu, D., Morgansen: Limited Communication Control. Systems and Control Letters 37(4), 193-205 (1999)
- [12] Vidyasagar, M.: Nonlinear Systems Analysis. Prentice Hall, Englewood Cliffs (1993)
- [13] Bambang, R., Arifin, I.: Passivity Synthesis of Networked Control Systems: Output Feedback Case (submitted for publication)
- [14] Tan, Z., Soh, Y.C., Xie, L.: Dissipative Control for Linear Discrete Time Systems. Automatica 35, 1557-1564 (1999)
- [15] Gao, H., et al.: Passivity and Passification for Networked Control Systems. SIAM Journal on Control and Optimization 46(4) (2007)
- [16] Gao, H., Chen, T.: Networked Based H_∞ Output Tracking Control. IEEE Trans. Automatic Control 53(3) (2008)

Controlled Switching Dynamical Systems Using Linear Impulsive Differential Equations

Endra Joelianto and Herman Y. Sutarto

Instrumentation and Control Research Group
Department of Engineering Physics
Bandung Institute of Technology, Indonesia
ejoel@tf.itb.ac.id

Abstract. Switching controller for plants with changing modes is a complex problem. Many methods have been developed for this problem. The paper investigates a unified approach to the switching controller by formulating the phenomena as a hybrid system. State jumps and mode changing of the controller responding to switched of plant dynamics are exploited and discussed. To analysis the dynamics of the controlled linear switching plants with switching controller, a hybrid system representation using linear impulsive differential equation is developed to investigate the property of changing modes of the controllers. In this paper, the switching controller is designed by using LMI method that will guarantee H_2 -type cost. A mini scale helicopter is considered as an example due to its complex dynamic and changing modes operation between hover and cruise. The performance of the switching controller is demonstrated by SIMULINK and STATEFLOW and compared to that of LQR approach.

1 Introduction

Hybrid systems are used for modeling and analyzing systems which have interacting continuous-valued and discrete-valued state variables. The continuous state variable may be the value of the state in continuous time, discrete time or a mixture of the two. The mathematical model of the continuous state is described by a differential or difference equation. The discrete state variable is generally represented by a finite state digital automaton or an input/output transition system. The behavior of the hybrid system is influenced by state variables which interact at an *event* or (*trigger*) time which occurs whenever the evolution of the system satisfies a particular condition which then initiates changes in the state variables.

The modeling framework for hybrid systems has received considerable attention over the past few years. The aim is to build a mathematical model which is suitable for complex dynamical analysis and control synthesis using hybrid systems. The models proposed in the literature reflect a wide range of both applications and justifications. An overview of hybrid system modeling can be found in [1]. In that paper, a unified approach is also proposed which is a generalization of five models of hybrid control systems developed from system and control perspectives as summarized in [2]. The unified mathematical model tries to capture all possible important aspects of continuous and discrete valued variables as well as their interaction.

The impulsive vector representation provides a general characterization of external disturbances, perturbations or even impulsive controls [2]. The impulsive ordinary differential equations of interest are those characterized by linear systems. The equations studied here are consequently referred to as linear impulsive differential equations, or simply as *linear impulsive systems* (LIS). LIS modeling can be extended to cover the problem of systems with switching dynamics which is commonly found in hybrid control system design [3]. The major development of impulsive dynamical systems is to capture the behavior of an instantaneous jump of state of a dynamical system. However, impulsive vectors may also be used to describe a dynamical system subjected to the output of a higher order model.

This paper considers the dynamical properties of controlled switching dynamical systems in the framework of linear impulsive dynamical system. The representation of this complex dynamical system in linear impulsive differential equation gives different viewpoint in understanding, analyzing and designing switching controller for switched linear dynamical systems.

2 Switching Linear Systems

Consider a minimal order continuous time linear time invariant plant with states $x(t) \in R^n$, output $y(t) \in R^l$, and input $u(t) \in R^m$ subjected to impulsive vectors $\{d(t_k), t \neq t_k, k \in Z^+\}$ at time instant t_k on the plant state as described by

$$\begin{aligned} \dot{x}(t) &= Ax(t) + Bu(t) && ; t \neq t_k \\ y(t) &= Cx(t) \\ x(t_k) &= x(t_k^-) + d(t_k) && ; t = t_k \end{aligned} \tag{1}$$

where $x(t_k^-) := \lim_{t \uparrow t_k} x(t)$, both the times t_k and values $d(t_k)$ are unknown. The impulsive vectors $d(t_k)$ may represent the external disturbances, failure of the system's components or an impulsive control.

The solution of a system with impulsive effects (1) in the extended state space begins from the initial condition (t_0, x_0) and moves along the trajectory $(t, x(t))$. If at time instants $t_k \geq t_0$ there is an impulsive jump $d(t_k)$, then the state is instantaneously changed to the new state $x(t_k) = x(t_k^-) + d(t_k)$. The state then follows the trajectory with the new initial condition $x(t_k)$ until the occurrence of the next transition time instant at time t_{k+1} in $[t_k, t_{k+1})$. That is, the solutions of impulsive systems are characterized by three components: the dynamics of ordinary

differential equations, the transition time instants t_k and the impulsive vectors $\{d(t_k)\}$ [2].

Jump in Switching Systems

Let $\{t_k\}_{k=0}^\infty$ and $\{i(k)\}_{k=0}^\infty$, $k \in \mathbb{Z}^+$ be the time instants and the i -th mode indicator respectively. Let r denotes the finite distinguished modes of dynamics by $I = \{1, 2, \dots, r\}$. In addition, define $S \subset I \times I$ as the set of pairs $(i(k+1), i(k))$ that can occur in a certain switching time t_k . Let $i(k) = i \in I$ in $[t_k, t_{k+1})$ and consider a feedback control system under an external switching law. We represent the plant dynamics by

$$\begin{bmatrix} \dot{x}(t) \\ z(t) \\ y(t) \end{bmatrix} = \begin{bmatrix} A_i & B_{i1} & B_{i2} \\ C_{i1} & 0 & D_{i12} \\ C_{i2} & D_{i21} & 0 \end{bmatrix} \begin{bmatrix} x(t) \\ w(t) \\ u(t) \end{bmatrix} \tag{2a}$$

where $x(t) \in R^n$ is the state, $w(t) \in R^{m_1}$ is the external input, $u(t) \in R^{m_2}$ is the control input, $z(t) \in R^{p_1}$ is the controlled output and $y(t) \in R^{p_2}$ is the measured output. Let the state jump of the plant are represented in the matrix form as follows

$$x(t_{k+1}) = E_{hi} x(t_{k+1}^-), \quad h = i(k+1) \tag{2b}$$

which occur if $E_{hi} \neq I$ is not the identity matrix. To illustrate, if the impulsive vector $d(t_k)$ is given as a function of the state $d(t_k) := \Theta x(t_k^-)$ then $E_{hi} = (I + \Theta)$.

Let the switching controller is in the state space form

$$\begin{bmatrix} \dot{x}^c(t) \\ u(t) \end{bmatrix} = \begin{bmatrix} A_i^c & B_i^c \\ C_i^c & 0 \end{bmatrix} \begin{bmatrix} x^c(t) \\ y(t) \end{bmatrix} \tag{3a}$$

where $x^c(t) \in R^{n_c}$ is the state of the controller with initial value $x^c(t_0) = x_0^c$. Denote the state jumps of the controller by

$$x^c(t_{k+1}) = E_{hi}^c x^c(t_{k+1}^-), \quad h = i(k+1) \tag{3b}$$

The description in (2a)-(2b) and (3a)-(3b) includes jumps of the coefficient matrices, jumps of the state or both. Even though the states of the plant are continuous and never jump, jumps of the controller's state can either bring better performance or degrade transient response of the closed loop system.

Unified Representation of Switching Controllers

The dynamical representation of switching controller (3a) and (3b) with an indicator of controller mode $i(t)$, $t \geq 0$ can be written in a compact form as follows

$$\begin{bmatrix} \dot{x}^c(t) \\ u(t) \\ \dot{i}(t) \end{bmatrix} = \begin{bmatrix} A_i^c & B_i^c & 0 \\ C_i^c & 0 & 0 \\ 0 & 0 & 0 \end{bmatrix} \begin{bmatrix} x^c(t) \\ y(t) \\ i(t) \end{bmatrix}; t \neq t_k \tag{4}$$

where $i(t) \geq 0$ is integer and denotes indicator of controller mode. Let the state jumps and sequence of mode jump of the switching controller in impulsive vector representation as follows

$$\begin{bmatrix} x^c(t_k) \\ i(t_k) \end{bmatrix} = \begin{bmatrix} x^c(t_k^-) \\ i(t_k^-) \end{bmatrix} + \begin{bmatrix} E^c(t_k) \\ D(t_k) \end{bmatrix}; t = t_k \tag{5}$$

where $E^c(t_k)$ and $D(t_k)$ denote impulsive vector of the state of the controller and impulsive vector for changing controller respectively. In this case, $i(t) = 1$ at $t = 0$ is the initial mode and $D(t_k)$ is given by

$$D(t_k) = \begin{cases} 1, & \text{next} \\ -1, & \text{back} \end{cases}$$

which is 1 for next state transition or -1 to return to the previous state. Figure 1 shows state transitions of the switching controller and the value of $D(t_k)$ and the corresponding state $i(t_k)$. The transition of the states of the controller describes a step function for a sequence of $D(t_k) := \{1,1,0,0\}$ is given by

$$i(t) = \begin{cases} 1, & 0 \leq t < t_k \\ 2, & t_k \leq t < t_{k+1} \\ 3, & t_{k+1} \leq t < t_{k+2} \end{cases}, \quad \text{for } D(t_k) = 1$$

and

$$i(t) = \begin{cases} 3, & t_{k+1} \leq t < t_{k+2} \\ 2, & t_{k+2} \leq t < t_{k+3} \\ 1, & t_{k+3} \leq t < t_{k+4} \end{cases}, \quad \text{for } D(t_k) = -1$$

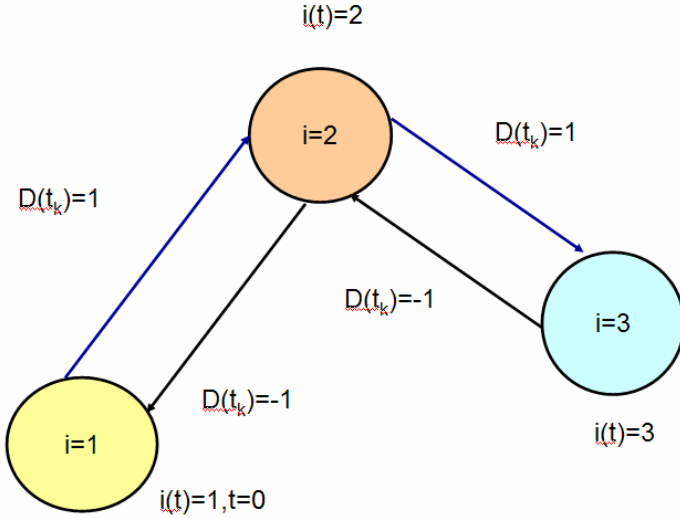


Fig. 1. State Transition of Switching Controller

Inserting equation (4) into (2) leads to closed loop dynamical system which is given by

$$\begin{bmatrix} \dot{x}(t) \\ z(t) \\ y(t) \end{bmatrix} = \begin{bmatrix} A_i & B_{i1} & B_{i2}C_i^c \\ C_{i1} & 0 & D_{i12}C_i^c \\ C_{i2} & D_{i21} & 0 \end{bmatrix} \begin{bmatrix} x(t) \\ w(t) \\ x^c(t) \end{bmatrix}$$

where $x^c(t)$ follows the dynamics of the controller in equation (4). In term of the state of the plant, the state of the controller and the indicator of the mode, the representation of closed loop system dynamics is

$$\begin{bmatrix} \dot{x}(t) \\ \dot{x}^c(t) \\ \dot{i}(t) \end{bmatrix} = \begin{bmatrix} A_i & B_{i2}C_i^c & 0 \\ B_i^c C_{i2} & A_i^c & 0 \\ 0 & 0 & 1 \end{bmatrix} \begin{bmatrix} x(t) \\ x^c(t) \\ i(t) \end{bmatrix} + \begin{bmatrix} B_{i1} \\ B_i^c D_{i21} \\ 0 \end{bmatrix} w(t)$$

When it is understood that $i(k) = i \in I$ in $[t_k, t_{k+1})$, $k \in \mathbb{Z}^+$ the equation can be reduced to

$$\begin{bmatrix} \dot{x}(t) \\ \dot{x}^c(t) \end{bmatrix} = \begin{bmatrix} A_i & B_{i2}C_i^c \\ B_i^c C_{i2} & A_i^c \end{bmatrix} \begin{bmatrix} x(t) \\ x^c(t) \end{bmatrix} + \begin{bmatrix} B_{i1} \\ B_i^c D_{i21} \end{bmatrix} w(t)$$

The equation can be written in more compact form as

$$\dot{\bar{x}}(t) = \bar{A}_i \bar{x}(t) + \bar{B}_i w(t); \quad \bar{x}(t) = [x(t) \quad x^c(t)]^T, \quad i = 1, 2, \dots, n \quad (6)$$

This switched dynamical system with switching controller (6) can then be written as a linear impulsive dynamical system as follows

$$\begin{aligned} \begin{bmatrix} \dot{\bar{x}}_1(t) \\ \vdots \\ \dot{\bar{x}}_n(t) \end{bmatrix} &= \begin{bmatrix} \bar{A}_1 & 0 & 0 \\ 0 & \ddots & 0 \\ 0 & 0 & \bar{A}_n \end{bmatrix} \begin{bmatrix} \bar{x}_1(t) \\ \vdots \\ \bar{x}_n(t) \end{bmatrix} + \begin{bmatrix} \bar{B}_1 \\ \vdots \\ \bar{B}_n \end{bmatrix} w(t); t \neq t_k \quad (7) \\ \begin{bmatrix} \bar{x}_1(t_k) \\ \vdots \\ \bar{x}_n(t_k) \end{bmatrix} &= \begin{bmatrix} \bar{x}_1(t_k^-) \\ \vdots \\ \bar{x}_n(t_k^-) \end{bmatrix} + \begin{bmatrix} F_1^c(t_k) \\ \vdots \\ F_n^c(t_k) \end{bmatrix}; t = t_k \end{aligned}$$

$$\bar{x}(t) = \bar{x}_i(t), i = 1, 2, \dots, n$$

where F_i^c and n denote matrix for state jump and the occurrence of switching respectively. The behavior of the system (6) respectively (7) depends on the properties of \bar{A}_i at each region. For two modes controller, $i = 2$, from mode 1 to 2, $F^c = [F_1^c; F_2^c] = [-\bar{x}_1(t_k); \bar{x}_1(t_k)]$ and $F^c = [\bar{x}_2(t_k); -\bar{x}_2(t_k)]$ from mode 2 to 1, it is known that jump in the closed loop system can produce overshoot on the output [2]. Therefore, it is of interest to investigate the characteristics of the system (6) in the representation of (7) and the propagation of the controller's mode sequence. The overall representation is given in Figure 2 where solid line represents continuous signal and dashed line denotes discrete/digital variables.

For more complex switching control strategy, $D(t_k)$ can have any integer values which means that the transition of the switching controller is in arbitrary order, it can jump from one controller to the other. In this case, the mode changing of the

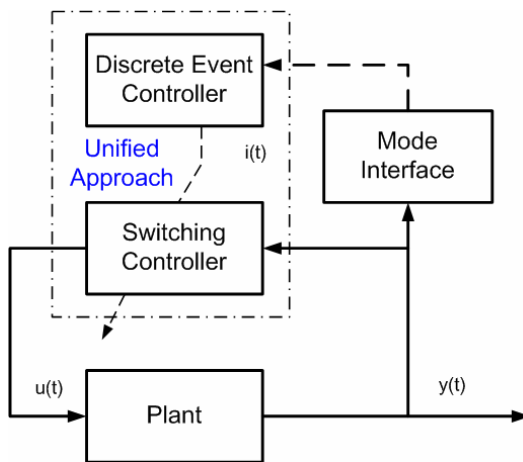


Fig. 2. Switched Control System

controller needs to be analyzed in order to guarantee that the mode changing has followed the correct sequence and it is not blocked (stopped) to a particular mode. The sequence of the mode changing can be viewed as discrete event systems and can be analyzed by using, to illustrate, signal interpreted Petri nets [4]. Due to limited space, the discussion of the Petri nets is not included.

3 Switching Controller Design

As a result of the development in the area of convex optimization, we can now solve very rapidly many convex optimization problems for which no traditional *analytic* or *closed-form* solutions exist. Indeed, the solution of many convex optimization problems can now be computed in a time which is comparable to the time required to evaluate a *closed-form* solution for a similar problem. This fact, in our opinion, has far-reaching implications for engineers; it changes our fundamental notion of what we should consider as a solution to a problem. In the past, a *solution to problem* generally meant a *closed-form* or *analytic* solution. Recently, this concept of *solution* should be extended to include many forms of convex optimization that involve Linear Matrix Inequalities (LMIs).

The critical challenge in practical hybrid system applications is finding appropriate Lyapunov functions that satisfy the stability conditions. Unfortunately, no general methods are available. However, for switched linear systems, there is an LMI problem formulation for constructing a set of quadratic Lyapunov-like functions. Existence of a solution to the LMI problem is a sufficient condition for hybrid system stability. A real advantage here is that LMI problems admit efficient and reliable numerical solutions with standard packages [5].

This main objective this paper is concerned with the synthesis of switched control system excited with external switches. Based on class of discontinuous Lyapunov-like functions, we conduct performance analysis of H_2 -type cost for linear switched system. In the synthesis problem to derive an output feedback switching controller with guaranteed H_2 -type cost, we employ state jumps of the controller to improve stability and H_2 -type control performance.

Stability Analysis

Let $x(t) \in R^n$ be the system state and $x(t_0) = x_0$ be initial value. For each k , the state $x(t)$ is continuous in $t \in [t_k, t_{k+1})$ and satisfies the following state equation

$$\dot{x}(t) = A_i x(t) + B_i w(t), \quad x(t_k) = x_k \quad (8)$$

where $w(t)$ is a function of some adequate class. The initial value $x(t_{k+1}) = x_{k+1}$ for each interval is given by

$$x_{k+1} = E_{hi} x(t_{k+1}^-), \quad h = i(k+1) \quad (9)$$

The equation (9) represents possible state jumps of the system, which occur if $E_{hi} \neq I$. In equation (8) and (9), the state $x(t) : t \in [0, \infty)$ is uniquely determined up to $\{i(k)\}_0^\infty, \{t_k\}_0^\infty, w(t)$ and x_0 . The above class of switched systems is a linear version of systems considered in [1] and [6].

Consider switched Lyapunov function of piecewise quadratic form given by the following equation

$$v_i(x) = x^T P_i x \tag{10}$$

where P_i is a positive definite symmetric matrix. The $a = \min_i \lambda_{\min}(P_i)$ and $b = \max_i \lambda_{\max}(P_i)$, and the above proposition is stated in terms of matrix inequalities for Lyapunov functions of piecewise quadratic form and then we only consider performance analysis for an H_2 -type cost of linear switched systems. Let $z(t) = C_i x(t), t = [t_k, t_{k+1}), i = i(k)$ and consider the following H_2 -type cost $\gamma^* = \inf \gamma$ such that

$$\left(\int_0^\infty \|z(t)\|^2 dt \right)^{1/2} \leq \gamma \|w_0\|, \forall w_0 \in R^m \tag{11}$$

Synthesis via Linear Matrix Inequalities (LMIs)

Consider a feedback control system under the external switching law with the plant dynamics by equation (2a) and (2b). The state jump of the plant is represented by $x(t_{k+1}) = E_{hi} x(t_{k+1}^-), h = i(k + 1)$. The controller is given by (5). Denote the state jumps of the controller by $x^c(t_{k+1}) = E_{hi}^c x^c(t_{k+1}^-), h = i(k + 1)$.

Remark: Even though the state of the plant is continuous and never jumps, jumps of the controller’s state can give better performance of the closed loop system.

Following the description of the paper [7,8], we give an upper-bound for the optimal H_2 -type cost (11) with numerically tractable LMI conditions and gives the LMI characterization as follow

$$\hat{P}_i \geq 0, i \in I, \alpha > 0, \mu > 0, \alpha T_D > \ln \mu \tag{12}$$

$$\hat{Q}_i = \begin{bmatrix} -\hat{A}_i^T - \hat{A}_i - 2\alpha \hat{P}_i & \hat{C}_i^T \\ & \hat{C}_i \\ & & \gamma I \end{bmatrix} > 0, i \in I \tag{13}$$

$$\hat{R}_i = \begin{bmatrix} \gamma e^{-2\alpha T_D} I & \hat{B}_i^T \\ & \hat{B}_i \\ & & \hat{P}_i \end{bmatrix} > 0, i \in I \tag{14}$$

$$\hat{S}_{hi} = \begin{bmatrix} \mu \hat{P}_i & \hat{E}_{hi}^T \\ \hat{E}_{hi} & \mu \hat{P}_h \end{bmatrix} > 0, (h, i) \in S \quad (15)$$

where

$$\hat{P}_i = \begin{bmatrix} V_i & I \\ I & W_i \end{bmatrix} \quad (16)$$

$$\hat{A} = \begin{bmatrix} A_i V_i + B_{i2} F_i & A_i + B_{i2} H_i C_{i2} \\ L_i & W_i A_i + G_i C_{i2} \end{bmatrix} \quad (17)$$

$$\hat{B}_i = \begin{bmatrix} B_{i1} + B_{i2} H_i D \\ W_i B_{i1} + G_i D_{i21} \end{bmatrix} \quad (18)$$

$$\hat{C}_i = [C_{i1} V_i + D_{i21} F_i \quad C_{i1} + D_{i21} H_i C_{i2}] \quad (19)$$

$$\hat{E}_{hi} = \begin{bmatrix} E_{hi} V_i & E_{hi} \\ Z_{hi} & W_h E_{hi} \end{bmatrix} \quad (20)$$

The LMI condition (12)-(15) is the equivalent of the bilinear matrix inequalities (BMI) of the optimal H_2 -type cost derived in [7]. This equivalent condition holds if only if for some feasible controller the LMIs (12)-(15) has a solution \mathbf{p} where $\mathbf{p} = \{V_i, W_i, F_i, G_i, H_i, L_i, Z_{jk}; i \in I, (j, k) \in S\}$. One of the solutions to the BMIs is given by the following equations

$$\begin{bmatrix} D_i^c & C_i^c \\ B_i^c & A_i^c \end{bmatrix} = \begin{bmatrix} I & 0 \\ B_{i2} & -W_i^{-1} \end{bmatrix} \begin{bmatrix} H_i & F_i \\ G_i & L_i - W_i A_i V_i \end{bmatrix} \begin{bmatrix} I & -C_{i2} V_i S_i^{-1} \\ 0 & S_i^{-1} \end{bmatrix} \quad (21)$$

$$E_{hi}^c = -W_h^{-1} (Z_{hi} - W_h V_i) S_i^{-1} \quad (22)$$

$$P_i^{cl} = \begin{bmatrix} V_i & S_i \\ S_i & S_i \end{bmatrix}^{-1}, \quad S_i = V_i - W_i^{-1} \quad (23)$$

The matrices $\{A_i^c, B_i^c, C_i^c, D_i^c\}$ of the switching controller given in (3) are then obtained by solving the equations (21)-(23).

4 An Example

We demonstrate the stability of the switched linear control system with two flight modes used by model helicopter, i.e. hover and cruise modes taken from [9]. The

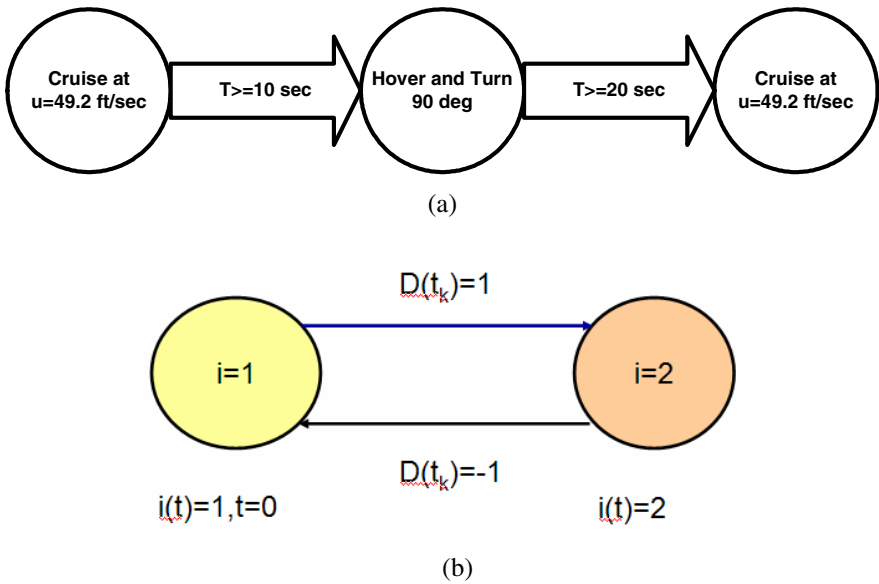


Fig. 3. Flight Scenario: (a) Flight mode (b) Mode of controller

flight scenario and the corresponding dynamics of the switching controller are shown in Figure 3.

A simple flight scenario is chosen in order to focus only on the switching phenomena. The cruise mode is selected as the initial flight mode with longitudinal speed of $u_0=49.2$ ft/sec. After 10 sec, the flight mode changes to stop over and turn 90 deg in hover mode. The entire hover mode is executed in 10 sec and then is switched to cruise mode at the same cruise speed. In this sequence, the impulsive vector $D(t_k)$ in the equation (5) takes value $D(t_k) = 1$ from cruise to hover, $D(t_k) = -1$ from hover to cruise with the initial mode indicator $i(t) = 1, t = 0$.

Helicopter flight dynamic model has 14 states consisting of states and yaw angle ψ and also 4 inputs [9]:

$$X = [u \quad v \quad w \quad p \quad q \quad r \quad \Phi \quad \theta \quad \psi \quad r_{fb} \quad a \quad b \quad c \quad d]^T$$

and

$$U = [\delta_{lat} \quad \delta_{lon} \quad \delta_{ped} \quad \delta_{col}]^T$$

To include turbulence effects, the linear system can be written as

$$\dot{X} = AX + B_t U_t \tag{24}$$

where the matrix input and the input vector respectively becomes

$$B_t = [B \quad A(:,1) \quad A(:,2) \quad A(:,3)] \tag{25}$$

$$U_t = [U \quad u_g \quad v_g \quad w_g] \tag{26}$$

We have thus obtained a linear model where inputs u_g, v_g, w_g can be deterministic functions of time, to describe wind, or random variable that can be generated in time domain to match statistical properties of turbulence models. In this simulation, we apply deterministic function such as lateral constant wind.

$$\begin{bmatrix} \dot{x}(t) \\ z(t) \\ y(t) \end{bmatrix} = \begin{bmatrix} A_i & B_{i1} & B_{i2} \\ C_{i1} & 0 & D_{i12} \\ C_{i2} & D_{i21} & 0 \end{bmatrix} \begin{bmatrix} x(t) \\ w(t) \\ u(t) \end{bmatrix} \tag{27}$$

According to (2)

$$B_{i2} = B \text{ and } B_{i1} = [A(:,1) \quad A(:,2) \quad A(:,3)]$$

where $z(t) = [u \quad v \quad w \quad \Phi \quad \theta \quad \psi]^T$, $y(t) = x(t)$ for the state feedback case and $y(t) = z(t)$ for the output feedback case.

The simulation results are shown in Figure 4 to Figure 16. The results show performance comparison among LQR synthesis, state and output feedback switched control. LQR is designed based on choosing or tuning the matrix Q and R in the cost function in order to achieve an optimal performance. This problem can be formalized by defining a performance index of the form:

$$\min_{u \in \ell_2[0, \infty)} \int_0^{\infty} [x^T(t)Qx(t) + u^T(t)Ru(t)]dt, \quad Q^T = Q \geq 0, \quad R^T = R > 0 \tag{28}$$

Here Q is a matrix that penalizes the deviation of the states x from the desired operating point, while R penalizes the control effort. Thus (28) represents a trade-off between regulation performance and control effort.

The details of this approach can be found in [10,11]. In the LQR synthesis, the following weight parameters have been chosen: $Q = I_{17}$, $R = I_4$ and $\eta = 5$. Meanwhile, the switched linear control (SLC) is designed based on setting α, μ . In this approach, the choice of the parameters α, μ is governed by (10) and (11). The parameters were obtained by using trial error method. Equation (9) represents the explicit handling of switching phenomena not appearing in the LQR approach. This step leads to the optimization objective given by (11) which ultimately gives rise to the LMI characterization. By setting $\alpha = 0.5$, $\mu = 127.352$ and $T_D = 10$, we minimized γ (11) via standard LMI solver in LMI Control Toolbox.

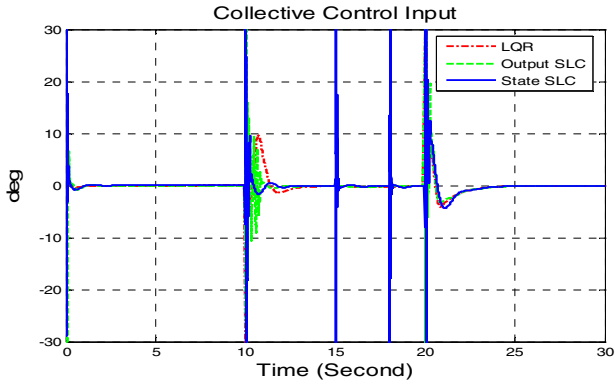


Fig. 4. Collective Control Input

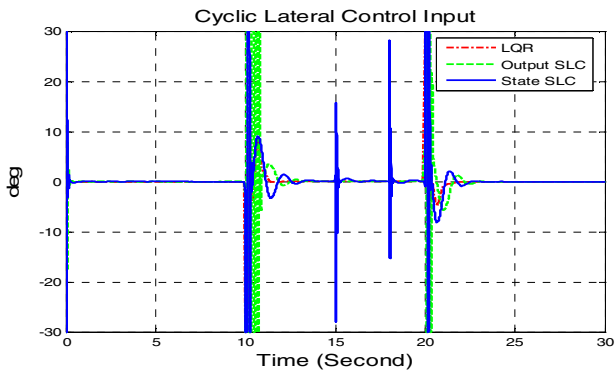


Fig. 5. Cyclic Lateral Control Input

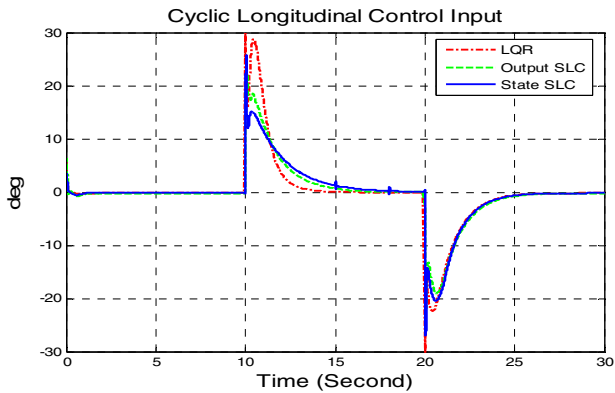


Fig. 6. Cyclic Longitudinal Control Input

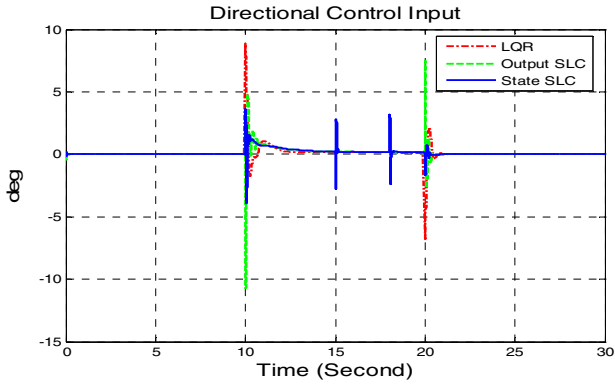


Fig. 7. Directional Control Input

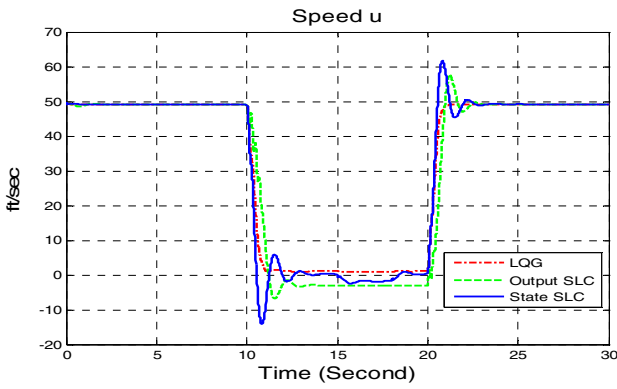


Fig. 8. Longitudinal Velocity

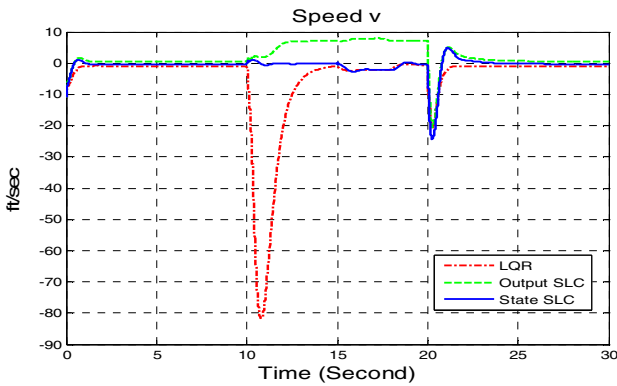


Fig. 9. Lateral Velocity

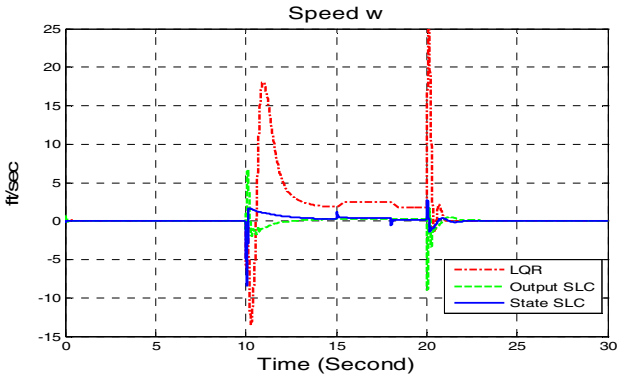


Fig. 10. Vertical Velocity

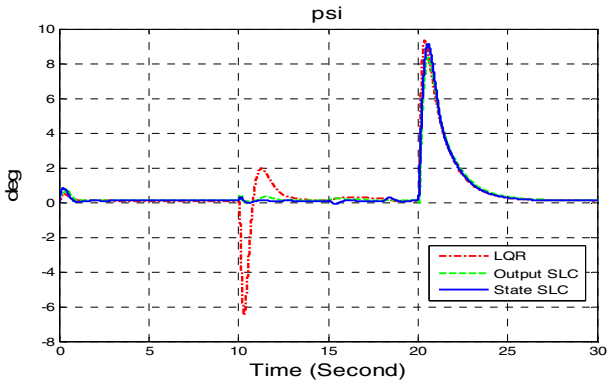


Fig. 11. Roll

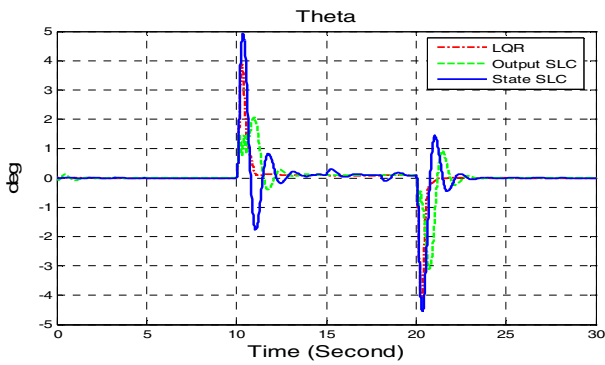


Fig. 12. Pitching

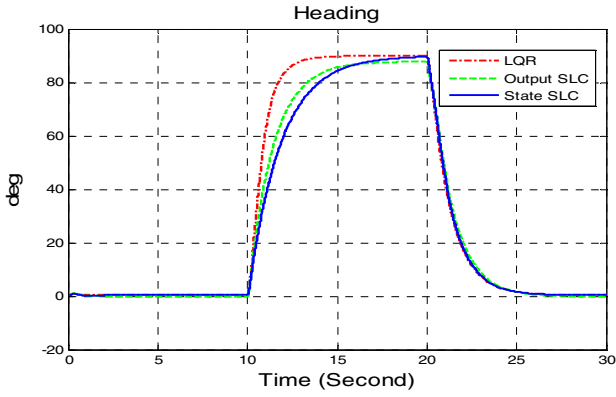


Fig. 13. Heading

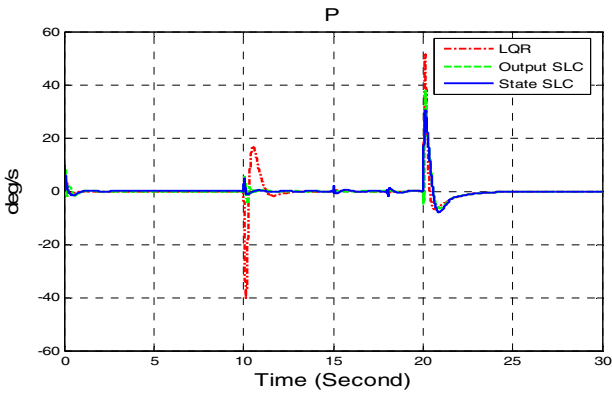


Fig. 14. Roll Rate

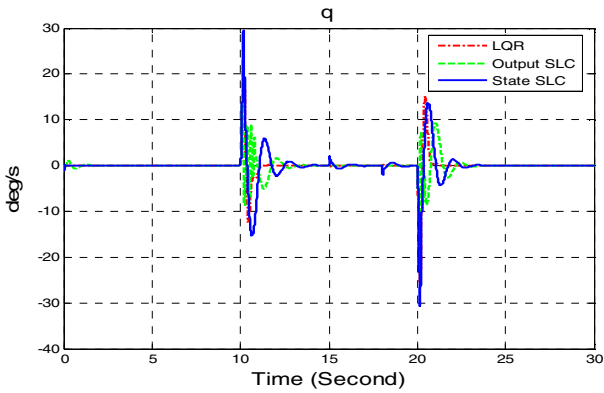


Fig. 15. Pitch Rate

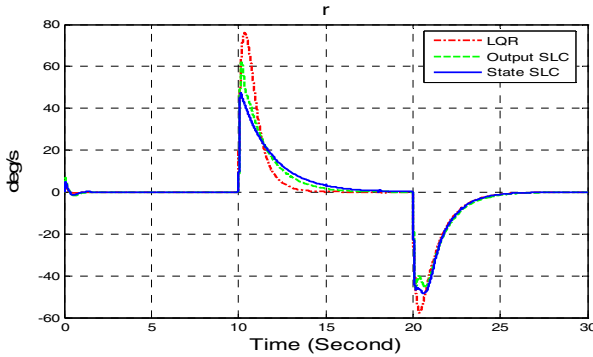


Fig. 16. Yaw Rate

In the real flight situation, both state and input variables have a constraint in the allowable space or invariant set. State constraint is imposed on the jumps of state when switching condition occurred and is judged qualitatively based on physical interpretation. The limitation of the control inputs for helicopter is governed by the maximum allowable deflection of its control surfaces. The control input limits for this study are:

$$\begin{aligned}
 -30^0 &\leq \delta_{lat} \leq 30^0 \\
 -30^0 &\leq \delta_{lon} \leq 30^0 \\
 -30^0 &\leq \delta_{ped} \leq 30^0 \\
 -30^0 &\leq \delta_{col} \leq 30^0
 \end{aligned}$$

Switching compensation with these LQR synthesized controllers could stabilize the switched systems under switching as shown in Figure 4 to Figure 16. It is evident that the LQR controller have poor performance on switching condition especially at lateral and vertical speed, roll and roll rate response even though other state and input command responses is comparable to response of SLC switched control. SLC showed particularly a better performance compared to LQR at the switching condition.

Predicted levels of Handling Qualities (HQs) have been evaluated to test compliance with Aeronautical Design Standard ADS-33 [12]. Almost Level-1 (Requirement for large amplitude attitude changes-hover and low speed) has been achieved by Output SLC for moderate agility category. The only aspect did not meet the requirement is yaw rate that bigger than 22 deg/s. In the simulation, the hovering helicopter is commanded to maintain an initial position despite a lateral step wind gust at t = 15 s for 2 seconds. All controllers reject the constant wind disturbance and successfully maintain hover flight.

Figure 4 to Figure 16 also show that the output of the plant and the controller has overshoot caused by switching the controller. From the linear impulsive differential equation, the state of the plant does not jump but mode changing yields those overshoot. This can be reduced by selecting an impulsive vector to cause the state to

jump to another state so that the output of the controller and that plant will not overshoot.

The safety problem for switched /hybrid system asks whether trajectory starting from a set of initial states reach a set of unsafe (final) state. This problem is closely related to invariant set analysis on impulsive dynamical system discussed in [6]. An invariant set is characterized by the property that if a point $x(t), t = 0$ is in the set then its whole path $\forall t$, either forward or backward, lies in the set. This definition says that once the trajectory is in the invariant set, it is impossible for the trajectory to go out from the invariant set. The stability of the trajectory with respect to the invariant set has been derived in [6]. Computational aspect for invariant set analysis needs more practical limitation both on the state and input constraint by considering in the polyhedral sets. The recent techniques that provide the ability to verify the safety properties of high dimensional system with realistic computation times have been shown [13,14]. By exploiting the structure of linear dynamical systems, the technique [14] converts the exact safety verification of linear system with certain eigen-structure as an emptiness problem for a semi-algebraic set.

5 Conclusions

This paper showed a performance design and application of switching controller of H_2 -type cost for helicopter linear switched systems. We investigate the control for transition dynamics between hover and cruise by recasting the phenomena as a hybrid system described by linear impulsive differential equation. In approaching the solution to the hybrid control problem, it is considered piecewise quadratic Lyapunov-like functions that leads to linear matrix inequalities (LMIs) characterization. The transition control performance has been demonstrated by SIMULINK and STATEFLOW and comparison LQR approach is shown. The SLC method accounts for state jumps explicitly and demonstrates a better transition control performance compared to LQR. In the area of control theory, the parameter of the SLC controller is presently achieved by using trial and error technique.

The mode changing and jump in the state of the plant and its effect were analyzed using liner impulsive differential equation. Using this approach, a better understanding on the sequence of switching controller and the transient response during switching can be described analytically. Further work is to integrate the sequence of switching controller, switching controller calculation and the stability analysis of the closed loop system. Some additional research is needed to make the approach more effective in meeting practical control design constraints by using invariant set.

References

- [1] Branicky, M.S., Borkar, V.S., Mitter, S.K.: A Unified Framework for Hybrid Control: Model and Optimal Control Theory. IEEE Trans. Automat. Contr. 43, 31–45 (1998)
- [2] Joelianto, E.: Linear Hybrid Reference Control Systems, PhD Thesis, The Australian National University, Canberra-Australia (2001)

- [3] Joelianto, E.: Linear Impulsive Differential Equations for Hybrid Systems Modeling. In: Proc. European Control Conference (ECC), Cambridge, UK (2003)
- [4] Joelianto, E., Loeis, K.: Application in Control of Boiler using Signal Interpreted Petri Nets. In: Proc. 6th Asian Control Conference (ASCC), Bali, Indonesia, pp. 858–863 (2006)
- [5] Gahinet, P., Nemirovski, A., Laub, A.J., Chilali, M.: LMI Control Toolbox for Use with MATLAB, The Mathworks (1995)
- [6] Joelianto, E., Williamson, D.: Stability of Impulsive Dynamical System. In: Proc. of 37th IEEE Confer. on Decision and Control, pp. 3717–3722 (1998)
- [7] Masubuchi, I., Tsutsui, M.: On Design of Controllers for Linear Switched Systems with Guaranteed H2 Type Cost. In: Proc. 14th Inter. Symp. on Mathematical Theory of Network and System (MTNS) (2000)
- [8] Masubuchi, I., Ohara, A., Suda, N.: LMI-Based Controller Synthesis: A Unified Formulation and Solution. *Inter. Journal of Robust and Nonlinear Control* 8, 669–686 (1998)
- [9] Sutarto, H.Y., Budiyo, A., Joelianto, E., Hiong, G.T.: Switched Linear Control of Model Helicopter. In: Proc. 9th Inter. Confer. Control, Automation, Robotics and Vision, Singapore, pp. 1300–1307 (2006)
- [10] Budiyo, A., Wibowo, S.S.: Optimal Tracking Controller Design for A Small Scale Helicopter. *Journal of Bionic Engineering* 4, 271–280 (2007)
- [11] Sutarto, H.Y., Budiyo, A., Wibowo, S.S.: LQG Optimal Tracking Controller Design for a Model Helicopter (In Indonesian Language). In: Proc. of Nat. Symposium on Aeronautical Science (September 2005)
- [12] Anonymous, ADS-33E-PRF Aeronautical Design Standard, Performance Specification, Handling Qualities Requirements for Military Rotorcraft, US Army Aviation and Missile Command, Aviation Engineering Directorate, Redstone Arsenal, Alabama (2001)
- [13] Yazarel, H., Pappas, G.J.: Geometric Programming Relaxations for Linear System Reachability. In: Proc. of American Control Conference, vol. 1, pp. 553–559 (2004)
- [14] Yazarel, H., Prajna, S., Pappas, G.J.: S.O.S. for Safety. In: Proc. of 43rd IEEE Confer. on Decision and Control, vol. 1, pp. 461–466 (2004)

Structural Damage Detection Using Randomized Trained Neural Networks

Ismoyo Haryanto¹, Joga Dharma Setiawan¹, and Agus Budiyo²

¹ Mechanical Engineering Department
Engineering Faculty - Diponegoro University
Jl. Prof. Sudarto, SH, Kampus Tembalang- Semarang

² Department of Aerospace Information Engineering
Konkuk University, Korea
budiyo@alum.mit.edu

Abstract. A computational method on damage detection problems in structures was developed using neural networks. The problem considered in this work consists of estimating the existence, location and extent of stiffness reduction in structure which is indicated by the changes of the structural static parameters such as deflection and strain. The neural network was trained to recognize the behaviour of static parameter of the undamaged structure as well as of the structure with various possible damage extent and location which were modeled as random states. The proposed techniques were applied to detect damage in a cantilever beam. The structure was analyzed using finite-element-method (FEM) and the damage identification was conducted by a back-propagation neural network using the change of the structural strain and displacement. The results showed that using proposed method the strain is more efficient for identification of damage than the displacement.

Keywords: back-propagation, damage detection, finite element method, neural network.

1 Introduction

Structural systems or machinery components tend to accumulate damage during their operation life. Therefore, an effective and reliable damage assessment methodology of the structural system is a very valuable tool. A determination of safety level of a structural system during its operational life is essential not only for safe operation but also maintenance cost reduction and failure prevention.

Occurrence of damage in a structural element reduces stiffness of the structure and generates a small perturbation in its static or dynamic responses. A perturbation on static responses can be identified by the behaviour of displacements or strains. Meanwhile, the behaviour of natural frequencies and mode shapes can be used to identify the perturbation on dynamic responses of the structure. A combination of measured response and finite-element-methods (FEM) then can be developed in order to identify these response perturbations which can be used to determine the size and location of the damage of the structure.

Response of damaged structure will follow the pattern of the size and location of the damage on its structure. Bishop has shown that this pattern can be generalized

using Artificial Neural Network/NN [1]. Therefore, the damage detection on a structural system or a machinery component can be conducted using NN which was trained to identify the pattern of response characteristic of the structure.

Maity and Saha have developed a damage assessment in structure from changes in static parameter using NN approach [7]. Unfortunately, this assessment was only focused on single element damage and multiple element damage which consists only of two damaged elements. In practical point of view this methodology is inadequate. Therefore, a more general damage assessment methodology has to be developed.

The objective of this research is to develop a structural damaged detection methodology from changes in static parameter, i.e.: displacement and strain of a simple cantilever beam using neural network combined with FEM. In the present work a random state is proposed to simulate stiffness reduction factor and damage location of the structure such that values of the stiffness reduction factor and the damage location are random. Using this random state the proposed method of structural damage assessment may be able to be applied in more general condition.

2 Problem Formulation

First step in damage detection of a structure using neural network is modelling of the structure to obtain data set which is used as input in the network training. This structural modelling has to be able to represent all possibilities of damage condition on the structure. The damage of the structure is modelled by stiffness reduction and consists of size and location on the structure. In order to obtain the data set as input for network training, values of the stiffness reduction are assumed to be random number between 0 and 1. The number and the location of damaged structural element are also assumed to be random and it may be multiple element damage. In this present work, structural response of strain and displacement due to specific loading obtained by FEM were chosen as data set used for training the network.

When the structural responses as input data set was obtained then training of the network is conducted until outputs of the networks satisfy the desired target or until the network reach desired performance which is indicated by error level (difference between output and desired target of network). Usually this error is formulated as mean square error (MSE). The above principle of neural network is illustrated by a simple schematic in Fig. 1 below.

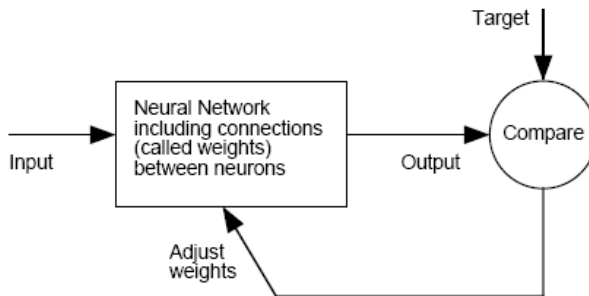


Fig. 1. A schematic of an artificial neural network [2]

At following section the structural modelling and the neural networks will be discussed more detail.

2.1 Structural Modelling

The strain energy of a structural element is formulated as

$$U = \frac{1}{2} \int_{Vol} \{\sigma\}^T \{\varepsilon\} dVol \quad (1)$$

Introducing the stress-strain relation in Eq. (1), we have

$$U = \frac{1}{2} \int_{Vol} \{\varepsilon\}^T [D] \{\varepsilon\} dVol \quad (2)$$

Note that $\{\sigma\} = [D] \{\varepsilon\}$, whereas D represents constitutive matrix of the structure material. At the other hand the strain-displacement relation is given by

$$\{\varepsilon\} = [B] \{d\} \quad (3)$$

where B is derivative of shape function and d is structural displacement. Finally the stiffness matrices of the structural element are formulated as

$$[K] = \int_{Vol} [B]^T [D] [B] dVol \quad (4)$$

and the strain of the structure is given by the following formulae [6]

$$\varepsilon(x, z) = \frac{du}{dx} = -z \frac{d^2v}{dx^2} = -zv'' \quad (5)$$

where u and v are vertical and transversal displacement, respectively. Whereas x and z are structural coordinate in horizontal and vertical direction as well as.

The nodal displacement due to applied load then can be calculated using following relation

$$[K] \{d\} = \{F\} \quad (6)$$

where $\{F\}$ is the applied load node.

The damaged modelling on the structure can be conducted by a reduction of the structural stiffness which is represented by reduction of the cross section area of the structural elements. In structural modelling using FEM the stiffness matrices of the damaged structural element are formulated as follows:

$$[K_d] = ee[K] \quad (7)$$

where: $[K_d]$: stiffness matrix of damaged structural element

$[K]$: stiffness matrix of undamaged structural element

ee : stiffness reduction factor

It should be noted that the value of stiffness reduction factor is between zero and one ($0 < ee \leq 1$). For undamaged structural element $ee = 1$, meanwhile $ee < 1$ represents damaged structural element.

2.2 Neural Network

An Artificial Neural Networks (ANN) is computational system which is inspired by the biological brain in their structure, data processing and learning ability with some assumptions as follows [2][5][8][9]:

- The information processing is conducted at the simple element called neuron
- The signals are transmitted from neuron to other neuron through the connection
- Each connection between neurons has a specific weighting factor
- In order to determine the output, an activation function is applied in the input and then the output of the system compared to an desired target.

Generally, the neural network is characterized by: network architecture which simulates relation pattern of neurons, activation function, and training method. Fig.2 illustrates multilayer network, the most common architecture of network. Besides input and output, this network also consists of hidden layers although it is possible to build a network without hidden layer. The network in Fig. 2 consists of R number of input unit (p_1, p_2, \dots, p_R), two hidden layers and one output layer.

The input layer receives input pattern and transmits the signal directly to the next layer. Meanwhile, the hidden layer consists of a certain number of processing units and each node in the preceding layer is fully connected to all processing units. These connections are called the weights that represent different weighting scales to the input signals. The weighted signals then are summed up by the processing unit and a response transmitting is activated to the next layer. The activation function may be linear or non-linear function. The above procedure is illustrated in Fig 3.

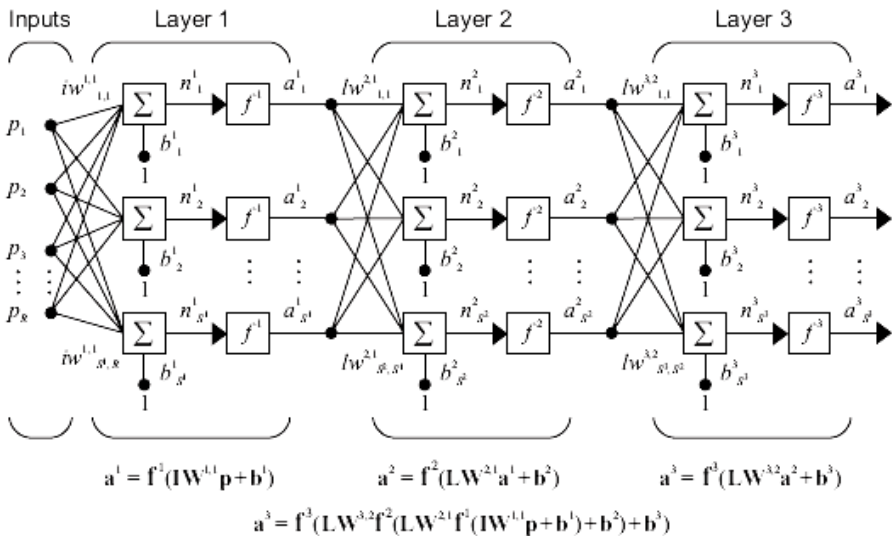


Fig. 2. Multilayer network [2]

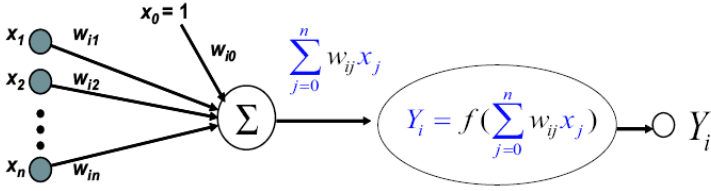


Fig. 3. Artificial neuron

The input pattern is propagated forward and actual responses are obtained. The difference between the actual and the desired outputs is then through network propagated backward to modify the weights such that the mean-square error (MSE) is minimized. This supervised training continues until the training process complete. In present work, Lavenberg Merquardt algorithm was applied as training algorithm.

Using Lavenberg Merquardt algorithm the mean square error (MSE) is used as performance function, which is formulated as follows

$$MSE = \frac{1}{N} \sum_{i=1}^N (e_i)^2 = \frac{1}{N} \sum_{i=1}^N (y_i - t_i)^2 \quad (8)$$

where t_i is desired target, y_i is actual output, and N is number of training data. According to Lavenberg-Marquardt [2][4]

$$\Delta w = [J^T(w).J(w) + \mu I]^{-1} J^T e(w) \quad (9)$$

where $J(w)$ is Jacobian matrix

$$J(w) = \begin{bmatrix} \frac{\partial e_1(w)}{\partial w_1} & \frac{\partial e_1(w)}{\partial w_2} & \dots & \frac{\partial e_1(w)}{\partial w_n} \\ \frac{\partial e_2(w)}{\partial w_1} & \frac{\partial e_2(w)}{\partial w_2} & \dots & \frac{\partial e_2(w)}{\partial w_n} \\ \vdots & \vdots & \ddots & \vdots \\ \frac{\partial e_N(w)}{\partial w_1} & \frac{\partial e_N(w)}{\partial w_2} & \dots & \frac{\partial e_N(w)}{\partial w_n} \end{bmatrix} \quad (10)$$

The Marquardt modification to the back-propagation algorithm thus proceeds as follows [4]:

1. Present all inputs to the network and compute the corresponding network outputs and MSE over all inputs (using Eq. (8)).
2. Compute the Jacobian matrix Eq. (10).
3. Solve (9) to obtain Δw
4. Recompute MSE using $w + \Delta w$. If this new MSE is smaller than that computed in step 1, then reduce μ by β , and go back to step 1. If the MSE is not reduced, then increase μ by β and go back to step 3.
5. The algorithm is assumed to have converged when the MSE has been reduced to some error goal.

3 Numerical Example

The computer codes which have been developed in the present work were applied on a simple cantilever beam structure. For training the neural network the calculated static displacement and strain at several nodal points were used. Reducing of EI values is applied in order to define the damage of the structural element.

Fig. 4 shows a cantilever beam with rectangular cross-section subjected to vertical load of 100 N at the tip. The beam has 0.2 m in length, uniform cross section with $h = 0.01$ m and $b = 0.02$ m, whereas the Young's Moduli of the material is $E = 200$ GPa. The beam was divided into eight element to find the deflection and the strain using FEM.

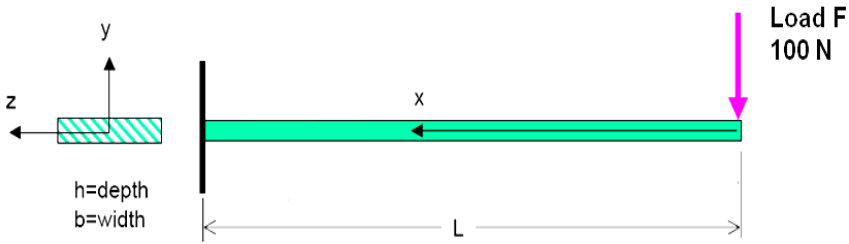


Fig. 4. Cantilever beam with tip loading

As mentioned previously, in the present work the displacement and the strain of the structure are used as the input for NN training. Therefore, a validation of the analysis results of the strain and the displacement of the beam are needed. Table 1 shows the displacement of the cantilever beam. It can be seen that the displacements obtained in present work showed very good agreement with those obtained by MSC-Nastran and exact calculation. A very good agreement is also shown by the strain of the beam obtained in present work, by MSC-Nastran and exact calculation as depicted in Table 2. From comparisons in Table 1 and Table 2, it can be concluded that the results using FEM in the present work is acceptable.

Table 1. Displacement of Cantilever Beam Used in Present Work

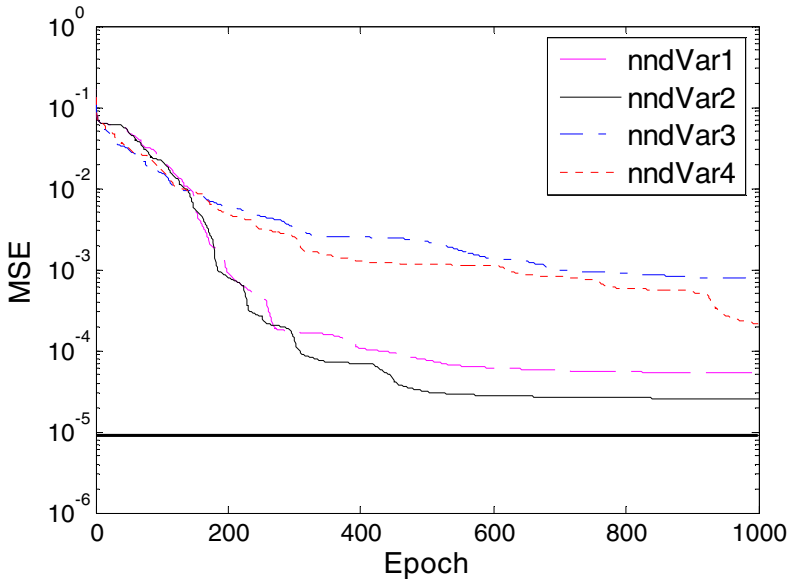
Node	Present Result (m)	MSC-Nastran (m)	Exact (m)
1	0	0	0
2	0.179×10^{-4}	0.182×10^{-4}	0.179×10^{-4}
3	0.688×10^{-4}	0.691×10^{-4}	0.688×10^{-4}
4	1.477×10^{-4}	1.483×10^{-4}	1.476×10^{-4}
5	2.500×10^{-4}	2.508×10^{-4}	2.500×10^{-4}
6	3.711×10^{-4}	3.720×10^{-4}	3.711×10^{-4}
7	5.063×10^{-4}	5.074×10^{-4}	5.062×10^{-4}
8	6.508×10^{-4}	6.521×10^{-4}	6.508×10^{-4}
9	8.000×10^{-4}	8.015×10^{-4}	8.000×10^{-4}

Table 2. Strain of cantilever beam used in present work

Node	Present Result (m/m)	MSC-Nastran (m/m)	Exact (m/m)
1	3.000×10^{-4}	2.999×10^{-4}	3.000×10^{-4}
2	2.625×10^{-4}	2.624×10^{-4}	2.625×10^{-4}
3	2.250×10^{-4}	2.249×10^{-4}	2.250×10^{-4}
4	1.875×10^{-4}	1.875×10^{-4}	1.875×10^{-4}
5	1.500×10^{-4}	1.499×10^{-4}	1.500×10^{-4}
6	1.125×10^{-4}	1.124×10^{-4}	1.125×10^{-4}
7	0.750×10^{-4}	0.749×10^{-4}	0.750×10^{-4}
8	0.375×10^{-4}	0.378×10^{-4}	0.375×10^{-4}
9	0	0	0

Table 3. Variation of NN training and the result for displacement as input

Variation	Code	Layer	β	MSE	Epoch	t (s)
1	nndVar1	8 16 8	1	5.209×10^{-5}	1000	1679.266
2	nndVar2	8 16 8	2	2.549×10^{-5}	1000	1653.579
3	nndVar3	16 8	1	76.30×10^{-5}	1000	1289.312
4	nndVar4	16 8	2	21.30×10^{-5}	1000	1259.516

**Fig. 5.** Variation of training error with displacement as input

For training of NN the stiffness reduction factor was assumed to be random number from 0 to 1. The location of the damage in the structure is also assumed to be random. When the displacement is taken as the NN input, the training was conducted

Table 4. Variation of NN training and the result for strain as input

Variation	Code	Layer	β	MSE	Epoch	t (s)
1	nnsVar1	8 16 8	1	4.641×10^{-5}	1000	1665.719
2	nnsVar2	8 16 8	2	0.981×10^{-5}	592	1002.719
3	nnsVar3	16 8	1	0.987×10^{-5}	69	102.688
4	nnsVar4	16 8	2	0.976×10^{-5}	61	83.391

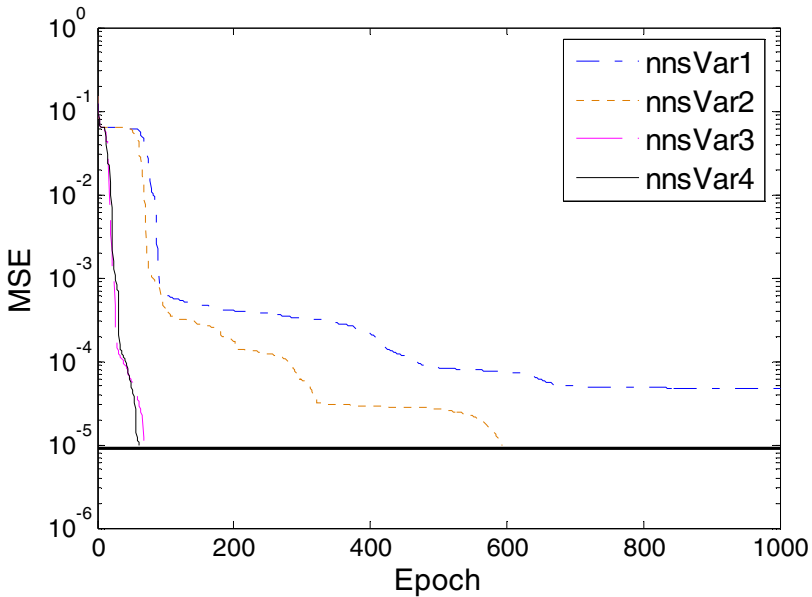


Fig. 6. Variation of training error with strain as input

using different values of layer and β . Table 3 shows the training results of NN with displacement as input. Meanwhile, the variation of training error with number of epoch for several variations is shown in Fig. 5. It is interesting to note that the error for nndVar1 and nndVar2 get reduced significantly after a few epoch (300 epoch). It can be observed that the variation of nndVar2 showed the best performance. However, the desired error (1.000×10^{-5}) was not reached as the testing error tends to constant at 2.549×10^{-5} after 600 epoch and taking enough computational time.

Strains of the beam are calculated at the same nodal point to that of the displacement. Thus in this case NN inputs also have nine nodes consisting of strain values. The stiffness reduction factor in this case is assumed to be a random number between 0 to 1 with randomized location of damage. A variation as shown in Table 4 was applied to train the NN with strains as input. The result show that the desired error level (1.000×10^{-6}) was reached by nnsVar2, nnsVar3 and nnsVar4 in a range of 1000 epoch. It can be observed from Fig. 6 that the variation of nnsVar4 showed the best performance. The desired error is reached by this variation in 61 epoch within short period of time.

From the results, it can be seen that NN with strains as input can reach the desired error in small number of epoch and low computational time. The comparison results between input of strains and of displacement are depicted in Figs. 7, 8 and 9. It is evident that it is better to use the strains as input in the NN training in order to achieve more efficient damage detection of structures or machinery components.

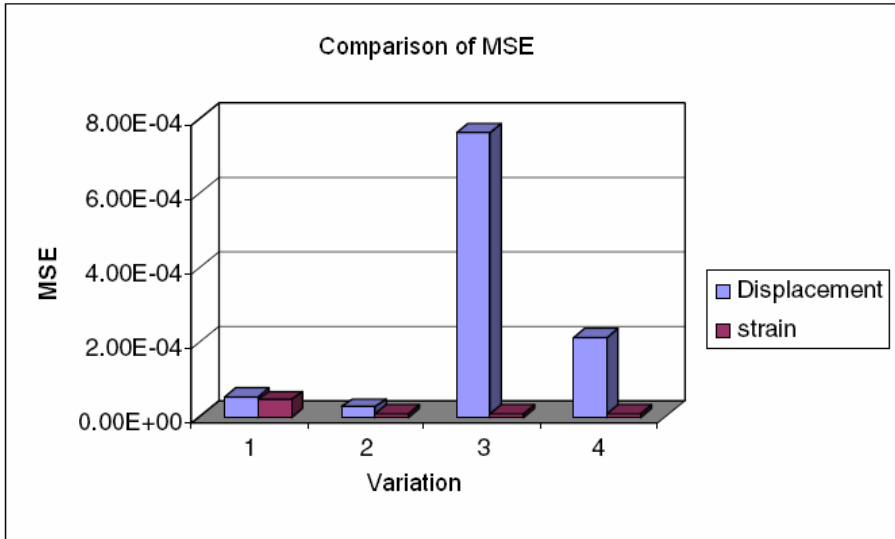


Fig. 7. Comparison of MSE for variation of NN training

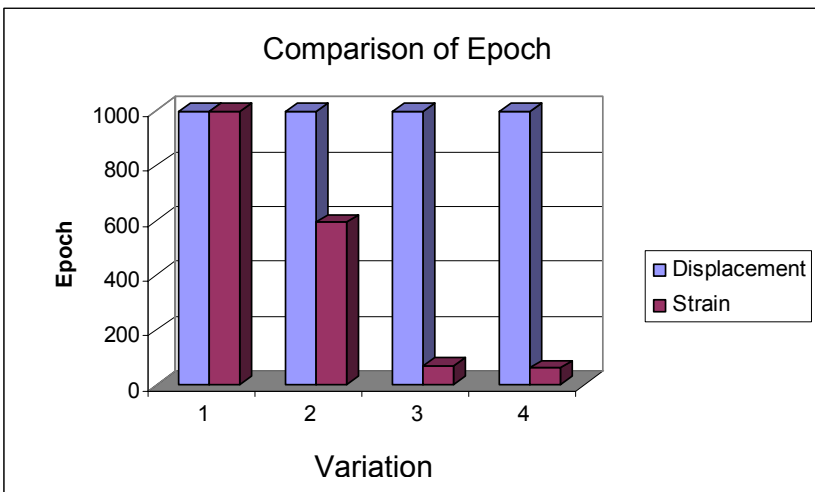


Fig. 8. Comparison of epoch for variation of NN training

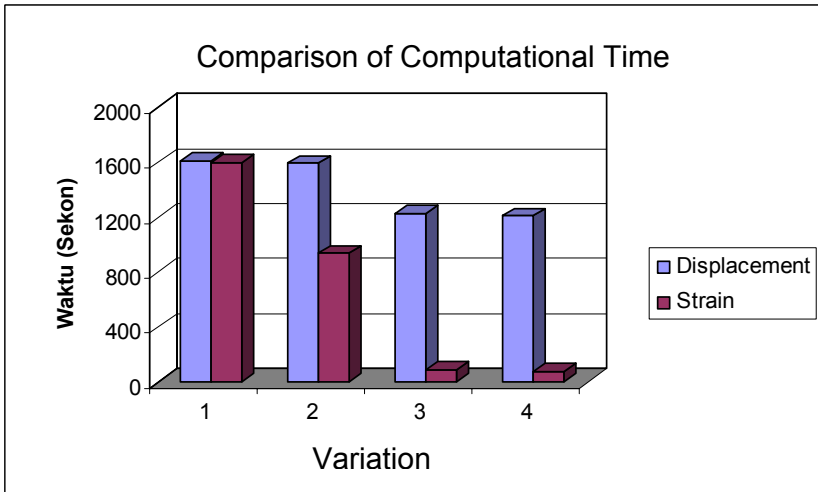


Fig. 9. Comparison of computational time for variation of NN training

4 Conclusions

The main objective of the present research is to identify the size and the location of damage of a cantilever beam structure using neural network. For this purpose, a computer code was developed in which structural response in forms of displacement and strain due to damage is carried out. The damage of the structure is modeled as a stiffness reduction of a structural element wherein the stiffness reduction factor is treated as random number between 0 and 1. In this research the location of the damage is also treated as randomized location. The response data then are used as the input of the network to determine the size and the location of the damage. It is clearly observed from the result that selection of NN architecture is very important in the accuracy of the result. The networks showed that lower number of hidden layers gives shorter computational time. The factor of β in training algorithm of Lavenberg Merquardt tends to accelerate computational time to reach the desired error. The output results also showed that the performance of network is improved when strain is used as input instead of displacement.

References

- [1] Bishop, C.: Neural Networks for Pattern Recognition. Oxford University Press, Oxford (1997)
- [2] Demuth, H., Beale, M.: Neural Network Toolbox For Use with MATLAB, Mathwork.Inc., USA (1998)
- [3] El-Sebakhy, E.A.: Artificial Neural Networks, Probabilistic Networks, Support Vector Machines, Adaptive-Neuro Fuzzy Systems, and Functional Networks. Elsevier Science, Saudi Arabia (2006)

- [4] Hagan, M.T., Menhaj, M.: Training Feed forward Networks With The Marquardt Algorithm. *IEEE Transactions on Neural Networks* 5(6), 989–993 (1994)
- [5] Kusumadewi, S.: *Membangun Jaringan Saraf Tiruan Menggunakan Matlab dan Excel Link*. Graha Ilmu, Yogyakarta (2004)
- [6] Kwon, Y.W., Bang, H.: *The Finite Element Method Using MATLAB*. CRC Press, Florida (2000)
- [7] Maity, D., Saha, A.: Damage Assessment in Structure from Changes in Static Parameter Using Neural Network. *Sadhana* 29(3), 315–327 (2004)
- [8] Siang, J.J.: *Jaringan Syaraf Tiruan*. Penerbit Andi, Yogyakarta (2005)
- [9] Yijun, L.: *Lectures Notes: Introduction to Finite Element Method*. University of Cincinnati, USA (1998)

Fault and Mode Switching Identification for Hybrid Systems with Application to Electro-Hydraulic System in Vehicles

Ming Yu¹, Ming Luo², Shai Arogeti¹, Danwei Wang^{1,*}, and Xinzheng Zhang³

¹ School of Electrical and Electronic Engineering,
Nanyang Technological University, Singapore
edwwang@ntu.edu.sg

² Singapore Institute of Manufacturing Technology (SIMTech), Singapore

³ College of Automation, Guangdong University of Technology, China

Abstract. This paper describes a methodology for simultaneous identification of fault parameters and mode switching events for hybrid systems. The method is developed based on the notion of Global Analytical Redundancy Relations (GARR) from the bond graph model of the hybrid system. A unified formula with mode change time sequence and initial mode coefficients (IMC) is derived to represent the mode switching. It employs Genetic Algorithm (GA) to search for fault parameters and mode switching time stamps. Fault parameters, mode switching time stamps and all IMC are encoded into one chromosome as a potential solution of the identification process. GARRs are used as a fitness index in GA search. An electro-hydraulic system of vehicle is studied to illustrate the efficiency of the proposed algorithm.

Keywords: Bond graph, mode switching, Global Analytical Redundancy Relation, Genetic Algorithm, hybrid system, fault parameter.

1 Introduction

Modern complex engineering systems are deployed in environments where reliability and safety are of primary importance, which in turn calls for effective and sophisticated fault detection and isolation (FDI) algorithms. FDI methods can be broadly classified into two categories, namely, data driven approach and model based approach (Luo *et al.*, 2005). The former requires transforming a large amount of historical data into a priori knowledge for building a diagnostic system; the latter requires a mathematical model governing system behavior, and it works by evaluating system behavior using parameter values and sensor data from the monitored system.

The first step of model based approach is to generate a set of residuals called Analytical Redundancy Relations (ARR) which express the difference between information provided by the actual system and that delivered by its normal operation model (Samantaray *et al.*, 2006). ARRs are static or dynamic constraints which link the time evolution of known variables when the system operates according to its

* Corresponding author.

normal operation model. ARRs have to be sensitive to faults and insensitive to perturbations.

For model based approach, an accurate behavior model is important for FDI purpose and difficulty increases with system complexity. A model must be constructed at a level of details such that system behavior can be mapped to system components and parameters. Bond graph (BG) provides an approach to model a complex system, which allows both a structural and a behavioral system analysis (Karnopp *et al.*, 2006). From the FDI point of view, the causal properties of BG models are used to determine the origin of a fault. In the BG diagnosis, it is important to have a BG model that includes all the parameters that are related to the faults under analysis.

A hybrid system consists of interacting continuous and discrete parts. They are described by several operating regimes, called modes, and each mode can be activated under certain conditions. Hybrid systems include examples of switched mode power converter (Umarikar *et al.*, 2005), automotives and high-speed printers. In order to model the discontinuous mode changes of a hybrid system, Mosterman *et al.* (1995) developed Hybrid Bond Graph (HBG) to include the notion of idealized switching junctions and thus represent hybrid systems in a compact manner.

Zhao *et al.* (2005) developed a timed Petri net to describe only temporal discrete event evolution of a system. This method requires domain specific knowledge for offline generation of fault-symptom table and only autonomous mode changes are considered. Narasimhan and Biswas (2007) utilized HBG to develop a diagnosis framework based on qualitative approach. However, this framework has some limitations. Firstly, this FDI framework requires FDI design for each operating mode individually and repetitive designs are needed for all modes. Secondly, this method only considers controlled mode changes and autonomous mode changes, it can not work with unobservable events (such as unknown discrete inputs). Moreover, the framework depends on linearization of nonlinear systems and thus the performance of the identification module is not guaranteed.

When mode switching events of a hybrid system are exactly known, FDI of such systems is easy because the knowledge of the active regime at any moment is available. However, lack of mode switching information will make it difficult to carry out a fault diagnosis scheme. This paper addresses the determination of mode switching and estimation of fault parameters for hybrid systems using Genetic Algorithm (GA). Global Analytical Redundancy Relations (GARR) are used to describe the behavior of a hybrid system at all modes. This method combines the benefits of both GA and GARR to simultaneously identify fault parameters and mode switching in a hybrid system.

2 HBG and GARR

BG provides a systematic way to model dynamic systems with different energy domains, such as electrical, hydraulic, mechanical, etc., in a unified framework. In BG modeling, a physical system can be described by BG components which include source elements Se and Sf , dissipative element R , storage elements C and I , four junctions 0 , 1 , TF and GY . These generalized BG components are connected by

bonds which represent energy exchange between two physical components. For each bond, there are two energy variables, effort and flow, to describe the states of the physical components. BG modeling utilizes these BG components and their bond connections to describe the behavior of a physical system (Karnopp *et al.* 2006).

A hybrid system may be viewed as an integrated system of two types of subsystems: continuous subsystems and discrete events. The class of hybrid systems under consideration here includes finite number of modes and the dynamic behaviors described by different models under different mode (Arogeti *et al.* 2008). Discrete events force the system to switch from one mode to another. Some discrete events are known (e.g. initiated by a supervisory controller) and some are unknown but measurable (e.g. triggered by measured continuous states). Others are unobservable events (e.g. caused by unknown discrete inputs), and unknown discrete dynamics.

In order to model discrete mode changes of a hybrid system, HBG expands the modeling capability of BG to include switching (controlled) junctions (Mosterman *et al.* 1995). In this way, a hybrid system can be represented by BG components in a concise manner. Controlled junctions behave like traditional 0 and 1 junctions when they are in ON state. To invoke configuration changes, controlled junctions can be turned off or deactivated, in which state they inhibit transfer of energy between model fragments. In other words, in the OFF state, a 0-controlled junction forces the effort value to zero at all connected bonds. Similarly, a 1-controlled junction forces the flow value to zero at all connected bonds.

Low *et al.* (2008a) developed a Quantitative Hybrid Bond Graph (QHBG) diagnosis framework for FDI. This framework is built on of the notion of GARRs which are a set of quantitative equations describing the behavior of a hybrid system at all modes. Without loss of generality, GARR equations take the following form

$$g_i(\theta, \alpha, De, Df, u) = 0 \text{ for } i = 1, 2, \dots, m \tag{1}$$

where m denotes the number of GARRs derived from the HBG; $\theta = [\theta_1, \theta_2, \dots, \theta_n]^T$ represents the nominal parameters of the HBG components which are assumed to be known during fault-free operation; $\alpha = [\alpha_1, \alpha_2, \dots, \alpha_q]^T$ indicate the mode switching states of the q controlled junctions. Consequently, there are number of 2^q modes; u contains system's inputs, De and Df denote the effort and flow sensors.

The QHBG framework for fault diagnosis consists of a GARR alarm generator, a fault detection module, a fault isolation module, a fault estimator, and a mode tracer (Arogeti *et al.* 2008). The mode tracer determines the instantaneous operating mode using sensors and input information obtained from the hybrid system. This instantaneous mode information allows users to effectively evaluate the GARR residuals at all operating modes. With these residuals, it is possible to detect and isolate faults. In this paper, it is assumed that the system can have only one fault, and then the faulty parameter can be uniquely determined. The fault detection module decides whether or not a fault has occurred when any of the residual signals exceeds a predetermined threshold.

For a continuous system, a residual r_l , defined by a GARR, is sensitive to a fault in those components whose parameters appear in the GARR. When the system is fault-free, all residuals are consistent with the system’s behavior and residuals $|r_l|$ are zeros or below a small threshold value ε_l . To apply these residuals for FDI, a binary coherence vector $C = [c_1 \dots c_m]$ is defined. Each component c_l of C is defined as follows:

$$c_l = \begin{cases} 1 & \text{if } |r_l| > \varepsilon_l \\ 0 & \text{otherwise} \end{cases} \quad \text{for } l = 1, 2, \dots, m \quad (2)$$

When the system is fault-free, the binary coherence vector C will be zero. On the other hand, if the system is faulty, then at least one entry of the coherence vector will take value 1. Fault monitoring ability of a system can be studied using a fault signature matrix (FSM) generated from the m ARR equations. A typical FSM is shown in Table 1 in which column headers consist residual r_1, \dots, r_m , fault detectability (D_b), and fault isolability (I_b). Each entry of the table holds a Boolean value. For each row, the Boolean entries under the columns r_1, \dots, r_m form the fault signature of the parameter θ_i corresponding to a fault in the parameter θ_i . Under a residual column, a value 1 in an entry indicates that the residual is sensitive to a fault in the parameter of the matching row. On the other hand, a 0 in the entry represents the residual is insensitive to the fault in the corresponding parameter. If at least a 1 appears in the fault signature of a parameter θ_i , then the parameter is said to be fault detectable. This ability is represented by a $D_b = 1$ in the matrix. When the fault signature of a parameter θ_i is unique, then a fault occurred in parameter θ_i is said to be fault isolable. This is denoted by $I_b = 1$.

Table 1. Fault signature matrix (FSM)

	r_1	...	r_m	D_b	I_b
θ_1	1 or 0				
.					
.					
.					
θ_p					

Table 2. MD-FSM at mode α^l

Mode α^l	r_1	...	r_m	D_b	I_b
θ_1	1 or 0				
.					
.					
.					
θ_p					

Unlike continuous systems, hybrid systems have multiple modes but only one mode is in operation at any time. This suggests that it is necessary to evaluate the system’s monitoring ability in different operating modes for FDI analysis and designs. By design, the global characteristic of the GARR can provide an efficient and effective means to generate a FSM for each operating mode. Such an FSM is referred as Mode Dependent Fault Signature Matrix (MD-FSM). Table 2 shows the MD-FSM at mode α^l and α^l denotes one of the 2^q modes.

Deployment of quantitative residuals for fault diagnosis is also applicable for hybrid systems. For simplicity, a binary coherence vector $C = [c_1 \dots c_m]$ is defined with each component c_l of C being a Boolean variable whose value is obtained by the following rule, similar to equation (2):

$$c_l = \begin{cases} 1 & \text{if } |r_l| > \varepsilon_l^i \\ 0 & \text{otherwise} \end{cases} \quad \text{for } l = 1, 2, \dots, m \quad (3)$$

where i denotes instantaneous operating mode.

When a hybrid system is fault-free, the binary coherence vector C will be zero. When a fault occurs, at least one entry of the coherence vector takes value 1. Note that the threshold ε_l^i is mode dependent. In this parameter estimation module, it is assumed that mode stays unchanged after fault occurrence. For those isolable faults, GARRs generate a unique set of residual values and allow the identification of a faulty parameter. For those non-isolable but detectable faults, the module will select a set of potential fault candidates. Eventually, the parameter estimation module estimates the selected fault parameters to access the health status of the system and computes the non-isolable parameter.

3 GA Based Identification of Fault Parameters and Mode Switching

Isolation of fault candidates leads to identification of fault parameters and evaluation of system health. However, if mode switching is unknown, the choice of a correct model is difficult after fault occurrence, model based mode tracing can't function well. In order to overcome this problem, GA method is used within QHGB framework for identification of fault parameters and mode switching time stamps simultaneously. This GA based mechanism consists of four major modules: initialization and encoding, evaluation, selection and reproduction, and crossover and mutation.

(1) Initialization and Encoding

In this paper, a fault candidate is represented by a component parameter. It is also assumed that there are at most of p mode changes during an observation period.

Definition 1. For a hybrid system, during the observation window $[t_0 \ t_f]$, $\alpha = [\alpha_1, \alpha_2, \dots, \alpha_q]^T$ is defined as a switching vector whose components a_i , $i = 1, 2, \dots, q$, take the form of

$$a_i(t, T_i) = \lambda_i \cdot a_i^1(t, T_i) + (1 - \lambda_i) \cdot a_i^0(t, T_i) \quad (4)$$

where λ_i are the initial mode coefficients (IMC), whose values are obtained by the following formula

$$\lambda_i = \begin{cases} 1 & \text{if the state of } i\text{th control junction at time } t_0 \text{ is } 1 \\ 0 & \text{if the state of } i\text{th control junction at time } t_0 \text{ is } 0 \end{cases} \quad (5)$$

$a_i^1(t, T_i)$ and $a_i^0(t, T_i)$ are defined as

$$a_i^1(t, T_i) = \tau(t) - \tau(t - T_i^1) + \tau(t - T_i^2) + \dots + (-1)^p \tau(t - T_i^p) \text{ for } \lambda_i = 1 \quad (6)$$

$$a_i^0(t, T_i) = \tau(t - T_i^1) - \tau(t - T_i^2) - \dots - (-1)^p \tau(t - T_i^p) \text{ for } \lambda_i = 0 \quad (7)$$

Define function

$$\tau(*) = \begin{cases} 1 & \text{if } * \geq 0 \\ 0 & \text{if } * < 0 \end{cases} \quad (8)$$

where $T_i = [T_i^1 \ T_i^2 \ \dots \ T_i^p]$ is the switching time stamp vector whose elements are the time stamps for mode changes with $t_0 \leq T_i^1 \leq T_i^2 \leq \dots \leq T_i^p \leq t_f$. \square

By definition, if all switching time stamps T_i^j , $i = 1, 2, \dots, q$ and $j = 1, 2, \dots, p$, are equal to t_f , then there are no mode changes during the time interval $[t_0 \ t_f]$.

If the switching time stamps and IMC are known, the mode switching vector $\alpha = [\alpha_1, \alpha_2, \dots, \alpha_q]^T$ can be expressed as functions of time t . The fault candidate parameter values, switching time sequence and all IMCs are encoded into a chromosome, as shown in Figure 1. In the Figure, s is the number of fault candidates.

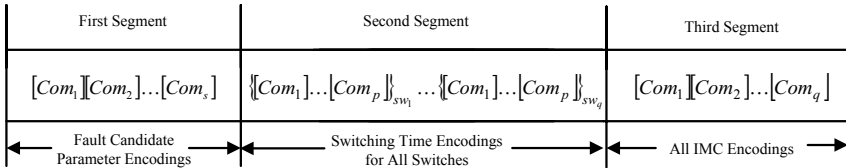


Fig. 1. Encoding scheme of a chromosome

(2) Evaluation

A fitness function measures the optimality of each chromosome, and the choice of fitness function depends on the nature of search and it is problem specific. In the undertaken problem, the objective is to search for the fault parameter values and switching time stamps with the minimum residual values in certain operating mode.

To evaluate the fitness, N samples are collected after a fault is detected. If the parameter values estimated are the true physical parameters and mode switching vector is accurately estimated, all GARRs, g_i , for $i = 1, 2, \dots, m$, as defined in equation (1), are zero. These lead to the definition of the following fitness function

$$\text{Fitness} = 1 / \left(\sum_{i=1}^m \sum_{n=1}^N |g_i^n| + \varepsilon \right) \quad (9)$$

with n representing the sampling time index, and ε is a small positive constant. Since GARR is used to identify the targeted fault parameters, only those GARRs containing targeted parameters are selected.

(3) Selection and Reproduction

Chromosomes with the highest fitness values are retained in the next generation, while those with the lowest fitness values are discarded. Here the elitism mechanism is adopted, so the fitness of the current and previous best individuals are compared. If a fitter individual is not generated, the previous best individual is kept in the new population. For the remaining population, individuals are copied according to their fitness values, i.e., individuals with a higher value have a higher probability of contributing one or more offspring in the next generation.

(4) Crossover and Mutation

Once a chromosome is selected for reproduction, an exact replica of the chromosome is made. This chromosome is then entered into a mating pool, a new population, for further genetic operator action. When two parents are selected, GA combines them to create two new offspring. The crossover operator performs combination and one-point crossover is used in this paper. Mutation is another way to create chromosomes during a reproduction to differ from their parents. Mutation is occasional (with small probability) random alteration of the value of a chromosome position. It is defined by user and usually the lower the rate is, the less chance the chromosomes of the children differ from those of their parents.

In this paper, the adaptive GA proposed by Mak *et al.* (2000) is used to adjust the crossover and mutation probability according to the current state of optimization. This method uses some rules to adjust the crossover and mutation rates adaptively according to the performance of the genetic operators. It increases the probability of the genetic operator if it consistently produces a better offspring during the search process; on contrast, it reduces the probability of the genetic operator if it always produces a poorer offspring. In this way, the global optimal solution can be achieved.

4 Case Study of Electro-Hydraulic Suspension

4.1 System Description

The model of the quarter-car active suspension system, shown in Figure 2, is used in this investigation. In the figure, M_s represents sprung mass; M_u represents the unsprung mass; K_s and K_t are the spring coefficients; x_s and x_u are the displacement of the car body and wheel; C_s is the damper coefficient; P_1 and P_2 are the pressure inside the two chambers of the cylinder, respectively, P_s is the supply pressure, P_r is the return pressure, r is the road disturbance.

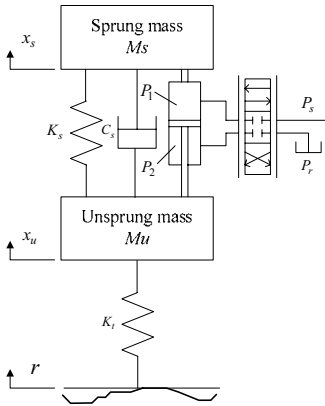


Fig. 2. Model of a quarter car

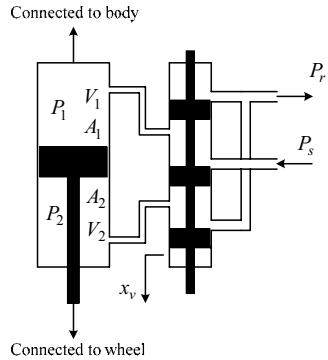


Fig. 3. Actuator with four way spool valve

Two types of discrete transitions for this system are considered in the study. The first type is in the four way spool valve. The spool valve flow rate dynamic equation has two modes, depending on the valve position as shown in Figure 3. The mode changes are autonomous and governed by the values of internal state variables. Using the equation for hydraulic fluid flow through an orifice, the relationship between spool valve displacement x_v , and the supply flow rate to the forward chamber (or cylinder end) Q_1 , the return flow rate of the return chamber (or rod-end) Q_2 , is given as (Merritt, 1967)

$$\begin{aligned}
 Q_1 &= C_d w_1 x_v \left[s(x_v) \sqrt{\frac{2}{\rho} (P_s - P_1)} + s(-x_v) \sqrt{\frac{2}{\rho} (P_1 - P_r)} \right] \\
 Q_2 &= C_d w_2 x_v \left[s(x_v) \sqrt{\frac{2}{\rho} (P_2 - P_r)} + (-x_v) \sqrt{\frac{2}{\rho} (P_s - P_2)} \right]
 \end{aligned}
 \tag{10}$$

where $s(*) = \begin{cases} 1 & \text{if } * \geq 0 \\ 0 & \text{if } * < 0 \end{cases}$, C_d is the discharge coefficient, ρ is the fluid density, w_1 and w_2 are the spool valve area gradients.

The second type of discrete transition is the road profile which has multiple modes. Since the transition from one mode to another mode is not determined by the state, and is also not decided by the driver, this type of mode transition can be considered as unknown mode changes, the proposed method can be used to identify these mode changes.

Without loss of generality, the road profile can be formulated as

$$r = a^T S F \tag{11}$$

where $a = [a_1 \ a_2 \ \dots \ a_n]^T$ is the state vector of control junctions; $SF = [Sf_1 \ Sf_2 \ \dots \ Sf_n]^T$ is the road input vector; and n is the total number of road profiles that the vehicle goes through. It is assumed that the following relationship be satisfied, meaning that at each time moment the vehicle can only go through one road profile

$$a_1 + a_2 + \dots + a_n = 1 \tag{12}$$

where $a_i, i = 1, 2, \dots, n$ can only be 0 or 1.

For simplicity, only two road profiles are considered. One is random road, and the other is bumpy road. The road profile under random road can be represented as (Chen et al., 2003)

Road 1
$$\dot{x}_1(t) = 2\pi q_0 \sqrt{G_0 V} w(t) \tag{13}$$

where q_0 is the reference spatial frequency, G_0 is the road roughness coefficient, V is the vehicle forward velocity, $w(t)$ is zero-mean white noise.

The road displacement due to a bump is represented by (Chen and Guo, 2005)

Road 2

$$x_2(t) = \begin{cases} \frac{A}{2} \left(1 - \cos\left(\frac{2\pi V}{L} t\right) \right) & 0 \leq t \leq \frac{L}{V} \\ 0 & t > \frac{L}{V} \end{cases} \tag{14}$$

where A and L are the height and the length of the bump, respectively .

A HBG model of electro-hydraulic suspension is developed in Figure 4. Here four control junctions, 0_{a1} , 0_{a2} , 1_{a3} and 1_{a4} , are used and Boolean variables a_1 , a_2 , a_3 and a_4 to represent the state (ON/OFF) of these junctions.

The following relationships are valid

$$a_1 = 1 - a_2 \tag{15}$$

$$a_3 = 1 - a_4 \tag{16}$$

where a_3 depends on the state of the displacement of valve x_v , so

$$a_3 = \begin{cases} 1 & \text{if } x_v \geq 0 \\ 0 & \text{if } x_v < 0 \end{cases} \tag{17}$$

Then the road input can be represented as follows

$$r = a_1 Sf_1 + a_2 Sf_2 \tag{18}$$

where Sf_1 is Road 1 profile, Sf_2 is Road 2 profile.

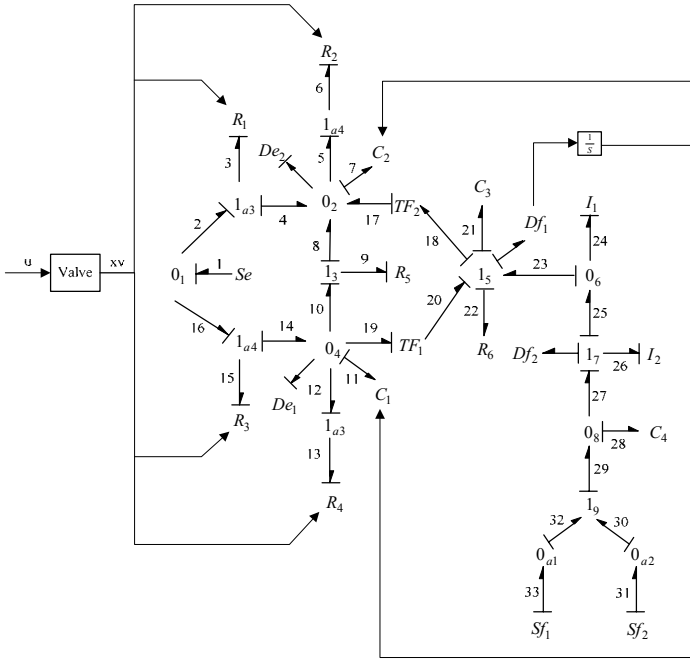


Fig. 4. HBG of quarter-car electro-hydraulic suspension system

In Figure 4, De_1 and De_2 represent the pressure sensors; Df_1 and Df_2 the velocity sensors; Se the supply pressure. Furthermore, the block *Valve* denotes the relationship between control voltage and spool valve

$$\frac{x_v}{u} = \frac{K_V}{\left(\frac{s}{\omega_V}\right)^2 + 2\xi \frac{s}{\omega_V} + 1} \tag{19}$$

where K_V is the gain of the servo-valve, ω_V is the natural frequency of the servo-valve, ξ is the damping ratio of the servo-valve.

Resistive elements, R_1 , R_2 , R_3 and R_4 , are the nonlinear relationships between flow rate and pressure in (10). The following nonlinear functions are used to represent the constitutive relations of these elements

$$f_3 = g_1(e_3) = -C_d \cdot w \cdot x_v \cdot \sqrt{e_3} \tag{20}$$

$$f_6 = g_2(e_6) = C_d \cdot w \cdot x_v \cdot \sqrt{e_6} \tag{21}$$

$$f_{15} = g_3(e_{15}) = C_d \cdot w \cdot x_v \cdot \sqrt{e_{15}} \tag{22}$$

$$f_{13} = g_4(e_{13}) = -C_d \cdot w \cdot x_v \cdot \sqrt{e_{13}} \tag{23}$$

External leakage flow is negligible in this study. Resistive element R_5 represents the internal leakage of the cylinder. TF_1 and TF_2 represent the relationship between velocity of the single-rod of the cylinder and the flow rate changes of two chambers. C_1 and C_2 represent the fluid compliance of the two chambers of the cylinder. The constitutive relations are nonlinear functions as follows

$$f_{11} = g_{C_1}(e_{11}) = \frac{V_1 - A_1 \int Df_1 dt}{\beta} \cdot \frac{d}{dt}(e_{11}) \quad (24)$$

$$f_7 = g_{C_2}(e_7) = \frac{V_2 + A_2 \int Df_1 dt}{\beta} \cdot \frac{d}{dt}(e_7) \quad (25)$$

where β is the effective bulk modulus of the hydraulic fluid, V_1 , V_2 are the original total control volumes of the two cylinder chambers, respectively (including the volume of the servo valve, pipelines, and cylinder chambers), A_1 , A_2 are the ram area of the two chambers, respectively. Elements C_3 and C_4 represent the compliance of two springs; R_6 the damper coefficient; and I_1 and I_2 the inertias of the unsprung mass and sprung mass.

The GARRs can be derived from the Diagnostic Hybrid Bond Graph (DHBG) of the system. DHBG is a HBG with suitable causalities such that every active BG component remains valid at all operating modes. This feature of the DHBG allows consistent causal description and derivation of GARRs of a hybrid system from its DHBG. By applying the procedure developed in Low *et al.* (2008b), the DHBG of the hybrid system is obtained as shown in Figure 5.

The constitutive relations of junctions 0_1 , 0_2 , 1_3 , 0_4 , TF_1 , TF_2 , 1_5 , 0_6 , 1_7 , 0_8 and 1_9 are given by the following equations

$$a_3 f_2 + a_4 f_{16} - f_1 = 0 \quad (26)$$

$$a_3 f_4 + f_8 + f_{17} - f_7 - a_4 f_5 = 0 \quad (27)$$

$$e_{10} - e_8 - e_9 = 0 \quad (28)$$

$$a_4 f_{14} - f_{10} - f_{11} - a_3 f_{12} - f_{19} = 0 \quad (29)$$

$$f_{19} - f_{20}/TF_1 = 0 \quad (30)$$

$$e_{20} - e_{19}/TF_1 = 0 \quad (31)$$

$$e_{18} - TF_2 e_{17} = 0 \quad (32)$$

$$f_{17} - TF_2 f_{18} = 0 \quad (33)$$

$$e_{20} + e_{23} - e_{18} - e_{21} - e_{22} = 0 \quad (34)$$

$$f_{25} - f_{23} - f_{24} = 0 \quad (35)$$

$$e_{27} - e_{25} - e_{26} = 0 \quad (36)$$

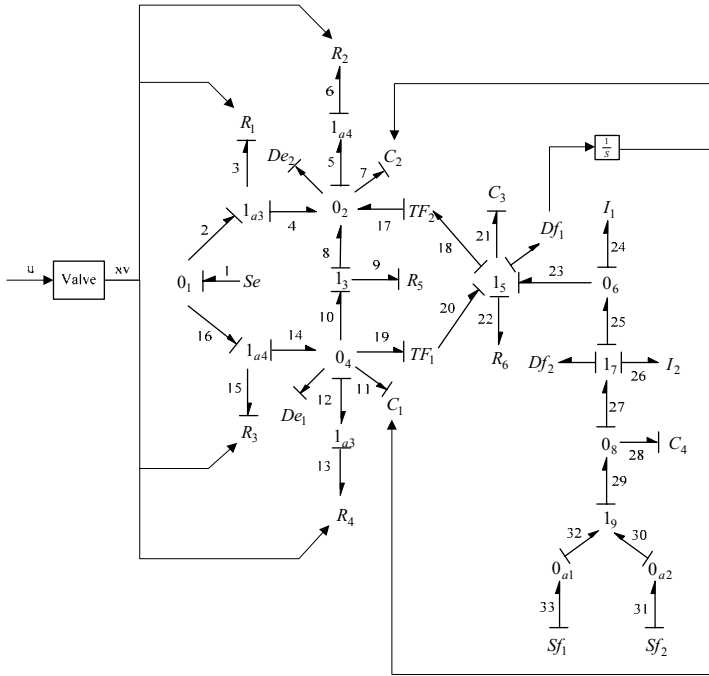


Fig. 5. DHBG of quarter-car active suspension system

$$f_{29} - f_{27} - f_{28} = 0 \tag{37}$$

$$a_1 e_{32} - a_2 e_{30} - e_{29} = 0 \tag{38}$$

Four structurally independent GARR equations can be generated from equations (27), (29), (34) and (37) after eliminating the unknown variables. The unknown variables elimination process is achieved by following the causal path, from known to unknown, on the DHBG model. For equation (27), the unknown variables f_4 , f_5 , f_7 , f_8 and f_{17} can be calculated as follows

$$f_4 = f_3 = g_1(e_3) = g_1(e_2 - e_4) = -C_d \cdot w \cdot x_v \cdot \sqrt{Se - De_2} \tag{39}$$

$$f_5 = f_6 = g_2(e_6) = g_1(e_5) = C_d \cdot w \cdot x_v \cdot \sqrt{De_2} \tag{40}$$

$$f_7 = g_{C_2}(e_7) = \frac{V_2 + A_2 \int Df_1 dt}{\beta} \cdot \frac{d}{dt}(De_2) \tag{41}$$

$$f_8 = f_9 = \frac{e_9}{R_5} = C_m \cdot (De_1 - De_2) \tag{42}$$

$$f_{17} = TF_2 \cdot f_{18} = -A_2 \cdot Df_1 \quad (43)$$

Then the first GARR is obtained as follows

$$\begin{aligned} GARR_1 = & -a_3 \cdot C_d \cdot w \cdot x_v \cdot \sqrt{Se - De_2} + C_m \cdot (De_1 - De_2) - A_2 \cdot Df_1 \\ & - \frac{V_2 + A_2 \int Df_1 dt}{\beta} \cdot \frac{d}{dt}(De_2) - a_4 \cdot C_d \cdot w \cdot x_v \cdot \sqrt{De_2} \end{aligned} \quad (44)$$

For equation (29), the unknown variables f_{10} , f_{11} , f_{12} , f_{14} and f_{19} can be calculated as follows

$$f_{10} = f_9 = \frac{e_9}{R_5} = C_m \cdot (De_1 - De_2) \quad (45)$$

$$f_{11} = g_{C_1}(e_{11}) = \frac{V_1 - A_1 \int Df_1 dt}{\beta} \cdot \frac{d}{dt}(De_1) \quad (46)$$

$$f_{12} = f_{13} = g_4(e_{13}) = g_4(e_{12}) = -C_d \cdot w \cdot x_v \cdot \sqrt{De_1} \quad (47)$$

$$f_{14} = f_{15} = g_3(e_{15}) = g_3(e_{16} - e_{14}) = C_d \cdot w \cdot x_v \cdot \sqrt{Se - De_1} \quad (48)$$

$$f_{19} = f_{20}/TF_1 = -A_1 \cdot Df_1 \quad (49)$$

Then the second GARR is obtained as follows

$$\begin{aligned} GARR_2 = & a_4 \cdot C_d \cdot w \cdot x_v \cdot \sqrt{Se - De_1} - C_m \cdot (De_1 - De_2) + A_1 \cdot Df_1 \\ & - \frac{V_1 - A_1 \int Df_1 dt}{\beta} \cdot \frac{d}{dt}(De_1) + a_3 \cdot C_d \cdot w \cdot x_v \cdot \sqrt{De_1} \end{aligned} \quad (50)$$

For equation (34), the unknown variables e_{18} , e_{20} , e_{22} and e_{23} can be calculated as follows

$$e_{18} = TF_2 e_{17} = -A_2 \cdot De_2 \quad (51)$$

$$e_{20} = e_{19}/TF_1 = -A_1 \cdot De_1 \quad (52)$$

$$e_{22} = R_6 \cdot f_{22} = C_s \cdot Df_1 \quad (53)$$

$$e_{23} = e_{24} = I_1 \cdot \frac{d}{dt}(f_{24}) = M_s \cdot \frac{d}{dt}(Df_2 - Df_1) \quad (54)$$

The constitutive relation of the component C_3

$$C_3 \cdot \frac{d}{dt}(e_{21}) = Df_1 \quad (55)$$

Then the third GARR is obtained from the component C_3 after combining (51) ~ (55)

$$GARR_3 = -A_1 \cdot \frac{1}{K_s} \cdot \frac{d}{dt}(De_1) + M_s \cdot \frac{1}{K_s} \cdot \frac{d^2}{dt^2}(Df_2 - Df_1) + A_2 \cdot \frac{1}{K_s} \cdot \frac{d}{dt}(De_2) - C_s \cdot \frac{1}{K_s} \cdot \frac{d}{dt}(Df_1) - Df_1 \tag{56}$$

For equation (37), the unknown variables f_{27} , f_{28} and f_{29} can be calculated as follows

$$f_{27} = Df_2 \tag{57}$$

$$f_{28} = C_4 \cdot \frac{d}{dt}(e_{28}) = \frac{1}{K_t} \cdot \frac{d}{dt}(e_{25} + e_{26}) = \frac{1}{K_t} \cdot \frac{d}{dt} \left[M_s \cdot \frac{d}{dt}(Df_2 - Df_1) + M_u \cdot \frac{d}{dt}(Df_2) \right] \tag{58}$$

$$f_{29} = a_1 f_{33} + a_2 f_{31} = a_1 sf_1 + a_2 sf_2 \tag{59}$$

Then the fourth GARR is obtained as follows

$$GARR_4 = a_1 sf_1 + a_2 sf_2 - \frac{1}{K_t} \cdot \frac{d}{dt} \left[M_s \cdot \frac{d}{dt}(Df_2 - Df_1) + M_u \cdot \frac{d}{dt}(Df_2) \right] - Df_2 \tag{60}$$

The following MD-FSM tables are obtained.

Table 3. MD-FSM at $a_1 = 1$, $a_3 = 1$

	r_1	r_2	r_3	r_4	D_b	I_b
C_d	1	1	0	0	1	0
w	1	1	0	0	1	0
C_{tm}	1	1	0	0	1	0
β	1	1	0	0	1	0
V_1	0	1	0	0	1	0
V_2	1	0	0	0	1	0
A_1	0	1	0	0	1	0
A_2	1	0	0	0	1	0
K_s	0	0	1	0	1	0
K_t	0	0	0	1	1	0
C_s	0	0	1	0	1	0
M_s	0	0	1	1	1	1
M_u	0	0	0	1	1	0
Se	1	1	0	0	1	0
Sf_1	0	0	0	1	1	0
Sf_2	0	0	0	0	0	0

Table 4. MD-FSM at $a_1 = 0$, $a_3 = 1$

	r_1	r_2	r_3	r_4	D_b	I_b
C_d	1	1	0	0	1	0
w	1	1	0	0	1	0
C_{tm}	1	1	0	0	1	0
β	1	1	0	0	1	0
V_1	0	1	0	0	1	0
V_2	1	0	0	0	1	0
A_1	0	1	0	0	1	0
A_2	1	0	0	0	1	0
K_s	0	0	1	0	1	0
K_t	0	0	0	1	1	0
C_s	0	0	1	0	1	0
M_s	0	0	1	1	1	1
M_u	0	0	0	1	1	0
Se	1	1	0	0	1	0
Sf_1	0	0	0	0	0	0
Sf_2	0	0	0	1	1	0

Table 5. MD-FSM at $a_1 = 1$, $a_3 = 0$

	r_1	r_2	r_3	r_4	D_b	I_b
C_d	1	1	0	0	1	0
w	1	1	0	0	1	0
C_{tm}	1	1	0	0	1	0
β	1	1	0	0	1	0
V_1	0	1	0	0	1	0
V_2	1	0	0	0	1	0
A_1	0	1	0	0	1	0
A_2	1	0	0	0	1	0
K_s	0	0	1	0	1	0
K_t	0	0	0	1	1	0
C_s	0	0	1	0	1	0
M_s	0	0	1	1	1	1
M_u	0	0	0	1	1	0
Se	1	1	0	0	1	0
Sf_1	0	0	0	1	1	0
Sf_2	0	0	0	0	0	0

Table 6. MD-FSM at $a_1 = 0$, $a_3 = 0$

	r_1	r_2	r_3	r_4	D_b	I_b
C_d	1	1	0	0	1	0
w	1	1	0	0	1	0
C_{tm}	1	1	0	0	1	0
β	1	1	0	0	1	0
V_1	0	1	0	0	1	0
V_2	1	0	0	0	1	0
A_1	0	1	0	0	1	0
A_2	1	0	0	0	1	0
K_s	0	0	1	0	1	0
K_t	0	0	0	1	1	0
C_s	0	0	1	0	1	0
M_s	0	0	1	1	1	1
M_u	0	0	0	1	1	0
Se	1	1	0	0	1	0
Sf_1	0	0	0	0	0	0
Sf_2	0	0	0	1	1	0

4.2 Simulation and Discussions

MATLAB SIMULINK is used to test the proposed GA based FDI method for the electro-hydraulic suspension system. The nominal parameters are:

$$M_s = 290\text{kg} , m^2 = 59\text{kg} , K_s = 16800\text{N/m} , K_t = 190000\text{N/m} , C_s = 1000\text{N} \cdot \text{s/m} , A_1 = 3.8 \times 10^{-4} \text{m}^2 , A_2 = 3.5 \times 10^{-4} \text{m}^2 , V_1 = 1.2 \times 10^{-4} \text{m}^3 , V_2 = 1.1 \times 10^{-4} \text{m}^3 , P_s = 1.5 \times 10^7 \text{Pa} , C_{tm} = 0.3 \times 10^{-12} \text{m}^3 \cdot \text{s}^{-1} / \text{Pa} , \rho = 900\text{kg} \cdot \text{m}^{-3} , \beta = 1.2 \times 10^9 \text{Pa} , C_d = 0.6 , w = 1.5 \times 10^{-3} \text{m} .$$

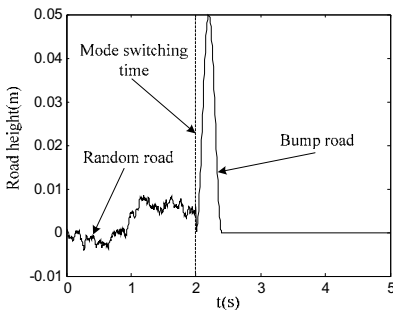


Fig. 6. Road profile of the first scenario

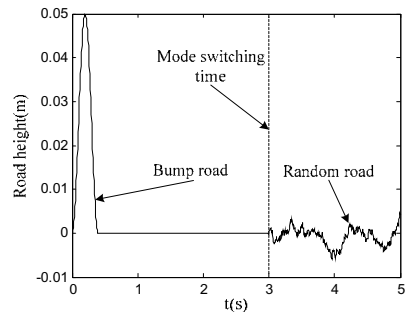


Fig. 7. Road profile of the second scenario

The input is $u = 2 \sin(3\pi t_s)$, sampling time t_s is 0.005 second. A fault occurrence is considered in unsprung spring K_t , with parameter value changes from 190000N/m to 95000N/m, which can also be taken as the fault of flat tyre. The QHBG framework is deployed for FDI, and estimates of fault values can be identified. With an observation window of 5 seconds, one thousand of sample data ($N=1000$) are collected after a fault is detected. Two scenarios have been simulated. In the first case, the road profile undergoes from Road 1 to Road 2, featuring a_1 changing from 1 to 0, the transition time is set at 2 second during the observation window. In the second case, the road profile undergoes from Road 2 to Road 1, featuring a_1 changing from 0 to 1, the transition time is set at 3 second during the observation window. Figure 6 and Figure 7 are the road profiles according to these two scenarios.

In the search process, λ_1 of a_1 takes only two values, 0 or 1 and p is chosen as 3. In all simulation runs, the parameters identified fall into the bounded ranges, including, $K_t \in [50000 \ 300000]$ N/m, $M_u \in [10 \ 150]$ kg, $T_1^1 \in [0,5]$ s, $T_1^2 \in [0,5]$ s and $T_1^3 \in [0,5]$ s (Wang *et al.*, 2004). Table 7 summarizes the identification results for the first scenario.

Table 7. Summary of the identification results for the first scenario

	M_u	K_t	T_1^1	T_1^2	T_1^3	λ_1
1 st run	62.0448	96452	2.0039	5.0000	5.0000	1
2 st run	58.8272	94946	1.9820	5.0000	5.0000	1
3 st run	59.5894	95161	1.9990	5.0000	5.0000	1
4 st run	59.1789	95054	1.9750	5.0000	5.0000	1
5 st run	61.4633	96022	1.9941	5.0000	5.0000	1
Average	60.2207	95527	1.9908	5.0000	5.0000	1

Table 8. Summary of the identification results for the second scenario

	M_u	K_t	T_1^1	T_1^2	T_1^3	λ_1
1 st run	59.1789	95054	3.0010	5.0000	5.0000	0
2 st run	61.2903	95591	3.1006	5.0000	5.0000	0
3 st run	63.1672	95914	3.0530	5.0000	5.0000	0
4 st run	59.8270	95946	3.0010	5.0000	5.0000	0
5 st run	58.5894	94356	2.9003	5.0000	5.0000	0
Average	60.4106	95372	3.0112	5.0000	5.0000	0

Table 8 summarizes of the identification results for the second scenario. These results illustrate that the proposed method can identify the fault of K_t , the flat tire fault, and rule out M_u , the unsprung mass, as a fault; and that the proposed method can estimate the parameters accurately. The estimated switching time stamps also shows a good matching with the implemented values.

5 Conclusion

This paper presents an algorithm for simultaneous identification of fault parameters and mode switching stamps for hybrid systems. The deployment of GARRs makes it possible to formulate the system behavior in a unified form at all modes. For simultaneous identification of parameter fault and mode switching stamps, a unified formula is developed to cater for the difficult situation where mode switching occurs after the fault. GA is an effective tool in such a searching process for fault, switching time stamp sequence and IMC. An adaptive method is used to adjust the GA parameters to improve the system performance. In the application to the electro-hydraulic suspension system, the identification results show the effectiveness and efficiency of the proposed algorithm.

Acknowledgements

This work was supported in part by the A*Star SERC under Grant No. 0521160078.

References

- Arogeti, S., Wang, D., Low, C.B., Zhang, D.H., Zhou, J.: Mode tracking of hybrid systems in FDI framework. In: The 3rd International Conference on Robotics Automation and Mechatronics, Chengdu, China, September 21-24 (2008)
- Chen, H., Sun, P.Y., Guo, K.H.: A multi-objective control design for active suspensions with hard constraints. In: Proceedings of the American Control Conference, vol. 5, pp. 4371–4376 (2003)
- Chen, H., Guo, K.H.: Constrained H_∞ control of active suspensions: an LMI approach. IEEE Transactions on Control Systems Technology 13(3), 412–421 (2005)
- Karnopp, D.C., Margolis, D.L., Rosenberg, R.C.: System dynamics, modeling and simulation of mechatronics systems. John Wiley & Sons Inc., New Jersey (2006)
- Low, C.B., Wang, D., Arogeti, S., Zhang, J.B.: Monitoring ability and quantitative fault diagnosis using hybrid bond graph. In: The 17th IFAC World Congress, Seoul, Korea, July 6-11 (2008a)
- Low, C.B., Wang, D., Arogeti, S., Zhang, J.B.: Causality assignment and modeling approximation for quantitative hybrid bond graph fault diagnosis. In: The 17th IFAC World Congress, Seoul, Korea, July 6-11 (2008b)
- Luo, M., Wang, D., Pham, M., Low, C.B., Zhang, J.B.: Model-based fault diagnosis/prognosis for wheeled mobile robots: a review. In: The 31st Annual Conference of IEEE Industrial Electronics Society (IECON 2005), pp. 2267–2272 (2005)
- Lo, C.H., Wong, Y.K., Rad, A.B.: Intelligent system for process supervision and fault diagnosis in dynamic physical systems. IEEE Transactions on Industrial Electronics 53(2), 581–592 (2006)
- Mosterman, P.J., Biswas, G.: Behavior generation using model switching: a hybrid bond graph modeling technique. Transaction of Society for Computer Simulation 27(1), 177–182 (1995)
- Mak, K.L., Wong, Y.S., Wang, X.X.: An adaptive genetic algorithm for manufacturing cell formation. International Journal of Advance Manufacture Technology 16(7), 491–497 (2000)

- Merritt, H.E.: Hydraulic Control Systems. Wiley, New York (1967)
- Narasimhan, S., Biswas, G.: Model-based diagnosis of hybrid systems. *IEEE Transactions on System, Man and Cybernetics – Part A: Systems and Humans* 37(3), 348–361 (2007)
- Samantaray, A.K., Medjaher, K., Bouamama, B.O., Staroswiecki, M., Tanguy, G.D.: Diagnostic bond graphs for online fault detection and isolation. *Simulation Modelling Practice and Theory* 14, 237–262 (2006)
- Umarikar, A.C., Umanand, L.: Modelling of switched mode power converters using bond graph. *IEE-Proceedings Electric Power Applications* 152(1), 51–60 (2005)
- Wang, J., Wang, J.D., Daw, N.Q., Wu, H.: Identification of pneumatic cylinder friction parameters using genetic algorithms. *IEEE/ASME Transactions on Mechatronics* 9(1), 100–107 (2004)
- Zhao, F., Koutsoukos, X., Haussecker, H., Reich, J., Cheung, P.: Monitoring and fault diagnosis of hybrid systems. *IEEE Transactions on System, Man and Cybernetics– Part B: Cybernetics* 35(6), 1225–1240 (2005)

Author Index

- Adachi, H. 135
Arifin, Imam 213
Arogeti, Shai 257
- Bambang, Riyanto 213
Budiyono, Agus 27, 63, 191, 245
Byun, Doyoung 101
- Ce, Guo 145
- Goo, Nam Seo 101
- Haryanto, Ismoyo 245
Hashimoto, N. 135
- Ichida, Keisuke 205
Ishii, Kazuo 155
Izumi, Kiyotaka 83, 205
- Jiurong, Sun 145
Joelianto, Endra 227
- Kamada, Yuichi 205
Kato, S. 135
Komoriya, K. 135
Kubota, Takashi 11
- Lesmana, H. 27
Luo, Ming 257
- Meng, Ding 1
- Nakatani, Ichiro 11
Nassiraei, Amir A.F. 155
Nguyen, Quoc Viet 101
- Okamura, Kensaku 83
- Park, Hoon Cheol 101
Park, Joon Hyuk 119
- Qing-xian, Wu 1
- Setiawan, Joga Dharma 191, 245
Shimoda, Shingo 11
Subchan, Mochamad 191
Sudiyanto, T. 27, 63
Sutarto, Herman Y. 227
Syam, Rafiuddin 83
- Takahashi, Kei 11
Tanaka, Kouki 83
- Wang, Danwei 257
Watanabe, Keigo 83, 205
Watanabe, Yoshio 179
Wenbo, Wang 145
- Yamaguchi, Tomohiro 179
Yoon, Kwang-Joon 119
Yoshimitsu, Tetsuo 11
Yu, Ming 257
Yun-feng, Cao 1
- Zhang, Xinzhen 257
Zhen, Zhang 1
Zhendong, Dai 145